Franz Pölzl, BSc

Mechanical Behavior of Cold-Bent Insulating Glass Units

Master's Thesis

to achieve the university degree of

Diplom-Ingenieur

Master's degree programme: Civil Engineering and Structural Engineering

submitted to

Graz University of Technology

Supervisor

Univ.-Prof. Dr.nat.techn. Dipl-Ing. Oliver Englhardt

Assistant Supervisors

Dipl.-Ing. Vlad Alexandru Silvestru, BSc

Dipl.-Ing. Georg Kolany, BSc

Institute of Building Construction

Graz, January 2016

Affidavit

I declare that I have authored this thesis independently, that I have not used other than the declared sources/resources, and that I have explicitly indicated all material which has been quoted either literally or by content from the sources used.
The text document uploaded to TUGRAZonline is identical to the present master‘s thesis dissertation.

Date

Signature

Acknowledgement

Univ.-Prof. Dr.nat.techn. Dipl-Ing. Oliver Englhardt for supervising me during this Master's thesis and providing me many resources of the institute.

Dipl.-Ing. Vlad Alexandru Silvestru, BSc for supervising me, reviewing my work and giving me many advices.

Dipl.-Ing. Georg Kolany, BSc for supervising me and giving me advice about scripting.

Dipl.-Ing. Jakob Harden, BSc for giving me advice on how to critical assess obtained results from the finite element method.

Dipl.-Ing. Rita Spiegelberg, BSc for giving me advice on issues about numerical problems which occur at the contact between glass and subconstruction.

Manuel Mitterrutzner, BSc for helping me with the Italian translation of the abstract and for the final review of my work.

Felix Klein, BSc for the final review of my work.

Furthermore, I want to thank the whole team from the institute of building construction and anyone who contributed in any way as an advisor or motivator to my Master's Thesis.

Finally, but, most importantly, I want to thank my family and my friends for making it possible to finish my Master's Thesis by giving me the required energy end endurance for it.

Abstract

Cold-bent insulating glass is opening up new possibilities when it comes to the design of a smooth and aesthetic building skin. However, limited knowledge is available up to this point about the mechanical behavior of cold-bent insulating glass units (IGU). This is especially true for spacer and sealing. The objective of this Master's Thesis is to gather new findings about the mechanical behavior of IGUs during the cold bending process.

At first, a comprehensive state-of-the-art review about glass in general and curved glass for building facades is provided. With regard to the subsequent simulations, a deeper insight into the components of an IGU is given.

In the main part of this work, a comprehensive numerical investigation is carried out. The aim is to derive a basic understanding about the mechanical behavior of an IGU during the cold bending process. This work especially focuses on single-bent and double-bent IGUs. Moreover, the simulations also take heed of the edge-zone by not simplifying it too much during the calculation. All results are obtained by taking material contact interaction, geometrical non-linear effects and plasticity for spacer's material into account.

The single-bent IGU is deformed displacement controlled onto an arc-shaped subconstruction which has a constant radius. An extensive parameter study is carried out. Concerning the variation of geometric values, the thickness of the glass panes, the height of the cavity and the aspect ratio of the IGU is varied. Concerning the variation of material properties, the Young's modulus of the secondary seal and the material of the spacers is varied.

The double-bent IGU is statically supported at 3 corners and gets out-of-plane deformed by an imposed movement at the fourth corner. By this means, an anticlastic shape is obtained. Because the double-bent IGU is sensitive to different boundary conditions, a case study is carried out. From this case study, the best support situation possible is obtained which is used in a subsequent parameter study. The parameter study varies the thickness of the glass panes and the aspect ratio of the IGU.

This work analyzes stresses, strains and the deformations which are depicted in graphs. The outcome of the work is a valuable contribution to cold-bent IGUs in order to advance the research in this promising branch of facade engineering.

Kurzfassung

Kaltgebogenes Isolierglas erlaubt neue Möglichkeiten im Bezug auf eine glatte und ästhetische Fassadenkonstruktion. Problematisch ist jedoch, dass wenig über das mechanische Verhalten von kaltgebogenen Isolierverglasungen bekannt ist. Dies gilt vor allem für den Randverbund. Das Ziel dieser Masterarbeit ist es, neue Erkentnisse über das mechanische Verhalten von kaltgebogenen Isolierverglasungen mit Hilfe numerischer Simulationen herauszuarbeiten.

Zuallererst bietet diese Arbeit einen Überblick über den Stand der Forschung von Glas im Bauwesen sowie von gebogenem Glas. Im Hinblick auf die nachfolgenden Simulationen wird vor allem auf die Eigenschaften der einzelnen Komponenten von Isolierverglasungen (wie z.B. Abstandhalter) eingegangen.

Umfassende numerische Untersuchungen über das mechanische Verhalten von kaltgebogenen Isolierverglasungen werden im Hauptteil der Arbeit durchgeführt. Um den Umfang dieser Arbeit zu begrenzen, liegt der Fokus auf einachsig gebogenen sowie zweiachsig gebogenen 2-Scheiben Isolierverglasungen.

Die einachsig gebogenen Isolierverglasungen werden auf eine kreisförmige Unterkonstruktion aus Stahl gebogen. Dabei werden verschiedenste Parameter variiert. Bezüglich der Geometrie werden die Glasscheibendicken, der Abstand des Scheibenzwischenraumes sowie das Seitenverhältnis der Isolierverglasungen variiert. Bezüglich der Materialkennwerte werden der E-Modul des Silikons sowie das Material des Abstandhalters variiert.

Zweiachsig gebogene Isolierverglasungen werden an drei Eckpunkten gehalten und am vierten Eckpunkt aus der Ebene heraus gebogen. Dabei ensteht eine antiklastische Krümmungsfigur. Aufgrund der Sensibilität der zweiachsig gebogenen Isolierverglasungen gegenüber verschiedenen Auflagerbedinungen wird eine Fallstudie durchgeführt. Diese Fallstudie evaluiert die optimale Auflagersituation, welche für die nachfolgende Parameterstudie verwendet wird. Die Parameterstudie variiert die Glasscheibendicken sowie das Seitenverhältnis der Isolierverglasungen.

Alle Ergebnisse, welche Spannungen, Dehnungen und Verformungen sind, werden in Graphen dargestellt. Diese Arbeit soll einen wertvolllen Beitrag zu kaltgebogenen Isolierverglasungen bieten, um die Forschung auf diesem vielversprechendem Teilgebiet des Fassadenbaus voranzutreiben.

Abstract

Il vetro isolante curvato a freddo offre nuove possibilità per la realizzazione di strutture dalla facciata liscia ed estetica. Tuttavia, il fatto che il comportamento meccanico del vetro isolante curvato a freddo non è ancora bene conosciuto rappresenta una problematica, in particolare per quanto riguarda il bordo del vetro.

La presente tesi è finalizzata all'elaborazione di nuove osservazioni riguardanti il comportamento meccanico del vetro isolante curvato a freddo mediante l'aiuto di simulazioni numeriche. Prima di tutto, il presente lavoro offre una panoramica sul paesaggio della ricerca di vetro nel settore edile, nonché sul vetro curvato. Con riferimento alla simulazione numerica, vengono spiegate le caratteristiche dei componenti del vetro isolante come, ad esempio, il telaio distanziatore.

Nella parte principale della tesi vengono eseguite estese analisi numeriche sul comportamento meccanico del vetro Isolante curvato a freddo.

Ai fini di limitare l'ampiezza del presente lavoro, sono stati posti al centro dell'attenzione il vetro curvato monoassiale ed il vetro curvato a due assi.

Innanzitutto, il vetro curvato monoassiale viene piegato 1. mediante / 2. per formare un cerchio in acciaio. I parametri che vengono alterati riguardano la geometria ed i valori del materiale.

Tre angoli del vetro curvato a due assi vengono tenuti, mentre il quarto angolo viene piegato dal livello andando così a creare una curvatura anticlastatica.

Inoltre, data la sensibilità del vetro curvato a due assi, viene eseguito uno studio di caso. Questo studio determina la situazione ottimale del appoggio, la quale viene poi usata per il successivo studio dei parametri. Infine, tutti i resultati della tensione, dell' allungamento e della deformazione vengono rappresentati nei grafici.

La presente tesi è diretta a dare un contributo prezioso al tema riguardante il vetro isolante curvato a freddo.

List of Abbreviations

$t_{gp,i}$	Thickness of the glass pane i (1=glass pane 1, 2=glass pane 2)
u_i	Deformation in the i-direction (i=1 for x, i=2 for y and i=3 for z)
α_1	Scalar for estimating $\sigma_{max,pr}$ in the glass for a single-bent IGU
ε_{av}	Average strain
$\varepsilon_{true,abs}$	Absolute values of the true principal strain
$\varepsilon_{true,pr}$	Maximum true principal strain
σ_{av}	Average stress
σ_e	Von Mises stress
$\sigma_{max,pr}$	Maximum principal stress
BC	Boundary condition
E	Young's Modulus
EPDM	Ethylene-propylene-diene-monomer
EVA	Ethylene vinyl acetate
F	Required force for the cold-bending of an IGU
FE	Finite element
FEA	Finite element analysis
FEM	Finite element method
h	Height of the spacer and also height of the secondary seal
h	Maximum diameter of a finite element in chapter 5
HSG	Heat-strengthened glass
IG	Insulating glass
IGU	Insulating glass unit
K	Gaussian curvature
l_{gp}	Length of a glass pane
NURBS	Non-uniform rational basis spline
p	Shape function, order p
PC	Polycarbonate
PE	Polyethylene
PIB	Polyisobutylene
PP	Polypropylene
PS	Polysulfide
PU	Polyurethane
PVB	Polyvinyl butyral

PVC	Polyvinyl chloride
QA/QC	Quality assurance and quality control
r	Bending radius
R&D	Research and development
SF_6	Sulfur hexafluoride
SSG	Structural sealant glazing
t	Time $0 \leq t \leq 1$ which represents the progress of cold-bending
t_{gp}	Thickness of a glass pane
TPS	Thermoplastic spacer
TPU	Thermoplastic polyurethane
t_{sp}	Sheet thickness of a spacer
t_{sub}	Thickness of a subconstruction
TTG	Thermally toughened glass
u_{enf}	Enforced/imposed/controlled displacement at w(t=1)
w(t)	Enforced/imposed/controlled displacement as a function of t
WET	Warm edge technology
w_{gp}	Width of a glass pane
w_{sp}	Width of a spacer
w_{ss}	Width of a secondary seal
w_{sub}	Width of a subconstruction
Δu_3	Non-linear edge deformation
$\Delta u_{3,i}{}'$	First derivative of Δu_3 with respect to 1 spatial dimension
$\Delta\alpha$	Shear deformation
ν	Poisson's ratio

Contents

1 Motivation and Objectives

Curved building envelopes are highly coveted by architects and their clients who are striving for demanding esthetics of their constructions as a mutually satisfactory result. Particularly with regard to not only curved - but also large-sized glass panes - the complexity in the manufacture and design process is challenging [1]. In addition, no standardization of curved glass has been achieved yet in Europe [2] [3]. Hence, these architectural demands and challenges are a stimulating factor for the research on curved glass and related product development.

This Master's Thesis aims to provide a comprehensive and thorough parameter study about cold-bent insulated glass units by finite element (FE) simulations. From this, theoretical inferences can be drawn which can be assessed in laboratory experiments. A state-of-the-art review of all the related fenestration components will provide the reader with an efficient overview on insulated glass and curved glass geometry. Such a state-of-the-art background knowledge is essential in order to understand firstly, how to build a sensible numerical model and secondly, which designs are worthwhile to be investigated in the subsequent parameter study.

1.1 Examples of cold-bent glass structures

There already exist some innovative examples of cold-bent glass structures. In this subchapter, three of them - each with a different application - are presented.

In Figure 1 the IAC Headquarters, which is located in New York, is an example of a façade with cold-bent insulated glass. During the installation process, the floor-to-ceiling insulated glass was forced on warped steel frames on the building site which is the process of cold bending. [4]. Construction tolerances were crucial; therefore a new anchoring system had to be developed which could compensate them [5]. More information about the production of cold-bent glass can be found in subchapter 3.2.

Figure 1: IAC Headquarters in New York [4]

In Figure 2 the glass envelope of the railway station in Strasbourg is depicted. The facade is made by cold lamination bending, which is a further development of cold bending. This cold bending method allows to deform a curved glass pane in the factory instead of bending it on the construction site [6]. More information about the cold lamination bending process can be found in subchapter 3.2.3.

In Figure 3 a sketch of an experimental cold-bent glass bridge is shown. All single glass panes of the laminated safety glass had to be butted against each other. In order to avoid a weakening of the cross section, the glass panes had to be butted in an offset. The stiffness of the interlayer of the laminated safety glass had to be high to accomplish exceptional structural demands. Therefore, the widely used polyvinyl butyral (PVB) interlayer was unsuitable and the stiffer SentryGlass interlayer was used [7]. More information about interlayers can be found in the subchapters 2.5 and 4.2.

Figure 2: Strasbourg Railway Station [6]

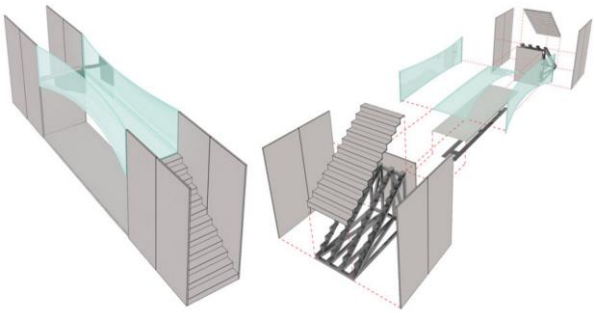

Figure 3: Cold-bent glass bridge [7]

1.2 Introduction and overview of the topic

Curved glass does not mean an approximation of a smooth façade by a polygonal chain through flat glass elements, but a consistent application of non-linear elements. Segmented glass does not create the sensation of a smooth surface. In addition, optical distortions in float glass like float lines and roller marks are visible in flat glass. In contrary to segmented glass, if the glass is curved, then these optical distortions became invisible and a smooth surface can be achieved. Nowadays, bent glass becomes gradually more economical as a result of R&D like moldless bending techniques, though it is still a challenging realm [8].

Certain structural-physical characteristics like a low U-value, airtightness, sound insulation, safety and permanent tightness against driving rain are indispensable. In Western Europe, gas-filled and pre-stressed insulating glass is prevalent [9]. National regulations and standards have to be fulfilled to obtain technical admission for windows and other glass façade products.

On the basis of all foresaid requirements, these are fixed boundary conditions for curved glass. Hence, all problems related to insulated curved glass have to subordinate themselves to these structural-physical problems.

2 State-of-the-Art Review: Insulating Glass

Insulated glass (IG) is made out of several glass panes which are aligned parallel to each other. The intermediate space between the adjacent glass panes, which is called cavity, is hermetically sealed. The glass panes are fixed onto a circumferential edge spacer system and additional sealing ensures demanded physical properties. IG is an indispensable façade element which melds the advantages of a transparent but at the same time thermal insulating and noise controlling element. IG also withstands wind loads and other type of loads as a secondary or tertiary structural element.

2.1 Properties of glass and glass products in structural glazing

In the field of structural glass, mostly soda-lime glass is used. Soda-lime glass has a theoretically high tensile strength through molecular bonding forces. Nevertheless, natural occurring and from the production process occurring surface defects are reducing the average tensile strength to a hundredth compared to the tensile strength on the molecular scale. If the tensile strength is exceeded, then crack tips or notches are the origin from where crack propagation starts. Due to the absence of plasticity, once started, the crack propagation under load is inexorable and sudden which leads to an undesired sudden failure which most building codes prohibit [13].

Glass is obtained from different raw minerals and is a transparent, amorphous material which can be produced very economically in large quantities. According to the standard EN 572, the final glass product for buildings consists out of 75% silicon dioxide (SiO_2), 13% sodium oxide (Na_2O) and 12% calcium oxide (CaO), minor traces of other oxides are also present [14].

According to [12] and [13], soda-lime silica glass has a Young's modulus of $70{,}000\ \left[\frac{N}{mm^2}\right]$, a Poisson's ratio υ of $0.23\ [-]$ and a thermal expansion coefficient of $9.0 * 10^{-6}\ \left[\frac{1}{K}\right]$.

Glass is an ideal elastic, isotropic and homogenous material which fails brittle. Local occurring stress peaks cannot be redistributed because glass has no plastic properties at all. Hence, exceeding the material resistance leads to a sudden failure of the glass through cracking [17]. From this follows, that it is essential to ascertain the location

and the value of all occurring stress peaks in the glass, because just a single stress peak will be the origin of failure if it is exceeding the materials resistance. Prevalently, such kind of engineering problems are conducted with aid of finite element analysis (FEM) whereas the calculation of stress peaks is still a challenge. Stress peaks often coincide with singularities; for instance, both may occur at a corner of a glass pane, and the problem is that a mesh refining in the vicinity of a singularity usually leads to an overestimation of the stress peak. Consequently, the brittle behavior of glass necessitates sophisticated numerical models to predict stress peaks in the glass.

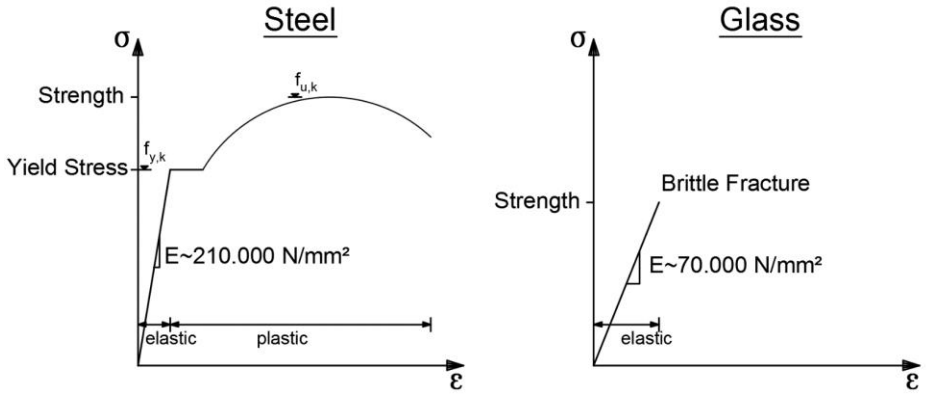

Figure 4: Stress-strain curves of steel and glass for an uniaxial tensile loading scenario, redrawn from [18]

Glass is notch-sensitive therefore very small notches on the glass surface will lead - under a certain constant load - to failure, which is called subcritical crack growth. As a consequence, the resistance of glass for long load durations is significantly lower than for short load durations [19].

Because the design principle of the Eurocode standard demands structural failure with prior announcement, ductility is crucial. This demand can be fulfilled in structural steel design through the ductility of steel or in concrete construction through a minimum amount of reinforcement [20]. However, in structural glass a certain residual load bearing capacity is demanded after a brittle failure of a glass structure. For instance, for an overhead glazing the glass pane as a whole must not fall down after failure as well as glass splinters which are exceeding a certain size.

Through pre-stressing of glass, which is carried out chemically or thermally, surface defects of the glass undergo internal pressure whereas the bending resistance and residual resistance are altered by the pre-stressing process.

Toughened glass has the highest bending strength but the lowest residual strength because it breaks into small dices. Heat strengthened glass has a lower bending resistance than toughened glass but a higher residual strength because the splinters are bigger. Annealed glass will break into big glass fragments which leads to a good residual strength. However, if annealed glass is exposed to high in-plane loads, the breaking pattern is similar to heat strengthened glass.

Heat-strengthened glass melds the expectations of a good bending resistance and a good residual load bearing capacity and hence is most suitable for common structural glass applications. Before the glass undergoes the pre-stressing process, all mechanical works like chamfering, cutting, drilling and grinding must be completed [21].

The overall residual strength of a glass construction can be considerably enhanced if laminated glass is used due to the interaction of the interlayer with the glass. Some types of common intermediate layers are polyvinyl butyral (PVB), ethylene vinyl acetate (EVA), thermoplastic polyurethane (TPU) or ionoplast interlayers (Sentry Glass®). Of special interest is the overall shear strength of the interlayer and the loss of stiffness as a function of increasing temperature. In addition, optical clarity, ageing resistance, relaxation and viscoelastic properties of the interlayers are all important criteria, therefore interlayers have a great influence on the final properties of fenestration products.

The production of laminated glass happens generally under an autoclave environment. However, due to high initial costs of machinery for companies, R&D is carried out in order to abolish autoclave lamination in the future [22].

2.2 Glass panes

According to [14], 95% of all flat glass is produced by the float glass method. Therefore, the focus of this subchapter lies on float glass.

The standard production thickness of float glass varies from $2.0\ [mm]$ to $25\ [mm]$ according to [19]. Maximum dimensions of float glass are limited through the production process whereas the width significantly influences the cost of a float glass. Maximum dimensions are $3.20\ [m]$ in width and $6.00\ [m]$ in length according to [14] or

$3.00\ [m]$ in width and $10.00\ [m]$ in length according to [20]. However, the maximum width should be chosen after consultation with the manufacturer in order to avoid waiting times, production problems such as deficient quality and unexpected costs.

Thermally toughened glass (TTG) has a much higher bending strength than float glass due to its thermal pre-stressing process. However, its residual strength is low because in case of failure, TTG breaks into small glass splinters.

Heat-strengthened glass (HSG) is thermally pre-stressed glass with a splinter pattern like annealed glass. The purpose of HSG is to have an increased strength compared to float glass but also with a certain residual strength which is ensured by large glass splinters in case of failure [18].

Annealed glass is heated up to its annealing point in order to relief internal stresses. Annealed glass is cautiously cooled down [23]. Annealing of glass is a common process which most float glass products undergo, therefore HSG and TTG are products which are made from annealed glass. At the end of the float glass production process, float glass becomes annealed glass [24].

In Figure 5, the stress distribution over the thickness of a thermally pre-stressed glass pane is depicted whereas the internal stress distribution is parabolic and the stress from an external loading is linear. As a result, the obtained advantage from pre-stressing is a reduced maximum tension stress, were (-) is pressure and (+) is tension.

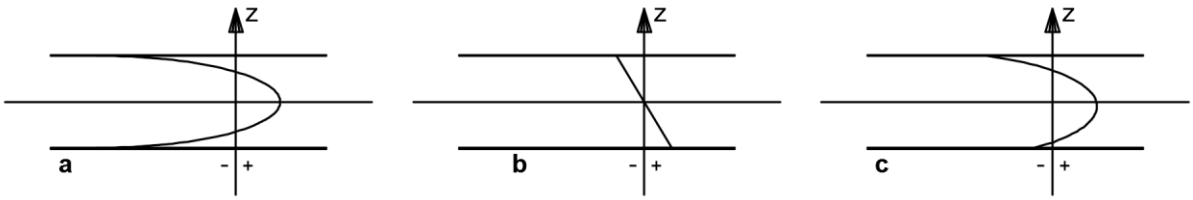

Figure 5: (a) Thermally pre-stressed glass pane, (b) External loading, (c) Sum of (a) and (b), redrawn from [19]

According to several glass standards like DIN 18008, ÖNORM B3716 or ASTM C1172, laminated safety glass is demanded for most applications, especially for horizontal load bearing glass and overhead glazing. In general, laminated safety glass is preferred because of a high residual strength. The minimum requirements for residual strength are depending on the field of application thus some easements or stricter requirements can result from that [19].

Type of glass	Bending strength	Required Characteristic strength	Residual Compressive surface stress	Quality Standards	Breakage characteristics
Annealed glass	Low	45 N/mm² (EN 572-1, ÖNORM B 3716-1, DIN 1249-10)	-	ASTM C 1036, EN 572-1, EN 572-2	Forms sharp edged, pointed shards
Heat strengthened glass	Higher than annealed glass	75 N/mm² (EN 1863-1) 70 N/mm² (ÖNORM B 3716-1)	24-69 N/mm²	ASTM C 1048, EN 1863-1	Similar to annealed glass
Toughened glass	Higher than heat strengthened glass	120 N/mm² (EN 12150-1, ÖNORM B 3716-1, DIN 1249-12)	Over 69 N/mm²	ASTM C 1048, EN 1250-1	Breaks into small, relatively blunt glass fragments (dice)

Table 1: Summarized data of different safety glasses used as structural materials [23] with additional references from ÖNORM and DIN standards

2.3 Edge region of IGUs

The edge region of an insulating glass unit (IGU) poses a thermal bridge whereby low thermal conductivity is essential for a state-of-the-art IGU. Therefore, most designs will aim at a low U-value. Of course, the edge region of any IGU has to be air-tight to retain its gas filling and prevent the IGU from damage and deterioration. Additional demands like a certain sound insulation, a certain fire resistance class and various other criteria have to meet the standards and approvals of local authorities. Finally, an edge region will consist of various components, whereas every component will likely be made out of a different material.

This is cumbersome when it comes to an evaluation in the stress distribution of the edge region. Therefore, the aim of this subchapter is to take a closer look at every single component, in order to be able to draw conclusions on how to build a numerical model in a reasonable way.

All glass panes of an IGU have to be adhered on a seal whereas contemporary windows are made out of a primary and a secondary seal. A spacer bar, which

normally is made out of a stiffer material than the seal itself, like aluminum or stainless steel, will ensure a controlled force flow and small deformations. Disadvantageous about such metallic spacer bars is, that they are limiting the thermal performance, because they act as a thermal bridge. A desiccant, which often is enclosed in a spacer bar and also the primary sealant and secondary sealant are components which have a great impact on the thermal performance of the stress distribution in the edge region.

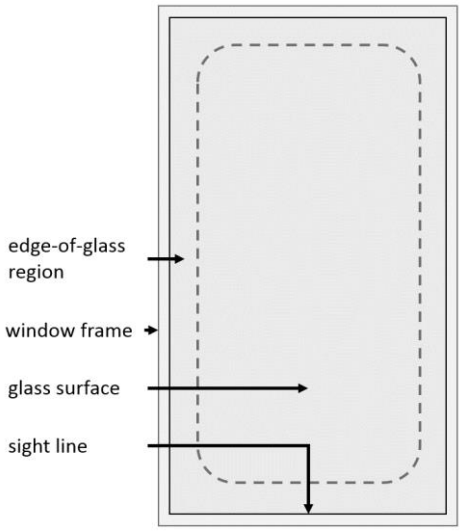

Figure 6: Centre region and edge region of an IGU, redrawn from: [25]

2.4 Primary and secondary seal

Most commonly used as a primary seal is polyisobutylene (PIB). PIB as a primary seal acts as a water and gas barrier. However, its strength is sensitive to temperature, therefore the primary seal is not sufficient to ensure durability of the whole IGU [25].

According to the numerical parameter study of [26] the primary sealant is attached on both sides to a metallic spacer. This lead to the conclusion that the metallic spacer with the butyl strips adhered on both sides can be interpreted as a cooperation of three springs in a row.

Moreover, the numerical parameter study concluded that the primary sealant - which in this case are both butyl strips - plays a key role in mechanical behavior because their material flexibility is much lower compared to other components of the edge region [26]. A cross section through the edge region of a typical IGU is shown in Figure 7 which shows the position of the primary seal and the secondary seal in the IGU.

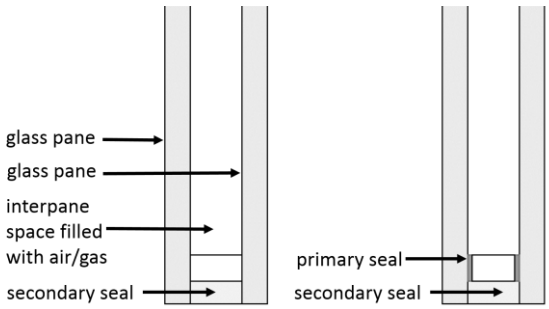

Figure 7: Cross section through the edge region of an IGU, redrawn from: [25]

Furthermore, the butyl strips can be modelled with a hyperelastic material behavior if the load scheme complies with a monotonous compressive load scenario [26]. In the numerical parameter study of [26] the butyl strip was modeled isotropic linear-elastic whereas the poisons ratio υ was close to $0.5\ [-]$ (rubbery behavior). PIB is highly nonlinear therefore a more sophisticated material law for butyl is required which is able to describe load cycling scenarios by taking the load history into account [26].

PIB is an elastomer and polymer which is superior to other polymers in several aspects. For example, it is practically impermeable to gases. In comparison to other polymers, the viscosity and the relaxation behavior do have a less pronounced temperature dependency [27].

The secondary sealant is also called edge sealant and holds the spacer bar in place [26].

The secondary sealant must restrict movement of the edge zone and is responsible for holding the whole edge zone in place. Like the primary sealant, the secondary sealant acts also as an adhesive. As secondary sealants, Polyurethane (PU), silicone (Si) and polysulfide (PS) are widely in use, furthermore hot-melt butyl- or epoxy-based sealants are also conceivable [25].

All of these aforementioned materials which are used as a secondary sealant have a higher gas permeability than PIB therefore the primary seal provides substantial contribution to the gas impermeability whereas the secondary sealant does not [25].

Because the secondary sealant is a relatively big component of the edge zone it has a significant impact on the overall thermal performance [25]. Therefore, knowledge of the used material is desirable. According to [25] PIB has the lowest thermal

conductivity with a value of $0.2\ \left[\frac{W}{m^2K}\right]$ followed by butyl rubber, PU, silicone and finally by PS, whereas the last one has a thermal conductivity value of $0.4\ \left[\frac{W}{m^2K}\right]$ [25].

Also [28] found that the thickness of the sealant has a large influence on the thermal performance if metal spacer bar systems with low thermal conductivity (below $2\ \left[\frac{W}{mK}\right]$) are used [28].

Secondary sealants can have a thermal conductivity which can be as low as $0.24\ \left[\frac{W}{m^2K}\right]$ which is not groundbreaking in comparison to other high performance products. However, secondary sealants are acting as adhesives, sealants, have to limit movement and have to be durable at the same time which might limit further development [25].

Silicone has a 30% higher UV resistance compared to PU and PS and is therefore used in structural sealant glazing facades. Silicone is the only sealant which is internationally approved as a secondary sealant and as a structural bonding plastic [27].

Ozone and oxygen are also a further reason for polymer degradation beside from UV radiation. PU and PS are vulnerable to ozone and oxygen especially in combination with UV exposure. Moreover, water also leads to degradation of the sealant. In particular, PU is very sensitive to water degradation even at ambient temperature [27].

2.5 Interlayer

Laminated safety glass is made out of at least two panes which are connected through one more intermediate layers [29]. The interaction of laminated safety glass is ensured through a certain shear stiffness of the intermediate layer.

In Figure 8, the stress distribution resulting from external loading over the thickness of a laminated glass is illustrated. Note that the offset of the stress distribution between the PVB interlayer results from partial shear connection. The stress distribution is linear in the glass but nonlinear in the PVB interlayer.

An interlayer is important to increase the overall strength of a glass construction through shear force interaction. Moreover, in case of glass failure, the job of the

interlayer is to ensure residual strength and to hold the glass splinters in place to prevent them from falling out and therefore from doing damage and causing injuries. Thus, some general statements can be specified about interlayers, which can be expressed by the following quotation: *"If an interlayer is too soft or adhesion with glass is too low, then the interlayer will not have the strength to resist high wind loading after an impact. On the other hand, if the interlayer is too stiff and adhesion to glass is too high, then the interlayer will not have a high level of impact resistance"*[1] [23]. In conclusion, this means that the stiffness is crucial because it allows to diminish occurring stress peaks in the glass to a certain degree as well as the adhesion properties which ensure the shear flow at the interface between interlayer and glass.

Misalignments have to be smaller for safety glass with bonding resin than for laminates because the glass panes must be aligned manually [29].

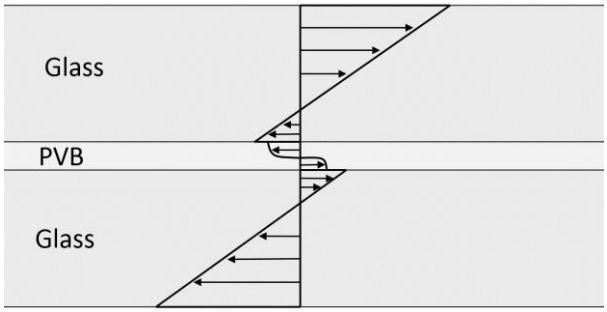

Figure 8: Stress distribution of a laminated safety glass due to partial shear of the PVB interlayer, redrawn from [30]

Interlayers are made out of either polyvinyl butyral (PVB), ethylene vinyl acetate (EVA), thermoplastic polyurethane (TPU) [31], ionoplastic polymer (commonly known under the brand name Sentry Glass ®) [32], polyethylene (PE) [33], polycarbonates [23] or bonding resin [29]. A more in-depth description of these aforementioned interlayer is provided in subchapter 4.2.

2.6 Spacer bars

Spacer bars can be divided into metallic and non-metallic spacers whereas metallic spacers are more common but less effective in hindering heat transmission. In

[1] Citation from [23], Chapter 3.1, Page 1266

addition, there are composite systems which are made out of a metallic spacer which is coated with a polymer to improve thermal performance.

Apart from conventional spacers, improved spacer bars have been introduced whereas design improvements mainly focused on less thermal conductivity. The abbreviation WET which means "warm edge technology" relates to such kind of spacer bars as well as other improved components in the edge zone of the IGU [25].

WET spacer bars can be defined according to [34]: *"WET spacer bars have either a thermal break in the spacer assembly or are constructed of materials with low thermal conductivity"*[2].

Spacer bars can have a significant influence on the overall thermal performance of a window, according to [25], in the case of a high-performance window, it is possible to improve the overall U-value of a glazing unit up to 12% by the choice of a high-performance WET spacer bar instead of a conventional metallic spacer bar.

However, if the thermal conductivity of the spacer bar is roughly about or bigger than $2\ \left[\frac{W}{mK}\right]$ then an improvement of the overall U-value of a window is negligible [25].

A high risk of condensation and high heat flux rate originates from metallic spacer bars due to their high thermal conductivity [25].

In general, non-metallic spacer are superior over other types of spacer systems when it comes to thermal performance [35] [36].

"…it is clear that non-metal spacer are the most promising future approach for window spacer designs. Among non-metal spacer materials, foam exhibits overall good thermal performance, generally somewhat better than thermoplastic spacer"[3] [25].

The classification of spacer bar designs in this subchapter is leaned on [35] and [25]. In Figure 9 three different spacer designs are depicted whereas these were investigated regarding to their thermal performance by [34]. The spacer bar design to the very left had an outstanding thermal performance, in the middle of the image, a conventional aluminum spacer bar is shown and to the right, a thermally broken aluminum spacer is shown, which is a further development of the conventional aluminum spacer bar.

[2] Citation from [34], Chapter "Improved Spacer Bar Design Enhances Window Performance", Page 1
[3] Citation from [25], Chapter 6, Page 22

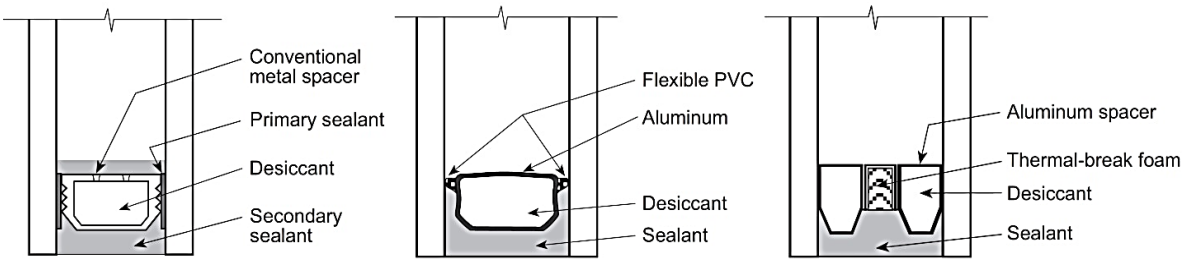

Figure 9: Different spacer bars [34]

2.6.1 Metallic spacer

Spacer bars made from **stainless steel** have a much lower thermal conductivity than spacer bars which are made from aluminum or galvanized steel. For most of stainless steel spacer bar systems the thermal conductivity is below $1\ \left[\frac{W}{mK}\right]$ regardless of whether they are dual-sealed or single-sealed [25] [28].

It was found, that the sheet thickness of a stainless steel spacer bar influences the overall thermal performance of the window system, which is not obvious, because this is not true for other metallic spacer bars. So called improved metal spacer can be U-shaped or thermally broken instead of being D-shaped to interfere the heat flux [28] [25].

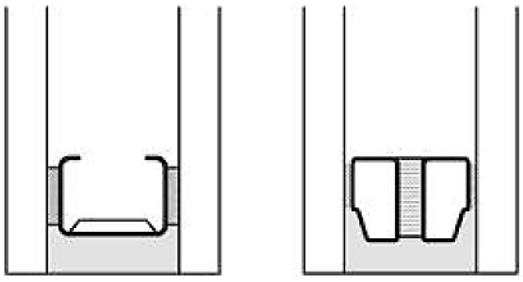

Figure 10: Improved spacer bar design, to the left: U-shaped metallic spacer bar, to the right: a thermally broken metallic spacer bar [25]

Spacer bar systems made from **galvanized steel** have a thermal conductivity between $1\ \left[\frac{W}{mK}\right]$ and $3\ \left[\frac{W}{mK}\right]$ whereas dual-sealed systems perform slightly better than single-sealed systems [28] [25].

Aluminum is a conventional material for metallic spacer bars. Due to aluminum's relatively high thermal conductivity, such kind spacer is posing a higher risk to condensation and mold formation than spacer bars which are made out of other

materials. Beside from conventional D-shaped aluminum spacer bars, where the heat flux can flow straight through, there are also thermally broken aluminum spacer. These thermally broken aluminum spacer usually are combined of two narrow spacers with a thermal breaker in the middle. Obviously, the thermal breaker should have a lower thermal conductivity than aluminum. The material of the thermal breaker normally is PU [37].

In [37] the difference of conventional and thermally broken aluminum spacer was numerically investigated. The findings showed a lower heat flux and a higher inner surface temperature for the whole edge region of the window system (IGU and window frame) if the thermally broken aluminum spacer was used instead of the conventional one [37].

In [28] a whole variety of spacer bars were investigated with regard to their thermal performance. The findings of the study show that different aluminum spacer bar systems as well as galvanized-steel spacer bar systems vary largely in their thermal conductivity. But, on the other hand, if the thermal conductivity of the spacer is too high (roughly higher than $2\ \left[\frac{W}{m^2K}\right]$) then the spacer does not affect the thermal performance of the whole window system anymore. Furthermore, the thickness of the aluminum spacer as well as the galvanized-steel spacer does not improve or worsen the thermal performance of the overall window system [28].

Most dual-sealed aluminum spacer bar systems have a thermal conductivity of around $2\ \left[\frac{W}{mK}\right]$, most single-sealed aluminum spacer bar systems have a thermal conductivity of around $4\ \left[\frac{W}{mK}\right]$ but these systems can reach up to even $8\ \left[\frac{W}{mK}\right]$. Therefore it can be stated that single-sealed aluminum spacer bar systems are not state-of-the-art anymore [28] [25].

2.6.2 Composite spacer

Composite spacers are made out of more than one material in order to improve thermal performance. Normally composite spacers are metallic spacers with incorporated non-metallic components with low thermal conductivity. Often, the components of composite spacer are low conductive plastics, a moisture barrier, a top coating which is desiccated and a stiffening component. Alternatively, also structural

foams can be used for composite spacer which are often either silicone or ethylene-propylene-diene-monomer (EPDM) [25]. Most composite spacer bar products normally have an effective conductivity which ranges from $0.3\ \left[\frac{W}{mK}\right]$ to $0.6\ \left[\frac{W}{mK}\right]$ [25].

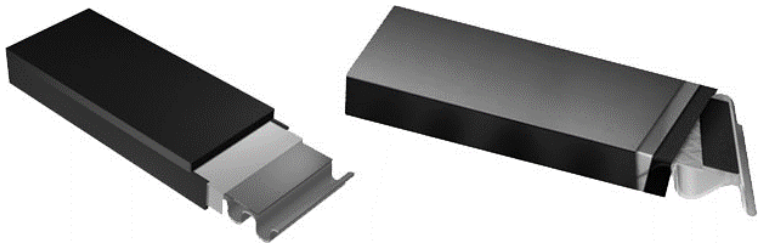

Figure 11: Two different composite spacer systems [37]

2.6.3 Non-metallic spacer

It was found that all non-metallic spacer systems have a very low thermal conductivity compared to metal spacer systems. It is important to notice that non-metallic spacer systems cannot be distinguished into dual-sealed and single-sealed. Thermal conductivity of non-metallic spacer have been found to be always below $1\ \left[\frac{W}{mK}\right]$ and can be as low as $0.15\ \left[\frac{W}{mK}\right]$ for foam spacer from Edgetech® [28] [25].

Foam spacer are made out of structural foam. This structural foam is either silicone or EPDM with incorporated desiccant. Depending on the foam spacer system the desiccant ratio can be up to 40%. The thermal conductivity of foam spacer is the lowest of all spacer systems and ranges from $0.15\ \left[\frac{W}{mK}\right]$ up to $0.22\ \left[\frac{W}{mK}\right]$ [25].

Thermoplastic spacers are made from either PIB alone or a mix out of PIB and synthetic rubber. The desiccant is incorporated in the mix like in foam spacer. Thermoplastic spacer, often abbreviated TPS, have a slightly higher thermal conductivity than foam spacer which lies between $0.25\ \left[\frac{W}{mK}\right]$ and $0.30\ \left[\frac{W}{mK}\right]$ [28] [25].

In comparison to conventional spacer bar systems, thermoplastic spacer systems are different to manufacture which also leads to a different final IGU. Because a thermoplastic spacer replaces the primary seal, the desiccant and the former metallic spacer bar, the manufacturing process becomes much easier [38]. As it is illustrated in Figure 12, the desiccant is incorporated in the thermoplastic spacer and an elastomeric sealant is in charge of the tasks of the secondary sealant.

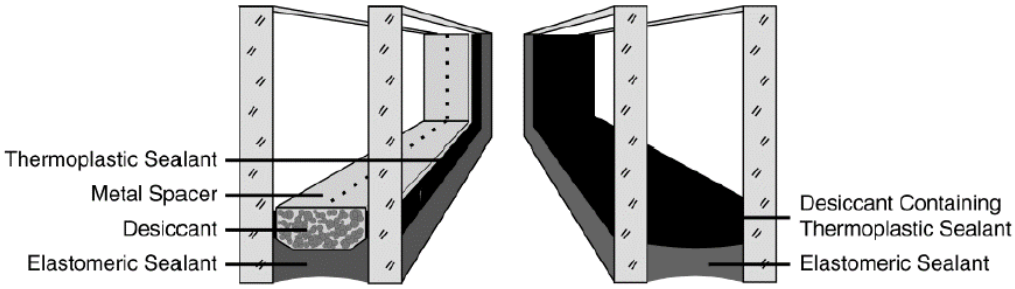

Figure 12: On the left side, a traditional edge seal system is depicted, on the right side, a thermoplastic edge seal system is depicted [38]

2.7 Cavity

The intermediate space between the glass panes of an IG is called cavity. The cavity of an IG is hermetically sealed to ensure durability and a low overall conductivity of sound and heat. Due to hermetically sealing, the cavity is exposed to cyclical pressure differences which are posing a long-term dynamic load which can initiate crack growth in brittle and therefore aged plastics of the edge-sealing. Heat loss happens, as generally known, through radiation, convection and transmission. Crucial for the cavity in order to lower the heat loss rate is a low convection rate which is controlled through the distance between the adjacent glass panes. Furthermore, by replacing the air with a gas which has a lower thermal conductivity, the thermal conductivity gets lowered even further.

A leaking cavity leads to the onset of several deterioration mechanisms and will finally terminate the service life of the glazing unit, therefore a lot of deterioration mechanisms which are treated in subchapter 2.8 are related to the aforementioned problem.

2.7.1 Gas fillings

The cavity width and the enclosed gas are affecting the thermal conductivity as well as the sound propagation. For most applications, a low thermal conductivity is desired in the first place therefore the air is replaced by a noble gas like argon, krypton or xenon whereas argon is the cheapest and therefore most used noble gas [39].

Sulfur hexafluoride gas (SF_6) improves sound insulation due to its high mass which lowers the speed of sound. Recent R&D aims to replace the potent greenhouse gas SF_6 by a less harmful gas and instead fulfill those noise control requirements through an improved window design [40].

Argon as a gas filling is economical because it reduces thermal conductivity of the IG up to 25% and is relatively cheap at the same time. However, when the argon concentration of conventional IGUs was measured at a construction site in Canada, 61% of all cavities had an argon concentration below 50% ($n = 100$ window units) [41].

In another QA/QC (abbreviation for quality assurance and quality control) case, 111 out of 245 window units had an argon concentration below 50% which means the argon concentration is so low that it has no impact anymore. The survey suggests that such a fault is caused by manufacturing error and that it is very improbable that this low argon concentration comes from argon loss [42].

Thus it appears that the gas concentration of an IGU is also a parameter because the QA/QC field studies show that it must be assumed that the noble gas content of a brand new IGU will vary in a wide range. However, declared U-values will match the reality if they are obtained through empirical studies.

By using krypton or xenon instead of argon as a gas filling component, the U-value of the IG can be improved even more whereas xenon is superior over krypton. Krypton is often used in triple glazing windows in order to produce a narrower cavity gap and also to decrease the weight of the window. Due to relatively high acquisition costs, xenon is more seldom used than krypton. It is also possible to mix different type of gases to obtain a certain gas blend [43] [35].

According to EN 1279-3 [44] loss rate of gas from inside the cavity must be lower than 1% per year if the concentration of the gas is higher than 15%.

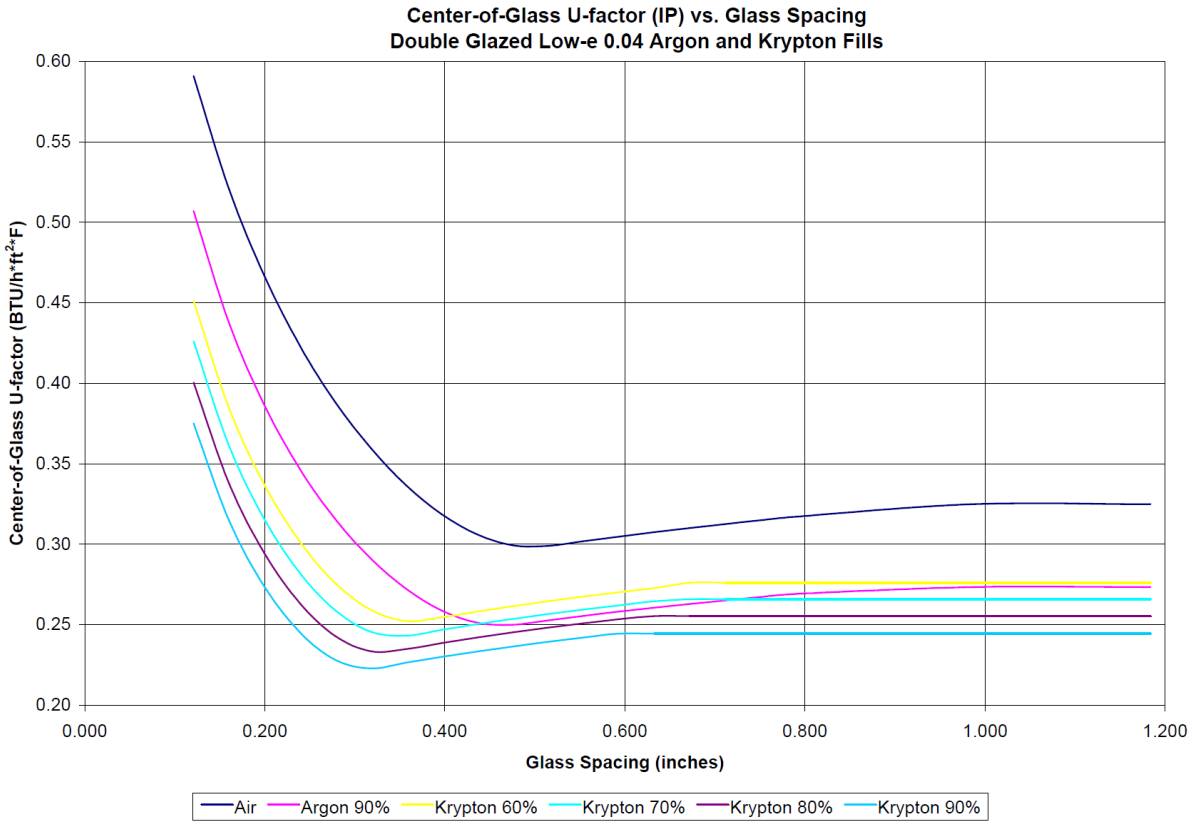

Figure 13 Center-of-Glass U-factor vs. Glass Spacing for different gas fillings and gas filling blends [43]

2.7.2 Internal pressure

The internal pressure of the cavity of an IG is not constant but it depends on various parameters like the pressure at the production site of the IGU and its initial volume, the climate load and the deformation capacity of the IGU which eventually **leads** to different cavity volumes. A gas pressure difference between outside and inside the cavity will lead to a deformation of the glass pane were the equilibrium between the deformed cavity volume and cavity gas pressure is found with the external gas pressure. It is difficult to find this equilibrium for curved IG through calculation.

For flat IG there are standards like ÖNORM B 3716-1 [45] which are providing convenient formulas, suitable for hand calculation. Applying the constant gas law, which provides a relationship between volume and pressure, there are two limit states which are firstly, the isochoric and secondly, the isobaric state whereas the equilibrium will lie practically always between these two states [45]. The internal pressure for curved IG under consideration of various parameters like climate load can be calculated according to [45] which can be helpful for a validation of a numerical model.

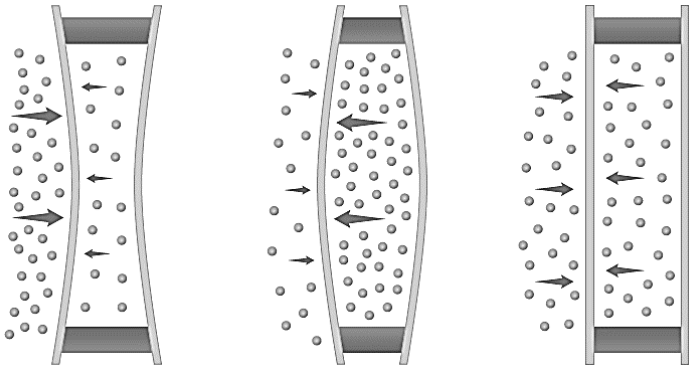

Figure 14: Climate loading [43]

In Figure 14 the climate loading is shown in principle. Inside the cavity, the volume of the gas is enclosed and cannot change, but temperature changes are forcing the cavity gas to expand or to contract. Simultaneously, the barometric pressure of the atmosphere is changing. Furthermore, an average shift in atmospheric pressure is omnipresent due to sea level difference between factory and building site. To the left of the image, a high atmospheric pressure coincides with a low cavity temperature, in the middle, a low atmospheric pressure coincides with a high cavity temperature and to the right of the image an equilibrium is found.

2.8 Deterioration mechanisms

Transparency of an IGU is impaired through condensation, moisture fogging, volatile fogging, chemical fogging and corrosion of glass coatings [41]. Algal formation and dust from the air can accumulate at the surface of a glazing unit for which self-cleaning glazing systems with special coatings of polymers with hydrophilicity are available [35].

Volatile fogging is a process where volatile organic compounds escape a desiccant which is not designed to be tight at high temperatures. These volatile organic compounds will condense on the cooler surface parts of the cavity. Volatile fogging can subsequently lead to corrosion of glass coatings and damage glass sealants. In order to avoid volatile fogging, a desiccant which is able to absorb a sufficient high amount of volatile organic compounds and hold them captive at high temperatures is required [41].

Chemical fogging is triggered for instance by organics in sealants, cleaning agents, polymeric spacers and other polymeric parts of the IGU [46].

Organics which float around in the gas mixture of the cavity will react with the moist glass surface. As a consequence, the glass surface gets optically impaired. This process is called chemical fogging.

In order to avoid chemical fogging, the porosity of the sealant plays an important role. A sealant with a porosity of $3.0 * 10^{-3}$ $[m]$ exclusively absorbs water vapor where silica gel with a porosity between $20 * 10^{-3} \leq porosity\ of\ silica\ gel \leq 200 * 10^{-3}$ $[m]$ will absorb a whole variety of problematic substances. A blend made out of these two aforementioned components is able to avoid chemical fogging [25].

In order to avoid **moisture ingress** into the IGU, the primary seal has to act as a vapor barrier. The primary seal deteriorates over time through physical or chemical attacks which will allow vapor - and for some types of chemical attacks - also water to penetrate into the cavity. Often, isobutylene is used as a primary seal which is tight against water vapor but susceptible to chemical attacks in general and especially to UV-radiation. Foils or setting blocks which are made out of EPDM are containing plasticizer which can come in contact with the isobutylene. Once happened, the primary seal gets chemically destroyed. [47]. Therefore, the chemical compatibility of window components and a good window construction are necessary to avoid moisture fogging. As a result, a too high rate of moisture ingress over time into the cavity of an IG leads to condensation for sufficient low temperatures.

Condensed water will shorten the life cycle of any IGU whether the condensation happens outside or inside an IG but condensation inside the cavity of an IG is a much more severe problem. Rooms with high relative humidity are prone to condensation.

When it is not possible to avoid condensation, it is sometimes necessary to control the temperature through an electronic controller, accordingly electrical heated glazing is an unobtrusive architectural solution and the energy need is relatively low [48].

The main cause for a failure of an IGU is water vapor condensation in the cavity. Hence, the edge seal must have a very low moisture vapor transmission rate which will extent the service life [25].

Through a water film on the glass pane, Sodium, Calcium and Magnesium are chemically extracted which leads to glass corrosion [19].

Also important to consider is the sea level difference between the place of manufacturing and the construction site because the average barometric pressure can be considerably high. Resulting from that, an average pressure difference occurs which will bend the glass. Consequentially, over time, creeping effects will resulting from that constant pressure and under the influence of temporarily high temperatures this will lead to a displacement of the edge spacer [41].

Gas loss happens through the sealant of the edge zone. In General, the primary sealant is responsible for retaining the gas inside the cavity. External loads and climate load leads to permanent movement in the edge zone which further lead to gas loss because the primary sealant gets impaired by this movement. The gas loss rate has to be lower or equal to 1% per year according to the EN 1279 A low gas loss rate is substantial in order to ensure a long service life. Argon gas concentration can be measured either by spark emission spectroscopy, which is a non-destructive testing method, or by invasive gas chromatography [50].

3 State-of-the-Art Review: Curved Glass

Curved glass has its challenges, not only with regards to geometry and structural design but also to put it into practice. Therefore this main chapter is divided into two main parts, in chapter 3.1, the geometry of curved glass is treated and in subchapter 3.2, different ways to produce curved glass are introduced. However, to enable a functional state-of-the-art building skin, curved insulating glass must be used which is described in subchapter 3.3.

3.1 Geometry of curved glass

This subchapter is dedicated to the geometry of curved glass. Theoretically, the geometry of curved glass can be any arbitrary shape. Nevertheless, it can be convenient to divide the geometry into single curved glass, double curved glass and arbitrary formed glass whereas an arbitrary geometry still should be derived from geometrical relations in order to be analyzable. This classification correlates with manufacturing complexity, calculation efforts and building costs. Single curved shapes are the easiest to manufacture and to calculate while arbitrary shapes cause high costs and are complex to manufacture.

3.1.1 Single curved glass

Single curved glass is in use since the 18th century. At that time annealed glass was cold-bent - mainly for building skins of greenhouses [49].

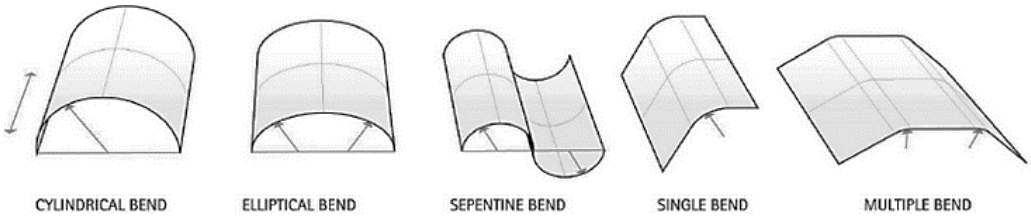

Figure 15: Single curved glass shapes [52]

ASTM C 1464 [53] divides single curved glass into cylindrical bent, elliptical bent, serpentine bent, single bent and multiple bent which are also depicted in Figure 15. Curved glass has in general a higher bending moment resistance due to its geometry [51].

From a single glass pane which is cylindrical shaped, the paper in [49] derived a simple relationship where E is the Young's modulus, t is the thickness of the glass and r is the bending radius

$$\sigma = \frac{Et}{2r} \qquad \textit{Equation 1}$$

Where σ is the maximum stress caused through the bent geometry. It is easy to figure out which parameters are responsible for the internal bending stress. Based on the fact that in practice a certain geometry thus radius is demanded, the only parameter that is left to vary is the thickness t of the glass pane, which consequentially should be as thin as possible.

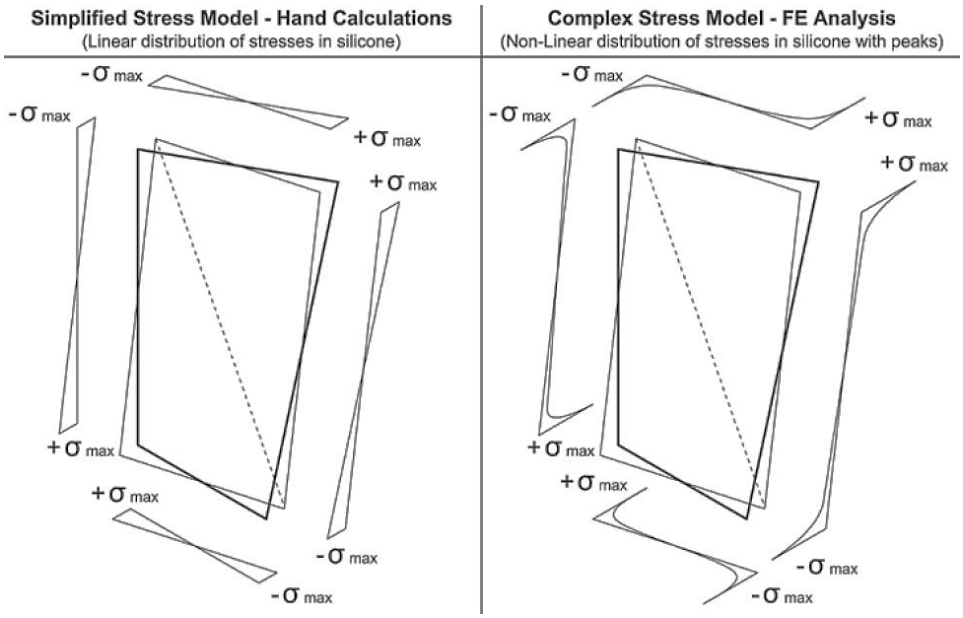

Figure 16: Stress peaks occur in a FEM analysis for a curved SSG façade compared to a hand halculation [52]

For a hand calculation of structural sealant glazing facades (SSG facades) it can be assumed that the constraint stress from the glass is equally distributed to the sealant and that the stress distribution is linear. For that reason, the stress distribution can easily be calculated by hand. For a FEM analysis, stress peaks will occur at the corner of the glass. Mainly the constraint stresses at the edge of the glass are a function of the shear displacement of the seal, which itself is depending on the degree of warping. That means, as expected, that the higher the warping is the higher the constraint forces are [52].

According to [52] it is possible to cut the stress peaks of a FEM analysis out for a maximum of 1.5 of the bite dimension because the stress peaks occur in a very small area. In the end, a hand calculation will give more conservative results compared to a FEM analysis which is neglecting the stress peaks.

3.1.2 Double curved glass

Double curved surfaces can be differentiated by an either anticlastic or synclastic pan shape. Recalling the Gaussian curvature K which is the product of both bending radii κ, so $K = \kappa_1 * \kappa_2$, the Gaussian curvature can be either a positive or negative figure. If the Gaussian curvature is negative, then the shape is called anticlastic otherwise synclastic. Anticlastic shapes can be either a saddle area or a hyperbolic paraboloid. A synclastic shape is mathematically called paraboloid [55].

In order to obtain hot-bent double curved glass, gravity bending is required, which is not favored for various reasons [54] which are mentioned in subchapter 3.2.1.

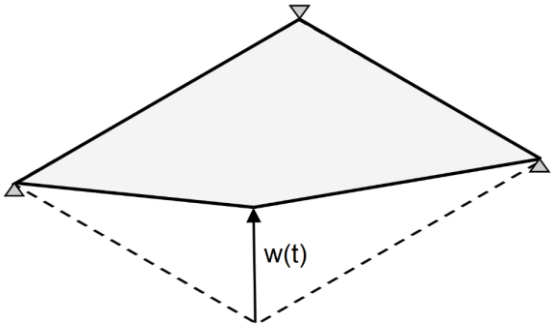

Figure 17: Raise one corner point while fixing all other corner points at one plane to obtain a double curved surface, redrawn from [49]

A convenient procedure to obtain a double curved glass pane is cold-bending by putting force on the pre-stressed glass pane and fixing it afterwards at the substructure of the façade. For small bending curvatures, a hyperbolic paraboloid pan shape is obtained, which means by definition that the edges of the glass pane are straight. If the bending radii is too small, then buckling is going to occur which leads to curved edges. It is important to understand that - in this case - the shape is not hyperbolic parabolic anymore. In this case a description of the geometry is by far more complex, moreover the curved edges are provoking constraint forces to the substructure [54]. In case of stability failure, the glass shape is prone to a sudden change between

anticlastic and synclastic shape accordingly to the load direction. In other words, it can undergo different buckling modes according to the load direction [55].

For cold-bent double curved glass, the thickness of the glass pane is a subordinate factor when it comes to the determination of the minimal bending radius. Through geometric nonlinearities, internal constraint forces are the main factor, because in the end the tension forces of the glass are limiting the bending curvature.

According to the parameter study of [55], the bending radius influences temperature stress only insignificant. Furthermore, high local stresses occur at the corners of the glass pane if the bearing area is minimized – if the bearing is linear and rigid then the stresses in the shell are increasing rapidly correlating to an increasing spring stiffness. Interestingly, synclastic shapes seem to be much more susceptible to stability failure than anticlastic shapes. A soft bearing in the direction of the surface normal is recommended by [53]. Moreover, for anticlastic shapes, a bearing in the tangential direction of the shell is recommended, which will optimize the shear force flow.

3.1.3 Free form curved glass

Nowadays, single and double curved glass are perceived as an obstacle within the architectural process, which gives the need for free form design. However, the geometry has to subordinate itself to a certain logic in order to be structurally consistent and efficient. A well-chosen geometry is the foundation for an efficient and slender primary load-bearing system and unobtrusive joints [56].

Progressively increasing demands for free form designed glass structures are correlating with incrementally increasing computer power as well as sophisticated geometric software which is getting more and more user friendly and affordable. Thus it appears that the application of cold-bent glass for free form designs is a field of interest. Crucial for free form design is a possibility for a comprehensive evaluation and depiction of an arbitrary surface which got feasible thanks to Bezier surfaces. Nowadays also 2nd and 3rd order B-splines and non-uniform rational basis splines (NURBS) are used in software applications. There may be also other types of splines in use. A big advantage of these aforementioned algorithms is that a smooth representation of a surface is an inherent part of them, an insight is provided by [57].

However, if the applied logic of these parametric surfaces is ignored then the underlying basis functions for a geometrical evaluation are not known although a graphical representation is no problem because such a task always is an approximation which is obtained through subdivision. Such types of surfaces require rather computational intensive algorithms which are far out of a standard process, an insight is provided by [58].

However, so called form-finding routines are rather complex regarding the software implementation as well as the user application. Generally, free form glazed surfaces are composed out of several glass panels with a predefined geometry. Hence the decision of panel orientation and panel size has a big influence on stress distribution and stress peaks [59].

Mathematically and geometrically, the subdivision of a NURBS surface mesh or another type of surface mesh for panelization, which is the decomposition of a surface into smaller panels, is a challenge. The geometry of all curved glass panel elements has to be incorporated into the global mesh. Furthermore, geometric information has to be obtained in order to produce and mount everything. This is only feasible through an efficient cooperation of different experts through the planning process [60].

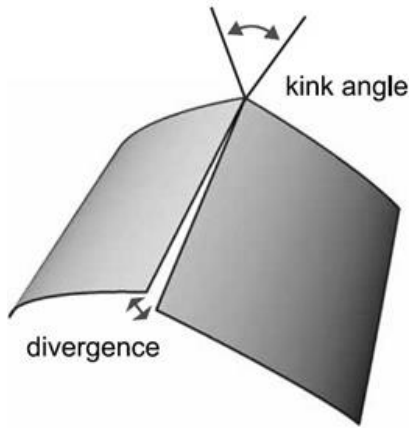

Figure 18: Deviations from the intended geometry though geometric simplifications and construction tolerances [61]

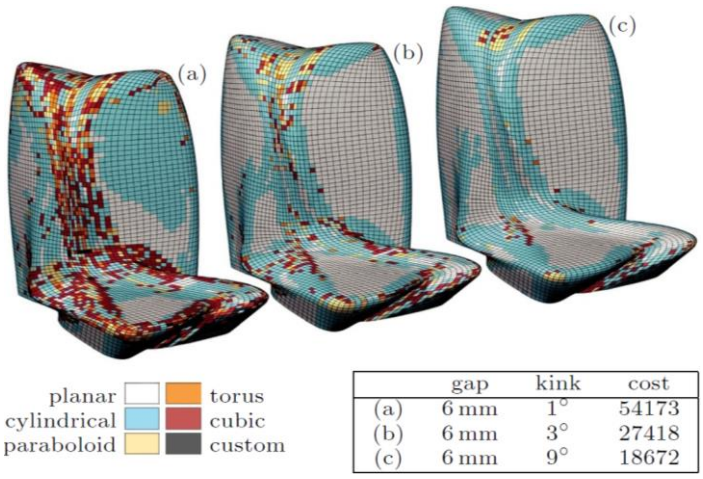

	gap	kink	cost
(a)	6 mm	1°	54173
(b)	6 mm	3°	27418
(c)	6 mm	9°	18672

Figure 19: Different decomposition schemes of a free-form surface with different gaps and kink angles; the expense for calculation increases with a less repeatable deviation [64]

In freeform surfaces, many geometry related problems have to be faced. In order to obtain the best possible smoothness, double curved glass is required, but in most cases this is still an approximation [61]. In order to keep the costs under control, not

every glass panel of an arbitrary free-form surface should be unique. The goal is to find a panel form which is repeatable and convenient for manufacturing. Normally, numerous possibilities for a panel scheme can be found with different grades of deviation from the originally intended free-form surface [64].

From this follows a certain kink angle and a certain divergence. Practically, costs influence most decision making processes considerably, therefore also single bent glass or even flat glass is used to approximate a freeform surface [61].

3.2 Production of curved glass

Curved glass can be obtained through cold bending or hot bending. Hot bending is a standard technique in the automobile industry and related industries where mass production is deemed sensible but for individual geometries within the building sector hot bending is uneconomic. Either cold bending or cold-lamination bending poses a sensible way of obtaining curved glass surfaces for building constructions.

In general, curved glass can be divided into hot-bent and cold-bent glass, a further development of cold bent glass is cold-lamination bending. Bended shell structures like curved glass have a structural behavior which is related to an arch and membrane effect, whereby both effects respectively arise in plane panes only under large deformations [62].

All kind of bent glass panes are more susceptible to installation restraints due to their high rigidity and consequential high constraining forces can occur. Current research shows that it is not possible to transfer assumptions from plane panes to curved panes [63].

Bent glass is sensible to constraint forces therefore a limitation of construction tolerances is crucial. Some parameters like warping, parallelism and deviation of the contour can give a hint whether the quality of the bent glass is good or not [3].

Currently no standardization is provided for bent glass. Therefore bent glass structures have to undergo elaborated authorization procedures through local planning authorities which normally is time and cost consuming [2] [3].

3.2.1 Hot-bent glass

One possibility to obtain hot bent glass is through gravity bending which is a well-tried way of bending glass since years. An ordinary flat glass is heated up to $620°C$ $(1150°F)$ so that the flat glass is able to reshape accordingly to an underlying formwork – hence the name gravity bending. Finally, the quenching process is crucial for the final properties of hot bent glass. Normally, annealed or heat-strengthened glass is desired. For this reason the controlled cooling process is conducted with a high temperature gradient whereas nowadays the bending and cooling process is carried out in the same furnace [64].

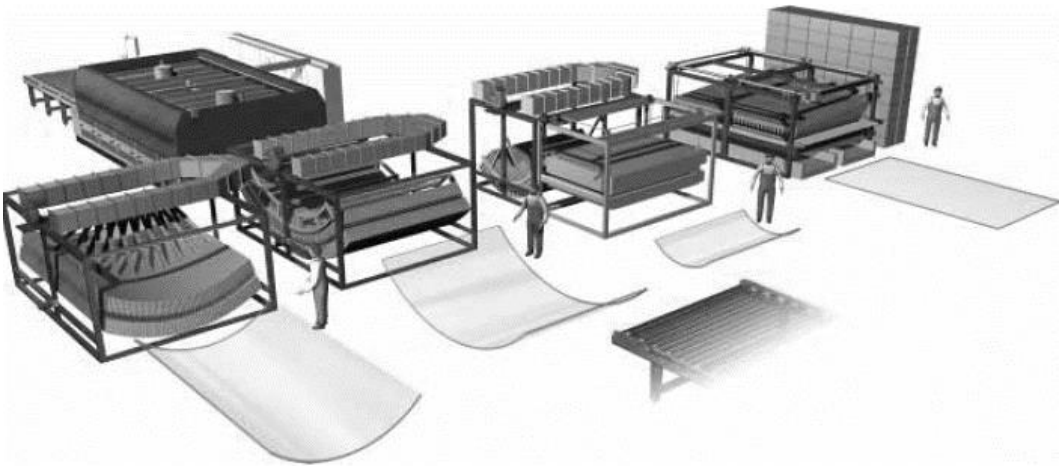

Figure 20: Conveyor which is able of hot bending and quenching of glass panels [1]

If double curved glass is desired, it can be obtained through pressure bending where the heated glass is forced into a certain shape through pressure forces [18].

According to [65] the flat glass can be heated up to $800°C$ $(1500°F)$ to obtain small bending radii which is an advantageous opportunity over cold bending procedures.

Maximum sizes of hot bent glass panels produced with the latest bending and quenching conveyor machines range up to 2400 $[mm] x$ 4200 $[mm]$ [1].

For curved laminated glass, two glass panes get bent pairwise to ensure maximum parallelism. Thorough edge finishing of the flat glass has a great influence on the bending process to minimize rejection rate. But for all that effort, hot bent laminated glass still imposes unknown stress due to shoddy surface parallelism. Manufacturers are not able to produce annealed hot bent glass which at the same time has a high bending stiffness and a high optical quality as well as low geometric imperfections [62].

3.2.2 Cold-bent glass

Cold-bent glass is obtained by imposing a deformation on a flat glass (either monolithic glass or laminated safety glass) or an IG by fixing the flat glass permanently to a curved substructure. Cold-bent glass is experiencing permanent internal stresses therefore pre-stressed glass must be used instead of float glass. Limitations of cold-bent glass are particularly given through the bending strength, geometric conditions and - regarding laminated glass - the partial shear rate of the intermediate layers [65] [66].

Cold-bent glass is superior to warm-bent glass for applications in building construction because it gives a better optical quality at lower cost unlike hot-bent glass where local warping can occur [7]. Surface coating, pre-stressing and other processing steps can be carried out in the plane configuration which is very like for float glass therefore no further expenses need to be considered [55].

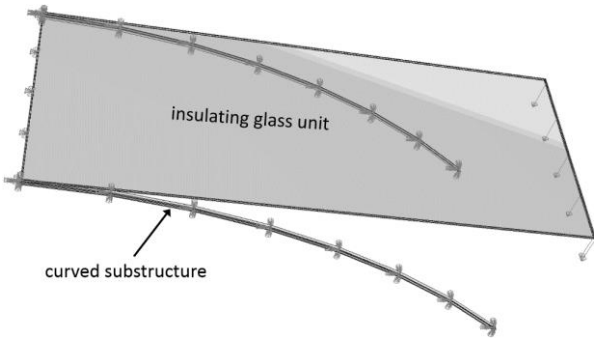

Figure 21: A planar glass pane is mounted on a curved substructure on the construction site which results in cold-bent glass

On the one hand, cold-bent glass is more economical than hot-bent glass, especially for irregular curvatures, but on the other hand, the bending radius of cold-bent glass is much higher than for hot-bent glass. For example, for cylindrical shapes, the bending radius is about three times bigger for cold-bent glass than for hot-bent glass [29].

When using cold-bent laminated glass, it should be considered that less but thicker glass panes are giving higher imposed stresses compared to thinner glass panes, which also was mentioned in subchapter 3.1.1 in more detail.

Intermediate layers for cold-bent glass have a lower stiffness than the glass itself therefore an end slip occurs. Such a plastic behavior is advantageous to a certain degree because it reduces imposed stresses in the intermediate layer [67].

Most cold-bent laminated glass structures are made with PVB interlayers. Nevertheless, the shear stress resistance of PVB depends highly on its temperature as well as the loading time which plunges down to roughly half of its strength if the material temperature raises from $23°C\ (73°F)$ up to $40°C\ (104°F)$ whereas the material resistance for short impact loads is higher at any temperature [68].

3.2.3 Cold-lamination bending of glass

Cold-lamination bending is convenient for pre-stressed thin glass with big bending radii [66].

Cold-lamination bent glass is made from flat glass which has to be pre-stressed like cold-bent glass and gives a curved laminated safety glass as a final product. After stacking the single float glass panes and the interlayer on top of each other, they get cold-bent on an auxiliary scaffold under autoclave conditions.

According to [69] the manufacturing process can be divided into four steps. Firstly, the flat glass panes and the intermediate layers are stacked on top of each other. Secondly, the loose composite of flat glass and intermediate layers gets deformed and subsequently the autoclave lamination process is carried out. In the final step, the laminated glass is released from the scaffold. Due to inner stress, which originates from bending, the glass pane curls up a bit therefore the final shape is obtained after - and not before - the lamination process. The autoclave conditions do not affect the quality of the glass or the glass coatings due to its low temperature [55].

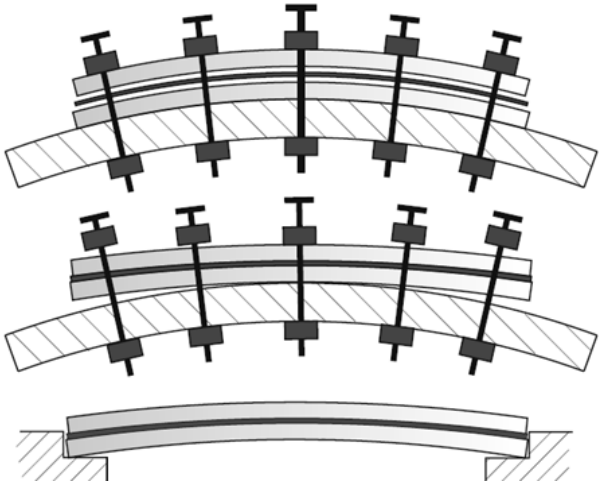

Figure 22: Cold-lamination bending process of glass, from top bottom: Firstly, cold-lamination bending process, secondly, a gradual release of the cold-laminated glass pane with a spring back deformation, thirdly, the final product [75]

A challenge of cold-laminated glass is not only the spring back after releasing it from the auxiliary scaffold but also long-term relaxation effects whereas the big challenge in particular is the prediction of deformation through convincing calculation models. Practically, the spring back deformation is restrained to a certain degree through a time delayed unfixing after lamination [70]. The spring back deformation is a function of the shear modulus of the interlayer and therefore SentryGlas is often used to get the spring back deformation under control [71].

A sinusoidal bending shape is advantageous over a circular bending shape and should therefore always be the preferred choice if a cold-lamination bending process is conducted [72].

According to [73] the intermediate layer should have a sufficient thickness because otherwise stress peaks occur due to impaired shear stress redistribution. Furthermore, their findings states that all PVB laminates are having a visco-elastic behavior under constant loading as well as for unloading cycles.

3.3 Curved insulating glass

IG is made out of more than one glass pane - which is either a laminated glass pane or a single glass pane and a gas filled cavity between the glass panes. Prevalent IGs are either double glazed or triple glazed. In addition, quadruple glazing is beginning to emerge. An IGU is the whole system including the IG which often is covered with some

type of glass coating, gas cavity, primary and secondary sealer, spacer bar, desiccant and additional features [41].

Curved IG can be obtained through the process of assembling curved glass panes and glass spacer which has the advantage that the glass panes are bent already [65]. Obviously such a procedure demands either cold-laminated or hot bent glass panes.

The curvature of an IG is affecting the internal pressure of the cavity. Firstly, the climate load in a bent IG is different compared to a flat IG just due to geometric reasons. Secondly, the interaction of the different glass panes is affected as well – because the stiffness of the glass panes is higher. Hence the interaction is lower which leads to higher stress at the load facing glass pane. This is because the cavity pressure is sensitively linked to a small volume change of the cavity volume. That leads to two inferences: firstly, the deformation capacity of the edge compound is not negligible anymore and secondly, the bending stiffness is lower for a higher curvature. These parameters are considerably altering the internal cavity gas pressure [74] [51].

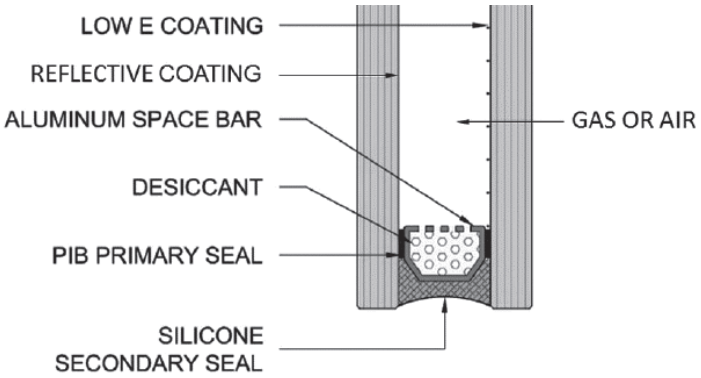

Figure 23: Classic example of an double seal insulating glass unit with low-E coating for improved thermal performance [41]

If an IGU gets cold-bent, different types of failure have to be considered which can be the structural failure of the frame and the glass pane, a failure of structural silicone or another adhesive or a failure of the PIB seal. However, structural silicone is not expected to be the weakest structural part of a fenestration product. The location of the maximum strain of the PIB as a primary seal is a function of the frame stiffness and many other factors and is usually outside the corner regions. Structural failure is more likely to happen for a smaller bending radius and can be predicted through a FEM calculation [78].

A comprehensive full-scale testing of cold-bent IGU was conducted in [78]. It was found, that the retention of argon inside the cavity as well as thermal durability is entirely feasible in case of proper workmanship. Epoxy resin was used for relatively small windows to attach the tested IGU onto a steel frame. A durability testing, more specific an accelerated weather cycling test, resulted in a failure of the epoxy resin. Therefore, if there is a need for a tough adhesive, a high-strength silicone should be opted instead of an epoxy resin. It was also found, that due to creeping of the structural silicone the displacement increased. Furthermore, it was found that the edge seal is durable against moisture infiltration even if it is strained. It is mentionable, that [78] states that the testing was conducted according to ASTM and it cannot be transferred to European standards.

4 Adhesives and Plastics in Structural Glazing

Adhesives are still a challenge concerning the calculation of stresses not only in cold-bent glass but also for common structural sealant facades as well as glued point fixing systems. Therefore, an overview of this topic is given. In addition, degradation mechanisms and high temperatures are still a problem for adhesives [75]. In order to succeed with transparent glazing systems, engineers have to meet the challenge despite all the difficulties which come along with adhesives.

In general, adhesives can be classified under various aspects. A common subdivision makes a difference between their macro molecular properties as thermoplastics, duroplastics and elastomers. Thermoplastics like polypropylene (PP), polyethylene (PE) or polyvinylchloride (PVC) can be heated up to reshape them in a plastic way whereby this procedure is repetitive for thermoplastics as often as desired. This is because thermoplastic materials do not lose their properties through heating. Duroplastics like epoxy resin or polyurethane (PU) cannot change their properties once they are cured and are decomposed if they get heated. Elastomers are exhibiting a rubbery material behavior and are decomposed similar to duroplastics if they get heated. Elastomers lose their elastic rubbery behavior below the glass point temperature, which has to be considered for cold climatic conditions [76] [77].

Radiation curing adhesives, epoxy resin adhesives, PU adhesives and silicones are widely used in the field of structural glazing [77].

Durability of adhesives is the ability to withstand external influences in a way that slows down the ageing process which implicates that the process of chemical decomposition happens at a low rate. Main factors for polymer ageing are UV-radiation, heat exposure and humidity [77].

Several factors can impair an adhesive joint to a certain degree and have to be considered. Sodium, calcium and magnesium get dissolved out of the silicon dioxide crystal structure with the aid of water which leads to corrosion of the glass surface [19]. Moreover, also organic contamination and other atmospheric influences determine the condition of the glass surface which is forming a so called gel layer. Practically, it is not possible to eliminate this gel layer which impairs the adhesive forces between glass and adhesive [82]. There is a direct correlation between the surface energy of the glass and its gel layer thickness. Therefore, it is advantageous

to reduce the gel film before gluing in order to improve the quality of an adhesion joint [77].

In General, and as it can be seen in Figure 24, rubber toughened adhesives are undergoing large deformations and also plastic deformations before failure. Therefore, a non-linear material description is advisable to obtain good results. For more sophisticated calculations, the viscoelastic behavior which is present in all polymers, can be taken into account [78].

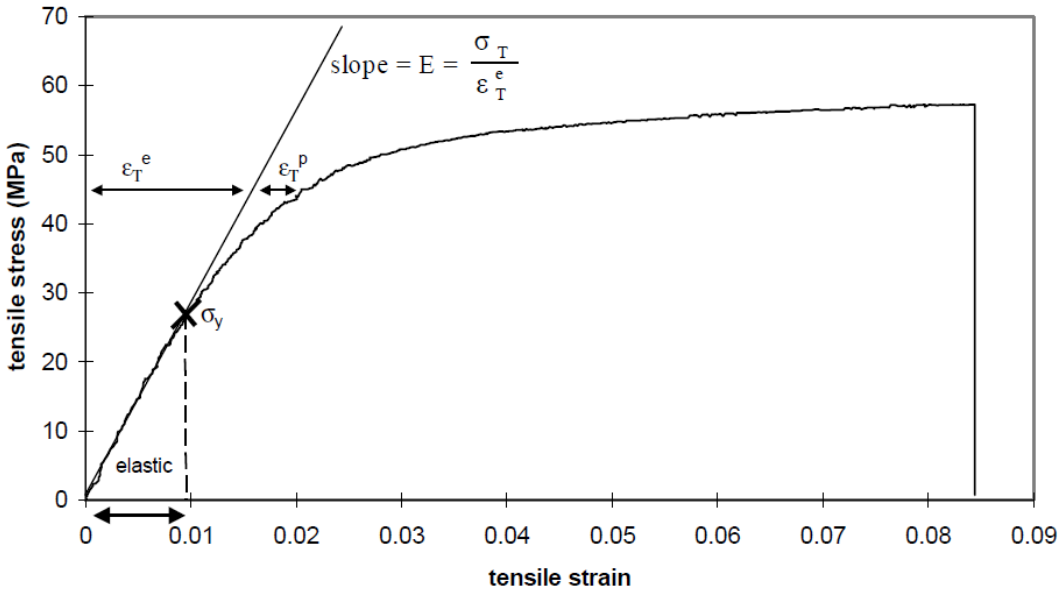

Figure 24: Stress-strain relationship for uniaxial tension of toughened epoxy adhesive as an textbook example for the mechanical behavior of stiff polymers which have a quasi-elastic section for small strains [78]

According to [75] adhesive joints should fail due to a limitation of cohesion. Furthermore, an adhesive failure cannot be calculated due to lack of knowledge. Although some research on adhesive failure was carried out for example in [79] many uncertainties still remain.

Consequentially, for FEA, it has to be assumed that no adhesive failure occurs, but this must be a consistent assumption with regard to adherents and adhesive, and therefore testing is advisable to support calculations.

Adhesive joints are failing mainly because of crack propagation. For all different adhesives the failure is a function of the geometry and the load history. If a certain strain and stress is exceeded, then the crack growth will lead to failure. In general, this happens slowly until a critical crack length is reached. Another reason for failure are localities with a high peel strength where the volumetric change is inhibited. Thus

stress prediction is uncertain in this case because mostly the calculation is based upon material values from uniaxial tests [78].

In Figure 25 different failure modes are depicted which are defined by the standard DIN ISO 10365 [86] and have to be used for the description of different failure modes for laboratory testing. However, these different failure modes are also helpful to get an overview on the behavior of adhesives [81].

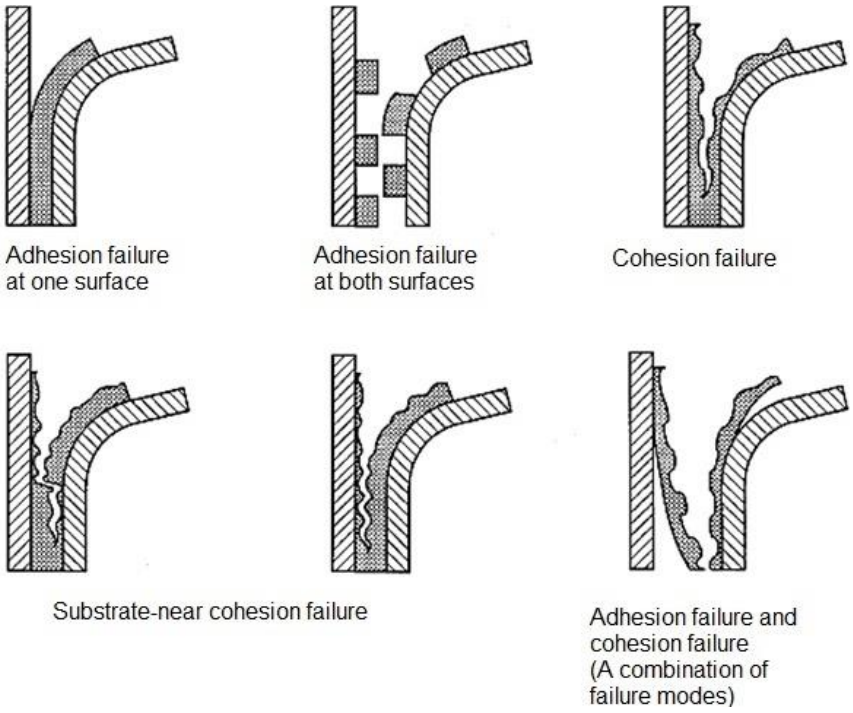

Figure 25: Different modes of failure for a bonding [81]

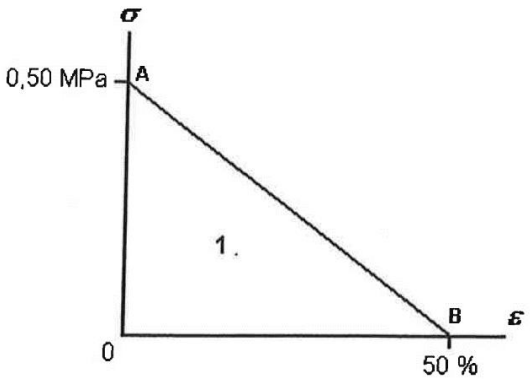

Figure 26: Inside this stress-strain triangle the bond of any adhesive must not fail regardless of its age [87]

As depicted in Figure 26, the European standard EN 1279-4 defines a section in a stress-strain diagram where any bond must not fail regardless of the age of the bond.

In Figure 27, different failures in a bond are shown according to the European standard EN 1279-4. A distinction is made between adhesion and cohesion failure inside or at the surface of the bond.

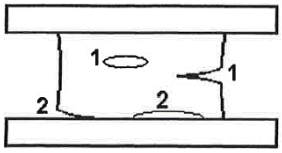

Figure 27: (1) cohesion failure, (2) adhesion failure [87]

4.1 Typical adhesives in structural glazing

In general, adhesives are polymers and all polymers have a non-linear viscoelastic material behavior. In Figure 28 a comprehensive description of three different adhesive types is shown. It can be seen that for a higher stiffness, the maximum stress is higher but at the same time the adhesive is more rigid in comparison with other adhesives. Epoxy resins and some PU adhesives behave similar to a tough, rigid adhesive layer, viscoplastic adhesive layer are for example acrylates which is shown in Figure 28. Flexible adhesives like silicones are suitable for sealing functions.

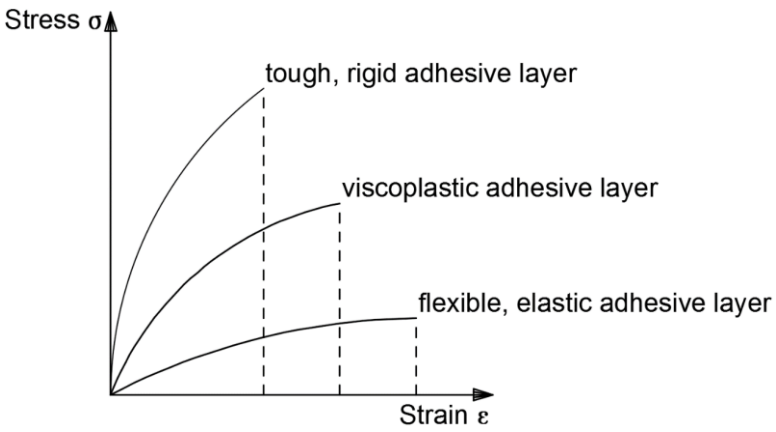

Figure 28: Typical stress-strain relationships of adhesives, redrawn from [81]

4.1.1 Epoxy resins

Epoxy resins are typically two-component systems with a high cohesion strength and their adhesion behavior is normally good against most materials which are used in the

building sector. The material behavior is usually rigid and epoxy resins have a high shear modulus compared to other adhesives.

Cold-curing epoxy resin has a low pot life and a lower bonding strength compared to warm-curing epoxy resin. Cold-curing epoxy resin is typical for two-component systems.

Warm-curing epoxy resin is inert at ambient temperature and has therefore a long pot life. Warm-curing epoxy resins are used as single-component system as well as two-component system, both reach higher strength as cold-curing epoxy resin but their curing time is longer. Toughened epoxy resins are chemically modified so that their stiffness is lower than usual which is advantageous to avoid stress peaks and allow some movement instead. Toughened epoxy resin possess a relatively high shear modulus but its stiffness decreases more at higher temperatures than for other epoxy resins [81].

A new development is transparent epoxy resin which shows promising results like high stiffness and good optical properties but it is still a challenge to ensure a reproducible curing process for consistent quality [84].

4.1.2 Polyurethanes

PU adhesives can be divided into single-component adhesives which cure with the aid of humidity and two-component adhesives which cure by the mixing of both components; a curing component in component A and an accelerator in component B react chemically whereas a good mixing of both components is advisable. Furthermore, PU dispersions, solvent-based adhesives, PU-elastomers and other types of PU adhesives are playing a tangential role for structural glazing.

Single-component PU will undergo the curing process if enough relative humidity is in the air therefore a curing accelerator can be added to the adhesive mix to shorten the curing time. Often, single-component PU is used as in-situ foam at the construction site.

Two-component adhesives with PU are advantageous compared to single-component PU because it is possible to choose a desired pot-time depending on the mix whereas the curing time can be shortened through a curing accelerator as well. Through the

selection of the starting material of PU it is possible to adjust the final properties of the adhesion layer.

Dispersions from PU are playing a more important role nowadays due to environmental protection reasons because solvents in adhesives are not desired anymore. There are mainly two different types of adhesives, the one which contain emulsifier and the other one which do not. Dispersions without emulsifier have better adhesive properties than dispersions with emulsifier and thus play a more important role. A great benefit of PU dispersions is the good bonding property with a lot of different materials. In addition they also have a high resistance to chemical and environmental impacts [81]

4.1.3 Silicones

Silicone adhesives are the only ones which are regulated in the ASTM C1401 standard and in the ETAG 002 concerning the use in structural glazing. Silicones have a wide application in SSG façade systems [85]. Silicones have good cohesion and adhesion properties and can be used as an adhesive between materials which have different thermal expansion coefficients. Silicone stays flexible at low temperatures and can resist high temperatures up to $300°C$ $(570°F)$ for short durations and temperatures up to $200°C$ for long durations. Due to the very low glass transition temperature of silicone, which can be as low as $-123°C$ $(-190°F)$, it also stays flexible at very frigid conditions. Moreover, silicones are durable against weathering and mild bases and acids.

Single-component systems undergo curing at ambient temperatures and like PU the curing process needs water which is obtained out of the surrounding air. Hence a high relative humidity in the air is advantageous for a faster hardening process. Usually the curing time lasts from several hours to a few days. If a faster curing process is desired, then accelerators are available.

Two-component systems are applicable where single-component silicone adhesives are inadequate. A need for two-component systems is predominant for instance if the relative humidity of the ambient air is very low or the adhesive layer is very thick from which follows either a very long or an incomplete curing process [81].

MS-Polymer is a type of silicone which melds properties of silicone and PU. MS-Polymer can endure a permanent temperature of $100°C$ and it is also flexible at low temperatures and does not behave rigid. Like other types of silicone, it has good adhesion properties on a lot of different materials and not to mention a high resistance against weathering and UV-radiation which is important for the application in facades. There are single-component and two-component systems available whereas the decision for the adhesive system depends on the same criteria as for common silicones [81].

4.1.4 Polyisobutylene

Polyisobutylene, often abbreviated as PIB is a thermoplastic polymer and is often used as a primary seal for insulating glass because it is practically impermeable to gas.

Through different polymerization processes, different types of PIB are obtained. PIB can be obtained in a fluid state, as a ductile material or as a rubbery material.

PIB is hydrophobic, has a low air and gas diffusion coefficient and it is also durable against UV-radiation. Moreover, the ageing rate is low and the flexibility at low temperatures is high. The flexibility in frigid conditions is a consequence from the low glass transition temperature of PIB which lies at -78°C [81].

4.2 Interlayer

In this subchapter, different types of interlayer are described in order to give an overview of the most important interlayer materials. A special focus lies on PVB and SentryGlas due to their importance in structural glazing applications. PVB is the most common used interlayer overall and SentryGlas is exceptional advantageous for special demands in structural glazing.

4.2.1 Polyvinyl butyral (PVB) interlayer

PVB is a thermoplastic vinyl polymer and a solid resin which can withstand acid and alkali attacks. Due to free hydroxyl groups which are forming hydrogen bonds on the glass surface, the adhesion strength of PVB is good. At $23°C$ $(73°F)$, the tearing

strength of PVB can be as high as $20\ [MPa]$ and it undergoes a large deformation before failure [33]. Furthermore, PVB has a high optical clarity, is durable against sunlight - hence also UV-radiation, has a high tear resistance and impact absorbing characteristics. The latter means that stress peaks from short load durations are well diminished and distributed [23].

The stiffness of PVB highly depends on its temperature, for temperatures above $80°C\ (176°F)$ the PVB interlayer undergoes delamination. EVA and bonding resin have a similar temperature depending behavior. The stiffness of EVA and bonding resin is much lower at $23°C\ (73°F)$ than that of PVB but it declines not so fast with increasing temperature as PVB does [29].

In [29] it was found that - for uniform loadings – the overall strength of laminated glass is increasing remarkably with increasing thickness of the PVB interlayer. More specifically, the effective section modulus increases linearly with increasing PVB thickness.

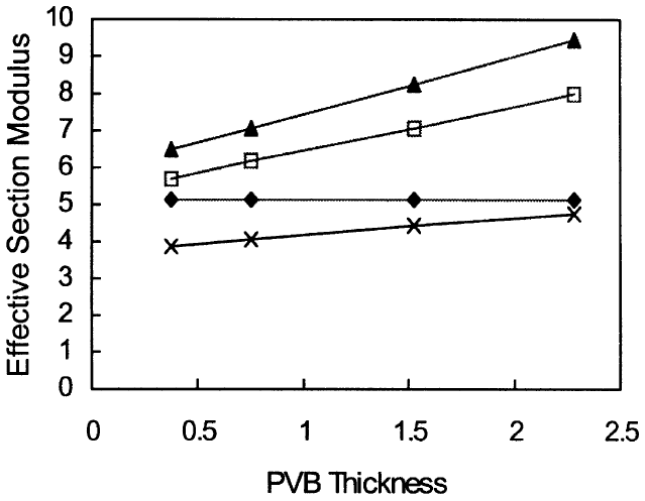

Figure 29: From top to bottom: The first line is for a shear transfer of q=107%, the second line for q=87%, the fourth line for q=31%, the third line represents a section modulus of 5.15 mm³ which is equal to a monolithic glass beam with a thickness of 6 mm [29]

In [86] commercial available PVB samples were analyzed whereas PVB with different polymer serial numbers was tested. The PVB samples did not show a significant difference in glass transition temperature or stress-strain behavior. Most PVB interlayer's glass transition temperature lies between $14°C\ (57°F)$ and $18°C\ (64°F)$. The stress-strain curves were obtained at ambient temperature, therefore the PVB was during testing above its glass transition temperature. The stress-strain

relationship was obtained from dumbbell-shaped strips which were cut out of the PVB interlayer. The stress-strain relationship is rubbery. The stress-strain relationship for virgin PVB and for recycled PVB in Figure 30 is showing no significant difference for a strain up to 1 [86].

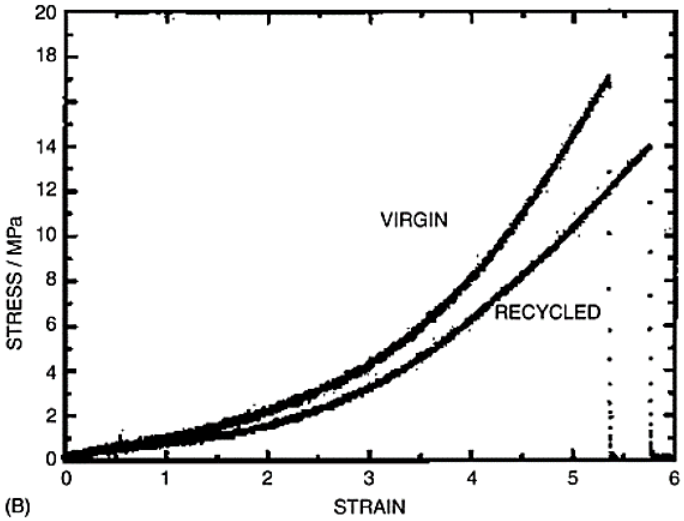

Figure 30: Stress-strain curve of virgin and recycled PVB, Source: [86]

Polymer serial number	Young's modulus E (MPa ± 0.03)	C_1 (MPa)	C_2 (MPa)
S-1	0.49	0.16	0.09
SR-1	0.46	0.26	-0.03
D-1	0.48	0.32	-0.08
DR-1	0.46	0.25	-0.02
M-1	0.38	0.33	-0.14
MR-1	0.40	0.36	-0.16

Table 2: Mooney-Rivlin analysis of tensile behavior of the PVB samples (5 samples for each polymer) [86]

4.2.2 Ionoplast interlayer (SentryGlass)

SentryGlas is an inonomeric polymer with improved mechanical properties compared to other interlayer materials. Like for other interlayer materials, the stiffness of SentryGlass declines with increasing temperature, though much slower. SentryGlass behaves quasi-elastic for small strains. Practically, the quasi-elastic stress-strain

behavior is determined by the quality of the bonding which is in a further consequence depending on the manufacturing quality [87].

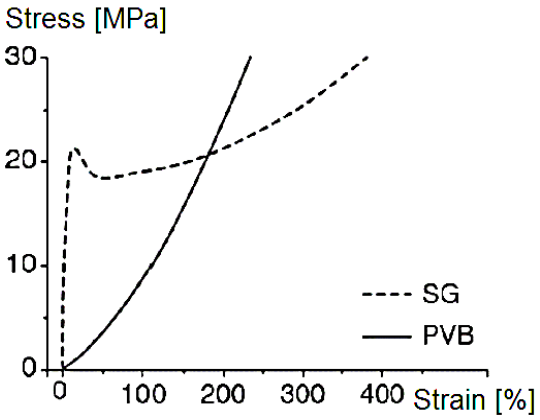

Figure 31: Stress-strain comparison of SentryGlass and PVB interlayer under ambient temperature [87]

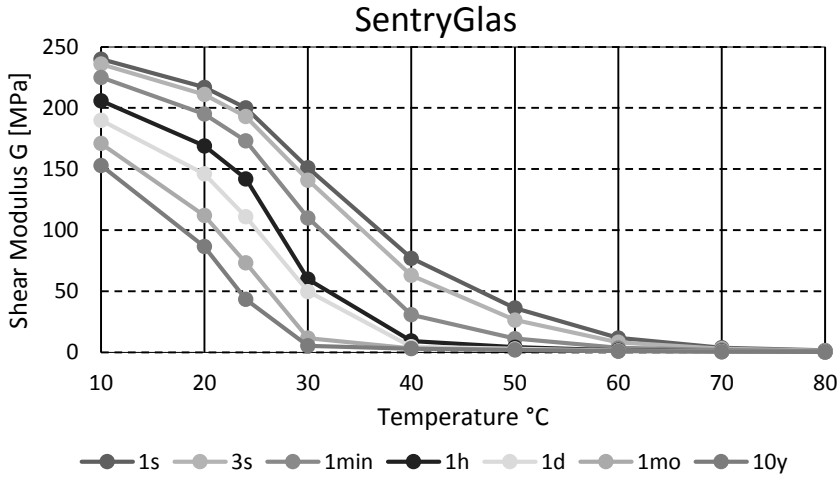

Figure 32: Shear modulus vs. temperature of SentryGlas for different load durations [88]

SentryGlass is a brand name of the company DuPont and a patent-registered product. DuPont provides comprehensive mechanical data about the Young's modulus, the shear modulus and the Poisson's ratio as a function of temperature and load duration which facilitates numerical investigations [88]. The mechanical data from the manufacturer were investigated in [87] and it was found that the mechanical values are correlating although the manufacturer's data tend to be a little bit lower.

The stiffness of SentryGlas is bigger than all other in this chapter mentioned interlayers by orders of magnitude. Furthermore, the stiffness starts not to decline drastically until a temperature of $70°C$ $(158°F)$ is reached. Unfortunately, the temperature coefficient

of SentryGlass differs greatly from that of soda-lime silica glass, hence temperature stresses can be an issue [29].

4.2.3 Important types of interlayer beside PVB and SentryGlass

EVA is a thermoplastic polymer which shows elastic properties. EVA as an interlayer material is used in the solar industry and in structural glazing. EVA laminated safety glass is obtained through the process of vacuum lamination. EVA interlayers can reach a tearing strength up to $25\ [MPa]$ at ambient temperature. The cohesion and adhesion properties of EVA are good [33].

TPU is a PU product and behaves elastomeric. At ambient temperature, TPU is above its glass transition temperature and shows a rubbery behavior. TPU is durable to UV-radiation, abrasion, chemicals and shows good mechanical properties [33].

Beside from TPU, also **PU** is in use. PU is an elastomer similar to TPU. The mechanical properties of PU can be varied through chemistry mixture which is advantageous for special applications. Hence, the material properties can differ in a wide range between tough and rigid like epoxy resin to flexible hyperelastic like elastomers. PU is well-suited in many applications due to its high tensile strength, durability, mechanical resistance against abrasion and toughness [23].

Polycarbonates (PC) are used for bullet proof laminated glass because it is capable to store the energy of a bullet by softening during an impact. In comparison to other polymers, PC is very tough. PC has some outstanding properties which are a very pronounced clarity and an extreme toughness which comes along with a high impact resistance [23].

4.3 Bonding of adhesives

The bonding mechanism of an adhesive with an adherent is rather complex because the bonding mechanism depends on many factors, which are the adhesive itself, the adherent, the surface properties and environmental conditions. The latter is affecting the curing process and ageing process significantly.

A bonding process of an adhesive largely happens through adhesion. Adhesion can happen chemically, physically and through thermodynamic processes.

In addition, mechanical adhesion, which is the interlocking of the adhesive with the adherent can be improved through surface treatment [81].

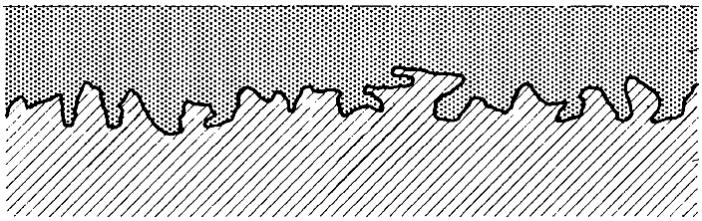

Figure 33: Mechanical adhesion: A liquid plastic acts as a form-locked connection between the adherent and the adhesive after hardening [81]

In the following paragraphs, an overview of the bonding properties between common adherents and adhesives is given which should be considered in an early stage of the design process.

Extensive research was done on aluminum which is the most investigated material regarding adhesive technology [81]. Therefore, it is safe to use for many different types of adhesives. Epoxy resin and aluminum is a very good adhesion-adherent combination because epoxy undergoes not only physical but also chemical bonding with aluminum [77].

Stainless steel takes advantage of special alloys which are inert, hence are preventing in such a way corrosion. Nevertheless, this is a problem for adhesives which imposes the need for special surface treatment before gluing [77]. Regarding the ageing resistance, highly interconnected single-component epoxy resins and two-component PU adhesives are working well for stainless steel [81].

Glass fiber reinforced plastic has nearly the same temperature expansion coefficient as glass but the polymers of the fiber have to be compatible with the polymers of the adhesive. In use are mainly epoxy resins and PU [77].

Wood as an adherent is a challenge not only because it is an inhomogeneous and anisotropic material but also it is sensitive to humidity which leads to swelling and shrinking. Adhesives interact mainly physical and not chemical. Therefore, the quality of the glue joint strongly depends on the surface pretreatment whereas the gluing must be executed within 24 hours after the surface pretreatment [77].

5 Numerical Modelling of IGUs

An application of the FEM is usually carried out in a software program and can be divided into the following steps: meshing of the model, definition of the boundary conditions, calculation of the stiffness coefficients, assembling of the stiffness matrix and finally solving of the Equation 2 in order to obtain the displacements [90].

A meshing procedure of a model is done with elements of a certain size and shape – hence finite element method. The discrete and finite area is subdivided by elements which can be either 1-, 2-, or 3-dimensional. The order and size of determines the quality of the results [90].

For static problems, a Dirichlet boundary condition is defining the type of support and the Neumann boundary condition is defining the type of force.

For static problems, the FEM is approximating the displacements of a structural system. Through numerical derivation of the displacement field, the stress field is obtained. It is essential to notice that the error of the stress is always bigger than the error of the displacement.

A further insight into the FEM for engineering is given in [93] and [94] for example.

For the finite element method, it can generally be stated that the following problem has always to be solved

$$K_{ij}u_i = F_i \qquad \textit{Equation 2}$$

K is the positive definite, sparse and symmetric stiffness matrix, u is the displacement vector, F is the force vector and $i, j = 1 \dots n$. All displacements u can be obtained by calculating the inverse of the stiffness matrix K^{-1} which is utterly inefficient.

An efficient way of calculating the displacements u is the conjugated gradient method because it is optimized for positive definite and symmetric matrices. In order to get small calculation errors, K has to be well-conditioned which means that the entries of K must not differ in orders of magnitude. For smaller matrices with up to 10^5 unknowns, the lower upper decomposition is also an option [94].

The FEA is converging with the converging order e if

$$||u - u_h|| \leq Ch^e \qquad \textit{Equation 3}$$

where u is the exact solution, u_h is the approximated solution, C is a constant which often is unknown and h is the maximum diameter of a finite element. The converging order e is normally known from general error estimations. From Equation 3 it can be seen that a small element size h is important for a good approximation.

If $h = 0$ then it follows from Equation 3 that

$$\big|\,||u - u_h||\,\big| = 0 \qquad \textit{Equation 4}$$

which means that the exact solution is found by the finite element method [89].

If the region is not convex (especially in corner regions) then the convergence rate is not affected through a higher shape function order p [89].

For an optimal convergence rate, it is important that the – often unknown – solution has smooth properties. Practically, the convergence rate of non-smooth areas can only be improved by h-refining but not by p-refining [92].

If the mesh size is too big, then stress peaks and singularities can be overseen [94].

In a convergence rate study from [92], it is shown that for non-smooth integrands, a p-refining does not improve convergence but increases the calculation effort, therefore it is advisable to use linear shape functions.

Structures which undergo bending stress are prone to numerical locking. This issue can be faced by a strong h-refining and also by p-refining [92].

Convergence studies are essential for residuum estimation in order to assess the required refining. It is important to consider that the convergence of an unsuitable model is worthless from a physical point of view [92].

For a beam-plate element, a linear rectangular element has better converging properties than a linear triangle element because latter is behaving too stiff but higher order triangle elements are appropriate. Square-shaped elements are just slightly better than linear triangle elements [91].

For a plate element, rectangular plate elements are converging better than triangular plate elements. In addition, square-shaped plate elements are prone to locking [91].

Element distortions will lead to unacceptable calculation inaccuracies. Element distortions can be identified by big differences in either side length, diagonal length or through acute angles. If an element distortion occurs, then a remeshing of the affected area is required [94].

Non-linear FEM problems can be solved through direct integration and Newton-Raphson iteration whereas both are cumbersome because the stiffness matrix has to be recalculated for every iteration step. A modified Newton-Raphson iteration, where the slope of the tangent hence also the stiffness matrix stays constant, is much more efficient. In case of no convergence, incremental explicit algorithms have to be used [94].

It is important to notice that for every non-linear problem, a start value has to be guessed, and the quality of guessing determines the calculation expense. Further, careless chosen start values can make a convergence impossible [94]. Besides that, for an unsuitable start point, a non-linear problem can give a mathematically sensible solution which might be senseless in a physical way.

Hyper elasticity, plasticity and viscoelasticity are common non-linear problems for FEM as well as non-linear geometry. In regards to this Master's Thesis, elastic as well as plastic materials are used in fenestration products. In addition, non-linear geometry is inherent to curved glass.

Contact problems occur if different structural components interact. For a FEM analysis, so called contact elements are used as an interface between bodies. Even for the two most known contact problems, Coulomb friction and Hertzian stress, the contact problem is highly non-linear and expensive to calculate. An admissible simplification is the assumption that contact problems like friction are quasi-static in order to neglect dynamic effects [94].

For modelling a contact problem, there is always a master surface and a slave surface. The program algorithm is checking if the slave surface is penetrating into the master surface. Therefore, some rules have to be obeyed for FE modelling. If the contact surfaces are symmetric, then it does not bother which surface is slave and master. Otherwise, the more convex or more flat surface (of the two considered bodies) should always be the master surface [94].

In order to evaluate the stress in structural silicone with a FEA, some recommendations can be given beforehand. It is advisable to model the structural silicone using spring elements or elastic beams, if a reliable value for the spring stiffness is known. The Young's modulus of the silicone should take the load direction into account. Generally, hyperelastic models should be chosen except it can be ensured that the strain stays within a certain range which does not affect the result. Furthermore, it must be noted that a FEM analysis can not only be based on a stress evaluation due to large deformations; for example if the silicone undergoes a very large elongation, then the material model might not be accurate anymore or the manufacturer of the particular silicone does not guarantees a use for such big strains [51]. Such principles are not only valid for structural silicone but for all plastics due to their characteristic mechanical behavior. Subsequently, several examples of numerical studies related to curved glass are summed up in order to get an idea of how to make a sensible FE model.

In a numerical study in [24], D-shaped aluminum spacers and steel spacers were investigated. It was found that the results between a 2D-model and a 3D-model do not differ remarkably. Because metallic spacers are much stiffer than butyl strips, they have a sensitive effect on the mechanical behavior of the edge zone.

For a FEA of butyl strips which are used as a primary seal, a hyperelastic material model is advisable due to its very low stiffness. A linear-elastic material model can only give a superficial insight of the behavior and is rather inaccurate. Since butyl is a hyperelastic polymer, it has a Poisson's ratio υ which is near 0.5, which means butyl is almost incompressible. Testing in [24] shows an inelastic behavior after unloading which only an elasto-plastic material is able to consider.

In Figure 34, a suggestion for a simplified model of the edge zone of an IGU is given according to [24]. Both, the D-shaped metallic spacer and the adjacent butyl strips on both sides are replaced by a simple spring. Numerical results show no significant difference, if the equivalent spring stiffness and the position of the spring is known.

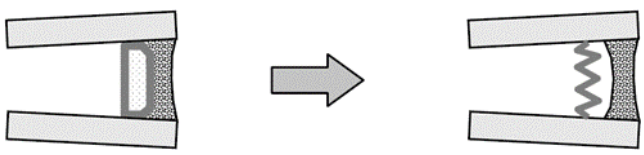

Figure 34: Suggestion for a more simple mechanical model of the edge zone [24]

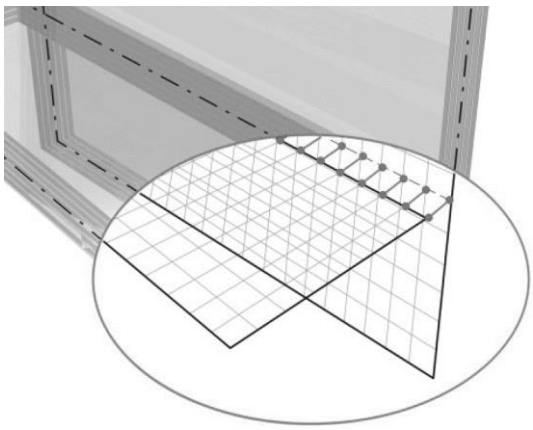

Figure 35: FEM model of a steel-glass joint [7]

In [7], a cold-bent glass bridge was designed. A FE model of a glued steel-glass joint is depicted in Figure 35 in which the FE model is spatial and the glued joint was modeled with coupling members of an equivalent stiffness. All glass panes were modeled as shell elements with an equivalent thickness which takes the interaction of the interlayers with each glass pane of the laminated glass into account. In this particular case, SentryGlass was used as an interlayer which comes close to a full shear connection under ambient temperature. A curved glass pane undergoes membrane stresses and multiaxial bending moments. Therefore, membrane effects as well as shell and plate effects should be considered [55].

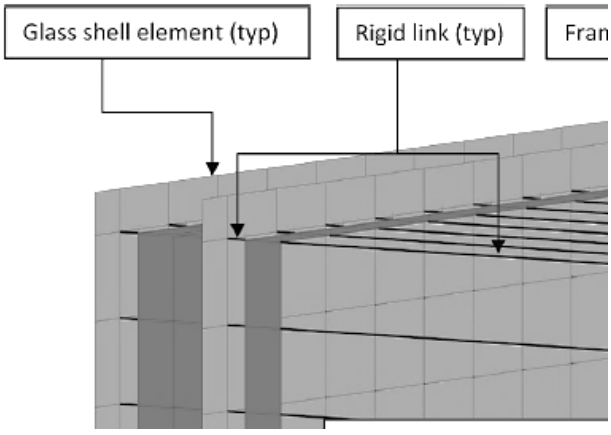

Figure 36: Corner region of a cold-bent IGU with aluminum frames [78]

In [78] a FEA of a cold-bent IGU with aluminum frames was modeled which is also illustrated in Figure 36. The stiffness of the PIB was discarded. All laminated glass panes were modeled with shell elements. Rigid coupling members were used to fix the three dimensional position of the elements. The structural silicone was modeled as a non-linear material, no further detail - if a hyperelastic material model was used

or not - is given. The cavity volume was modeled with the aid of fluid elements with a certain bulk stiffness which depends on the glass filling blend. An important fact is that the torsional behavior of the aluminum frame plays an important role for the behavior of the overall system [78].

In [100], an IGU with a foam spacer was investigated which is also depicted in Figure 37. It was assumed that only the secondary seal does make a significant contribution to the mechanical system. Solid elements are used in the edge zone and shell elements are used to model the glass pane for a FEA. It was found that the principal strain in the secondary seal is increasing exponentially under a certain climate load for a smaller bending radius. However, this is only valid if the arc length is longer than the broadside of the glass pane. Otherwise the effect is less pronounced or even inverted. In order to limit the strain hence also the stress in the secondary seal, it is advisable to avoid glass panes with a small bending radius, which at the same time have a bigger arc length than its broadside.

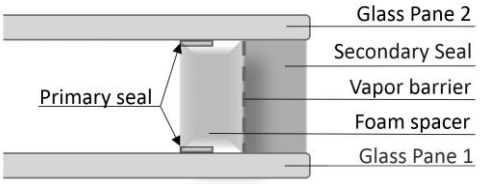

Figure 37: A foam spacer system, redrawn from [100]

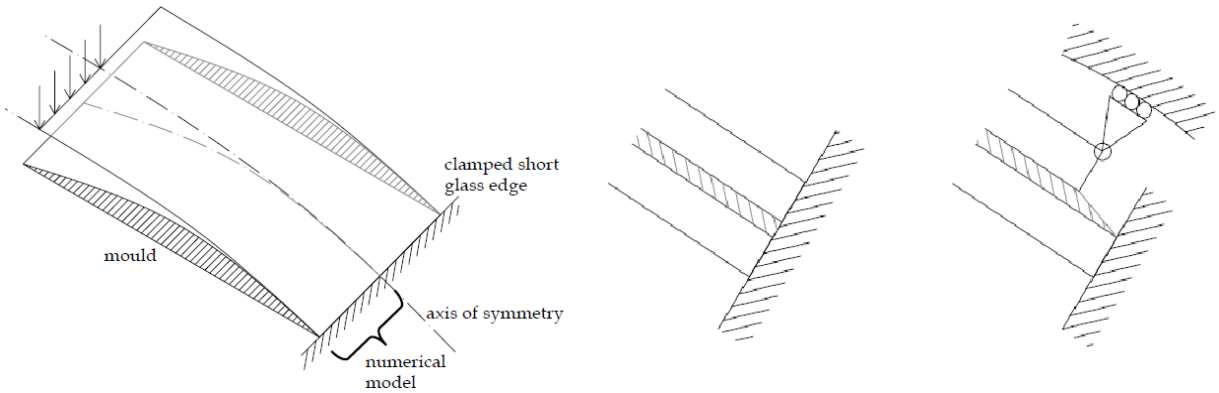

Figure 38: Left: Numerical model, middle: both glass panes fixed, right: one glass pane fixed [76]

In Figure 38, a model of a cylindrical curved laminated glass pane for a numerical study in [76] is shown. In contrast to the previous numerical models, the structural effect of the interlayer is now taken into account. Therefore, different bearing situations can occur: a variable number of glass panes is/ are fixed with a certain stiffness to the

bearing. In this certain case, volume elements were used for a FEA. Particularly, the interlayer material was PVB and the material model was visco-elastic.

A limited amount of numerical investigations about cold-bent glass where done up to date (2017). All numerical models are simplified in such a way that it makes them usable for the considered problem. It is challenging to deduce recommendations for a different problem about cold-bent IGU. In case of doubt, simplifications in the numerical model must be avoided. Nevertheless, some recommendations are also true for the ongoing numerical investigation in main chapter 6:

- The FEs in the glass pane must be able to consider membrane stress
- Dynamic effects of the contact problem are neglected in this work
- The the butyl strip (or primary seal) will be neglected because its mechanical contribution is low
- Close to non-convex areas of the FEM-region, an h-refining will be done
- Triangle-shaped FEs will not be used because they might behave too stiff
- An element distortion control will be used in the FE software Abaqus
- The adhesive surface is modeled as a rigid connection between the considered parts

6 Parameter Study of Cold-Bent IGUs

A comprehensive understanding of the mechanical behavior of double-glazed cold-bent insulated glass is the aim of this parameter study, which focuses on single-bent and double-bent insulated glass. In the first step, a reference model for the single-bent and the double-bent case will be the subject of numerical investigations, in chapter 6.1 and 6.3 respectively.

This approach assures that a sensible numerical and mechanical model will be chosen for the subsequent parameter study in chapter 6.3 and 6.4 for the single-bent and the double-bend case, respectively. An overview about the parameter study is also illustrated in Figure 39.

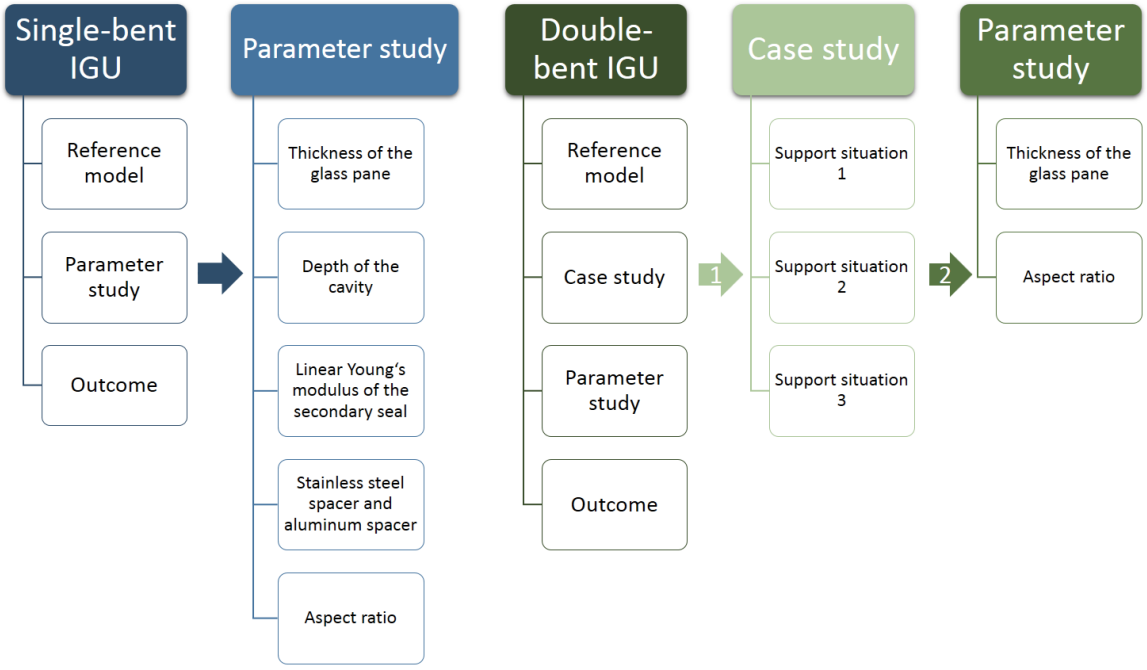

Figure 39: Overview about the parameter study of cold-bent IGUs

Due to the application in façade engineering, the approach "force follows form" was chosen in the numerical models, which means that an imposed deformation rather than a certain force is determining the final curved shape.

The whole parameter study was conducted with the aid of the finite element method (FEM) with the software Abaqus, version 6.14. The model was calculated implicit, static and considers non-linear effects (also referred to as 3rd order theory). Dynamic influences such as the strain-rate effect or the acceleration and velocity of the model due to the imposed movement were neglected. This is a sensible simplification,

because for any realistic cold-bending velocity, no pronounced strain rate effect is expected. This helps to to reduce complexity and instability in the numerical model and expensive calculation effort. Furthermore, influences from temperature or long time periods are not of interest in this work. This parameter study is therefore only valid for the cold-bending process itself – and not for the period of use -, and only then, when it is carried out under ambient temperature with sufficiently low velocity.

For simplification, the material properties are the same for both models over the whole parameter study, with an exception to parameter studies which are analyzing the influence of the material's properties. Therefore, the materials are described in this main chapter in Table 3 and in Figure 40. This also is the case for the geometry, but for a better readability, the geometric values are provided again next to the illustration of the single-bent and the double-bent model in the chapters 6.1 and 6.3, respectively.

An extensive convergence study was carried out and can be found in the annex in chapter 11.1. The input script, written in the programming language Python, which was used to generate the numerical model for the software Abaqus, can be found in the annex in chapter 11.3 in the digital version or is on the CD in the printed version.

Name of the Material	Young's Modulus	Unit	Poisson's Ratio	Unit	Plasticity
Glass [13]	70E9	Pa	0.23	-	No
Silicone (assigned to the secondary seal) [100]	2E6	Pa	0.48	-	No
Stainless steel[4] (assigned to the spacer) [101]	189E9	Pa	0.305	-	Yes
Steel[5] (assigned to the subconstruction, single-bent case) [102]	210E9	Pa	0.3	-	No
Aluminum[6] (assigned to the spacer for parameter study 4) [103]	70E9	Pa	0.3	-	Yes

Table 3: Linear-elastic material values used in the parameter study

[4] According to EN 10088-2:2014, the stainless steel alloy X5CrNi18-10 with the material number 1.4301-C was chosen
[5] According to EN 1993-1-1:2005, Chapter 3, the steel product S235 was chosen
[6] According to EN 1999-1-1:2007, the aluminum alloy 6060 with the material number T66. ($t \leq 3$ [mm]) was chosen

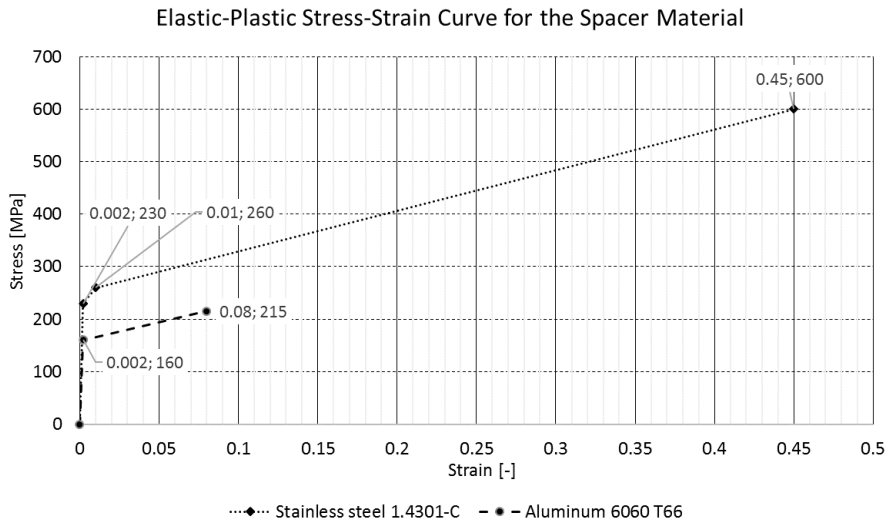

Figure 40: Elastic-plastic stress-strain curve used in the parameter study for the spacer material

6.1 Reference Model: Single-bent IGU

Single-bent insulation glass units (IGU) are examined in a parameter study in chapter 6.2. In order to choose a sensible bending radius and definitions such as boundary conditions (BCs) which can provide useful stress and strain outcomes, a reference model is investigated in the first place which is also depicted in Figure 42.

The reference model, as well as all other models in chapter 6.2, are bent displacement controlled onto an underlying subconstruction. Every result which is printed in a graph refers to an axis which is shown in Figure 41, Figure 42 and Figure 43. The arrow of the axis shows the result path. All geometrical values can be found in Table 4, more detailed information about the numerical model is given in the subchapter 6.1.1.

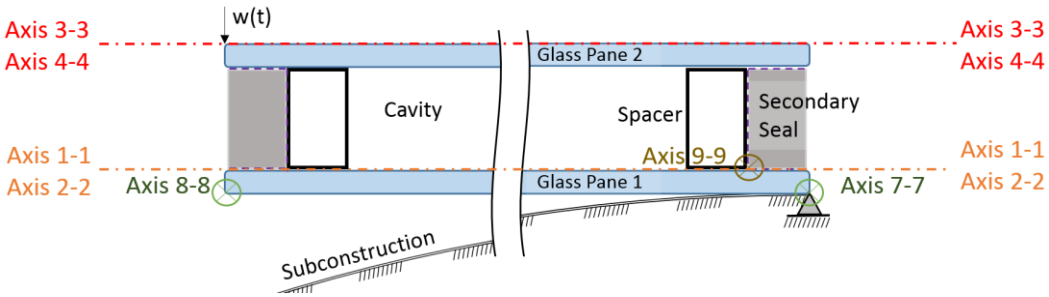

Figure 41: Schematic longitudinal section of the single-bent IGU

Name	Abbreviation	Value	Unit
Length of the glass pane	l_{gp}	3.50	m
Width of the glass pane	w_{gp}	1.50	m
Thickness of the glass pane	t_{gp}	8	mm
Height of the spacer, which is equal to the height of the secondary seal	h	16	mm
Width of the spacer	w_{sp}	6.5	mm
Sheet thickness of the spacer	t_{sp}	0.18	mm
Width of the secondary seal	w_{ss}	5	mm
Width of the subconstruction	w_{sub}	40	mm
Thickness of the subconstruction	t_{sub}	10	mm

Table 4: Geometrical values of the single-bent model

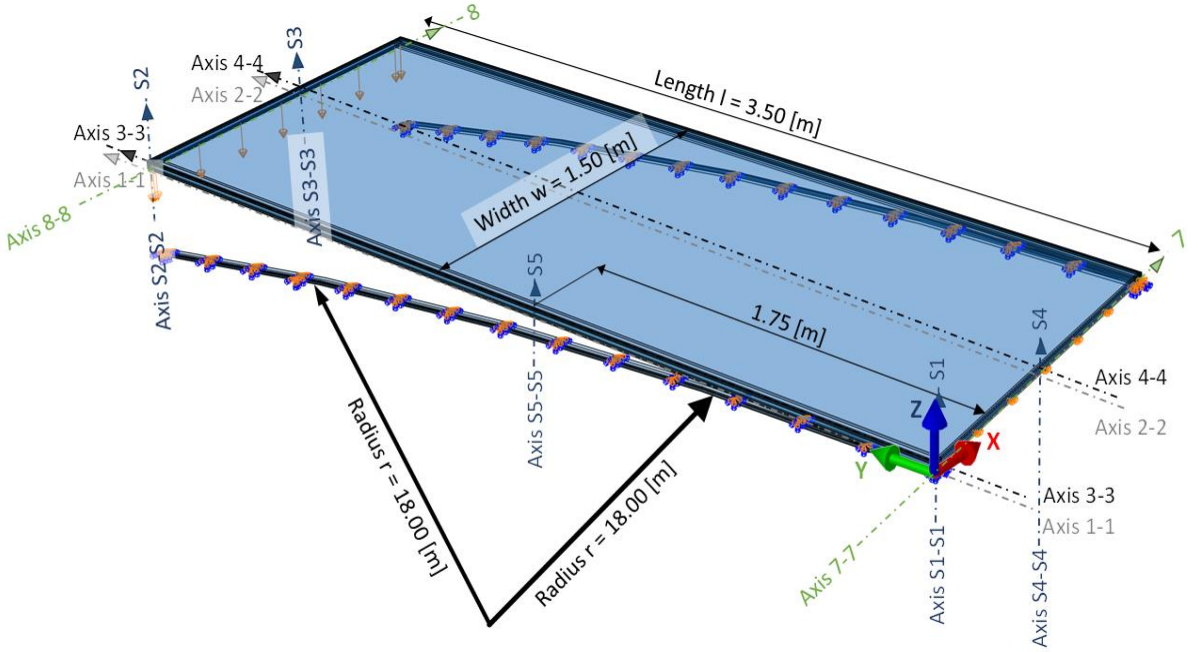

Figure 42: Reference model of the single-bent IGU

Annotation: The bending radius r is $18.0\,[m]$ which comes from an extensive numerical parameter study which was done beforehand. For a smaller r, the significant stress and strain values in the silicone and in the spacer bars are too high for a sensible parameter study. For a bigger r, the parameter study would not push the envelope of what is feasible. In order to restrict the scope of this work, this is not shown in this chapter. However, a numerical parameter study in [104] treats the influence of the bending radius for a laminated safety glass.

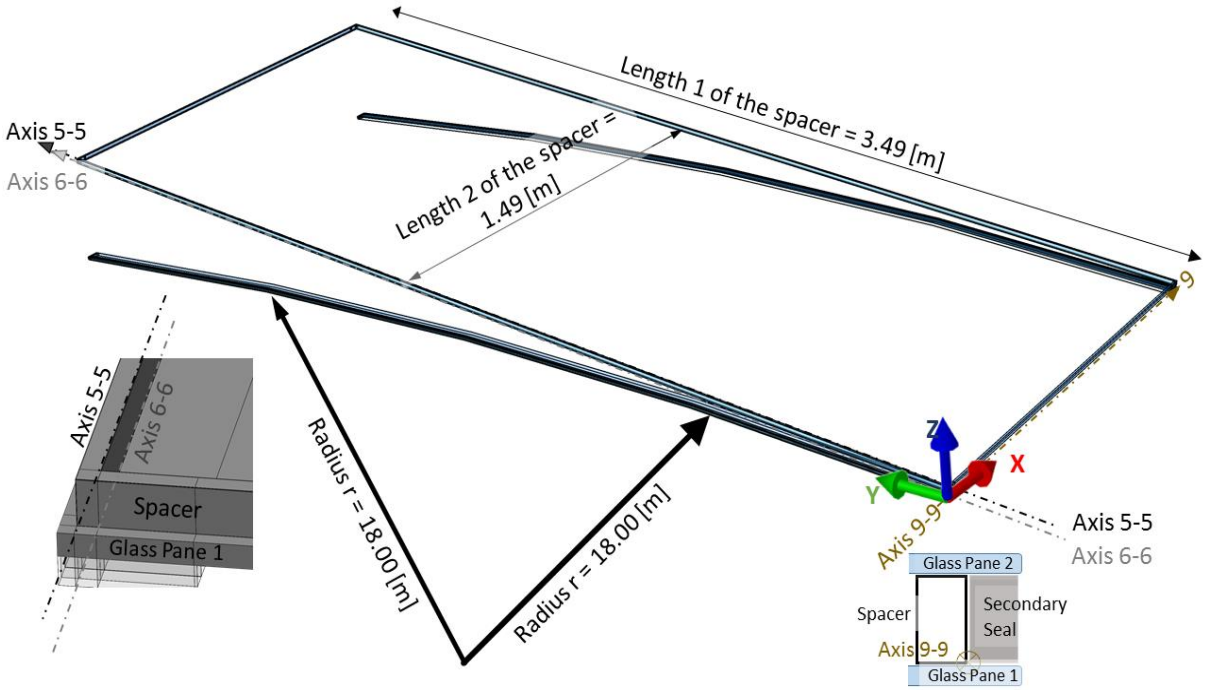

Figure 43: Spacer bars of the single-bent IGU

6.1.1 Finite element model of the single-bent IGU

The FE model consists of several parts, which are two longitudinal spacers parallel to the y-axis, two spacers along the width parallel to the x-axis, a circumferential secondary seal, two glass panes and two rectangular-shaped steel arcs for the subconstruction. Each part is assigned to a certain FE type, which are listed in Table 5 and show to be numerically stable and leads to sufficiently accurate results at the same time. Figure 44 shows the assigned element types in the edge region of the single-bent IGU. Moreover, Figure 44 shows the line support along axis 7-7, which is applied at the lower edge of glass pane 1. The movement in all 3 directions x, y and z is hindered and the rotation around the x-axis is permitted.

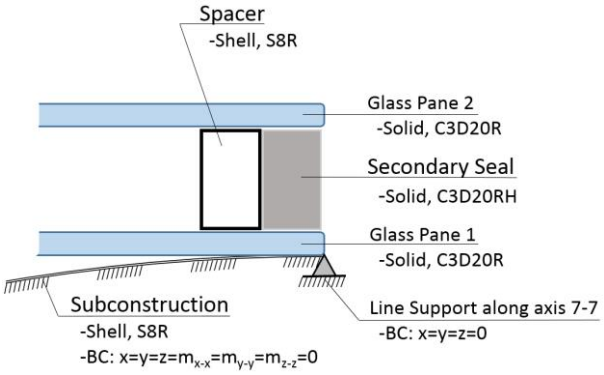

Figure 44: Finite elements used for the single-bent model

Part of the Single-Bent Model	Element Type	Specific Element Type	Name in Abaqus
Glass pane	Solid	20-node quadratic brick, reduced integration	C3D20R
Spacer	Shell	8-node doubly curved thick shell, quadratic, reduced integration	S8R
Secondary Seal	Solid	20-node quadratic brick, hybrid with linear pressure, reduced integration	C3D20RH
Subconstruction	Shell	8-node doubly curved thick shell, quadratic, reduced integration	S8R

Table 5: Finite elements used for the single-bent model

In order to choose the best numerical interaction property, it is vital to understand the interplay between the different parts of the IGU model. Because structural silicone sticks to the glass and to the spacer like an adhesive, it is reasonable to "tie" the finite element surfaces of the adjacent parts together.

The mechanical contribution of the primary seal is nearly zero but it's shear distortion becomes rather huge. This leads to serious numerical instabilities in the model and hence a slip-free interaction represents the butyl strip. Therefore, the spacers in the model are interacting with the underlying and overlying glass panes. In order to represent the interaction spacer – primary seal – glass pane, the spacers and the glass panes are allocated to a surface to surface interaction with a frictionless and hard contact, whereby the glass is the master, because the spacer is deformed easier due to its thin sheet thickness. Because the subconstruction is embedded rigidly, in order to avoid result interpretation difficulties, it is the master for glass pane 1. A frictionless and hard contact seemed to be sensible because the results compared to a soft contact were the same.

Furthermore, the friction between steel and glass in this case is negligible. It is assumed that the cavity is filled up fully with the noble gas argon which was modeled with pneumatic elements. All interactions and constraints are listed in Table 6 and are also shown in Figure 45.

Name	Interaction and Constraints	Further information
Glass-spacer surface	Surface-surface interaction, glass is master	Hard contact, frictionless, can separate after contact
Glass-secondary seal surface	Surface-surface tie constraint, glass is master	
Spacer-secondary seal surface	Surface-surface tie constraint, spacer is master	
Spacer-spacer shell edges	Shell-shell tie constraint	Position tolerance 1E-5 m
Gas filling	Fluid cavity interaction, pneumatic	
Subconstruction-glass	Shell-surface interaction, subconstruction is master	Hard contact, frictionless, cannot separate after contact

Table 6: Interaction and constraints for the single-bent model

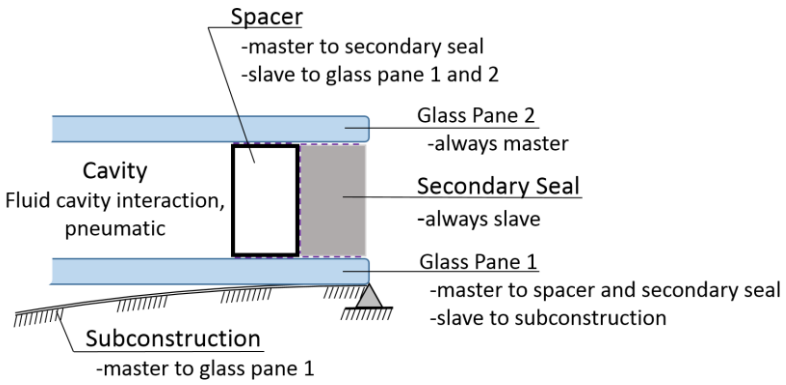

Figure 45 Interaction and constraints for the single-bent model

Based on the convergence study, which can be found in annex 11.1, an optimized mesh size was chosen. It is mentionable that all elements have quadratic shape functions, hence the integration points will be twice as fine as the mesh size. Moreover, the mesh size also greatly depends on the assignment of master and slave of the respective parts, since the numerical model shows a more stable behavior if the slave part is having a finer mesh than the master part. The mesh size for each part is listed in Table 7.

Annotation to Table 7: Seeding method refers to vertexes which define the corner points of a finite element. Seeding method "double" in this case means, that at the ends of an edge, the seeds are finest and in the middle of the edge, the seeds are grossest.

Part	Seeding method	Mesh size
Glass pane	By size, double	0.01 to 0.1 m
Secondary seal, circumferential	By size, double	0.005 to 0.05 m
Secondary seal along its height/width	By number, 4/3	0.005/0.003 m
Spacer along its length	By size, double	0.005 to 0.05 m
Spacer along its height/width	By number, 4/3	0.005/0.003 m
Subconstruction	By size, double	0.02 to 0.2 m

Table 7: Mesh size for the single-bent model

In Figure 46, the meshed single-bent model is shown. A close-up view of the meshed model in the corner region, from which it can be seen that the slave parts have a finer mesh than the master parts, is illustrated in Figure 47.

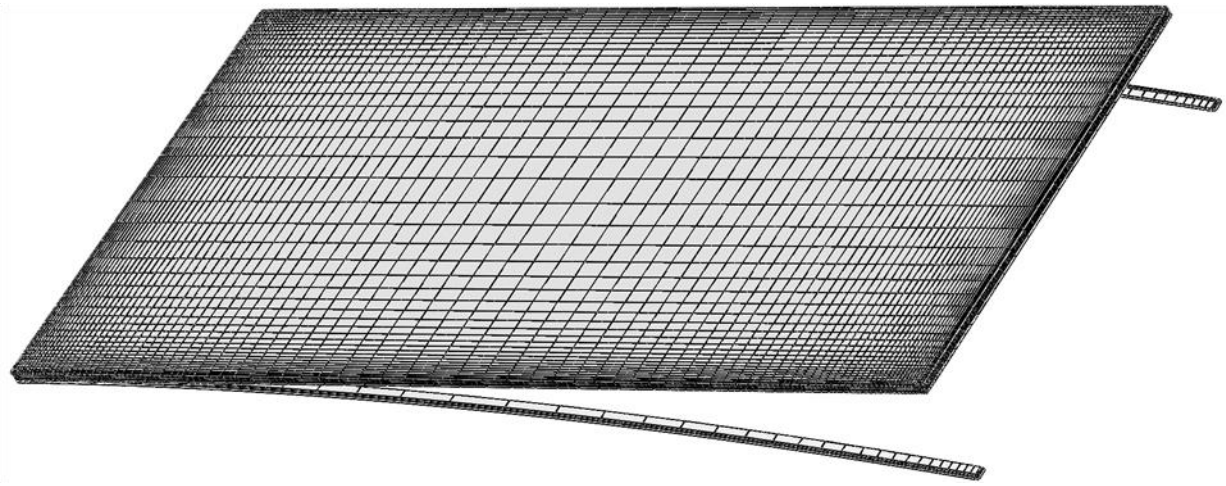

Figure 46: Meshed FE model, single-bent

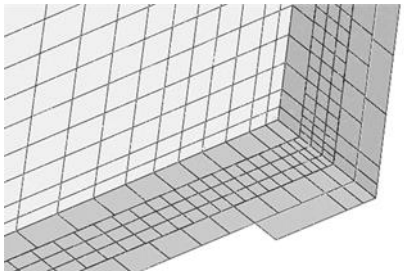

Figure 47: Close-up view of the mesh in the corner region

6.1.2 Time dependent results of the single-bent reference model

In this subchapter, the results of the single-bent reference model are provided with respect to time t whereby time refers to the progress of the simulation in place of physical time (at $t = 0$, the displacement $w(t = 0)$ is zero and at $t = 1$, the IGU is in it's final shape), which is also illustrated in Figure 48. In addition, it should be noted, that time in this case is dimensionless and does not represent dynamic properties such as acceleration but rather the progress of cold bending.

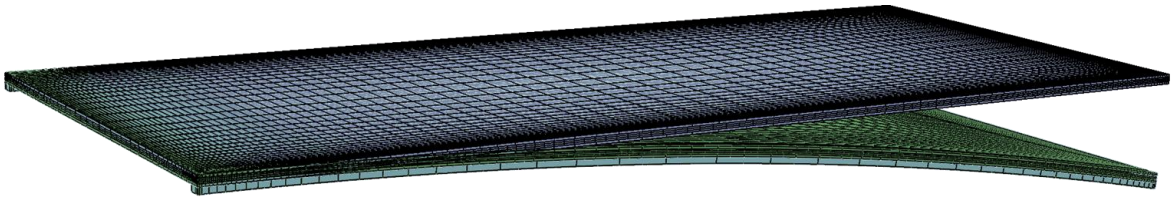

Figure 48: Meshed single-bent reference model at t=0 (grayish blue) and at t=1 (moss green)

Annotation: Because the radius $r = 18.0\,[m]$ *and the length of the IGU is* $l_{gp} = 3.5\,[m]$*, the enforced displacement at* $t = 1$ *is* $u_{enf} = w(t = 1) = r\left(1 - cos\left(\frac{l_{gp}}{r}\right)\right) \approx 0.3392\,[m]$*, furthermore* $w(t = 1/3) \approx 0.1131\,[m]$ *and* $w(t = 2/3) \approx 0.2261\,[m]$.

6.1.2.1 Qualitative results of glass pane 2

In Figure 49, the maximal principal stress $\sigma_{max,pr}$ on the top surface of glass pane 2 is shown in a sequence for $t = \frac{1}{3}, t = \frac{2}{3}$ and $t = 1$.

At $w\left(t = \frac{1}{3}\right) = 0.113\,[m]$, the stress peaks, which are about $10\,\left[\frac{N}{mm^2}\right]$, show clearly the location where the contact of the IGU with the subconstruction is happening. It is noticeable that the stress at the free end of the glass pane is almost zero. At the back end at $l_{gp} = 0\,[m]$ next to axis 7-7, where the IGU is in contact with the subconstruction, the stress distribution is non-linear while it approaches a more constant distribution at the front end at $l_{gp} = 3.50\,[m]$ next to axis 8-8.

At $w\left(t = \frac{2}{3}\right) = 0.226\,[m]$, the stress peaks have moved a little bit upwards and have increased from about $10\,\left[\frac{N}{mm^2}\right]$ to $20\,\left[\frac{N}{mm^2}\right]$. It is also conspicuous, that the stress in the lower half of the glass pane is almost distributed over the broadside of the IGU,

except from the stress peaks and the locally declining stress next to the line support area. Furthermore, in the upper half of the glass pane, the stress is declining at a much slower rate and almost linearly which is in strong contrast to the stress distribution in the lower part. Due to the ongoing bending process and the growing contact surface at $t = \frac{2}{3}$, the system is highly asymmetrical.

Roughly speaking, at $w(t = 1) = 0.339\ [m]$, the stress distribution is symmetrical, despite the fact that the static system is not symmetric. This leads to the fact that the IGU system is quite stiff for the upper glass pane. Exceptionally striking are the double-symmetric occurring stress peaks at the edge of the glass pane which are originating from the arc shaped subconstruction. This means, that the natural occurring shape from the controlled displacement is not circular-shaped, which makes sense, since the distribution of stiffness over the IGU is not equal, therefore regions with a higher stress gradient are inevitable. Since the maximum stress values do not increase to a remarkable degree from $t = \frac{2}{3}$ to $t = 1$, the occurring stress peaks are acceptable and do not pose a structural problem to the material.

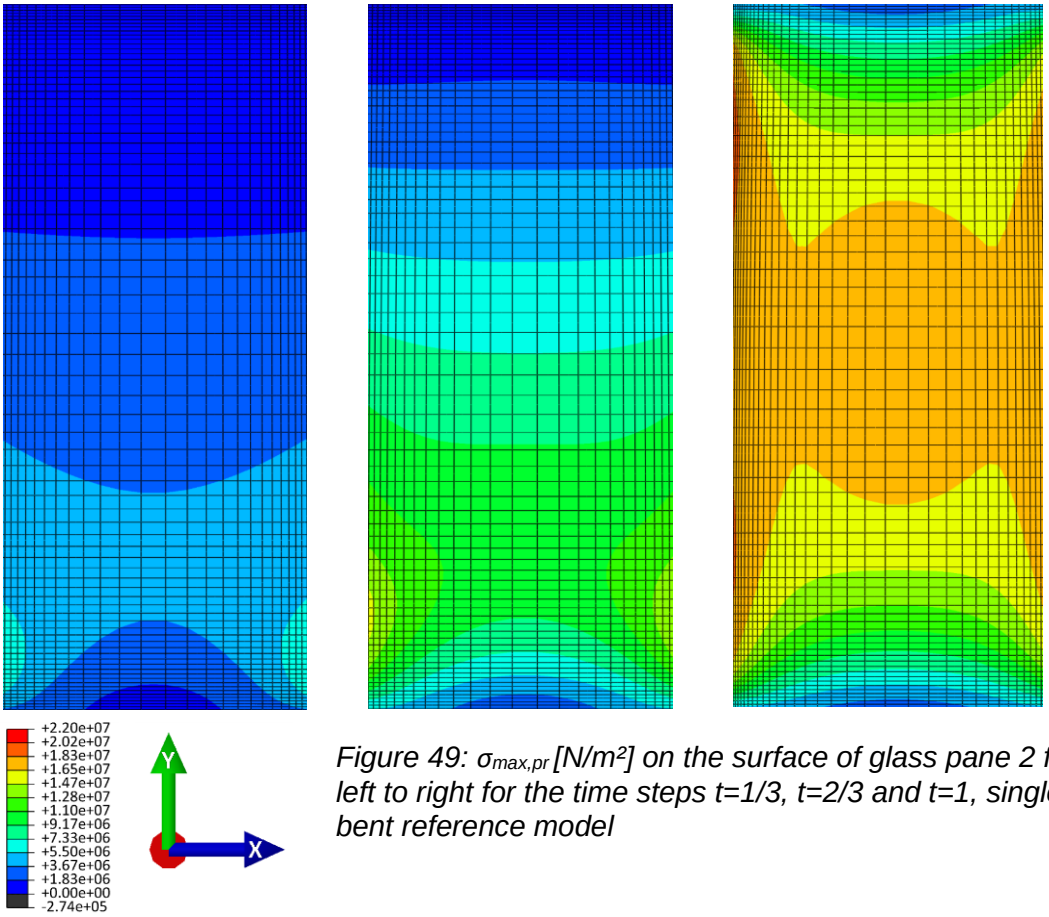

Figure 49: $\sigma_{max,pr}$ [N/m²] on the surface of glass pane 2 from left to right for the time steps t=1/3, t=2/3 and t=1, single-bent reference model

6.1.2.2 Qualitative results of the spacer bars

In Figure 50 and Figure 51, the von Mises stress distribution σ_e of the stainless steel spacer along the longitudinal side of the IGU system is shown in a sequence for the time steps $t = \frac{1}{3}, t = \frac{2}{3}$ and $t = 1$. In the close-up view of Figure 51, it can be seen that for the spacer at the upper end A, the stainless steel yields at $t = 1$. At this yielding area at $t = 1$, the first stress peaks occurred at $t = \frac{1}{3}$. The same fact is also true for the lower end B of the spacer. At $t = 1$ in Figure 51, a neutral axis can be seen from the false color plot which is gradually vanishing near the corner region of the IGU.

At $w(t = 1) = 0.339\ [m]$ in Figure 51, it can be seen that the stress distribution gets more parallely aligned when moving away from the ends of the spacer. From this context, the influence of the corner region can be estimated, which is about $0.2\ [m]$. It can be stated that from $0.20\ [m]$ to $3.30\ [m]$ the influence of the corner region is insignificant.

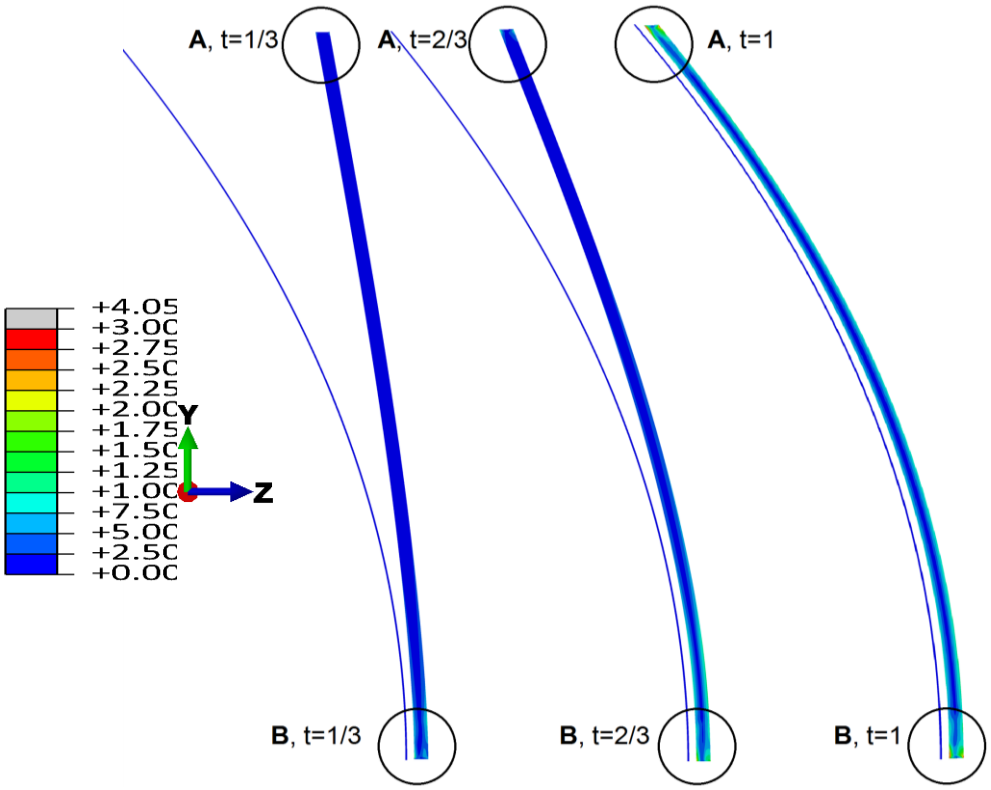

Figure 50: σ_e [N/m²] on the surface of the spacer from left to right for the time steps t=1/3, t=2/3 and t=1, single-bent reference model

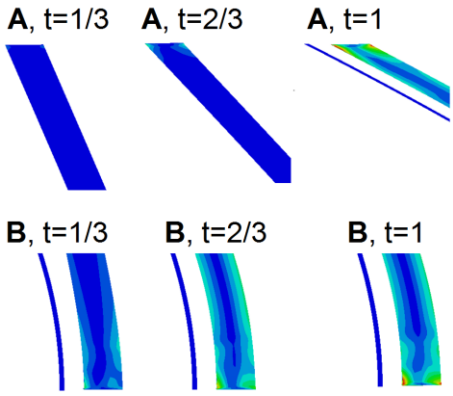

Figure 51: σ_e [N/m²] on the surface of the spacer from left to right for the time steps t=1/3, t=2/3 and t=1, single-bent reference model, close-up view of the lower and upper end

6.1.2.3 Qualitative results of the secondary seal

In Figure 52, $\sigma_{max,pr}$ of the secondary seal is shown in a sequence for $t = \frac{1}{3}, t = \frac{2}{3}$ and $t = 1$ from top to bottom in order to understand the stress development during the cold bending process in the single-bent model. Because the silicone, which is used for the secondary seal, is the only element which transmits shear force through the IGU, it has an important influence on the behavior of the IGU.

At $w\left(t = \frac{1}{3}\right) = 0.113\ [m]$, the stress is highest in the corner regions and is increasing there over time but in particular distributes over the broadside of the secondary seal. The reason for this is that the top glass pane is slipping forward during the bending process which leads to a deformation of the edge zone in y-direction (see also Figure 60). Because the rate of deformation in the secondary seal per length unit in y-direction is higher along the broadside, the stress has also to be higher.

At $w(t = 1) = 0.339\ [m]$, a significant stress peaks occurs at the inner side of both corners next to axis 8-8. At these inner corners, the silicone has a $\sigma_{max,pr}$ of about $1.6\ \left[\frac{N}{mm^2}\right]$. The broadside of the silicone has to withstand a stress of about $0.7\ \left[\frac{N}{mm^2}\right]$. Worth mentioning is also the fact, that $\sigma_{max,pr}$ along the longitudinal side increases with a lower rate compared to the broadside. At the broadside, $\sigma_{max,pr}$ stays well below stress values of $0.5\ \left[\frac{N}{mm^2}\right]$.

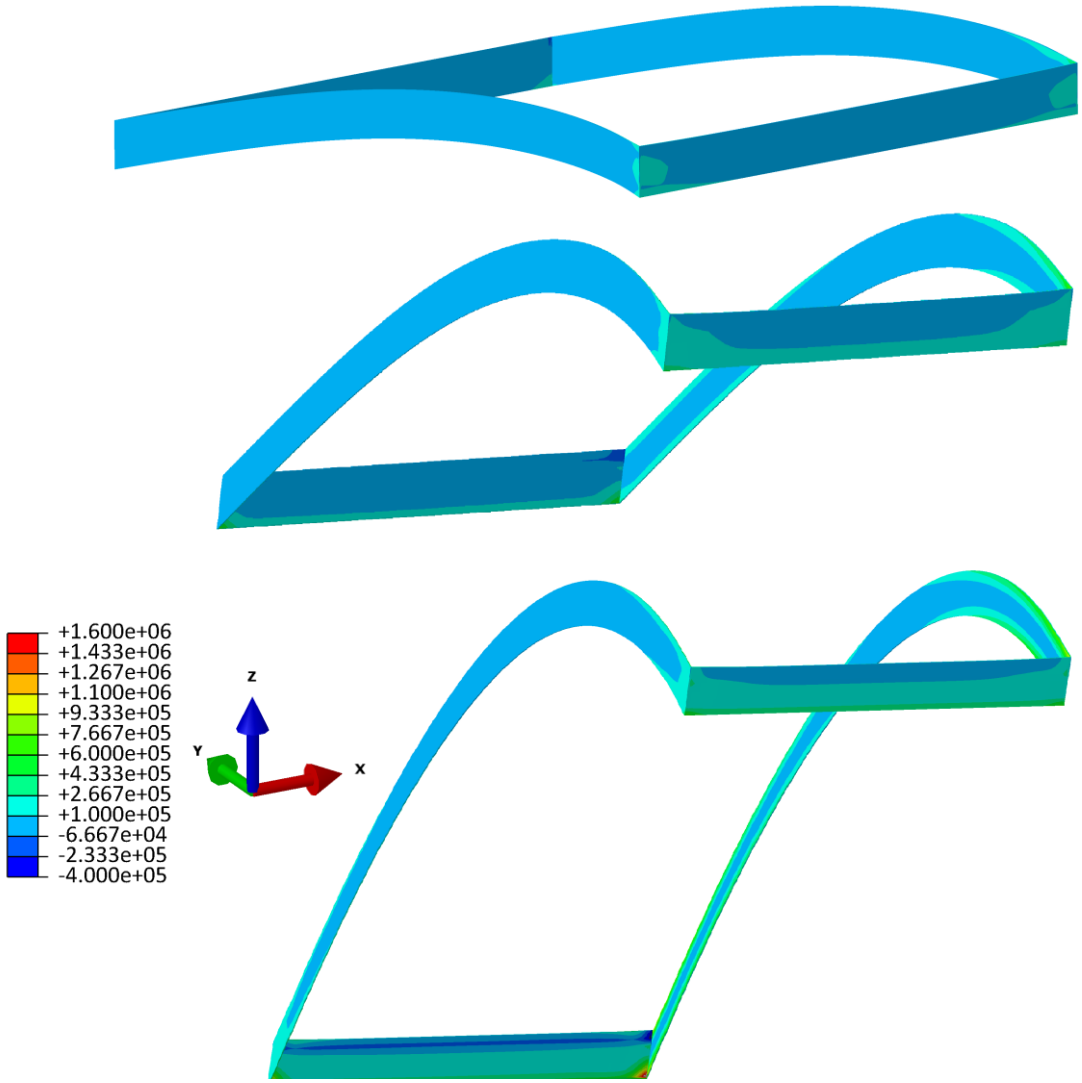

Figure 52: $\sigma_{max,pr}$ [N/m²] for the secondary seal at the time steps t=1/3, t=2/3 and t=1 from top to bottom, single-bent reference model, z is upscaled 10 times

6.1.2.4 Required force for the cold bending process

In Figure 53, the required force F for the cold-bending process is shown as a function of the enforced displacement. It takes just $100\ [N]$ to bent the IGU $0.15\ [m]$, for the next $0.15\ [m]$ it takes another $200\ [N]$. The total required force to bent it $0.3\ [m]$ is $300\ [N]$. For the last few centimeters, it takes over $1100\ [N]$ which means that almost 80% of the total force is required for the last 12% of enforced displacement. The reason for this is that most of the contact between the subconstruction and the IGU is realized mainly in the last centimeters.

During the first $0.3\ [m]$ the IGU builds up the contact with the subconstruction only at a small area (see also Figure 52). A constant deformation rate during the cold-bending

process can avoid unforeseen stress peaks due to an unconsidered strain rate effect. Therefore, the force has to brought onto the IGU very low at first and then should increase exponentially. If this construction approach seems not to be practically feasible, then the strain rate effect should be examined beforehand.

It should be noted, that the exponential increase of F is less pronounced for a bigger bending radius r and stronger pronounced for a smaller bending radius r, which was examined in a parameter study in [104].

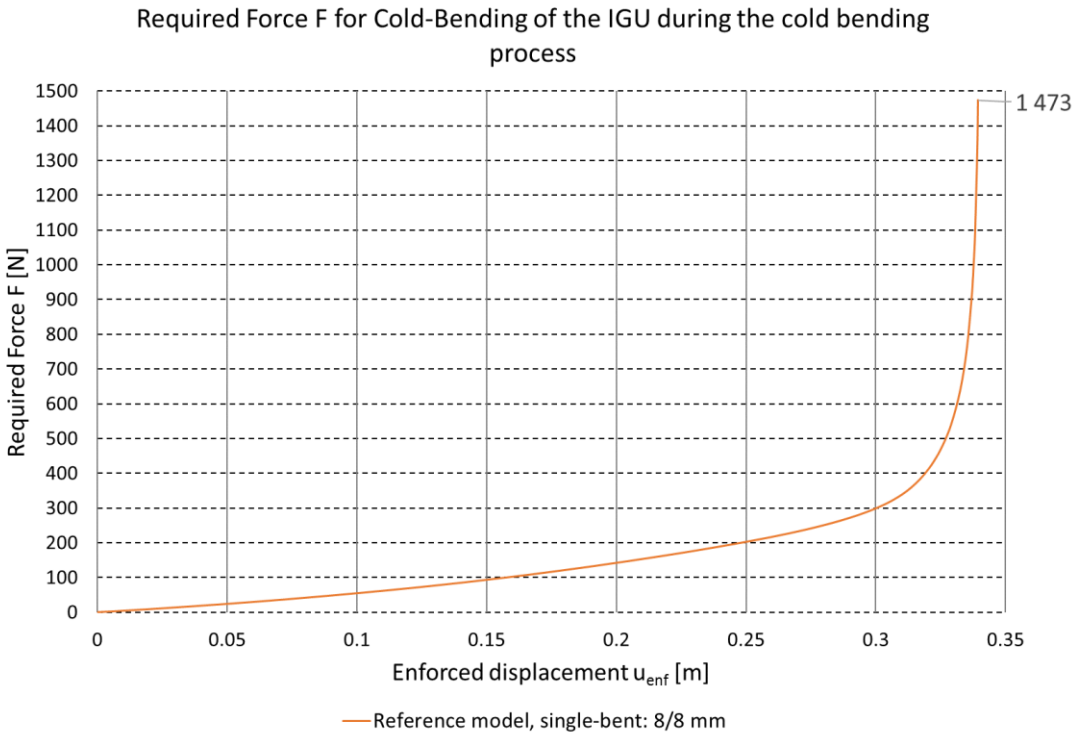

Figure 53: Reference model single-bent, required force F for cold-bending of the IGU

6.1.2.5 Glass pane

In Figure 54, $\sigma_{max,pr}$ along axis 1-1 is depicted. In Figure 55, $\sigma_{max,pr}$ along axis 2-2 is depicted. At a first glance, the stress distributions along both axes are developing over time very differently, the relevant stress values in the center of the glass pane being always lower. Nevertheless, the slope of the stress function is very steep for axis 1-1 from $0\ [m]$ to about $0.05\ [m]$ and does not change it's gradient over time. This means that the interaction with the subconstruction does not change once occurred.

Over time it can be seen, that the field where relatively high stress occurs is correlating with the increasing contact with the subconstruction. Conspicuous is the exponential growth of the stress plateau from $w(t = 0.8) = 0.271\ [m]$ to $w(t = 1) = 0.339\ [m]$,

where it extends from $0.1\ [m] - 1\ [m]$ to $0.1\ [m] - 3.3\ [m]$. This is in good correlation with the required force function for cold-bending in Figure 53. The stress along axis 2-2 in the middle of the glass pane shows the same exponential behavior, which can be seen in Figure 55. Noticeable in Figure 55 is a smoother slope for the stress functions which are not as steep as in Figure 54 for axis 1-1. This is due to the fact that there is no contact with the underlying subconstruction.

For all time steps $0 < t \leq 1$ in the first few centimeters of axis 2-2 and at $w(t = 1) = 0.339\ [m]$ from about $3.40\ [m]$ to $3.50\ [m]$, the stress function is V-shaped. The reason for this is, that the spacer hinders a free deformation of glass pane 1, but at the outermost region, there is the relatively soft structural silicone which permits the glass pane to deform. This V-shaped stress curve does not appear in Figure 54 because axis 1-1 is in contact with the longitudinal spacer from $0.005\ [m]$ to $3.495\ [m]$.

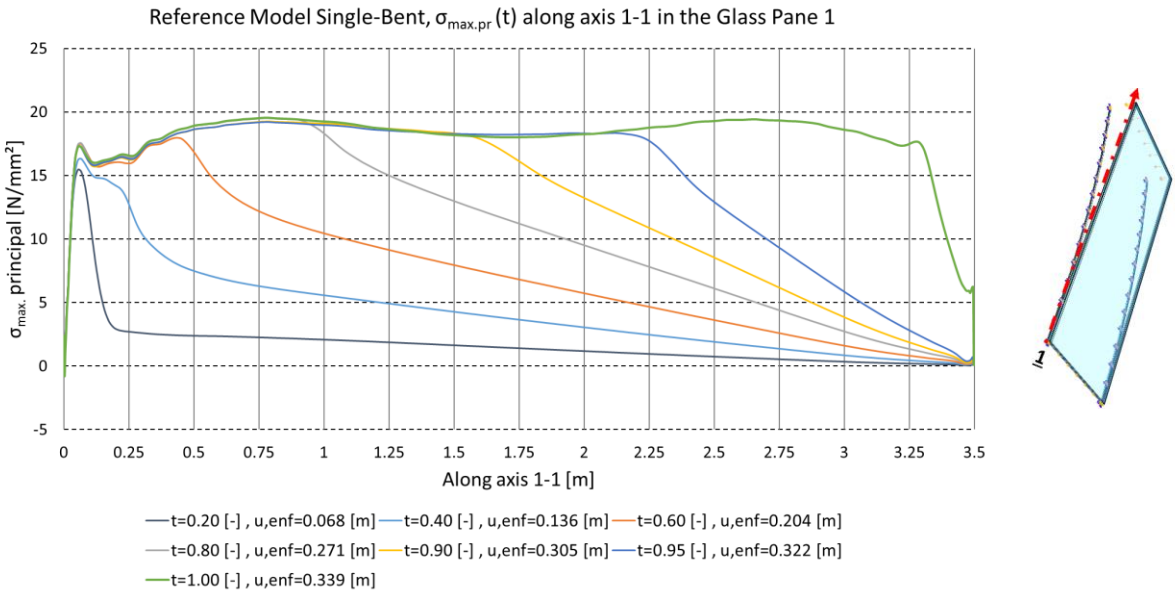

Figure 54: Reference model single-bent, $\sigma_{max.}$(t) principal along axis 1-1 in the glass pane 1

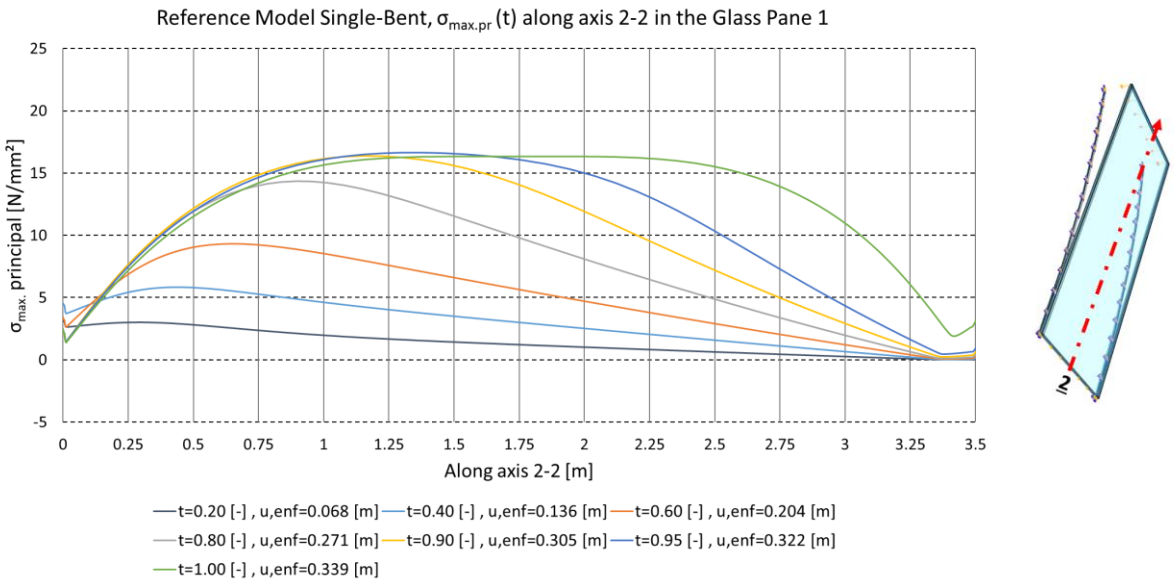

Figure 55: Reference model single-bent, $\sigma_{max.}$(t) principal along axis 2-2 in the glass pane 1

Glass pane 2, which is evaluated in Figure 56 for axis 3-3 and in Figure 57 for axis 4-4, exhibits the same characteristics in the stress function like glass pane 1.

Roughly speaking, the stress functions of glass pane 2 for axis 3-3 in Figure 56 and for axis 4-4 in Figure 57 look alike the stress functions in glass pane 1. For $w(t = 1) = 0.339\ [m]$, there is no notable difference between the maximum stress values. However, at $w(t = 0.8) \approx 0.2714$ the stress in glass pane 2 in axis 3-3 is the highest with a value of about $21\ \left[\frac{N}{mm^2}\right]$ whereby the maximum stress value for $w(t = 1) = 0.339\ [m]$ drops slightly below $20\ \left[\frac{N}{mm^2}\right]$. These stress peaks occur at the front end at of the contact area. However, these stress values are well beyond the characteristic value of the material's resistance, which for a monolithic TTG would be $120\ \left[\frac{N}{mm^2}\right]$[7] according to the Austrian standard ÖNORM B 3716-1 [12]. In addition, the slope of the stress function is not as steep as in glass pane 1 and reaches zero at length $l_{gp} = 3.50\ [m]$ at $w(t = 1) = 0.339\ [m]$. This is in contrast to glass pane 1, where $\sigma_{max,pr}$ is about $6\ \left[\frac{N}{mm^2}\right]$ due to the impediment on the lower side through the subconstruction and on the upper side through the secondary seal and the spacer.

[7] Obtained from the Austrian standard ÖNORM B 3716-1:2016, chapter 9.2 [12]

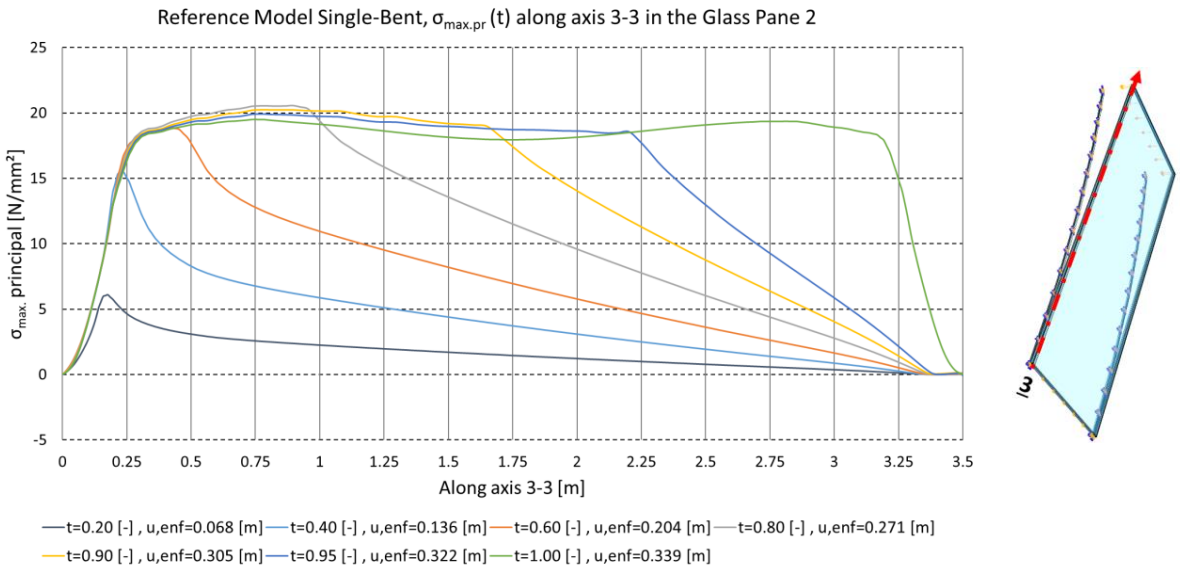

Figure 56: Reference model single-bent, $\sigma_{max,\,pr}$.(t) principal along axis 3-3 in the glass pane 2

Like in glass pane 1 for axis 2-2, the stress function in Figure 57 for axis 4-4 exhibits the same features with a significant stress value of $16\ \left[\frac{N}{mm^2}\right]$. However, a small difference is notable. For glass pane 2, the V-shaped stress function at the lower end is increasing until $w(t = 0.6) = 0.204\ [m]$ and then stays constant whereby for glass pane 1, the stress is increasing until $w(t = 0.4) = 0.136\ [m]$ and then drops and stays constant until $w(t = 1) = 0.339\ [m]$. This phenomenon occurs, because at first, the contact area with the subconstruction is small and thus the increase in stress is high. After a while, if the contact area is big enough, the stress can propagate better which leads to a decrease in stress. Furthermore, the stress does not change at all after $w(t = 0.8) = 0.271\ [m]$ because the contact area is big enough and therefore the influence of the subconstruction to the middle of the glass pane decreases.

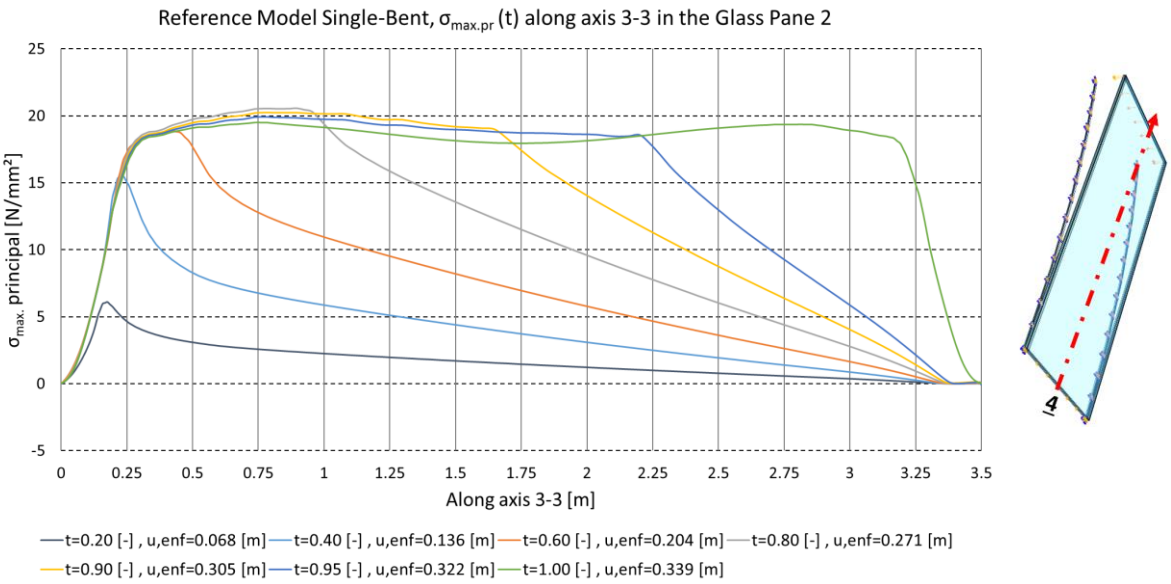

Figure 57: Reference model single-bent, $\sigma_{max.}(t)$ principal along axis 4-4 in the glass pane 2

6.1.2.6 Spacer bar

In Figure 58, the von Mises stress σ_e in axis 5-5 is shown. In Figure 59, σ_e in axis 6-6 is shown. Axis 5-5 lies at the upper inner edge and axis 6-6 lies at the lower inner edge of the longitudinal spacer.

The spacer plasticizes at the back end at $l_{gp} < 0.11\ [m]$ and at the front end at $l_{gp} > 3.39\ [m]$ in both axes. The maximal stress value is reached for axis 5-5 at $w(t = 1) = 0.339\ [m]$ at both ends and is approximately $380\ \left[\frac{N}{mm^2}\right]$.

For axis 6-6, the maximal stress value is approximately $400\ \left[\frac{N}{mm^2}\right]$ which occurs at $l_{gp} = 3.4885\ [m]$. At $l_{gp} = 0.0115\ [m]$, the maximum stress is reached for $w(t = 0.8) = 0.271\ [m]$ and is about $405\ \left[\frac{N}{mm^2}\right]$.

For both graphs, the stress functions outside the sphere of influence of the corner region are increasing their stress values until $w(t = 0.6) = 0.204\ [m]$. Subsequently, the stress functions have reached a stress plateau which propagates according to the contact area of the IGU with the subconstruction. The stress values $w(t = 1) = 0.339\ [m]$ outside of the corner region are almost $90\ \left[\frac{N}{mm^2}\right]$ for axis 5-5 and are slightly above $75\ \left[\frac{N}{mm^2}\right]$ for axis 6-6. The stress values at $w(t = 1) = 0.339\ [m]$ in the

plasticizing area in the corner region are greatly influenced by the controlled deformation and the numerical contact formulation between the parts. Because of this numerical influences, σ_e can vary up to about $\pm 5\%$ if the controlled displacement varies within a tenth of a millimeter. If σ_e gets varied within this range of uncertainty, it gets certain that the spacer plasticizes. The maximum stress value is (as an approximation at $l_{gp} = 0.0115\ [m]$ and $l_{gp} = 3.4885\ [m]$) about $400 \pm 20\ \left[\frac{N}{mm^2}\right]$ which is above the yielding stress of $230\ \left[\frac{N}{mm^2}\right]$ and well beyond the ultimate stress of $f_u = 600\ \left[\frac{N}{mm^2}\right]$.

Therefore, the stress outside the sphere of influence of the corner region will be considered. In short, the material utilization of the stainless steel spacer in the center region is low which leaves a high remaining elastic potential for service loads. It can be assumed, that the corner region of the IGU is not greatly influenced by bending moments from service loads.

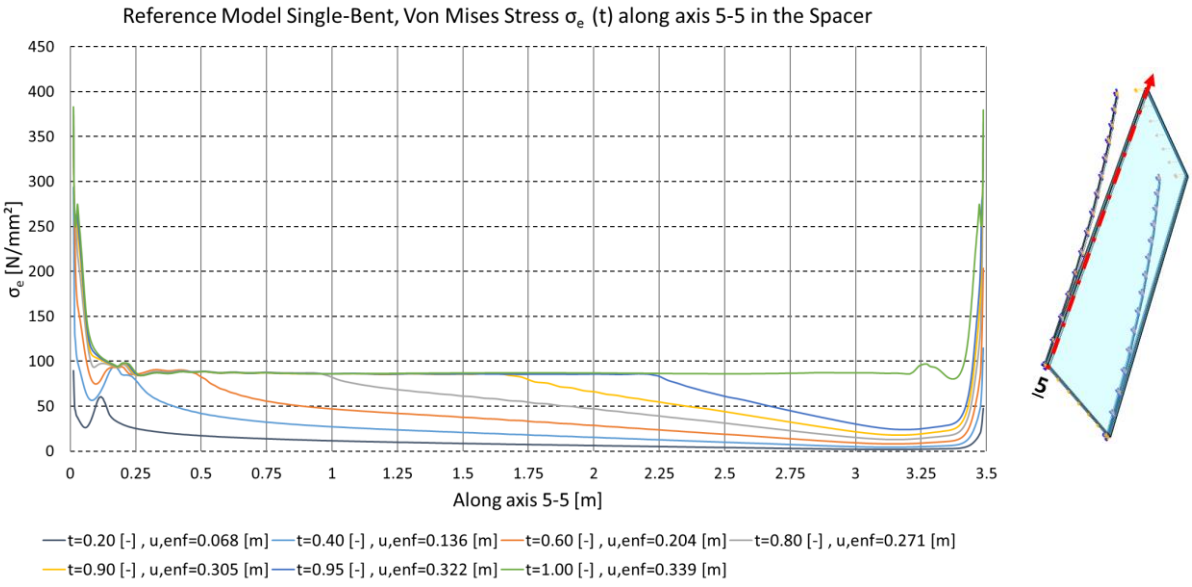

Figure 58: Reference model single-bent, von Mises stress σ_e. (t) along axis 5-5 in the spacer

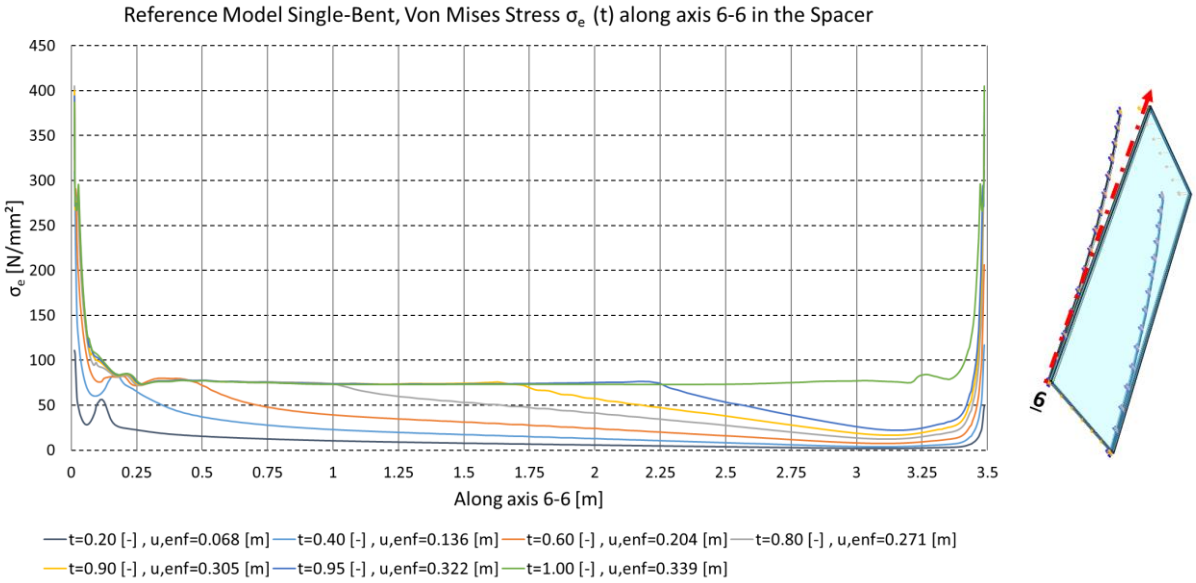

Figure 59: Reference model single-bent, von Mises stress σ_e. (t) along axis 6-6 in the spacer

6.1.2.7 Deformation of the edge zone

In Figure 60, the deformation of the edge zone in y-direction is shown at $w(t = 1) = 0.339\ [m]$ for the front end at $3.40 \leq l_{gp} \leq 3.50\ [m]$ (next to axis 8-8) and for the back end at $3.40 \leq l_{gp} \leq 3.50\ [m]$ (next to axis 7-7) without and with secondary seal. At the front end at $3.40 \leq l_{gp} \leq 3.50\ [m]$, the shear deformation in the glass panes and the spacer system is linear but the secondary seal deforms non-linear.

Because the spacer can slip between the glass panes, it deforms due to the controlled displacement. For the secondary seal, the situation is very different because it is bonded with both glass panes and the spacer. If glass pane 1 is in contact with the subconstruction, it will be clamped there at the time step in which the contact occurs and cannot separate or slip anymore. During the bending process, glass pane 2 does not elongate significantly, since shear is only transferred between both glass panes through the circumferential silicone. Therefore, it slips forward by virtue of fully adhesion with the secondary seal. Consequentially, the spacer also has to slip forward because firstly, it is bonded with the silicone as well and secondly, it is “pushed forward” by the deformation of the secondary seal next to axis 7-7 in y-direction. Because glass pane 2 is not aligned parallel in the radial direction but instead lies a little bit behind due to the low stiffness of the silicone, which allows more deformation, the silicone's deformation is non-linear. Nevertheless, the direction of deformation is

in accordance with the assumption, that it has to deform radial parallel for $w(t = 1) \approx 0.339[m]$ due to the circular shaped subconstruction.

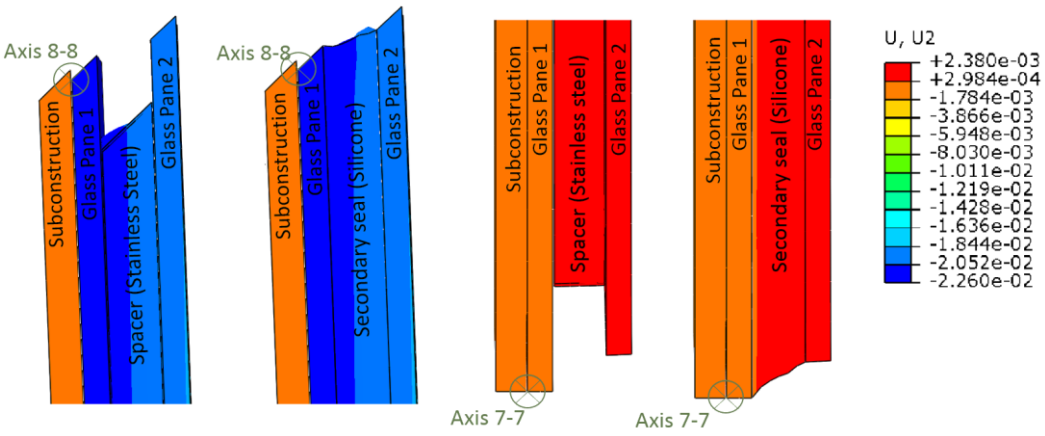

Figure 60: Deformation of the secondary seal in y-direction at t=1 (y-direction is upscaled) from left to right: Front end, without and with secondary seal, back end without and with secondary seal

6.1.2.8 Secondary seal

From Figure 61 to Figure 65, the maximum displacements in the secondary seal over $0 \leq z \leq 16\ [mm]$ from zero on on is depicted for the axes S1-S1 to S5-S5.

In Figure 61, the displacement for the axis S1-S1 is illustrated over time. The maximum displacement increases for every time increment $\Delta t = 0.2$ about $0.5\ [mm]$.

The maximum displacement for $t = 1$ is about $2.5\ [mm]$ which represents a shear displacement of $\Delta\alpha = 15.6\ \%$. It can assumed that the deformation function for any time step is almost linearly because at S1-S1 a contact between glass pane 1 and the subconstruction exists from $t <<$ on. Moreover, the line support is close to S1-S1 which provides relatively stable conditions over time compared to the other parts of the IGU.

In Figure 62 for axis S2-S2, the deformation over time $0 \leq t < 0.97$ growths at a small rate. At $w(t = 1) = 0.339\ [m]$, when the contact with the subconstruction is completed, the deformation increases fivefold from $0.2\ [mm]$ to $1.0\ [mm]$. The reason for this is, that at $t = 0.97$, the contact between subconstruction and IGU starts to affect the free deformation to a large degree. Therefore, an interaction between an exponentially increasing F, gradually emerging confinment at S2-S2 and a Poisson's ratio ν close to 0.50 [-] results in an increased deformation. For $w(t = 1) = 0.339[m]$, $\Delta\alpha = 6.2\ \%$. but for $w(t = 0.8) = 0.271\ [m]$, $\Delta\alpha = 1.3\ \%$.

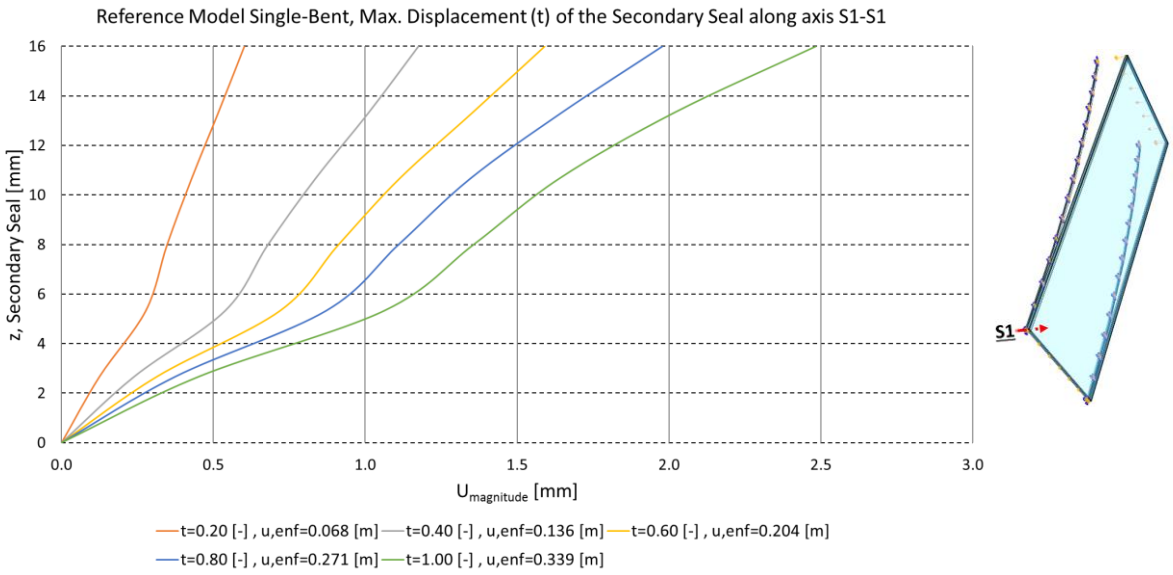

Figure 61: Reference model single-bent, max. displacement (t) of the secondary seal along axis S1-S1

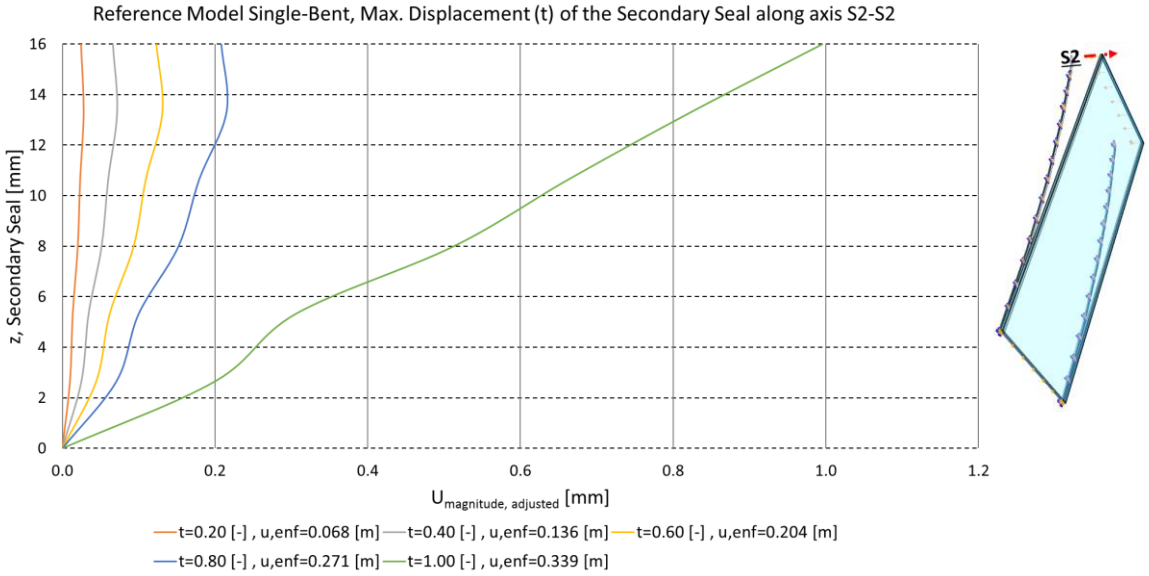

Figure 62: Reference model single-bent, max. displacement (t) of the secondary seal along axis S2-S2

The deformation of axis S3-S3 in Figure 63 poses several questions due to its shape with a pronounced turning point at $z = 13\ [mm]$. Considering the Poisson's ratio of the silicone, which is $\nu = 0.48$ in this case, the volume change is relatively low. Therefore, the spacer behind the secondary seal has also be taken into account, when analyzing the deformed shape. The spacer at the top shows a y-distance to $l_{gp} = 3.495\ [m]$ at glass pane 2 of $4.68\ [mm]$ instead of $5\ [mm]$. At the bottom, the spacer shows a y-distance of $5.06\ [mm]$ instead of $5\ [mm]$ to $l_{gp} = 3.50\ [m]$ at glass pane 1 which leads

to an additional inclination of 2.4%. Because of the missing shear force transmission between the glass panes and the spacers, glass pane 2 can slip if the spacer is deforming at a faster rate. About $0.38\ [mm]$[8] out of $0.63\ [mm]$ at $z(t = 1) = 16\ [mm]$ is contributed by the spacer's additional deformation. Furthermore, an exponential increase of the deformation curves over time is evident for axis S2-S2. Compared to axis S2-S2, the deformation in axis S3-S3 growths at a lower rate which reveals the smaller influence from the longitudinal edge zone.

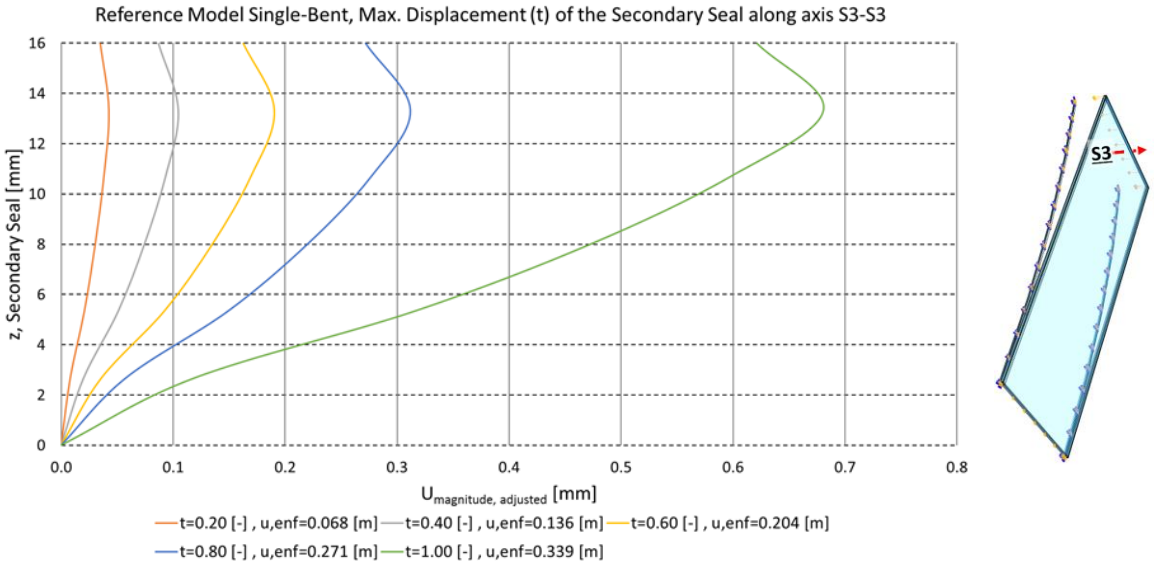

Figure 63: Reference model single-bent, max. displacement (t) of the secondary seal along axis S3-S3

Figure 64 depicts a more linear deformation for axis S4-S4 than in S1-S1. This is apparently owed to the fact, that due to the position of S4-S4 in the middle of the IGU next to the line support, the contribution to the deformation comes just from "forward sliding" of the spacer system and glass pane 2.

Figure 65 depicts an almost linear deformation for axis S5-S5. The deformation amplitudes are lying between the values of S1-S1, which are the highest, and S2-S2, which are the lowest. This means, that the rate of deformation along the longitudinal side of the IGU has a maximum at the back end at $l_{gp} = 0\ [m]$ and is decreasing continuously until $l_{gp} = 3.50\ [m]$.

[8] The difference of the additional deformation from the spacer at $l_{gp} = 3.495$ is $5.06\ [mm] - 4.68\ [mm] = 0.38\ [mm]$.

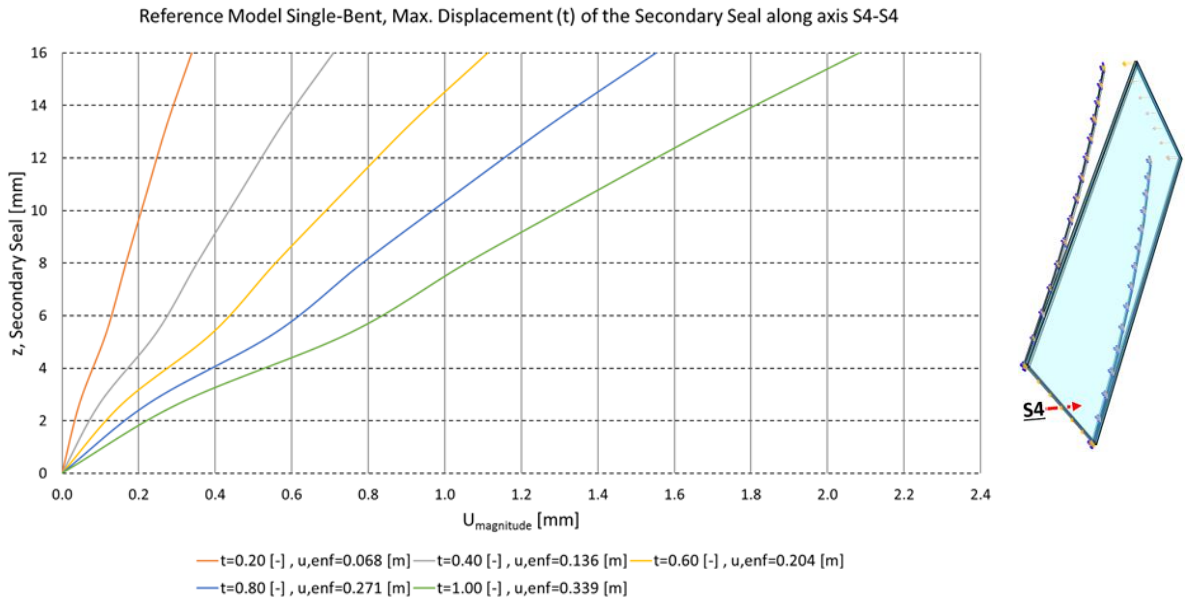

Figure 64: Reference model single-bent, max. displacement (t) of the secondary seal along axis S4-S4

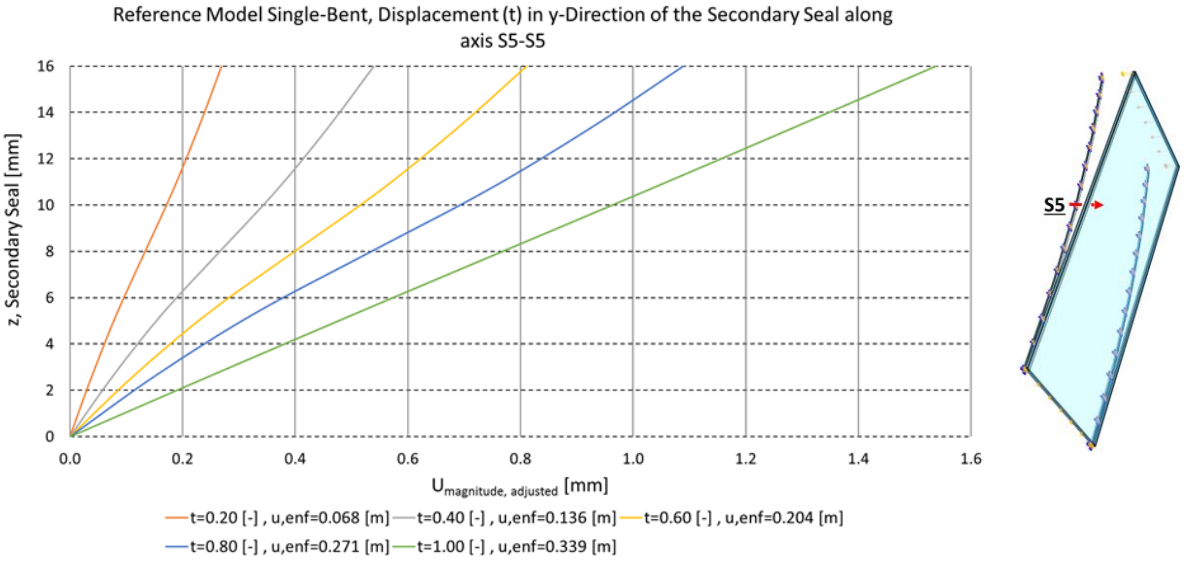

Figure 65: Reference model single-bent, max. displacement (t) of the secondary seal along axis S5-S5

The maximum deformation amplitude at any time step t occurs in axis S1-S1 which is roughly $0.6\ [mm]$ at $t = 0.2$ and $2.5\ [mm]$ at $t = 1$ which leads to an average shear displacement $\Delta\alpha(t = 0.2)$ of 3.8% and $\Delta\alpha(t = 1) = 15.3\%$. The growth rate of $\Delta\alpha$ is highest at $0 < t < 0.2$ and decreases then until $t < 0.8$. Between $0.8 < t \leq 1$, $\Delta\alpha$ increases again which is caused by the fully clinging of the IGU onto the subconstruction which leads to additional stress and displacement.

6.2 Parameter study: Single-bent IGU

Based on the single-bent reference model which was introduced in chapter 6.1 and was examined in the subchapter 6.1.2, a parameter study will be carried out in this chapter. The reference model shows a stress and strain utilization which leaves enough remaining potential for service loads. This is vital because this parameter study claims to be a basis for further work which will eventually result in a practical implementation.

In order to restrict the scale of this work, almost all results are examined for the final time step $t = 1$. Results as a function of the progress of the bending process or rather "time" are already examined for the single-bent reference model in in the subchapter 6.1.2.

All conditions – for example BCs, interaction properties, constraints and so forth, have been adopted from the reference model, unless they are utilized as a parameter value.

In subchapter 6.2.1, the thickness of the glass pane 1 $t_{gp,1}$ and glass pane 2 $t_{gp,2}$ is varied whereas the glass thickness $t_{gp,i}$ is either $6\,[mm]$, $8\,[mm]$ or $10\,[mm]$. All 9 possible combinations for a double-paned IGU are taken into account. The associated designations are 111 to 119 where 112 coincides with the reference model. It is expected that a thicker $t_{gp,i}$ will lead to increased stress but is often required due to safety regulations or high service loads. More background information is also given in subchapter 3.1.1.

In subchapter 6.2.2, the depth of the cavity h is varied from $8\,[mm]$ to $24\,[mm]$ in $4\,[mm]$ steps. The associated designations for the models are 211 to 215 where 213 coincides with the reference model.

In subchapter 6.2.3, the linear Young's modulus E of the secondary seal is being varied within a wide range from $0.8\,[MPa]$ to $4.5\,[MPa]$ with regard to the targeted product development of high-strength structural silicones which is expected to have a promising potential as a compound in curved insulation glass. The associated designations for the models are 311 to 319 where 314 coincides with the reference model.

In subchapter 6.2.4, the spacer material, which usually is stainless steel - due to reasons which are described in chapter 2.6 - is being replaced with aluminum. It is expected that the lower stiffness of aluminum is advantageous for curved insulation glass. The associated designations for the models are 411 and 412 where 411 coincides with the reference model.

In subchapter 6.2.1, the length l_{gp} of the single-bent IGU is being varied from $0.75\ [m]$ to $5.83\ [m]$ which leads to a variation of the aspect ratio from $\frac{1}{2} \leq \frac{l_{gp}}{w_{gp}} \leq \frac{5}{3}$. This parameter gets varied because it is expected to give a deeper insight into the mechanical behavior of single-bent IGUs. Furthermore, IGUs are being manufactured as individual constructions, therefore different geometries are of interest. The associated designations for the models are 511 to 518 whereas 516 coincides with the reference model.

Annotation: From the reference model in chapter 6.1, it is already known that certain axes are not decisive and hence are not evaluated in these parameter study. For reasons of clarity, this work does not examine all axes for each parameter study but instead omits irrelevant results in subsequent parameter studies, if it is obvious that they are not decisive. In that sense, it is advisable to read the subchapters in ascending order.

6.2.1 Thickness of the glass pane - Variation 1

In this subchapter, a parameter study about the influence of the thickness of the glass pane on the overall IGU system is carried out. The following glass thicknesses $t_{gp,i}$ are considered: $6\,[mm]$, $8\,[mm]$ and $10\,[mm]$. Because the IGU is double-glazed, there are 9 possibilities to combine the glass pane thicknesses. All associated designations for the models and the allocated glass thicknesses can be seen from the listing in Table 8.

Single-Bent	6 mm		8 mm		10 mm	
111.	1	2				
112			1	2		
113					1	2
114	1		2			
115	2		1			
116	1				2	
117	2				1	
118			1		2	
119			2		1	

Table 8:Variation 11: Thickness of the glass panes

6.2.1.1 Required force for the cold bending process

The required force F for cold-bending of the IGU from $w(t=0)=0\,[m]$ to $w(t=1)=0.339\,[m]$ is depicted in Figure 66. Because the relationship is strongly exponential, a close-up view of the graph for the last few centimeters is provided in Figure 67. The model (111: 6/6 [mm]) requires less bending force than (112: 8/8 [mm]) which also requires less bending force than (113: 10/10 [mm]). Model (111: 6/6 [mm]) requires overall the lowest bending force $F=738\,[N]$ and (113: 10/10 [mm]) requires the highest bending force $F=2628\,[N]$. Interestingly, (112: 8/8 [mm]) yields the median value for the force-displacement curve which indicates that the moment of inertia (around the x-axis) determines F (because for (112: 8/8 [mm] it yields also the median value).

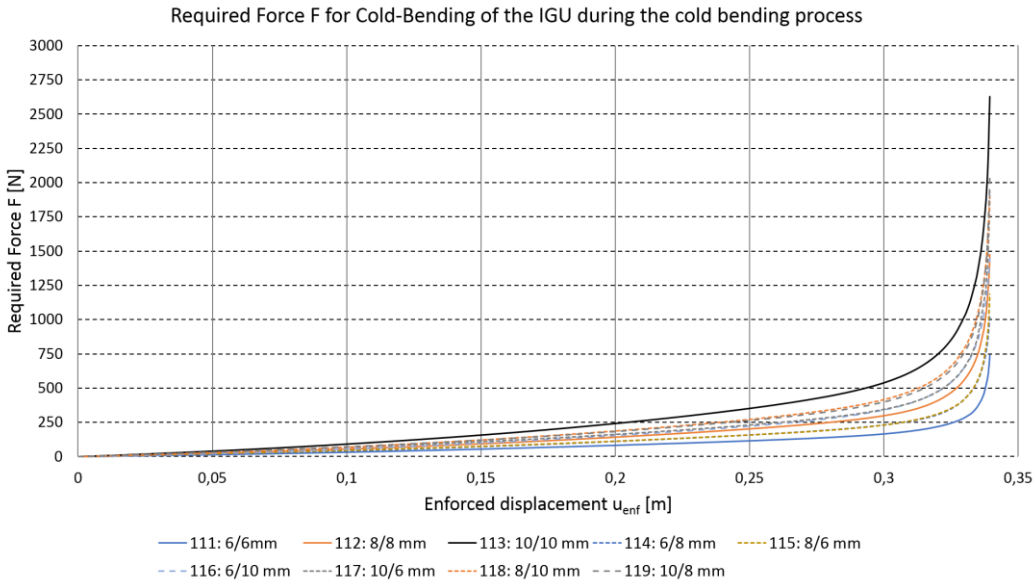

Figure 66: Single-bent model for variation 1, required force F for cold-bending of the IGU

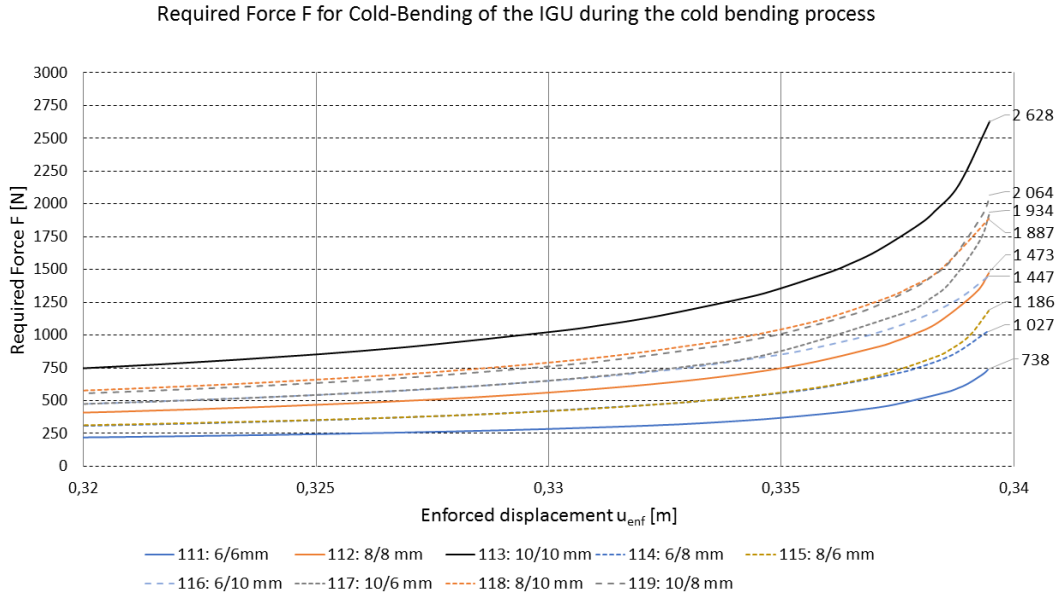

Figure 67: Single-bent model for variation 1, required force F for cold-bending of the IGU, close-up view

Primary, three important facts can be deducted from these graphs:

1.) $F(t)$ or rather $F(u_{enf})$ increases almost as exponential as the contact area between the IGU and the subconstruction in all 9 cases, which must be considered when the IGU is deformed force controlled instead of displacement controlled, in order to avoid a jerky bending procedure.

2.) F is not linearly dependent from the glass pane thickness, mainly because the moment of inertia increases cubic with increasing thickness.

3.) It can be assumed, that most of the time, a team of two or three trained workmen can bend a double-glazed IGU by manpower which can be a cost and time advantage for small construction sites.

In order to estimate easily F as a function of the glass panes, an empiric relationship is proposed as a function of the thickness of glass pane 1 $t_{gp,1}$ and the thickness of glass pane 2 $t_{gp,2}$ such that a non-linear initial function with two fitting exponents and a linear scalar was chosen. It should be noted, that this empiric formula is restricted to the use for this reference model and for $6 \leq t_{gp,i} \leq 10\ [mm]$ but might provide some guidance for subsequent investigations. The full derivation of Equation 5 is shown in the annex in chapter 11.2.

$$F = 5.508\left(t_{gp,1}^{2.45}[mm] + t_{gp,2}^{2.25}[mm]\right) \qquad \text{Equation 5}$$

The maximum error is 3.83% for case (119: 10/8 [mm]) which gives $2532\ [N]$ as a result instead of $2628\ [N]$ and the minimum error is 0.48% in case of (118: 8/10 [mm]). From the fitting exponent of $t_{gp,1}$ it can be seen, that glass pane 1 provides more resistance than glass pane 2. The fitting value 5.506 includes all other factors aside from $t_{gp,1}$ and $t_{gp,2}$ such as the constant bending radius r.

6.2.1.2 Glass pane

In this subchapter, the maximal principal stress $\sigma_{max,pr}$in glass pane 1 and in glass pane 2.

In Figure 68 for axis 1-1, a clear relationship between the glass pane thickness t_{gp} and the principal stress curve $\sigma_{max,pr}$ is visible. It can be stated, that t_{gp} and $\sigma_{max,pr}$ in glass pane 1 are increasing accordingly. Firstly, it can be stated that the thickness of glass pane 1 $t_{gp,1}$ has to be as thin as possible in order to realize small values of $\sigma_{max,pr}$ and secondly, it can be stated that if glass pane 2 $t_{gp,2} > t_{gp,1}$, then $\sigma_{max,pr}$ in $t_{gp,1}$ is sligthly increasing

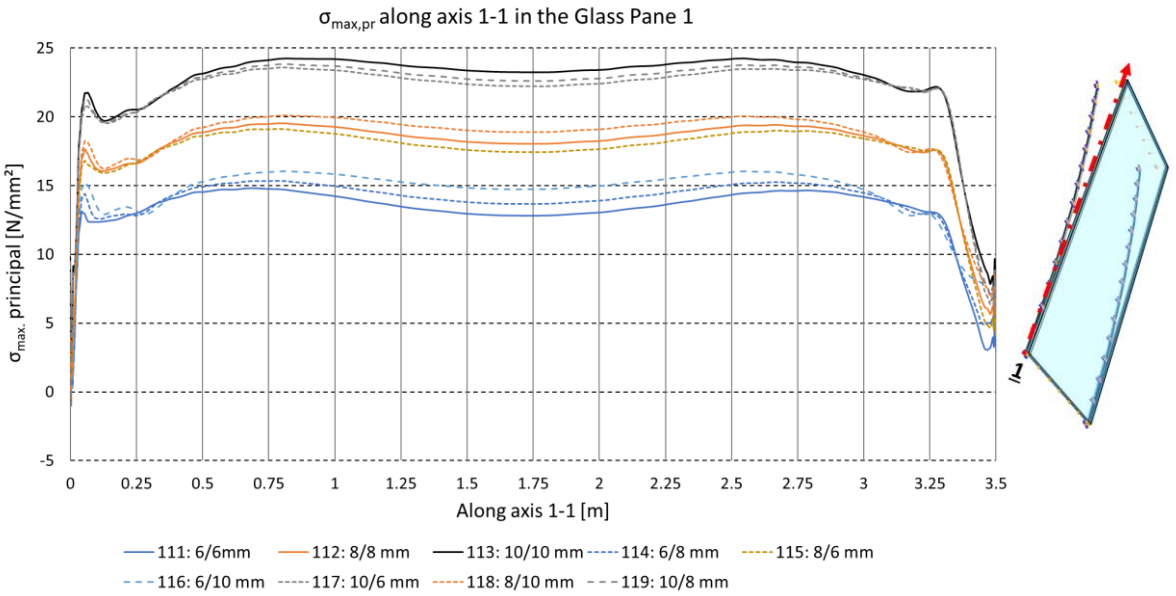

Figure 68: Single-bent model for variation 1, σ_{max}.principal along axis 1-1 in the glass pane 1

Figure 69 shows the same axis as Figure 68, but in a close-up view for the first 5 centimeters (back end next to axis 7-7) and for the last 5 centimeters (front end next to axis 1-1). It is important to notice, that from 0 to $0.005\ [m]$, glass pane 1 is just in contact with the secondary seal, but from $0.005\ [m]$ on, it is also in contact with the longitudinal spacer until $3.495\ [m]$. Approaching the edge region next to axis 7-7 (which range from $0\ [m]$ to $0.05\ [m]$) along axis 1-1 from the middle at $1.75\ [m]$, the stress function decreases until the back end of the longitudinal spacer at $0.005\ [m]$ and suddenly starts to increase again.

Interestingly, $\sigma_{max,pr}$ in the edge region is mainly determined by the thickest of both glass panes t_{gp} but never comes close to a global maximum. (This means, that the stress distribution in the considered corner region over the thickness of the overall IGU system works pretty well.)

As expected, the thicker $\max(t_{gp,1}, t_{gp,2})$ is, the higher the stress in the edge region is. The local maximum is reached at $0\ [m]$ for axis 1-1.

In the edge region of axis 1-1 next to axis 8-8 from $3.45\ [m]$ to $3.5\ [m]$, the principal stress curve $\sigma_{max,pr}$ differs a lot from $\sigma_{max,pr}$ in the edge region next next to axis 7-7 from 0 to $0.005\ [m]$. On the one hand, $t_{gp,1}$ as well as $t_{gp,2}$ are affecting the stress values of the edge region like for the back edge region (from 0 to $0.005\ [m]$), but on

the other hand, the maximum and minumum values do not differ significantly. For example, $\sigma_{max,pr}$ at $3.495\ [m]$ varies from about $5\ [N/mm^2]$ up to $10\ [N/mm^2]$ which is well beyond the global maximum. A local maximum at $3.495\ [m]$ indicates the structural transition between the longitudinal spacer and the structural silicone.

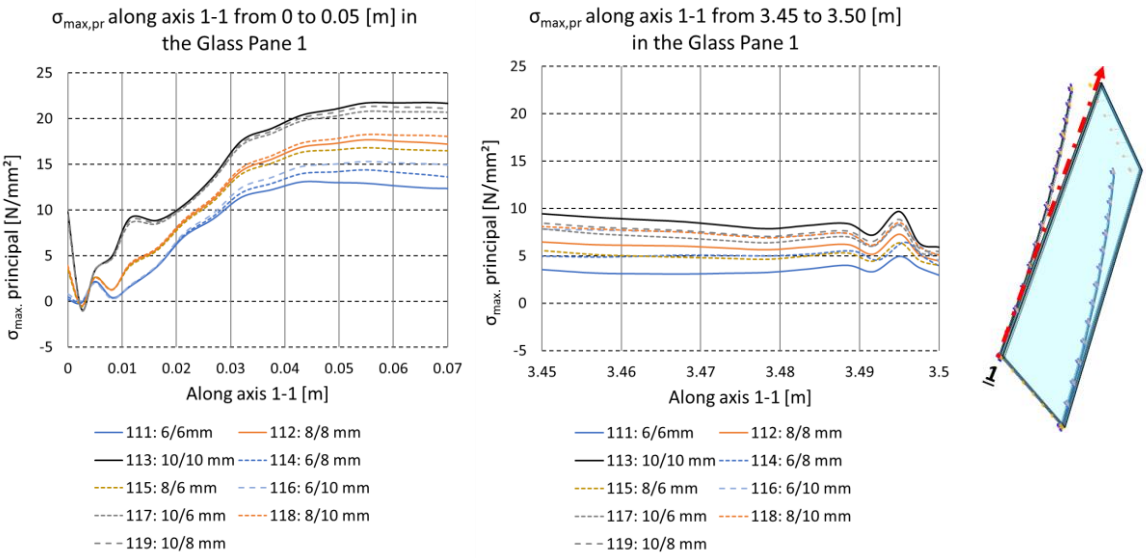

Figure 69: Single-bent model for variation 1, $\sigma_{max,pr}$ along axis 1-1 in the glass pane 1, close-up view

In Figure 70, $\sigma_{max,pr}$ in the glass pane 1 along axis 2-2 is depicted. Like for axis 1-1, the stress function is mainly determined by $t_{gp,1}$. The stress distribution along axis 2-2 is not as sensitive to a different $t_{gp,2}$ in glass pane 2 as along axis 1-1. Noticeable, but not crucial is the fact, that if $t_{gp,2} > t_{gp,1}$, then the stress function has slightly smaller values than for $t_{gp,2} = t_{gp,1}$.This means that a small amount of stress is redistributed into glass pane 2. Like for axis 1-1, a V-shaped stress function, which seems to be mainly determined by $t_{gp,1}$, occurs at the back edge zone from $0\ [m]$ to $0.005\ [m]$. Furthermore, a V-shaped stress function occurs at the front end from $3.35\ [m]$ to $3.50\ [m]$ in axis 2-2, which is not the case for axis 1-1. In this case, the deviation between $t_{gp,i}$ seems negligible. However, the significant stress in axis 2-2 is roughly about 20% lower than in axis 1-1, which is advantageous because significant moments from uniformally distributed service loads will occur at axis 2-2.

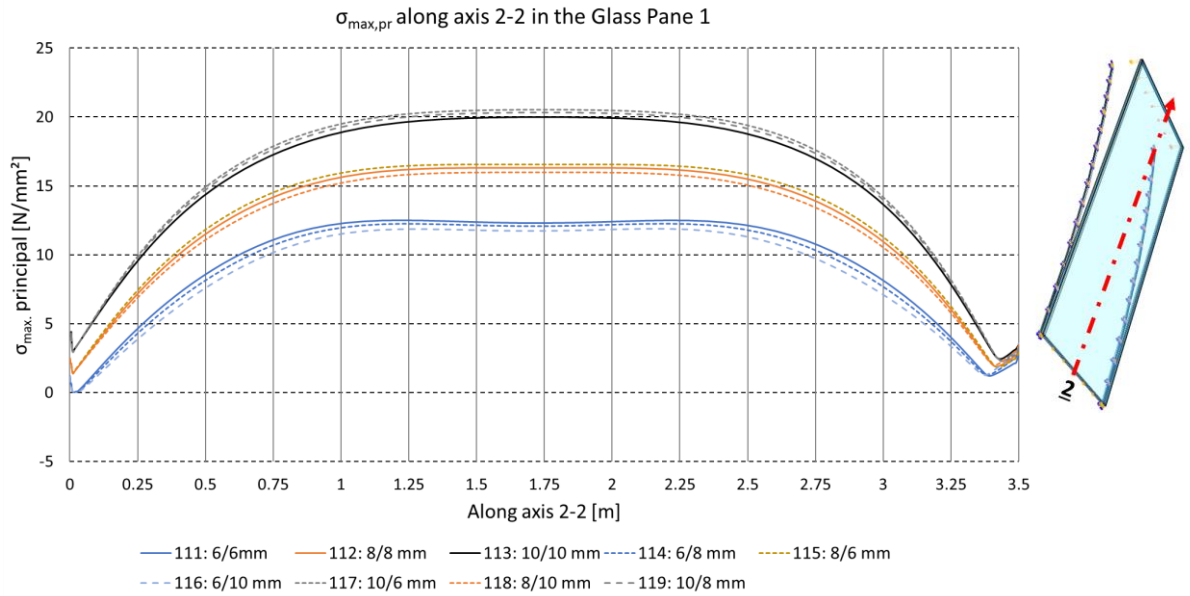

Figure 70: Single-bent model for variation 1, $\sigma_{max,pr}$ along axis 2-2 in the glass pane 1

Recalling Equation 5 from subchapter 3.1.1, which states that $\sigma_{max,pr} = \frac{Et_{gp}}{2r}$ and compairing $\max(\sigma_{max,pr})$ along axis 1-1 with this equation, the values in axis 1-1 can be up to 41% higher in case of (116: 6/10 [mm]). Hence, this analytical equation is underestimating $\sigma_{max,pr}$ in $t_{gp,1}$ at least 21% and up to 41%. It should be noted, thatEquation 1 fits better for axis 2-2 than for axis 1-1 but $\sigma_{max,pr}$ in axis 1-1 is higher. For a fast static preliminary design, it is advisable to increase with a conservative scalar α_1.

If the maximum deviation is multiplied with a safety factor γ, which for example is chosen to be $\gamma = 1.5$, which takes into account all uncertainties, and is rounded to one decimal place, the following suggestion for α_1 can be made:

If $t_{gp,1} = t_{gp,2}$, then $\alpha_1 = 1.4$ because the maximal deviation is 27%.

If $t_{gp,1} > t_{gp,2}$, then $\alpha_1 = 1.3$ because the maximal deviation is 21%.

If $t_{gp,1} < t_{gp,2}$, then $\alpha_1 = 1.6$ because the maximal deviation is 41%.

It is important to notice, that this equation is only valid for this parameter study and cannot be used for an arbitrary IGU.

In Figure 71, $\sigma_{max,pr}$ is depicted along axis 3-3 in glass pane 2 which lies directly above axis 1-1. If every stress curve is listed in ascending order as a function of their maximum value $\max(\sigma_{max,pr})$, this would lead to a cluster-like pattern which can be

also seen in the graph. Recalling the stress curves in axis 1-1, also a cluster-like pattern can be observed. From this, a more comprehensive statement can be formulated:

- An increasing $t_{gp,i}$ leads to a stark increase of $\sigma_{max,pr}$ in glass pane i.
- An increasing $t_{gp,j}$ leads to a slight increase of $\sigma_{max,pr}$ in glass pane i.
- If $t_{gp,i} > t_{gp,j}$, $\sigma_{max,pr}$ is mainly determined by $t_{gp,i}$.

Compairing the stress function in the edge-zone of axis 1-1 and axis 3-3 it is noticeable that the stress function for axis 3-3 looks much more smooth and does not exhibit any cusps and V-shaped turning points. The reason for this is, that glass pane 2 is not pressed onto the subconstruction but instead just follows the bending form of the IGU and it can deform more unconstrained.

In Figure 72, $\sigma_{max,pr}$ is depicted along axis 4-4 in glass pane 2 which lies directly above axis 2-2. Like in axis 2-2, $\sigma_{max,pr}$ in axis 4-4 exhibits a V-shaped stress function in both edge regions. However, both V-shaped stress functions do not show to be dependent to a remarkable dregree on t_{gp}. Like in glass pane 1, the corresponding stress function for axis 4-4 is not significant compared to the stress function along the longitudinal edge in axis 3-3. Therefore, only the stress along the longitudinal edge (along axis 1-1) has to be taken into account when evaluating the significant stress for the single-bent model in this case.

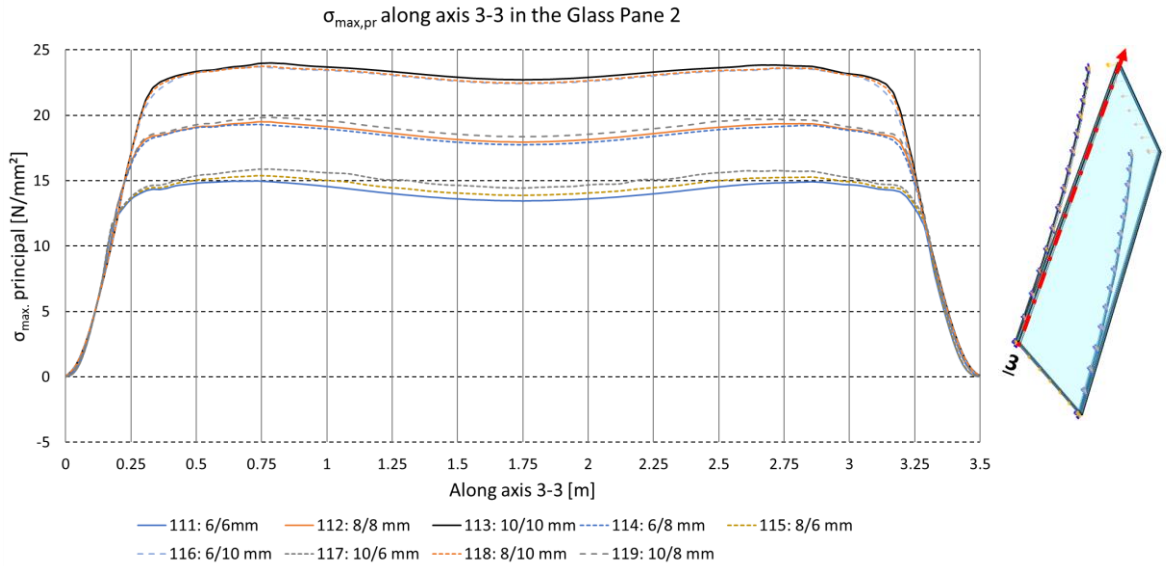

Figure 71: Single-bent model for variation 1, $\sigma_{max,pr}$ along axis 3-3 in the glass pane 2

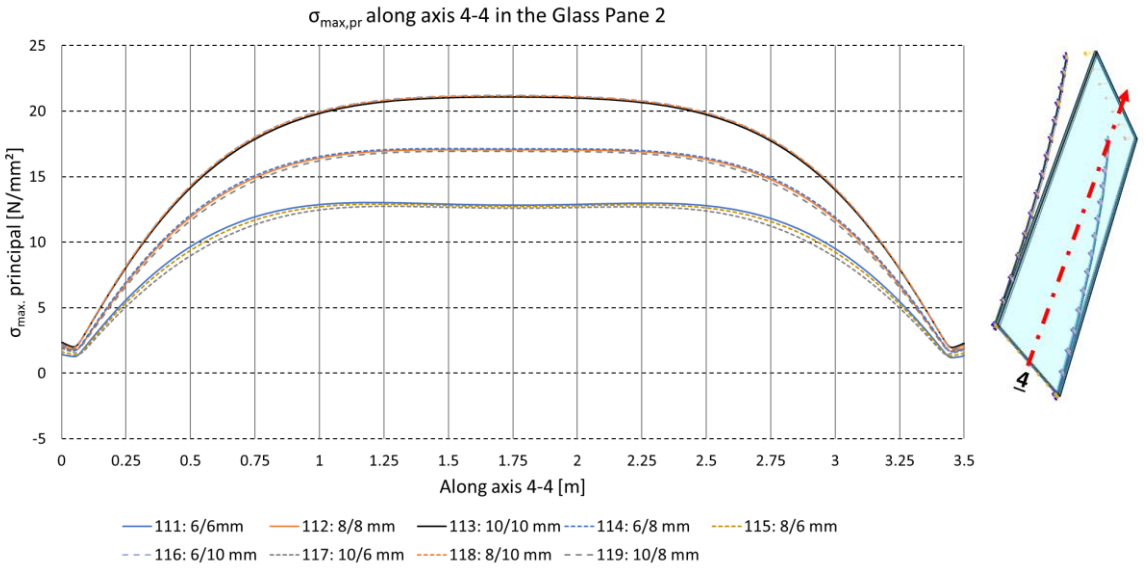

Figure 72: Single-bent model for variation 1, $\sigma_{max,pr}$ along axis 4-4 in the glass pane 2

6.2.1.3 Spacer bar

In Figure 73, the von Mises stress σ_e is depicted along axis 5-5 for the longitudinal spacer. In Figure 74, σ_e is depicted along axis 6-6 for the longitudinal spacer. The spacer is plasticizing for both longitudinal ends in both axes in the corner region where it is connected to the broadside spacer. The maximum value for σ_e is reached at the front end at $3.4885\ [m]$ of axis 6-6 for (112: 8/8 [mm]). The stress there is about $420\ \left[\frac{N}{mm^2}\right]$ which is equal to a material utilization of 70%.

Yielding just occurs locally in the corner region and mainly at the edges of the spacer but not over the full width or height. However, it should be recalled from subchapter 6.1.2.6 that the stress values in the corner region can vary up to $\pm 5\ \%$ depending on the chosen calculation method.

For axis 5-5, the stress outside the corner region varies between $82\ \left[\frac{N}{mm^2}\right]$ for (116: 6/10 [mm]) and $94\ \left[\frac{N}{mm^2}\right]$ for (117:10/6 [mm]). For axis 6-6, the stress outside the corner region varies between $65\ \left[\frac{N}{mm^2}\right]$ for (117:10/6 [mm]) and $80\ \left[\frac{N}{mm^2}\right]$ for (116: 6/10 [mm]). From this, it can be deduced, that a difference between $t_{gp,1}$ and $t_{gp,2}$ leads to a great difference between the upper and the lower region of the spacer.

Therefore, glass panes with $t_{gp,1} = t_{gp,2}$ ensure a uniform stress redistribution in the spacer, if required. This can be useful in order to increase the remaining material potential. It is assumed, that additional stress which is caused from service loads does not increase the stress in the corner region significantly. This is, because these stress peaks are mainly caused by constraining forces from interaction of the longitudinal spacer with the broadside spacer.

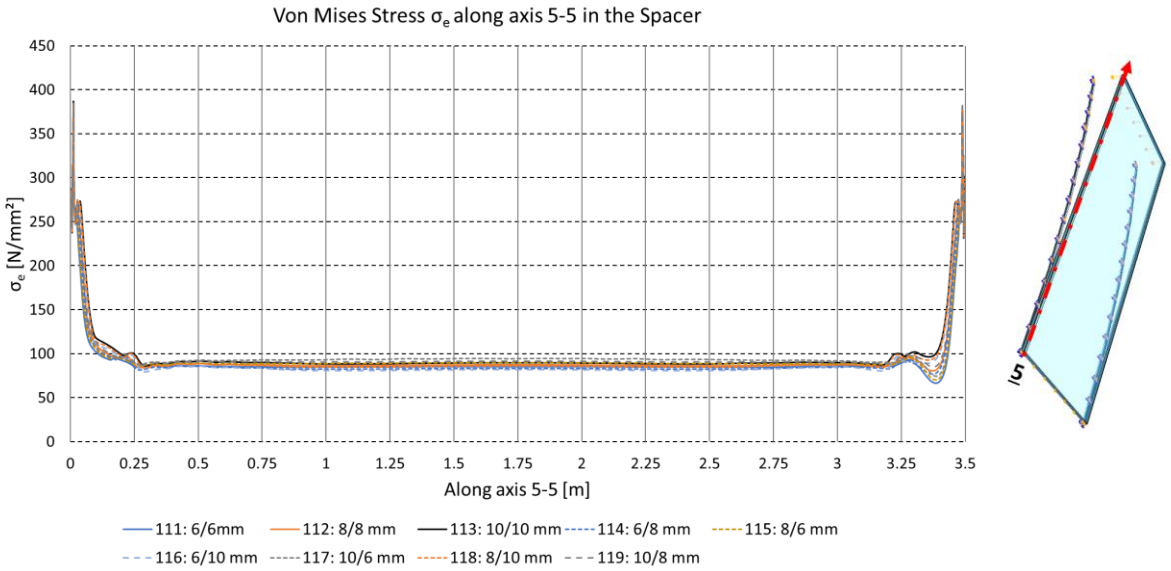

Figure 73: Single-bent model for variation 1, von Mises stress σ_e. along axis 5-5 in the spacer

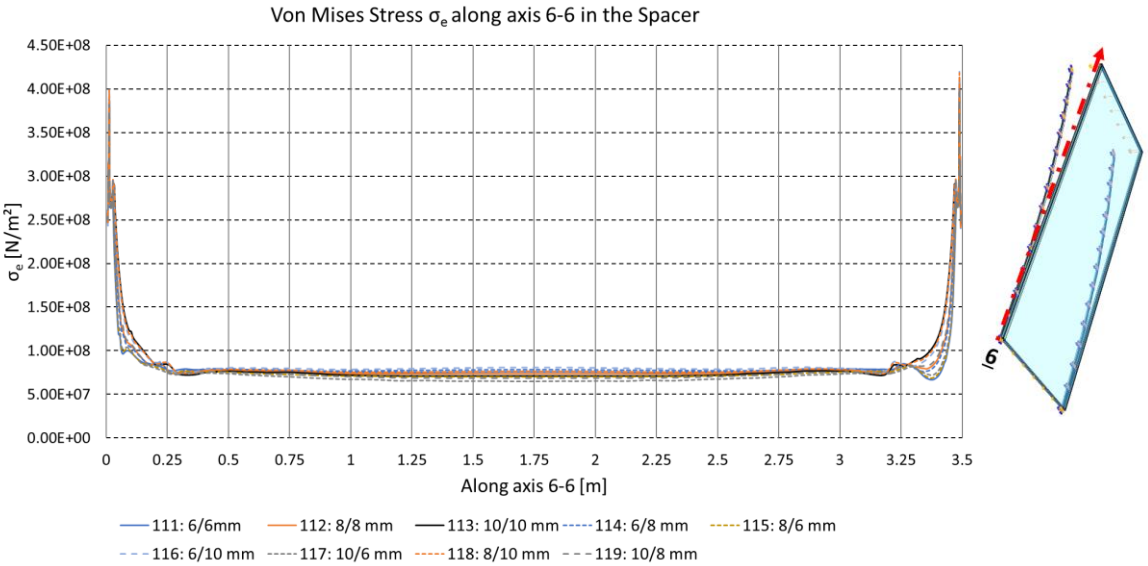

Figure 74: Single-bent model for variation 1, von Mises stress σ_e. along axis 6-6 in the spacer

6.2.1.4 Deformation of the edge zone

From subchapter 6.1.2, it is already known, that the maximum displacement of the secondary seal is significant for axis S1-S1 which is also true in this case, however S2-S2 is also described in order to understand the slip behaviour of the overall IGU system as a function of t_{gp} . The maximum displacement of the secondary seal for S1-S1 is illustrated in Figure 75 and for S2-S2 in Figure 76.

Firstly, all deformation curves do not cross each other. Despite that, these curves are not linear because they spread apart from each other. This behavior is less pronounced for axis S1-S1 than for axis S2-S2.

Secondly, all curves have the same characteristics. Mentionable features of the deformation curves are the same amount of turning points at almost the same z-value and a cluster-like relationship for S2-S2 which depends on $t_{gp,2}$. If the deformation amplitudes are listed in ascending order for both axes, then the same pattern as for glass pane 1 in axis 1-1 occurs. More important is the fact, that the same pattern is true for S1-S1 and S2-S2 which means that the elongation of glass pane 2 does not play a significant role. The maximum deformation values for S1-S1 range from about $2.2\ [mm]$ to $2.75\ [mm]$. The shear displacement Δα range from 13.8% to 17.2%. The maximum deformation values for S2-S2 range from about $0.7\ [mm]$ to $1.3\ [mm]$ hence $\Delta\alpha$ range from 4.4% to 8.2%. For (111: 6/6 [mm]), $\Delta\alpha$ at S1-S1 is more than three times of $\Delta\alpha$ at S2-S2. This means that the rate of change in deformation is high due to a low stiffness of the IGU.

A problem could be a too big $\Delta\alpha$ at axis S1-S1. This can be solved with high performing silicones. Of course, glass pane 2 could also be fixed by a line support which is not investigated in this work.

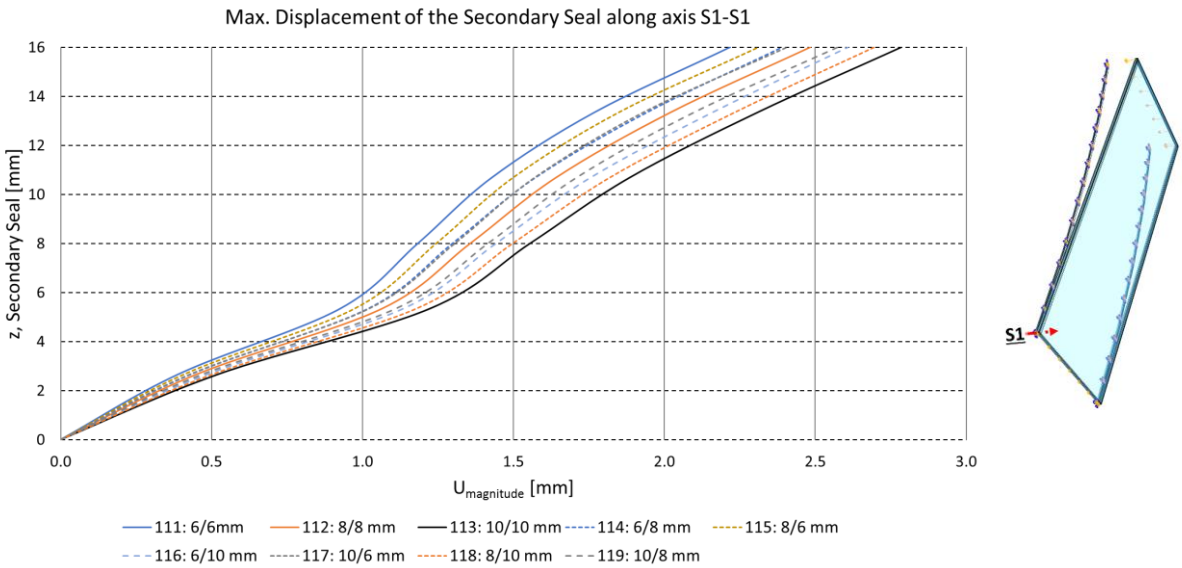

Figure 75: Single-bent model for variation 1, max. displacement of the secondary seal along axis S1-S1

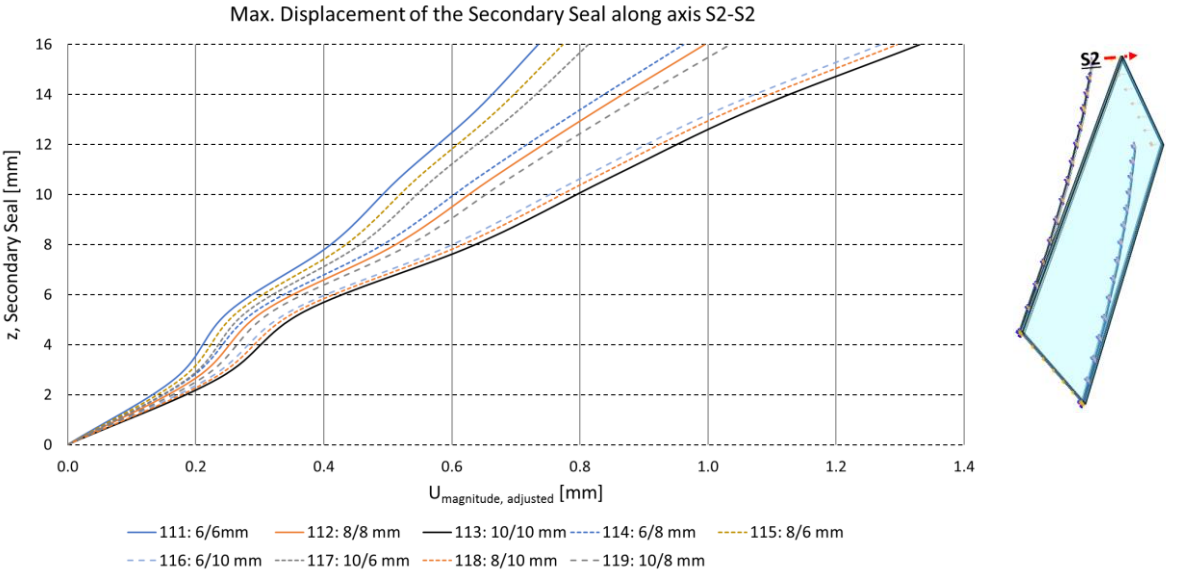

Figure 76: Single-bent model for variation 1, max. displacement of the secondary seal along axis S2-S2

6.2.2 Depth of the cavity - Variation 2

In this subchapter, a parameter study about the influence of the cavity depth or rather the distance between both glass panes over the overall IGU system is carried out. The following cavity depth are considered: $8\,[mm]$, $12\,[mm]$, $16\,[mm]$, $20\,[mm]$ and $24\,[mm]$, hence there are 5 different models calculated. All associated designations

for the models and the allocated cavity distances can be seen from the listing in Table 9.

Single-Bent	8 mm	12 mm	16 mm	20 mm	24 mm
211	X				
212		X			
213			X		
214				X	
215					X

Table 9: Variation 21: Different IGU cavities

6.2.2.1 Required force for the cold bending process

The required force F for cold-bending of the IGU from $w(t=0)=0\ [m]$ to $w(t=1)=0.339\ [m]$ is depicted in Figure 77. Like for variation 1, the curve is strongly exponential, therefore a close-up view in Figure 78 is given. However, even for the close-up view, the differences for F are relatively small. The lowest force $F=1431\ [N]$ is required for (211: 8 [mm]) and the biggest force $F=1528\ [N]$ is required for (215: 24 [mm]).

The small change of F can be explained by two reasons. Firstly, the spacer can slip between the glass panes, which does not increase the overall moment of inertia. Secondly, the silicone is bond to the glass panes but is not able to increase the moment of inertia due to its low stiffness.

The linear Young's modulus E used for the silicone is $2E6\ [Pa]$, while the spacer has an E of $189E9\ [Pa]$ which is 94500 times higher. Therefore, it is admissible to ignore the contribution of the secondary seal to the moment of inertia. Furthermore, the very small sheet thickness of the spacer gives almost no contribution as well. What remains is the contribution of the spacer from the parallel axis theorem. For example, the moment of inertia around the x-axis for both longitudinal spacers for (211: 8 [mm]) is

98 $\left[\frac{mm^4}{m}\right]$[9] and for (215: 24 [mm]) is 1456 $\left[\frac{mm^4}{m}\right]$[10] which gives a difference of 728 $\left[\frac{mm^4}{m}\right]$ which results in a difference of 151 $[N]$ for F.

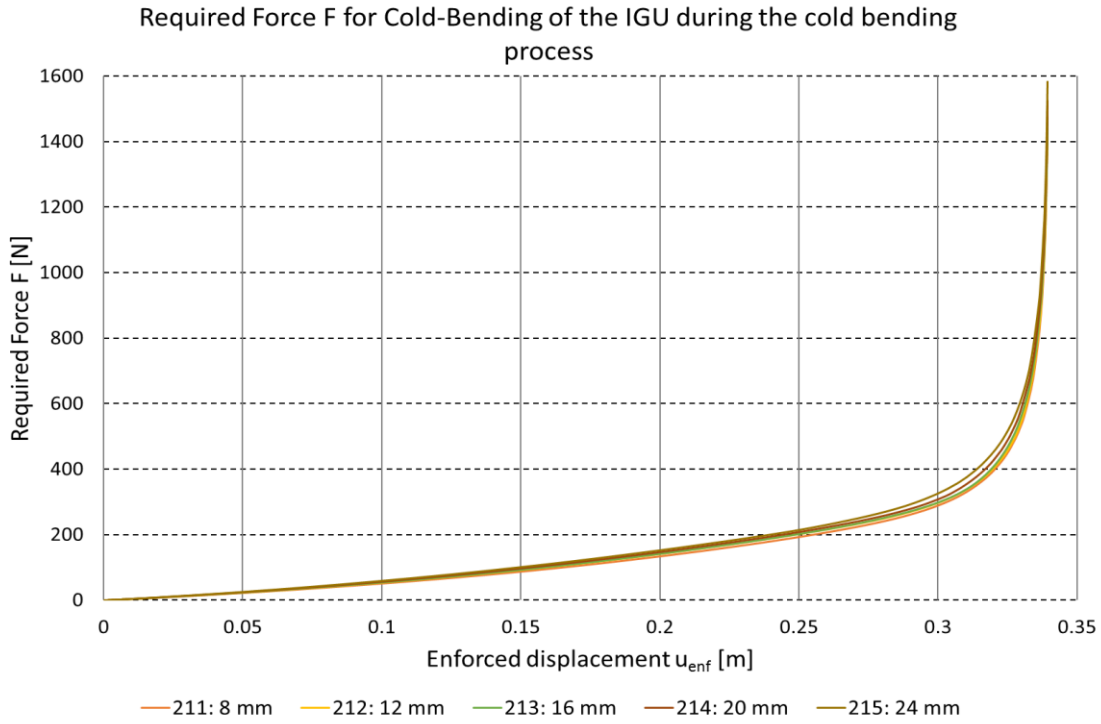

Figure 77: Single-bent model for variation 2, required force F for cold-bending of the IGU

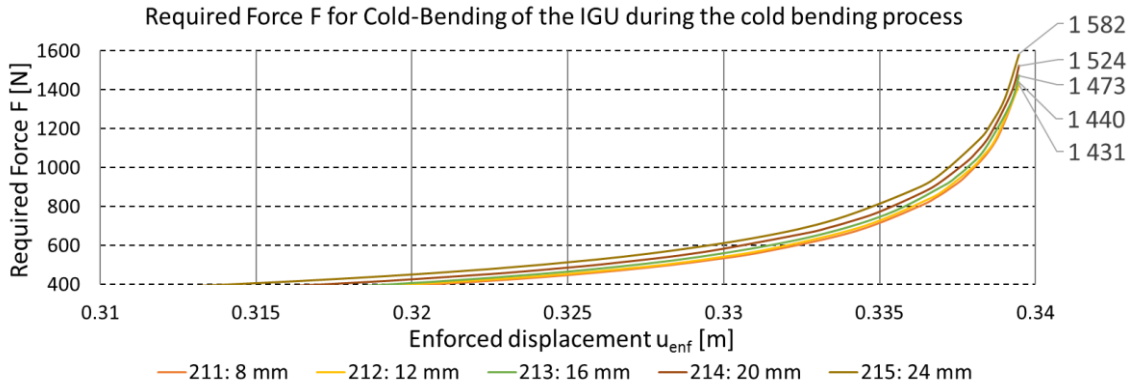

Figure 78: Single-bent model for variation 2, required force F for cold-bending of the IGU, close-up view

[9] I_{x-x} for (211: 8 [mm]) is
[((8-0.18*2)³*0.18+6.5*0.18³)/12+(0.18*6.5*(8/2-0.18/2)²]*4 = 98.30 [mm⁴/m]

[10] I_{x-x} (for 215: 24 [mm]) is
[((24-0.18*2)³*0.18+6.5*0.18³)/12+(0.18*6.5*(24/2-0.18/2)²]*4 = 1456.52 [mm⁴/m]
with t_{sp}=0.18 [mm], w_{sp}=6.5 [mm] and h=8/24 [mm]

6.2.2.2 Glass pane

In Figure 79, the maximal principal stress $\sigma_{max,pr}$ in the glass pane 1 is examined along axis 1-1. A closer examination for all other axes in the glass panes can be waived due to their repetitive behaviour which is represented by axis 1-1 and in addition, the stress values in axis 1-1 are significant for the overall IGU system. Recalling the stress curve for axis 1-1 for the reference model and compairing it to the stress curve in Figure 79 unveils that these results coincide over the whole length of axis 1-1.

Given the fact, that the results in axis 1-1 might differ in a range where numerical fluctuations can already happen, it can be deducted that the height of the cavity does not influence the stress in the glass panes at all - as long as the shear force transmission is negligible.

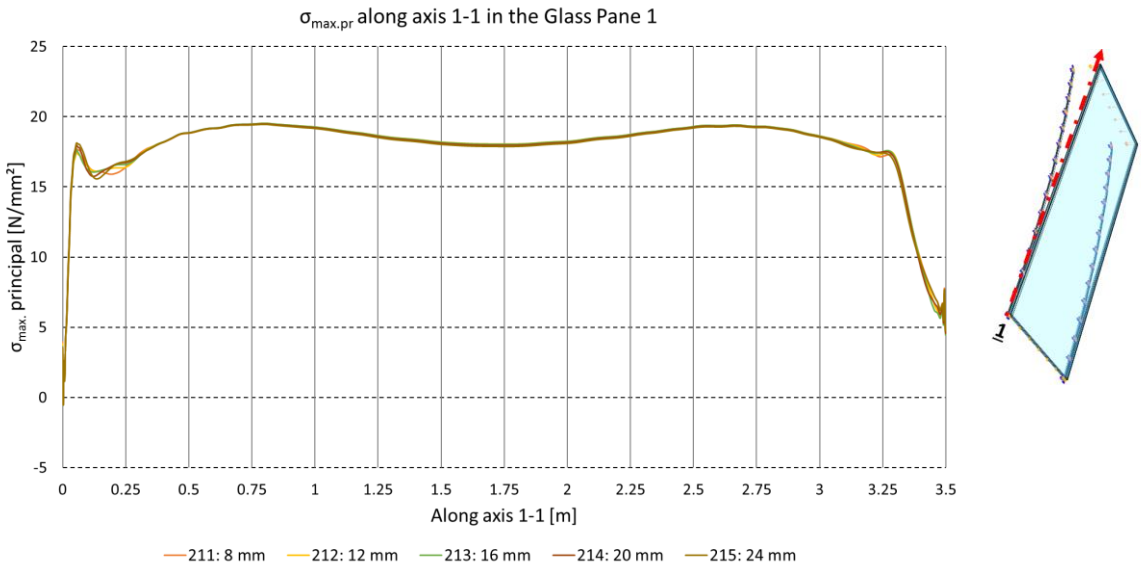

Figure 79: Single-bent model for variation 2, $\sigma_{max,pr}$ along axis 1-1 in the glass pane 1

6.2.2.3 Spacer bar

The von Mises Stress σ_e along axis 5-5 is depicted in Figure 80. The von Mises stress σ_e along axis 6-6 is depicted in Figure 81.

In Figure 80 it can be seen for axis 5-5 in the corner region that all spacers plasticize except for (211: 8 [mm]) at the back end next to axis 7-7. In axis 6-6, all spacers are plasticizing at the back end next to axis 7-7 and at the front end next to axis 8-8. For

both axes, the stress function stays almost constant between $0.25\ [m]$ and $3.25\ [m]$. These stress values increase in both cases in dependence of the cavity distance.

Figure 80: Single-bent model for variation 2, von Mises stress σ_e along axis 5-5 in the spacer

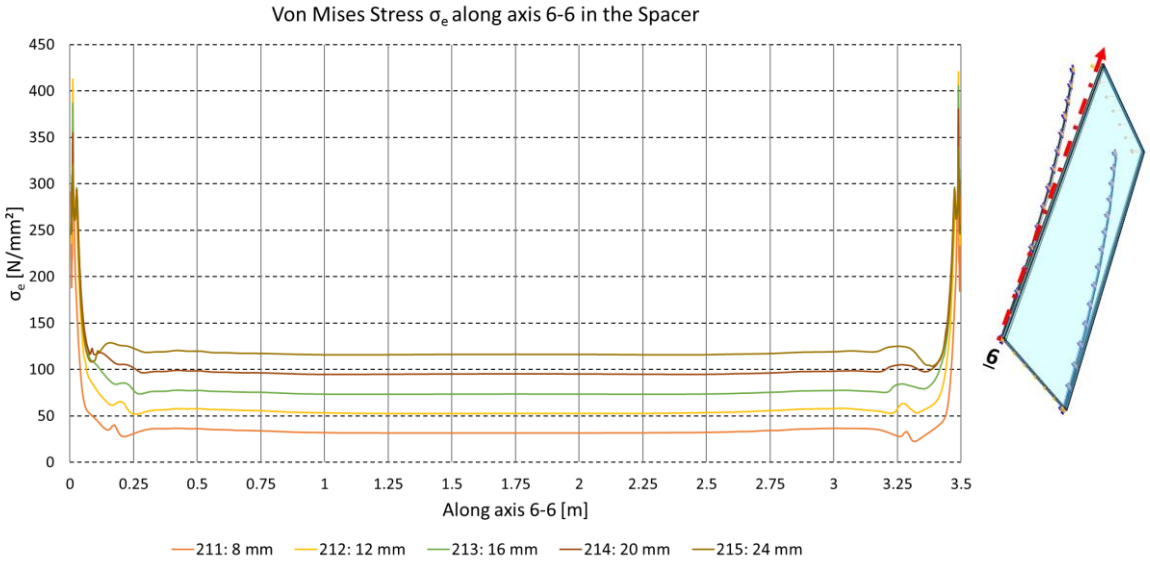

Figure 81: Single-bent model for variation 2, von Mises stress σ_e along axis 6-6 in the spacer

For axis 5-5, σ_e is in the range of $49\ \left[\frac{N}{mm^2}\right]$ for (211: 8 [mm]) and $128\ \left[\frac{N}{mm^2}\right]$ for (215: 24 [mm]). For (212: 12 [mm]), the stress is $69\ \left[\frac{N}{mm^2}\right]$ which is an increase of 41% compared to (211: 8 [mm]). However, the increase of stress from (214: 20 [mm]) to (215: 24 [mm]) is just 17%. A similar behavior can be seen in axis 6-6 where the stress

for (211: 8 [mm]) to (212: 12 [mm]) grows from $31\ \left[\frac{N}{mm^2}\right]$ up to $52\ \left[\frac{N}{mm^2}\right]$. This gives an increase of 68%. From (214: 20 [mm]) to (215: 24 [mm]) the stress grows from $95\ \left[\frac{N}{mm^2}\right]$ to $116\ \left[\frac{N}{mm^2}\right]$ which is an increase of 22%. Therefore, some observations can be made. As expected, all spacers are yielding in the corner region except for (211: 8 [mm]) at the lower end in axis 5-5. The maximum stress value σ_e, which is reached for (212: 12 [mm]) in axis 6-6 is about $421 \pm 20\ \left[\frac{N}{mm^2}\right]$ which is well beyond the material's resistance. Furthermore, σ_e outside the corner region is increasing degressively with linear increasing cavity distance with the the stress in axis 5-5 being always higher than in axis 6-6. The difference of σ_e between axis 5-5 and axis 6-6 strongly depends on the depth of the cavity and shows also to grow degressively with linear increasing cavity depth. This difference drops from 58% for (211: 8 [mm]) down to 10% for (215: 24 [mm]).

6.2.2.4 Deformation of the edge zone

In Figure 82, the maximum displacement of axis S1-S1 is illustrated and in Figure 83, the same is illustrated for axis S2-S2. As expected, the maximum displacement does increase accordingly to the cavity depth in both cases with the maximum values for axis S1-S1 being about 2.5 times higher than for S2-S2. Interestingly, the shear displacement $\Delta\alpha$ does decrease slightly with increasing cavity depth. For S1-S1, $\Delta\alpha$ is 22% for (211: 8 [mm]) but decreases to 13.8% for (215: 24 [mm]). For S2-S2, $\Delta\alpha$ is 8.8% for (211: 8 [mm]) but decreases to 4.8% for (215: 24 [mm]).

From this, the following observations can be made:

- The shear gradient $\Delta\alpha$ is bigger for a higher cavity depth.
- The shear gradient $\Delta\alpha$ in axis 1-1 is significant in any case.
- Along axis 1-1, the y-component of $\Delta\alpha$ decreases from $0\ [m]$ to $3.50\ [m]$.

The apparent contradiction between the insignificant changes for the overall IGU system but some significant changes for the displacement of the edge zone can be explained by the high resistance to shear distortion along the longitudinal side of the spacer. Mainly because all 4 webs of the longitudinal spacer can withstand shear forces well but the internal moment of the overall IGU system does not increase in a relevant order of magnitude; the resistance against bending does not increase.

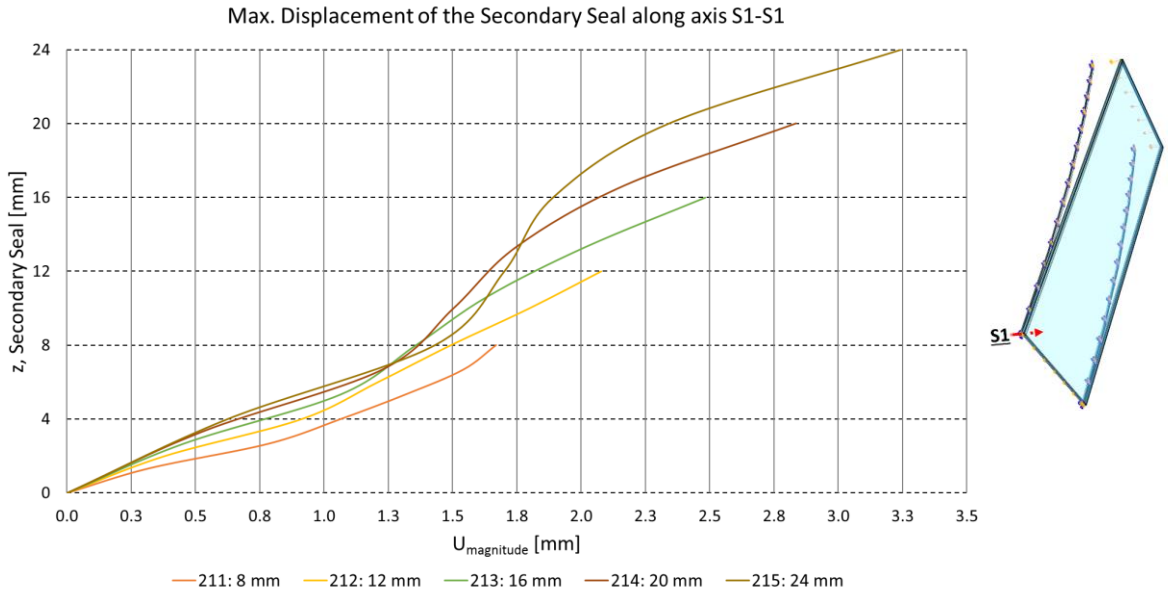

Figure 82: Single-bent model for variation 2, max. displacement of the secondary seal along axis S1-S1

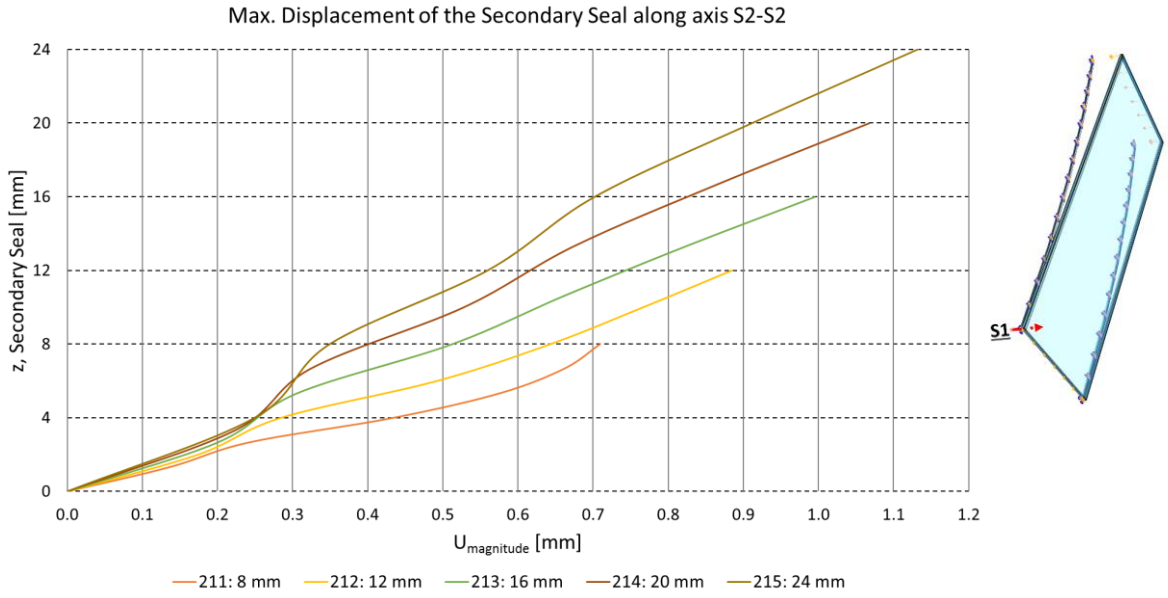

Figure 83: Single-bent model for variation 2, max. displacement of the secondary seal along axis S2-S2

6.2.3 Linear Young's modulus of the secondary seal - Variation 3

In this subchapter, a parameter study about the influence of the linear Young's modulus E on the overall IGU system is carried out. The following Young's moduli are considered: $0.8\ [MPa]$, $1\ [MPa]$, $1.5\ [MPa]$, $2\ [MPa]$, $2.5\ [MPa]$, $3\ [MPa]$, $3.5\ [MPa]$,

4 $[MPa]$ and 4.5 $[MPa]$. All associated designations for the models and the allocated Young's moduli can be seen from the listing in Table 10.

Single-Bent	0.8 MPa	1.0 MPa	1.5 MPa	2.0 MPa	2.5 MPa	3.0 MPa	3.5 MPa	4.0 MPa	4.5 MPa
311	X								
312		X							
313			X						
314				X					
315					X				
316						X			
317							X		
318								X	
319									X

Table 10: Variation 31: Different (linear) Young's moduli of the secondary seal

Because $\sigma_{max,pr}$ in both glass panes does not show a significant difference from the reference model it is not examined in this subchapter. Instead, this subchapter examines the behavior of the secondary seal in depth in order to understand it's structural contribution to the overall IGU system.

6.2.3.1 Required force for the cold bending process

The required bending force F for the cold-bending process of the IGU at the last time step $t = 1$ ranges from $1320\,[N]$ for (311: 0.8 [MPa]) up to $1622\,[N]$ for (319: 4.5 [MPa]) which is a difference of about 23% if E is increased about 5.5 times.

6.2.3.2 Secondary Seal

In Figure 84, the maximum true principal strain $\varepsilon_{true,pr}$ is depicted for axis 9-9. In addition, $\sigma_{max,pr}$ is depicted in Figure 85 for axis 9-9. For axis 9-9, the strain curve is symmetrical, which is also the case for the stress curve. In Figure 84, the strain curve has a peak at about $10\,[mm]$ away from both tips of axis 9-9. At this peak point, $\varepsilon_{true,pr}$ ranges from $0.71\,[-]$ for (319: 4.5 [MPa]) up to $0.80\,[-]$ for (311: 0.8 [MPa]). Hence, the stiffness of the silicone cannot reduce the strain peak significantly.

The reason for this is, that the expansion is enforced by a geometrical confinement in the corner region which dominates as an influence factor over the Young's modulus.

Looking at the center region, the strain reaches a minimum at $0.75\ [m]$. However, the minimum value stays almost the same between $0.25\ [m]$ and $1.25\ [m]$. At the global minimum point, $\varepsilon_{true,pr}$ shows to be depending significantly on E, $\varepsilon_{true,pr}$ ranginf from $0.29\ [-]$ for (311: 0.8 [MPa]) down to $0.11\ [-]$ for (319.: 4.5 [MPa]). Moreover, it can be clearly seen from Figure 84, that the strain curve has lower values if E is higher whereby this relationship is not linear but decreasing with a higher E. For an E of $4\ [MPa]$ and an E of $4.5\ [MPa]$, the difference in strain is about $0.01\ [-]$ but for an E of $1\ [MPa]$ and an E of $1.5\ [MPa]$, the difference in strain is about $0.03\ [-]$.

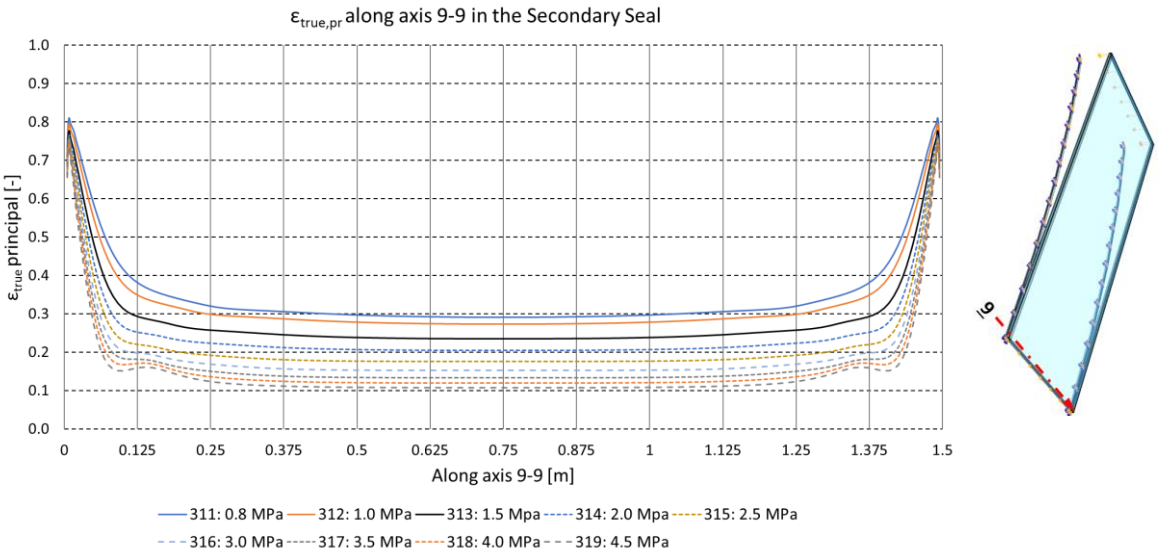

Figure 84: Single-bent model for variation 3, $\varepsilon_{true,pr}$ along axis 9-9 in the secondary seal

The findings from Figure 84 about $\varepsilon_{true,pr}$ can be found again in Figure 85 for $\sigma_{max,pr}$. Due to the increasing $\varepsilon_{true,pr}$ in the center region of axis 9-9 for a lower E, the stress values are not varying much but are almost constant. For the center region of axis 9-9, $\sigma_{max,pr}$ ranges from $0.25\ [MPa]$ for (311: 0.8 [MPa]) up to $0.47\ [MPa]$ for (319: 4.5 [MPa]). At the corner region, where $\varepsilon_{true,pr}$ has a peak point, a correlating stress peak in the stress function occurs, which ranges from $0.90\ [MPa]$ for (311: 0.8 [MPa]) up to $4.52\ [MPa]$ for (319: 4.5 [MPa]). For any higher E, the significant value for $\sigma_{max,pr}$ is increasing but at the same time, the significant value for $\varepsilon_{true,pr}$ is decreasing. This relationship is only weakly pronounced because the geometrical confinement in the corner region is dominating.

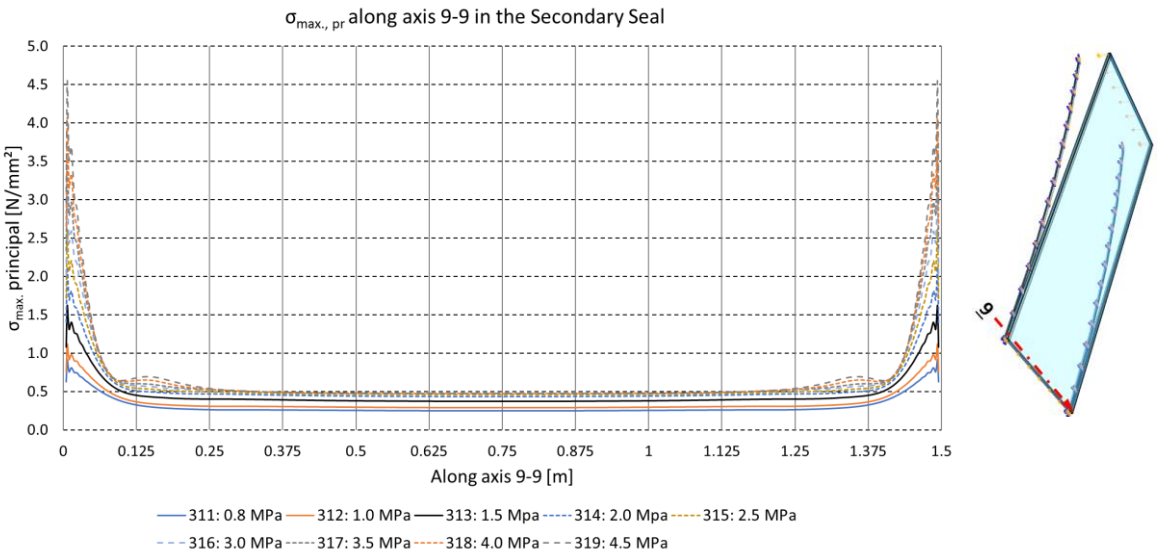

Figure 85: Single-bent model for variation 3, $\sigma_{max,pr}$ along axis 9-9 in the secondary seal

6.2.3.3 Deformation of the edge zone

From Figure 86, which depicts the displacement of the secondary seal along axis S1-S1, it can be seen that the shear displacement $\Delta\alpha$ as well as the maximum amplitude are not affected considerably by the variation of E.

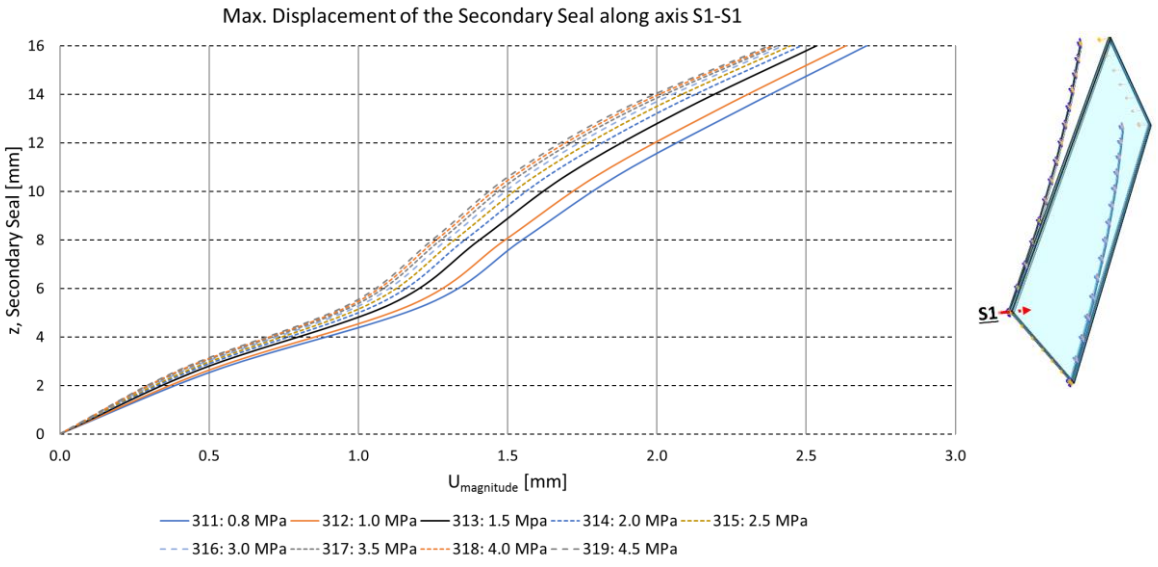

Figure 86: Single-bent model for variation 3, max. displacement of the secondary seal along axis S1-S1

For axis S1-S1, $\varepsilon_{true,pr}$ is depicted in Figure 87. For $z = 0\ [mm]$, $\varepsilon_{true,pr}$ ranges from $0.26\ [-]$ up to $0.34\ [-]$ and is decreasing to values between $0.03\ [-]$ and $0.07\ [-]$ up

to the first turning point at $z = 7\ [mm]$. After that, the strain is increasing again to the second turning point at $z = 11\ [mm]$ where $\varepsilon_{true,pr}$ ranges from $0.07\ [-]$ to $0.12\ [-]$. After the second turning point, $\varepsilon_{true,pr}$ is decreasing again. The strain at $z = 16\ [mm]$ ranges from about $0\ [-]$ to $0.04\ [-]$. In any case, a higher E correlates with a lower strain value. For $z = 0\ [mm]$, $z = 7[mm]$ and $z = 16\ [mm]$, all contributions from ε_{true} for 3.1.4: 2.0 [MPa] will be shown.

$$\varepsilon_{true}(z = 0) = \begin{bmatrix} -0.02 & -0.08 & -0.26 \\ & +0.00 & 0.26 \\ sym. & & +0.16 \end{bmatrix}$$

$$\varepsilon_{true}(z = 7) = \begin{bmatrix} -0.06 & +0.02 & -0.03 \\ & +0.06 & 0.01 \\ sym. & & +0.04 \end{bmatrix}$$

$$\varepsilon_{true}(z = 16) = \begin{bmatrix} -0.02 & +0.02 & -0.00 \\ & +0.02 & 0.02 \\ sym. & & -0.01 \end{bmatrix}$$

From the first strain tensor $\varepsilon_{true,ij}(z = 0)$, the hydrostatic strain $\frac{1}{3}\varepsilon_{true,kk}$[11] is about $0.047\ [-]$ which decreases to $0.01\ [-]$ for the second strain tensor and finally decreases to zero for the third strain tensor. From the decreasing hydrostatic strain from $z = 0\ [mm]$ up to $z = 16\ [mm]$, it can be perfectly seen, that the secondary seal is under confinement at $z = 0\ [mm]$, which is reasonable because the underlying glass pane 1 is in contact with the subconstruction. For $z = 16\ [mm]$, the hydrostatic stress diminishes. The maximum amount of shear strain $\tau_{max,true} = \max(\varepsilon_{ij,true}) - \min(\varepsilon_{ij,true})$[12] decreases also accordingly, from $0.52\ [-]$ at $z = 0\ [mm]$ to $0.04\ [-]$ at $z = 16\ [mm]$. An appreciable shear strain at $z = 0\ [mm]$ indicates a serious rate of distortion.

Finally, the turning points in Figure 87 cannot be explained clearly, but since the Poisson's ratio $\nu = 0.48$, a lateral volume expansion might play a role because glass pane 2 is pressing directly onto the spacer and the silicone, but glass pane 1 lies already on the subconstruction for $t = 1$. Due to the lower stiffness of the silicone, it has to give in at the height of the turning point, which is not possible next to the glass panes at $z = 0\ [mm]$ and $z = 16\ [mm]$.

[11] The hydrostatic strain is the trace of the strain tensor divided by 3 or $\frac{tr(\varepsilon_{true})}{3} = \frac{1}{3}\varepsilon_{true,kk}$

[12] The max. shear strain is obtained by the biggest difference of two entries of ε_{ij}

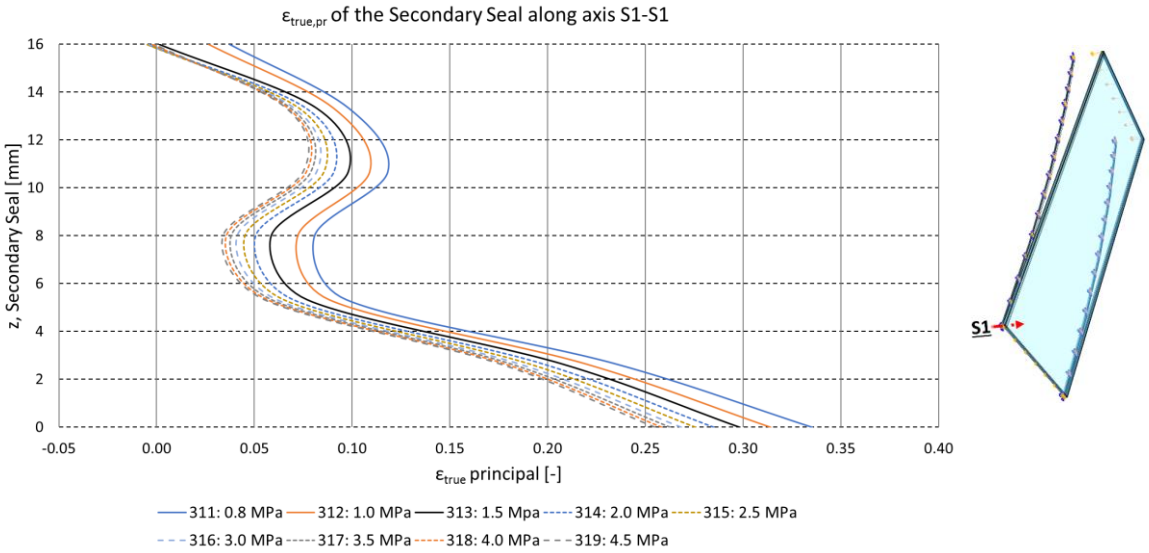

Figure 87: Single-bent model for variation 3, $\varepsilon_{true,pr}$ of the secondary seal along axis S1-S1

6.2.4 Stainless steel spacer and aluminum spacer - Variation 4

In this subchapter, the IGU system is evaluated with an aluminum spacer and is compared to the IGU system with a spacer which is made out of stainless steel. The exact material properties can be found in Table 3 in chapter 6.1. Both allocated designations for the models and the allocated spacer material can be seen from the listing in Table 11.

Single-Bent	Stainless Steel	Aluminum
411	X	
412		X

Table 11: Variation 41: Stainless steel and aluminum spacer bars

6.2.4.1 Required force for the cold bending process

The required force F for cold bending of the IGU from $t = 0$ to $t = 1$ is depicted in Figure 88. An exponential increase of F for the aluminum spacer in almost the same manner as for the steel spacer is baffling at the first sight. The linear Young's modulus E of stainless steel in this case is $E_{St.Steel} = 189E9\ [Pa]$ but for aluminum, it is $E_{Aluminum} = 70E9\ [Pa]$ which is 2.7 times lower. In order to verify this result, a roughly estimation of a weighted moment of inertia around the x-axis is done.

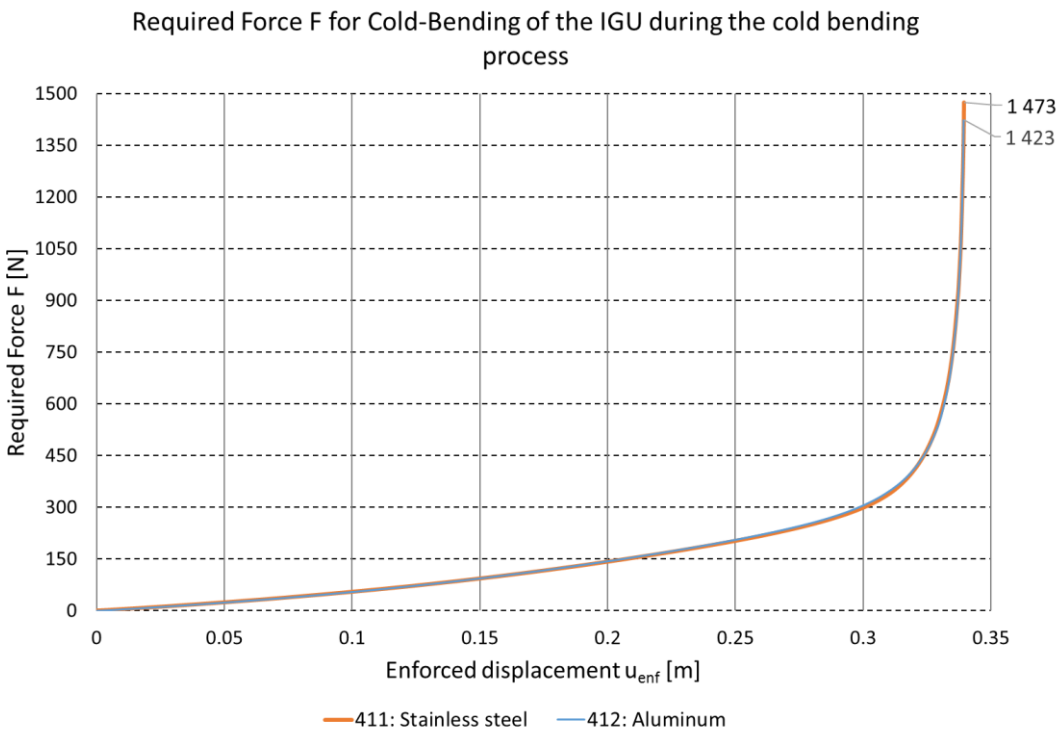

Figure 88: Single-bent model for variation 4, required force F for cold-bending of the IGU

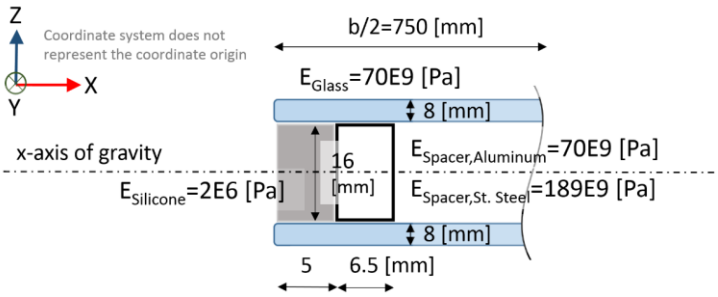

Figure 89: Sketch for a rough estimation of a weighted moment of inertia around the x axis

Considering half of the IGU, the moment of inertia I^*_{Glass} is composed out of half of glass pane 1 and half of glass pane 2, which have both the same thickness, therefore $2I^*_{Glass}$.with the glass pane thickness t_{gp} and the width of the IGU b is

$$2I^*_{Glass} = 2 * \frac{b}{2} * \frac{t_{gp}^3}{12} = \frac{b * t_{gp}^3}{12} = \frac{1500 * 8^3}{12} = 64000[m^4/m]$$

The proportion from the parallel axis theorem is reduced by 35000 times because E_{Glass} is weighted with $E_{Silicone}$ which yields to

$$2I_{Glass} = 2I^*_{Glass} + \left(\frac{b}{2} * t_{gp}\right) * \left(\frac{t_{gp}}{2} + \frac{h}{2}\right)^2 * 2 * \frac{E_{Silicone}}{E_{Glass}} = (750 * 8) * 12^2 * 2 * \frac{2E6}{70E9} = 64051\ [mm^4/m]$$

Furthermore, the silicone is bonded to the glass panes and to the spacer, but its stiffness is 35000 times smaller than the one of glass and aluminum and 94500 times

smaller than the one of stainless steel. Therefore, the weighted moment of inertia can be neglected $I_{Silicone} \ll\rightarrow I_{Silicone} = 0$.

The spacer, which is either made out of stainless steel or aluminum can slip between the glass panes and therefore does not transmit any shear force. It's sheet thickness t_{sp} is $0.18\ [mm]$.

The geometrical moment of inertia of one spacer I_{Spacer} is

$$I_{Spacer} = \left(\underbrace{t_{sp} \frac{\left(h - 2t_{sp}\right)^3}{12}}_{web\ of\ the\ spacer} + \underbrace{w_{sp} \frac{t_{sp}^3}{12}}_{flange\ of\ the\ spacer} + \underbrace{w_{sp} * t_{sp} \left(\frac{h}{2} - \frac{t_{sp}}{2}\right)^2}_{parallel\ axis\ theorem} \right) * 2 = 261\ [mm^4/m]$$

For the aluminum spacer, the weighted moment of inertia $I_{Spacer,Aluminum}$ is

$$I_{Spacer,Aluminum} = I_{Spacer} * \frac{E_{Aluminum}}{E_{Glass}} = 261\ [mm^4/m]$$

For the stainless steel spacer, the weighted moment of inertia $I_{Spacer,St.Steel}$ is

$$I_{Spacer,St.Steel} = I_{Spacer} * \frac{E_{St.Steel}}{E_{Glass}} = 704\ [mm^4/m]$$

Therefore, the IGU with the stainless steel spacer is roughly 0.61% stiffer around the x-axis than the IGU with the aluminum spacer, which is also shown with

$$\left(\frac{2I_{Glass} + I_{Spacer,St.Steel}}{2I_{Glass} + I_{Spacer,Aluminum}} - 1 \right) * 100 = 0.61\%$$

If the values for $F(t = 1)$ for aluminum and stainless steel are compared, then $F(t = 1)$ for the latter one is 0.61% higher which lies in the order of magnitude of the numerical result, which is 4.2%. Therefore, it can be stated, that the spacer's contribution to the required bending force is almost negligible.

6.2.4.2 Glass pane

On the basis of the fact that the maximal principal stress $\sigma_{max,pr}$ in the glass pane 1 and in the glass pane 2 along all four axes 1-1 to 4-4 does not change like in subchapter 6.2.3, no figures are shown in this subchapter. In this case, $\sigma_{max,pr}$ is the same as in the single-bent reference model. From this fact, it can be deduced, that if the spacer stiffness is reduced about 2.6 times, it does not affect the stress in the glass which is the same conclusion as for the secondary seal. Therefore, the prevailing part

of $\sigma_{max,pr}$ is owed due to geometrical distortions of the IGU instead of the interaction with the spacer and silicone during the bending process.

6.2.4.3 Spacer bar

In Figure 90, the von Mises stress σ_e is depicted for axis 5-5 and axis 6-6 in the same graph. At both ends of axis 5-5, the aluminum spacer reaches it's ultimate strength of $215\ \left[\frac{N}{mm^2}\right]$ which should be considered as critical. For the back end at $0.0115\ [m]$ of axis 6-6, the aluminum spacer reaches $189\ \left[\frac{N}{mm^2}\right]$, which is far above the yielding stress of $160\ \left[\frac{N}{mm^2}\right]$. At the front end at $3.4885\ [m]$ of axis 6-6, the ultimate strength is reached as well. Because no crack criterion is calculated in this model, it is not known if the aluminum spacer would crack or not. Since the ultimate strength is reached at the inner corners, the aluminum spacer does not suit for the cold-bending process due to low ductility.

It can be deduced, that the stainless steel spacer is more suitable than the aluminum spacer because of it's higher ductility. The stress in the center region of the aluminum spacer in axis 5-5 is about $33\ \left[\frac{N}{mm^2}\right]$ and in axis 6-6 about $28\ \left[\frac{N}{mm^2}\right]$. The stress for the stainless steel spacer in the center region in axis 5-5 is about $87\ \left[\frac{N}{mm^2}\right]$ and in axis 6-6 is about $73\ \left[\frac{N}{mm^2}\right]$. For the aluminum spacer, the stress in the center region in axis 5-5 is about 18% higher and for the stainless steel spacer, it is about 19% higher.

Besides from the high material utilization, a further problem shows up when looking at the local deformation of the spacer in x-direction, which is also illustrated in Figure 91. The outer side of the longitudinal spacer undergoes local buckling at the back end next to the intersection point of axis 7-7 and axis S1-S1. The deformation amplitude at $t = 1$ is $0.16\ [mm]$. This is relatively much because the sheet thickness of the spacer is $0.18\ [mm]$, which is due to a high compression stress in x-direction.

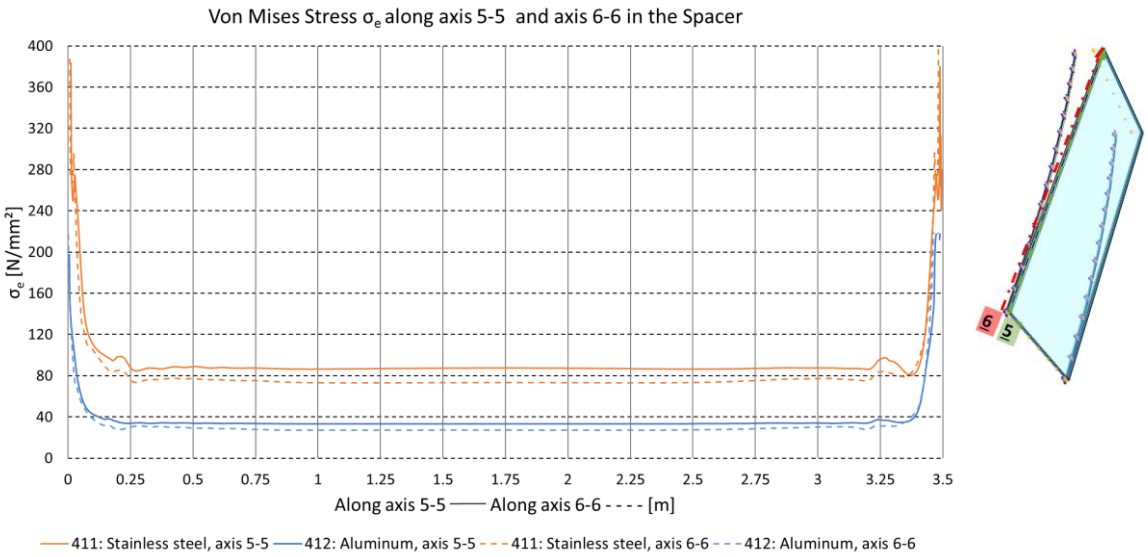

Figure 90: Single-bent model for variation 4, von Mises stress σe along axis 5-5 and axis 6-6 in the spacer

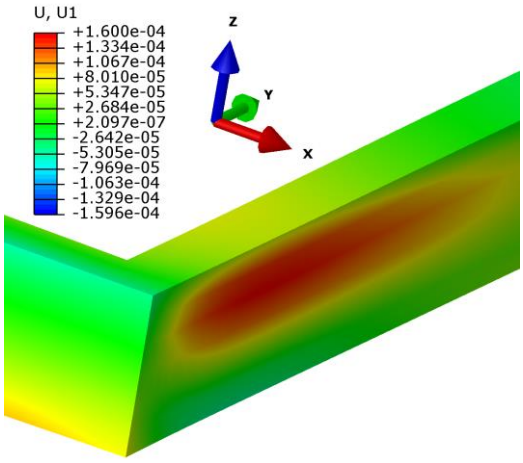

Figure 91: Lockal buckling of the longitudinal aluminum spacer next to axis S1-S1 at the lower end

6.2.4.4 Deformation of the edge zone

In Figure 92 and in Figure 93, a comparison between the displacements of the IGU system with aluminum spacer and stainless steel spacer are depicted for axis S1-S1 and axis S2-S2, respectively. In both cases, the displacements are practically the same. In addition, occurring differences are almost within the inaccuracy of the numerical model and can be neglected. From this observations, it can be deduced that the edge zone does not deform differently.

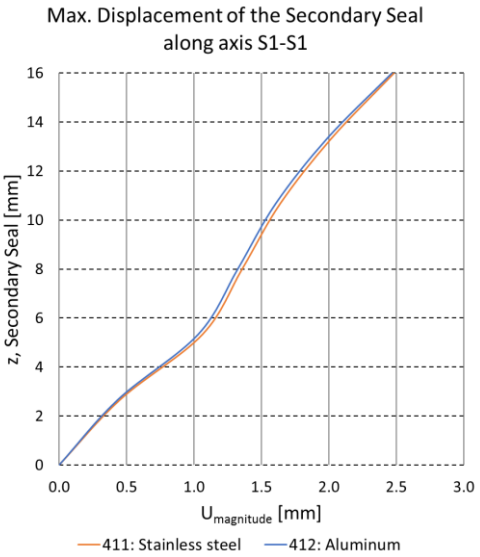

Figure 92: Single-bent model for variation 4, max. displacement of the secondary seal along axis S1-S1

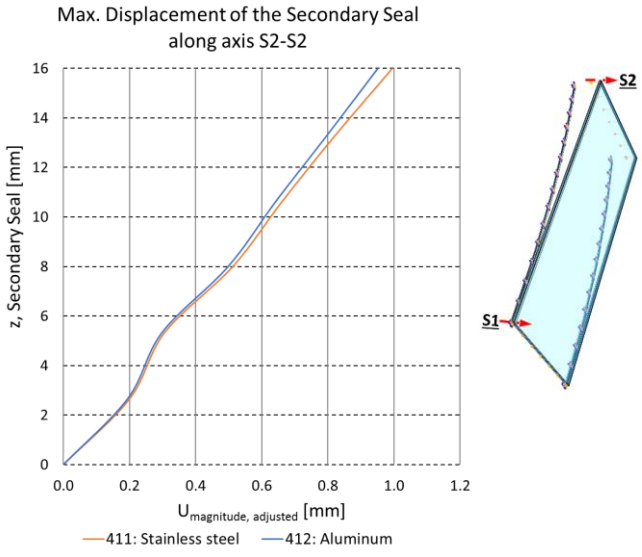

Figure 93: Single-bent model for variation 4, max. displacement of the secondary seal along axis S2-S2

6.2.1 Aspect ratio of the IGU - Variation 5

In this subchapter, a parameter study about the influence of the aspect ratio on the overall behavior of the single-bent IGU system is carried out. Different aspect ratios are obtained by varying the total length l_{gp} of the IGU whereas the width w_{gp} of the IGU stays constant during the whole parameter study. Note, that the radius r does not change but the maximum deformation u_{enf} gets bigger for a higher length l_{gp}.

The following l_{gp} of the IGU are considered: $0.75\ [m]$, $1.50\ [m]$, $2.00\ [m]$, $2.50\ [m]$, $3.00\ [m]$, $3.50\ [m]$, $4.67\ [m]$ and $5.83\ [m]$. The different models are also listed in Table 12 and are also depicted as a schematic longitudinal section in Figure 94.

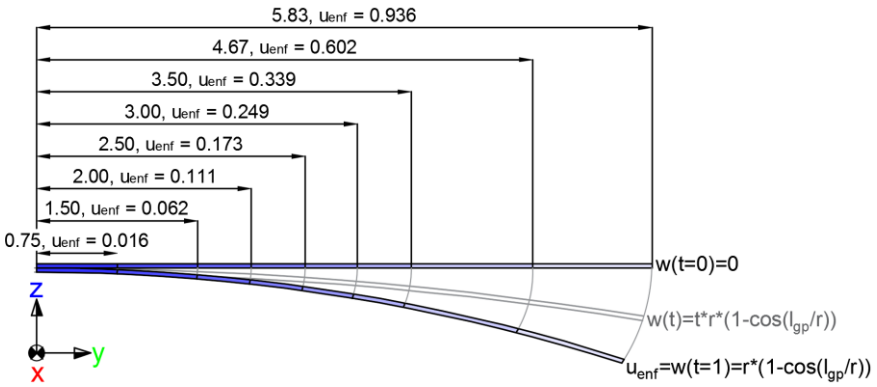

Figure 94: Variation 51: Different aspect ratios of the IGU, values in the sketch in meters

Single-Bent	0.75 m	1.50 m	2.00 m	2.50 m	3.00 m	3.50 m	4.67 m	5.83 m
511.	X							
512		X						
513			X					
514				X				
515					X			
516						X		
517							X	
518								X

Table 12: Variation 51: Different aspect ratios of the IGU

The crucial von Mises stress σ_e in the axes 5-5 and 6-6 do not change in the center region for different aspect ratios. The stress values stay almost the same for different aspect ratios. The values are like for the reference model in chapter 6.1 and are therefore not shown in this parameter study.

6.2.1.1 Required force for the cold bending process

The required force F for cold-bending of the IGU from $t = 0$ to $t = 1$ is depicted in Figure 95. All curves do exhibit an exponential behavior. However, looking at the average gradient before and after the turning point, it can be seen, that for a small t, F grows faster for the - roughly speaking - first 90% of the total imposed deformation. After that, all curves are almost parallel to each other, which indicates, that the aspect ratio does not impede or facilitate the clinging of the IGU to the subconstruction.

The total values for F are steadily increasing accordingly to l_{gp} in a non-linear relationship. This can be seen directly for the best linear fitting curve as a function of l_{gp} for $F(t = 1)$ which yields to $F(t = 1) = 155 * [N/m] * l_{gp}[m] + 989\ [N]$.

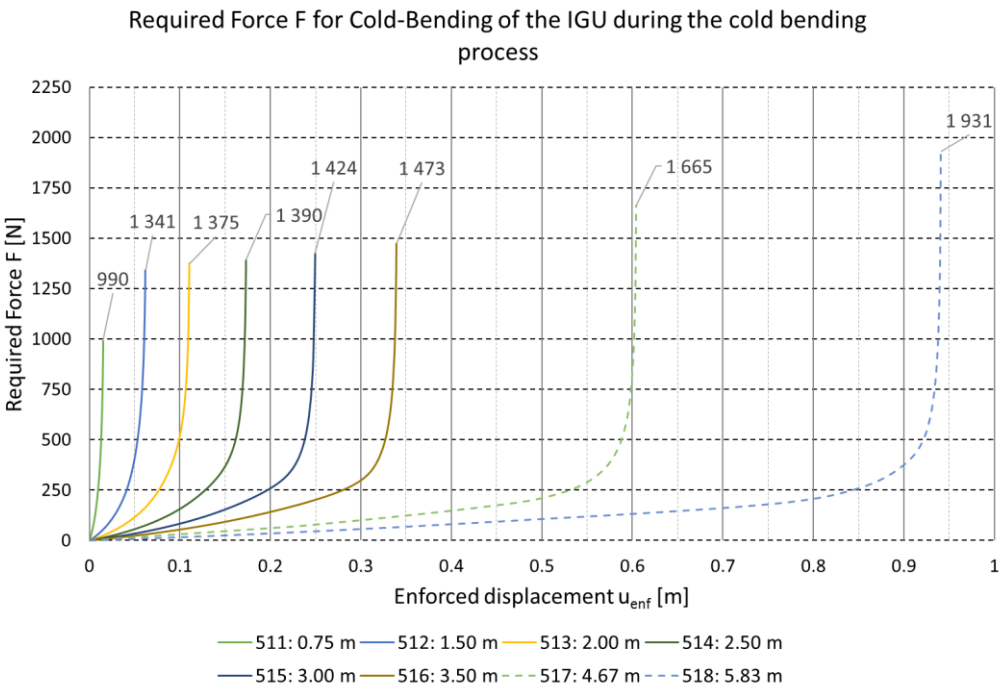

Figure 95: Single-bent model for variation 5, required force F for cold-bending of the IGU

6.2.1.2 Glass pane

In Figure 96, the maximum principal stress $\sigma_{max,pr}$ is shown along axis 1-1. In Figure 97, $\sigma_{max,pr}$ is shown along axis 3-3. Aside from (511: 0.75 [m]), the maximum values for $\sigma_{max,pr}$ are the biggest for (512: 1.50 [m]) and are decreasing for both axes until (515: 3.50 [m]). After that, $\sigma_{max,pr}$ starts to increase again. However, the global maximum of $\sigma_{max,pr}$ lies between 19 $\left[\frac{N}{mm^2}\right]$ and 21 $\left[\frac{N}{mm^2}\right]$ wich is not a significant difference. The situation is different for (511: 0.75 [m]), where $\sigma_{max,pr}$ is lower with a maximum of 18 $\left[\frac{N}{mm^2}\right]$ in axis 3-3 which is a slightly smaller value compared to (512: 1.50 [m]).

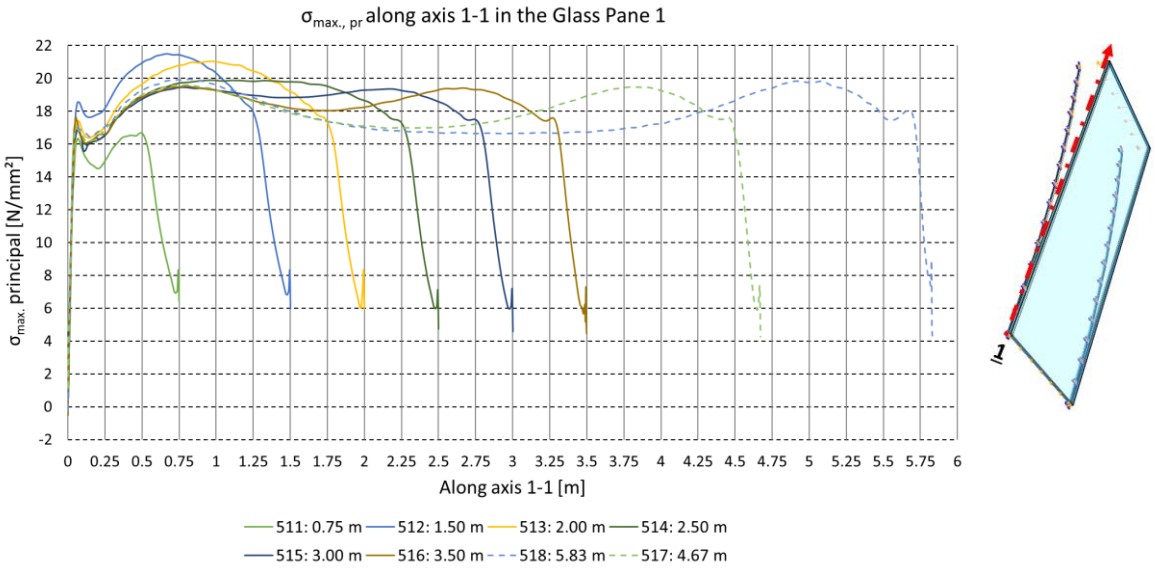

Figure 96 Single-bent model for variation 5, $\sigma_{max,pr}$ along axis 1-1 in the glass pane 1

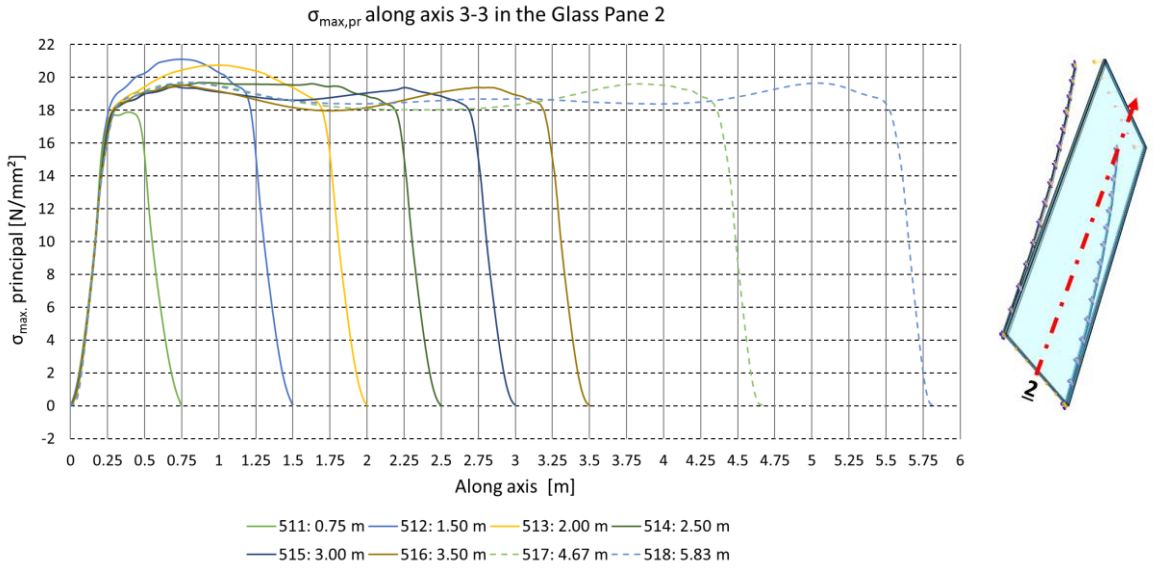

Figure 97: Single-bent model for variation 5, $\sigma_{max,pr}$ along axis 3-3 in the glass pane 1

A top view onto glass pane 2 which shows $\sigma_{max,pr}$ is provided for all different models from Figure 98 to Figure 105. Focusing on the stress peaks, which occur on the bended side (or broadside for 511: 0.75 [m]) it can be seen, that at first, the stress peak area grows according to l_{gp} until (514: 2.50 [m]) but then starts to bisect from (515: 3.50 [m]) on which indicates a different contact behavior of the IGU with the subconstruction. This leads also to a different stress pattern in the middle of the glass pane at $\frac{l_{gp}}{2}$.

The reason for this is that the main load-bearing direction in the glass is equal to the shortest distance between the stress peaks which gets evident in Figure 104 and Figure 105. Moreover, it can be seen, that the distribution of $\sigma_{max,pr}$ for $t = 1$ is always symmetrical in the y-direction and almost symmetrical in the x-direction.

These illustrations are depicting a half of glass pane 2 from 0 to $l_{gp}/2$ because $\sigma_{max,pr}$ is symmetrical at $t = 1$.

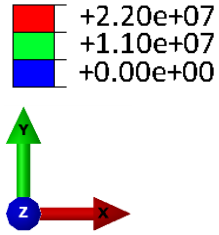

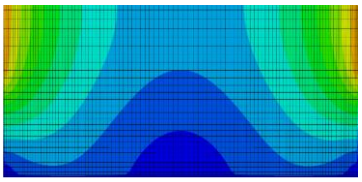

Figure 98: $\sigma_{max,pr}$ 511: 0.75 [m], glass pane 2

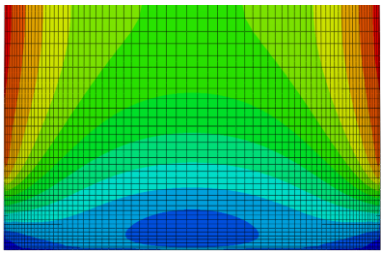

Figure 99: $\sigma_{max,pr}$ 512: 1.50 [m], glass pane 2

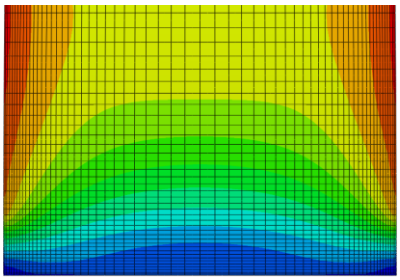

Figure 100: $\sigma_{max,pr}$ 513: 2.00 m, glass pane 2

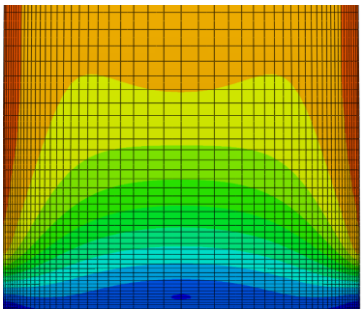

Figure 101: $\sigma_{max,pr}$ 514: 2.50 [m], glass pane 2

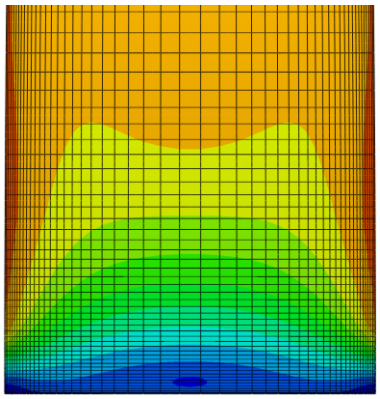

Figure 102: $\sigma_{max,pr}$ 515: 3.00 [m], glass pane 2

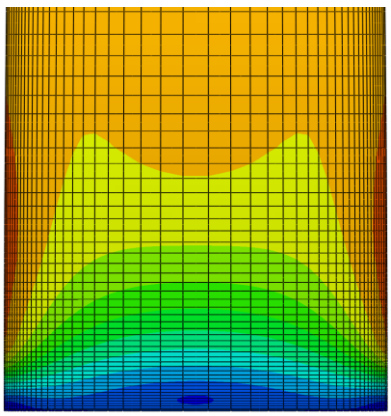

Figure 103: $\sigma_{max,pr}$ 516: 3.50 [m], glass pane 2

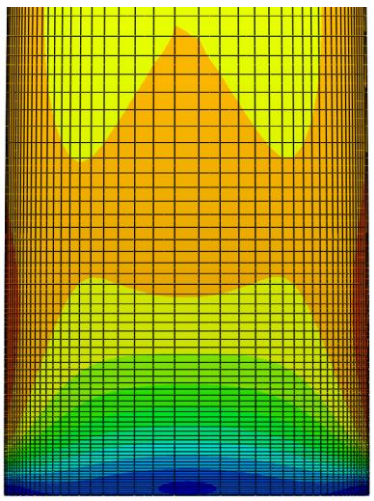

Figure 104: $\sigma_{max,pr}$ 517: 4.67 [m], glass pane 2

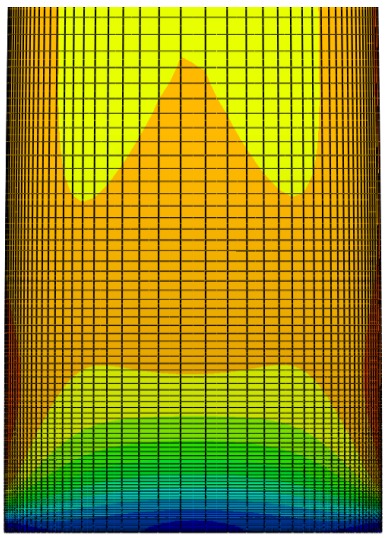

Figure 105: $\sigma_{max,pr}$ 518: 5.83 [m], glass pane 2

6.2.1.3 Deformation of the edge zone

In Figure 106, the maximum displacement of the secondary seal along axis S1-S1 is depicted. The maximum deformation amplitude increases from 0.9 $[mm]$ for (511: 0.75 [m]) up to 3.9 $[mm]$ for (518: 5.83 [m]) which indicates a higher slip for longer IGU's.

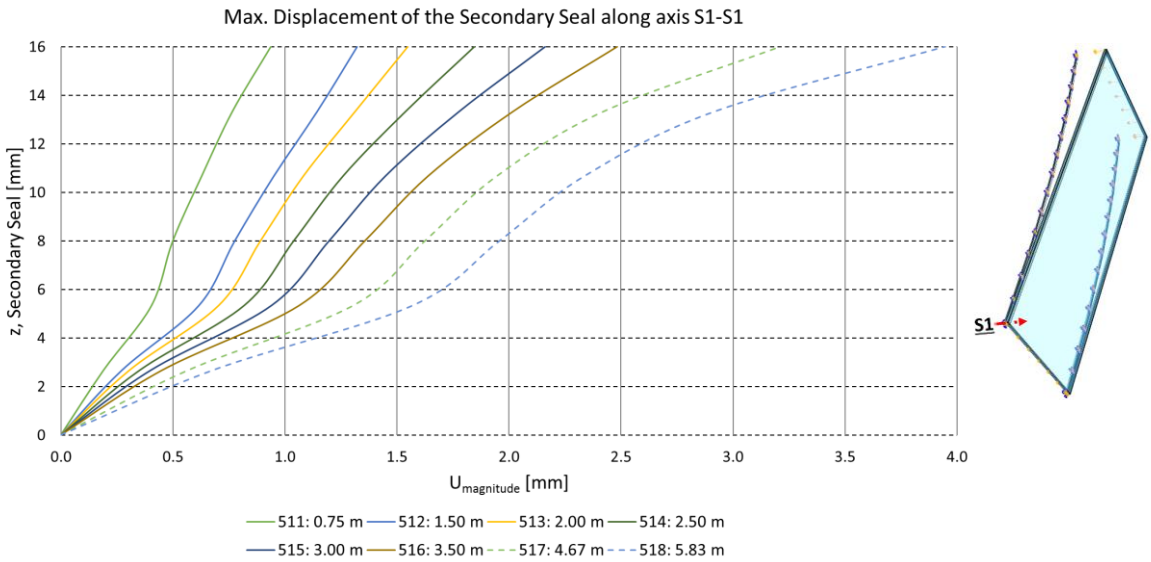

Figure 106: Single-bent model for variation 5, max. displacement of the secondary seal along axis S1-S1

6.2.2 Discussion of the results for the single-bent IGU

In this subchapter the most important findings from the single-bent parameter study in chapter 6.1 are summed up. For each parameter variation, the influence of the current parameter is described for the glass panes, the spacers and the secondary seal. An overarching summary is provided along with the conclusions in chapter 7.

Thickness of the glass pane - Variation 1

Variation 1 unveils a sensitive dependency between the significant maximum principle stress in the glass and the thickness of the glass pane. For a double-glazed IGU, the thicker of both glass panes mainly determines the significant stress. The thinner glass pane has always a lower significant stress than the thicker glass pane. The thinner glass pane does only have a marginal influence on the stresses in the thicker glass pane. In order to reduce the significant stress in the glass panes, it is advisable to

choose the same pane thickness. The results show that the significant stress occurs in the thicker glass pane outside of the influence area of the corner region parallel to axis 1-1 and axis 3-3. If both glass panes have the same pane thickness, then both glass panes have practically the same significant stress values.

All spacers undergo yielding in the corner region, which seems to be inevitable. Outside the influence of the corner region, the material utilization leaves enough remaining potential for variable loads. Neither in the corner region nor outside the corner region are any noteworthy changes in the von Mises stress depending on the different parameter values.

The deformation of the secondary seal depends on the thicker of both glass panes. The shear displacement at the front end next to axis 8-8 doubles if the thicker glass pane of the IGU is increased from $6\ [mm]$ to $10\ [mm]$. Next to the line support at axis 7-7, the shear displacement shows the same behavior, but it is less pronounced.

Depth of the cavity - Variation 2

In contrast to variation 1, the maximum principal stresses in the glass panes in variation 2 do not depend on the thickness of the cavity height.

Also in contrast to variation 1, the von Mises stresses in the spacers in variation 2 outside the influence of the corner region show to react sensitive to a change of cavity depth. Note, that the cavity depth has the same height as the spacer. Therefore, the von Mises stresses are increasing with a higher cavity depth except for the corner region. The significant stress occurs along axis 5-5 which is at the upper side of the spacer next to glass pane 2.

The shear displacement decreases with a higher cavity depth. The absolute maximum displacement doubles, if the cavity depth is increased threefold. Like in Variation 1, the shear displacement is bigger at the front end of the IGU next to axis 8-8 than at the back end next to axis 7-7.

Increasing the depth of the cavity also increases the von Mises stress in the spacers significantly. Therefore, the remaining potential for variable loads decreases. The shear displacement decreases for higher cavity depths, which is advantageous for

practical applications. However, the absolute displacement value of the edge zone still increases for higher cavity depths.

Linear Young's modulus - Variation 3

A change of the Young's modulus of the secondary seal does not have an influence in the stress of the spacers and the glass panes.

If the Young's modulus gets higher, then the maximum principal stresses of the glass panes in the corner region is increasing significantly. In addition, the stress outside the corner region increases slightly. True strain reaches maximum values in the corner region where also stress peaks occur. However, the maximum strain values for all different Young's moduli are almost the same. Outside the corner region, the true strain increases significantly with softer secondary seals but stays well beyond the strain in the corner region. In order to avoid a strong creeping effect, it can be advisable to choose a structural silicone with a higher Young's modulus. The shear displacement does slightly decrease for a higher Young's modulus. This is only owed to the silicone because the spacers behind the secondary seal do not change their shear displacement.

For single-bent IGUs, the advantage of a stiffer structural silicone is limited to a slight decrease of shear displacement in the edge region.

Stainless steel spacer and aluminum spacer - Variation 4

Two different materials were used in Variation 4 for the spacer bars: aluminum and stainless steel. There is no mentionable difference in the mechanical behavior of the glass panes and the secondary seal. However, speaking in terms of von Mises stress, the material utilization is significantly lower for the stainless steel spacers.

In the corner region, the aluminum spacer reaches its ultimate strength due to a low ductility compared to stainless steel. Furthermore, the longitudinal aluminum spacer undergoes local buckling in the corner region due to high compression forces. Aluminum as a material for spacers is not deemed suitable because the cold bending process requires a material with high ductility. This criterion can be fulfilled by stainless steel.

Aspect ratio - Variation 5

For all aspect ratios in variation 5, all significant maximum principal stress values in the glass panes are changing in a range of roughly 10%. Furthermore, the von Mises stress in the spacers does not change. However, a great difference is observed for the deformation of the secondary seal.

The shear gradient increases accordingly to a more elongated IGU. For an aspect ratio (longitudinal side over broadside of the IGU) of $1/2$, the shear deformation is approximately a quarter from that of an aspect ratio of about 4.

If the aspect ratio is varied, then no significant changes of the significant stress values have to be expected for the glass and the spacer. However, the shear displacement is sensitive to a change of the aspect ratio. The maximum shear displacement increases with a higher aspect ratio. This can be limited, if glass pane 2 is also supported like glass pane 1 along axis 7-7.

6.3 Reference model: Double-bent IGU

Double-bent insulation glass units are examined in a parameter study in chapter 6.4. In order to choose a sensible reference model for the parameter study, a case study for different boundary conditions is carried out in subchapter 6.3.4, 6.3.3 and 6.3.4.

As in the single-bent case, all double-bent models will be bent displacement controlled, but unlike for the single-bent models, which are bent onto a subconstruction, the double-bent models can reshape freely. Each result refers to an axis which is illustrated in Figure 107 and Figure 108. The arrow of the axis shows the direction for the result path. All geometrical values can be found in Table 13 and a more detailed description about the numerical model is given in the subsequent subchapter.

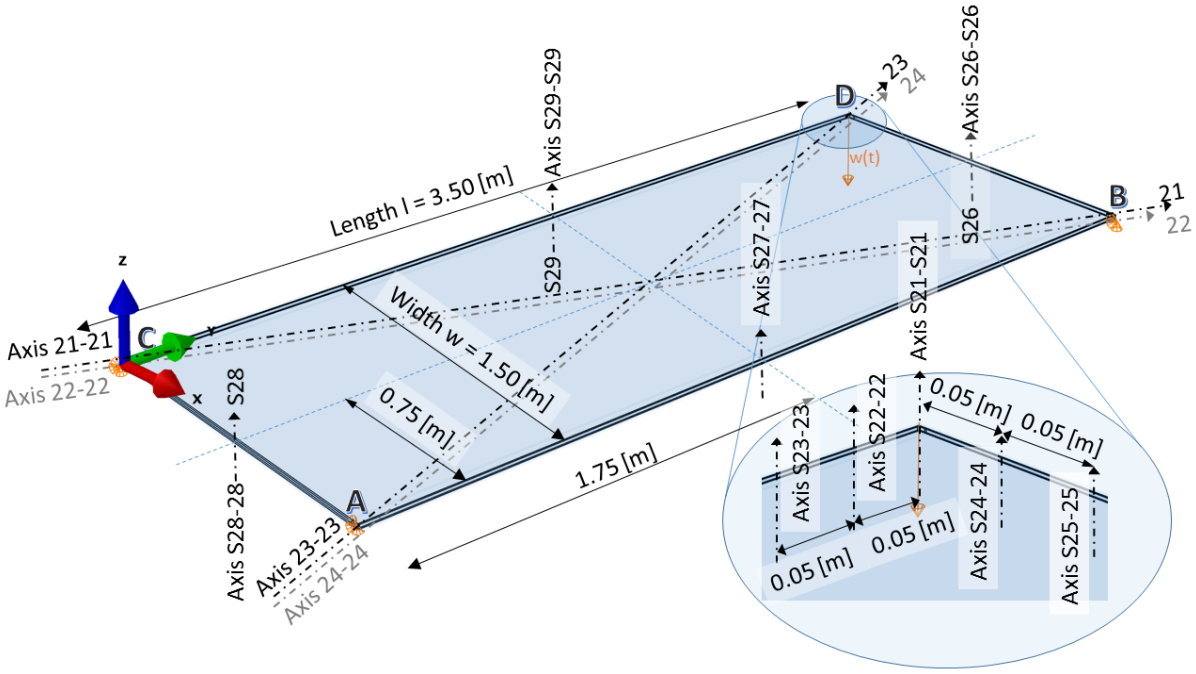

Figure 107: Reference model of the double-bent IGU, axes represent result paths, results are examined in direction of the arrow

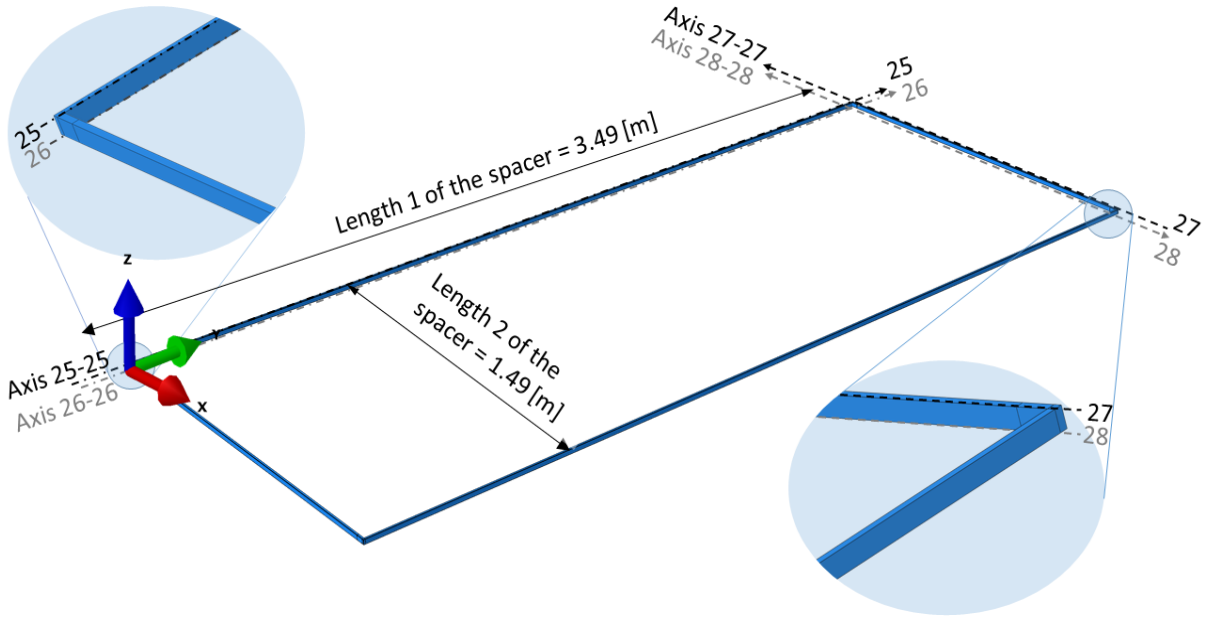

Figure 108: Spacer bars of the double-bent IGU

Name	Abbreviation	Value	Unit
Length of the glass pane	l_{gp}	3.50	m
Width of the glass pane	w_{gp}	1.50	m
Thickness of the glass pane	t_{gp}	8	mm
Height of the spacer is equal to the height of the secondary seal	h	16	mm
Width of the spacer	w_{sp}	6.5	mm
Sheet thickness of the spacer	t_{sp}	0.18	mm
Width of the secondary seal	w_{ss}	5	mm

Table 13: Geometrical values of the double-bent model

Annotation: All geometrical values in of the double-bent reference model are basically the same as for the single-bent model except from the subconstruction, which does not exist for this case. However, a repeated listing in Table 13 is done for a better readability.

6.3.1 Finite element model of the double-bent IGU

Almost like the single-bent model, the double-bent FEM model consists of several parts, which are two longitudinal spacers parallel to the y-axis, two spacers along the width parallel to the x-axis, a circumferential secondary seal, two glass panes but no subconstruction. Each part is assigned to a certain FE type, which are listed in Table

14 and show to be numerically stable and leads to sufficiently accurate results at the same time. Figure 109 shows the assigned element types in the edge region of the double-bent IGU.

Part of the Double-Bent Model	Element Type	Specific Element Type	Name in Abaqus
Glass pane	Solid	20-node quadratic brick	C3D20
Spacer	Shell	8-node doubly curved thick shell, quadratic, reduced integration	S8R
Secondary Seal	Solid	20-node quadratic brick, hybrid with linear pressure, reduced integration	C3D20RH

Table 14: Finite elements used for the double-bent model

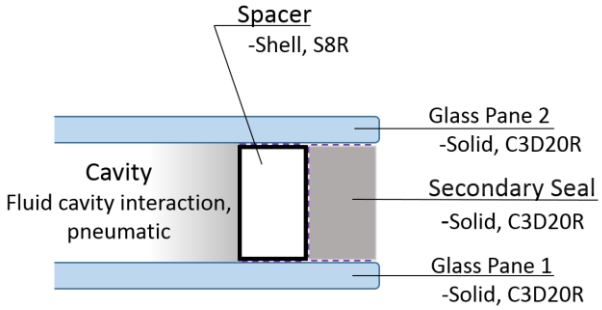

Figure 109: Finite elements used for the double-bent model

In Table 15, the interaction properties and constraint properties for the double-bent model are listed. They are also shown in Figure 110 and are basically the same as for the single-bent model. However, some adjustments seemed to be sensible due to a more complex distortion figure, which is shown in the column “further information”. For the double-bent model, the integration nodes at the joint, where the broadside spacer and longitudinal spacer are tied together, a position tolerance of $1E-5\ [m]$ led to a striking discontinuity in the stress function, which grows with time t and can be up to $\pm 15\%$[13]. If the position tolerance is computed automatically, the discontinuity still exists but shrinks to about a third of $\pm 15\%$. Interestingly, this problem does not occur for the single-bent model. It is thought that this problem is owed to the master-slave algorithm between the spacers which also has to consider the opening and closing contact interaction with the glass pane. Therefore, the stress values in the corner

[13] This value and all related values represent conservative estimations or rather an upper limit for occurring discontinuities

region of the IGU for the spacer system are deviating about $\pm 5\%$, depending on the position tolerance.

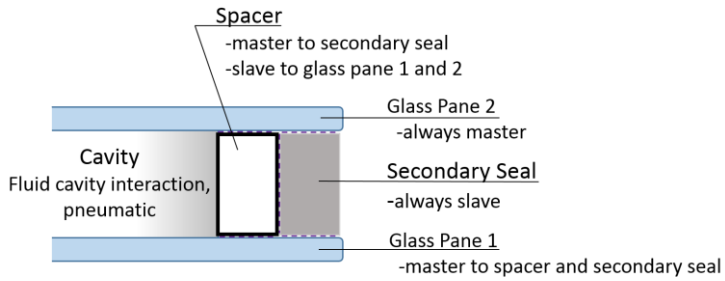

Figure 110: Interaction and constraints for the double-bent model

Name	Interaction and Constraints	Further information
Glass-spacer surface	Surface-surface interaction, glass is master	Hard contact, frictionless, can separate after contact, adjustment of the nodes to remove overclosure
Glass-secondary seal surface	Surface-surface tie constraint, glass is master	
Spacer-secondary seal surface	Surface-surface tie constraint, spacer is master	
Spacer-spacer shell edges	Shell-shell tie constraint	Position tolerance is computed automatically but less than 1E-5 [m]
Gas filling	Fluid cavity interaction, pneumatic	

Table 15: Interaction and constraints used for the double-bent model

Like for the single-bent model, a convergence study was conducted, which can be found in the appendix in chapter 11.1 with a special focus on the deformation of the edge region due to the complexity of a freely reshaping double-bent IGU. It was found, that the mesh size, which was chosen for the single-bent model also works for the double-bent model.

In Figure 111 a close-up view of a corner for the meshed double-bent model is shown. In Figure 112 a close-up view of the very same corner region without the broadside spacer and glass pane 2 is illustrated. The mesh size of the spacer and the secondary seal is in accordance to each other but finer as the glass panes because the latter is their master.

Part	Seeding method	Mesh size
Glass pane	By size, double	0.01 to 0.1 m
Secondary seal, circumferential	By size, double	0.005 to 0.05 m
Secondary seal along its height/width	By number, 4/3	0.005/0.003 m
Spacer along its length	By size, double	0.005 to 0.05
Spacer along its height/width	By number, 4/3	0.005/0.003 m

Table 16: Mesh size for the double-bent model

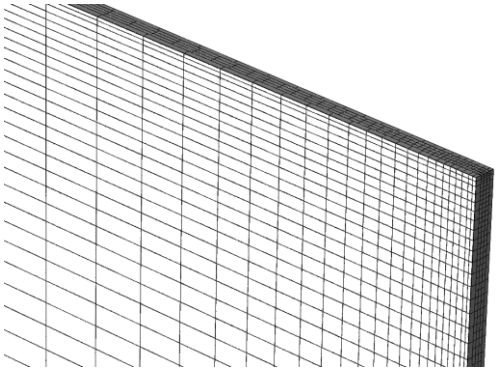

Figure 111: Close-up view of the mesh in the corner region, double-bent

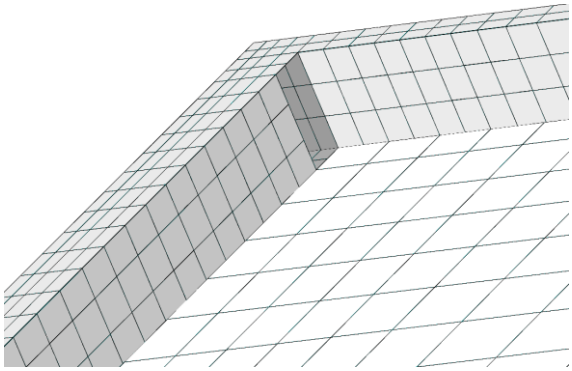

Figure 112: Close-up view of the mesh in the corner region without the spacer along the axis 27-27 and without glass pane 2, double-bent

In Figure 113, three different IGUs are depicted. The difference about these models is the definition of the BCs in the corners A, B and C.

On the left side of Figure 113, support situation 1 is illustrated, which is examined in subchapter 6.3.2. In the middle of Figure 113, support situation 2 is illustrated, which is examined in subchapter 6.3.3. On the right side, support situation 3 is illustrated, which is examined in subchapter 6.3.4.

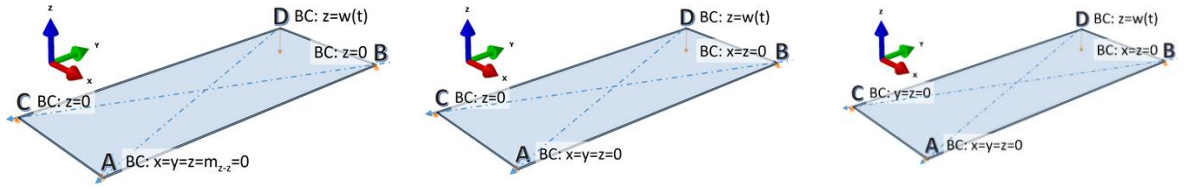

Figure 113: Case study models, left: support situation 1, middle: support situation 2, right: support situation 3

All three support situations are examined in the subsequent subchapters. This is necessary because during numerical investigations, the double-bent model showed to

be especially sensible to a change in the BCs. Furthermore, little is known up to date about the mechanical behavior for different BCs of a double-bent IGU.

Therefore, a comprehensive understanding can be obtained by examining the same IGU model for different BCs.

More important, a meaningful parameter study can only be done with BCs which ensure a mechanically stable behavior for a wide range of different IGUs.

6.3.2 Double-bent IGU, support situation 1

For the double-bent reference model, which is described in chapter 6.3, the influence of the BCs is being investigated. In this subchapter, support situation 1 is subject to investigations. An overview about the BCs is provided in Figure 114. The BCs are depicted in Figure 115 for the corner A and D and in Figure 116 for the corners B and C. In the subsequent part of this subchapter, the results from this support situation are presented. At corner A, a pinned support with an additional condition which impedes the rotation around the z-axis is applied on glass pane 2. In addition, the outer corner points of glass pane 1 at the corners B and C are supported in z-direction which can be understood as roller-like bearings. At corner D at the outside corner of the IGU at glass pane 2, a controlled displacement $w(t)$ is applied.

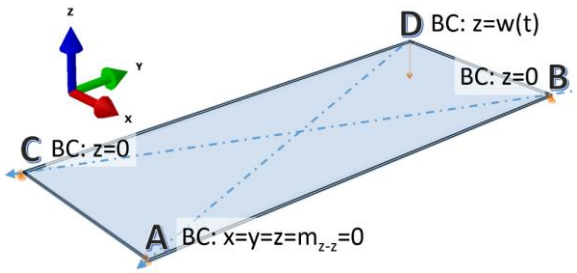

Figure 114: Schematic overview of boundary conditions for support situation 1

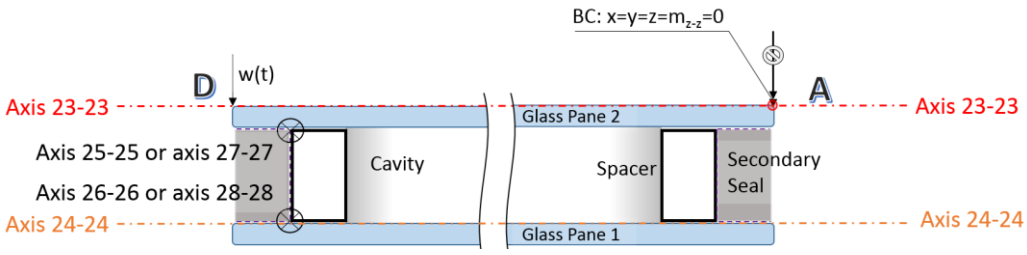

Figure 115: Schematic longitudinal section of the double-bent IGU along the diagonal 23-23, support situation 1

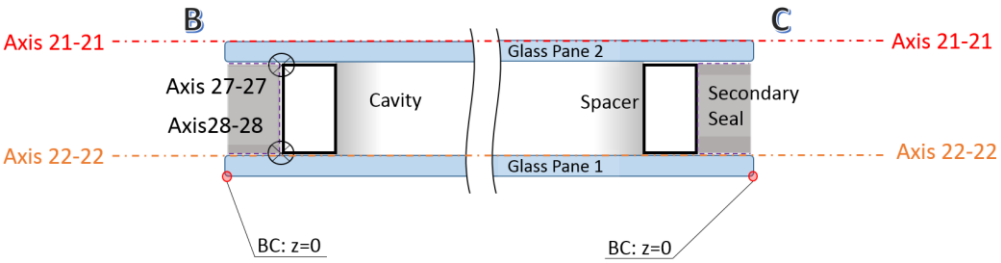

Figure 116: Schematic longitudinal section of the double-bent IGU along the diagonal 21-21, support situation 1

Annotation: $w(t)$*, which is the vertical imposed displacement, is* $w(t=0)=0\ [m]$, $w(t=1/3)\approx 0.053\ [m]$, $w(t=2/3)\approx 0.107\ [m]$ *and* $u_{enf}=w(t=1)=0.16\ [m]$ *for support situation 1. For support situation 2 and 3,* $w(t=0)=0\ [m]$, $w(t=0.578)=0.16$ *and* $u_{enf}=w(t=1)=0.277\ [m]$.

6.3.2.1 Qualitative result of glass pane 2

In Figure 117, the maximal principal stress , $\sigma_{max,pr}$ on the top surface of glass pane 2 is shown in a sequence for $w\left(t=\frac{1}{3}\right)=0.053\ [m]$, $w\left(t=\frac{2}{3}\right)=0.107\ [m]$ and $w(t=1)=0.16\ [m]$.

At $w\left(t=\frac{1}{3}\right)=0.053\ [m]$, the stress is uniformly distributed in the glass pane. A marginal increase of $\sigma_{max,pr}$ is evident at the corners A and D where BCs are applied as well as in the longitudinal edge region. At $w\left(t=\frac{2}{3}\right)=0.107\ [m]$, a basin-shaped stress distribution appears to indicate an extension of the glass in the edge region. In the middle of the glass pane, $\sigma_{max,pr}$ is about a third of $\sigma_{max,pr}$ in the edge region. At $w(t=1)=0.16\ [m]$, the formerly basin-shaped stress distribution has changed substantially at the corners A and D, where singularities are now clearly evident. These stress peaks occur because of the BCs which are applied at a single FE node.

The axis of symmetry of the stress "valley" in the center region of the glass pane is rotated against the axis of symmetry of the IGU system. This phenomenon happens during the whole bending process but becomes more visible at $w(t=1)=0.16\,m$ which is owed to non-symmetric BCs. A minor shift of the corners can be observed at $w\left(t=\frac{2}{3}\right)=0.107\ [m]$ which is more visible at $w(t=1)=0.16\ [m]$ and looks like a rotation even tough $BC\colon m_{z-z}=0$ at corner A. This means, that the vertex is too soft

for a rotation-rigid point. In Figure 123 in subchapter 6.3.2.5, the movement of point D with respect to t is examined, where a stability problem appears to be happening at $w\left(t=\frac{2}{3}\right)=0.107\ [m]$.

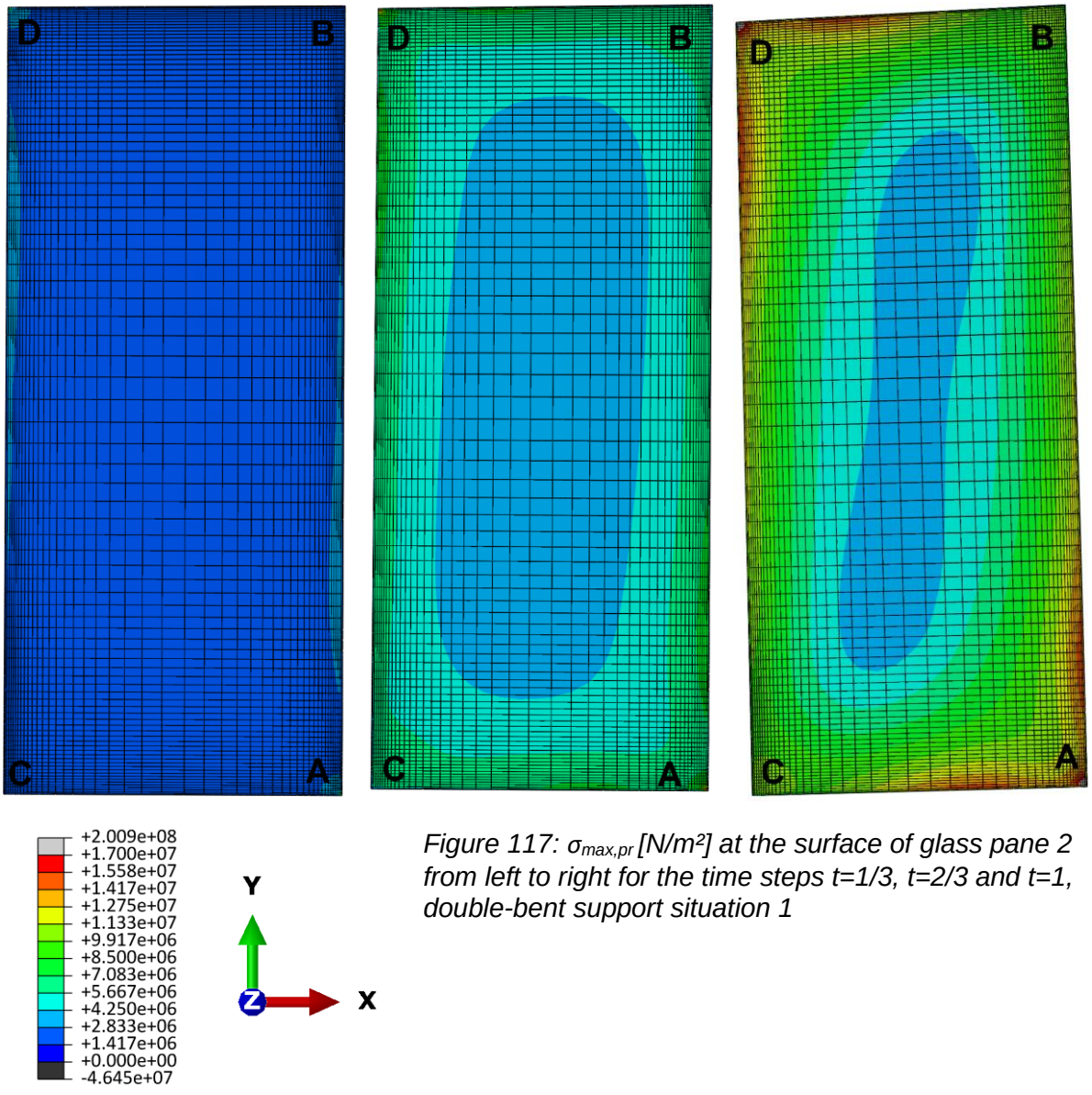

Figure 117: $\sigma_{max,pr}$ [N/m²] at the surface of glass pane 2 from left to right for the time steps t=1/3, t=2/3 and t=1, double-bent support situation 1

6.3.2.2 Qualitative results of the spacer bars

In Figure 118 and in Figure 119, σ_e of the stainless steel spacer in the corner region for the corners A and D is depicted in a sequence for the time steps $w\left(t=\frac{1}{3}\right)=0.053\ [m]$, $w\left(t=\frac{2}{3}\right)=0.107\ [m]$ and $w(t=1)=0.16\ [m]$. For both regions, the spacers undergo almost an identical stress distribution over time although corner D is being moved and point A is constrained by it's BCs. Stress peaks in the corner, which

can be as high as $350\ \left[\frac{N}{mm^2}\right]$, occur mainly due to pressing forces at the upper and lower side of the spacer (deviation forces are playing a tangential role). Local stress peaks which result in yielding can be accepted as the plasticizing stays restricted to a very local area.

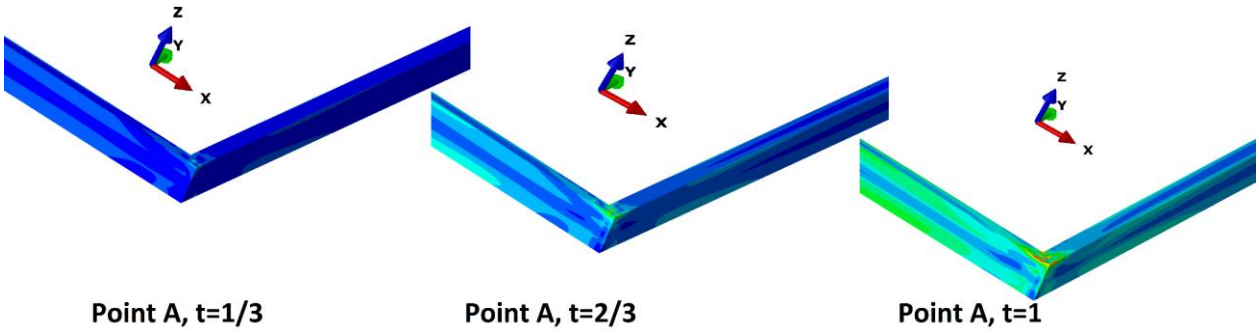

Figure 118: σ_e [N/m²] at the vicinity of point A of the spacer from left to right for the time steps t=1/3, t=2/3 and t=1, double-bent support situation 1, view from above

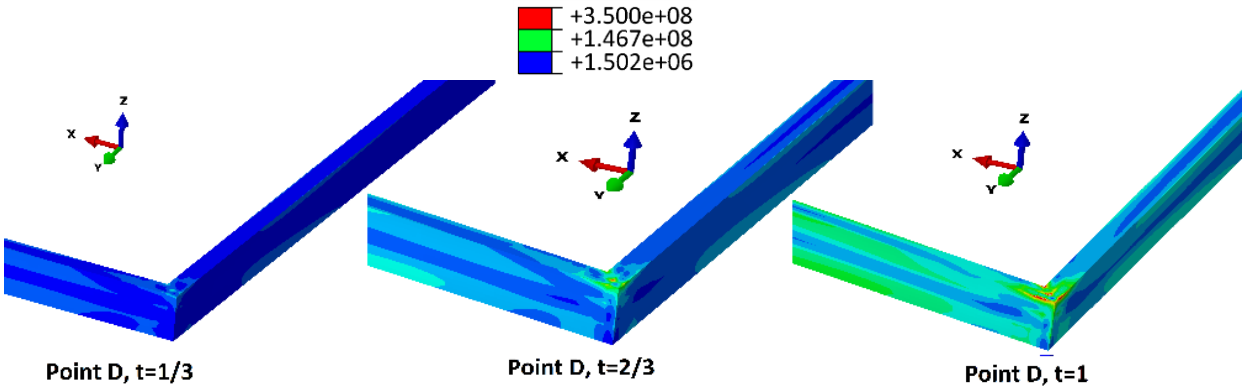

Figure 119: σ_e [N/m²] at the vicinity of point D of the spacer from left to right for the time steps t=1/3, t=2/3 and t=1, double-bent support situation 1, view from above

6.3.2.3 Qualitative results of the secondary seal

In Figure 120, $\sigma_{max,pr}$ of the secondary seal is shown in a sequence for $w\left(t=\frac{1}{3}\right)=0.053\ [m]$, $w\left(t=\frac{2}{3}\right)=0.107\ [m]$ and $w(t=1)=0.16\ [m]$. For all time steps the significant stress occurs at the inner corners C and D. At $w\left(t=\frac{1}{3}\right)=0.053\ [m]$, the stress in the corner can be as low as $-1\ \left[\frac{N}{mm^2}\right]$ which decreases up to $-0.2\ [N/mm^2]$ for $t=1$. Contrary to the crucial pressure values, tension is not so intense in the silicone. However, stress peaks for the maximal principal stress in the corner at $w\left(t=\frac{1}{3}\right)=0.053\ [m]$ is $0.3\ \left[\frac{N}{mm^2}\right]$ which increases to about $1\ \left[\frac{N}{mm^2}\right]$ for $w(t=1)=$

$0.16\ [m]$. Aside from the corner regions, the stress in the silicone reaches hardly a noticeable value for any time step. It can be stated that already available high performance structural silicones are suitable for this type of double-bent IGU.

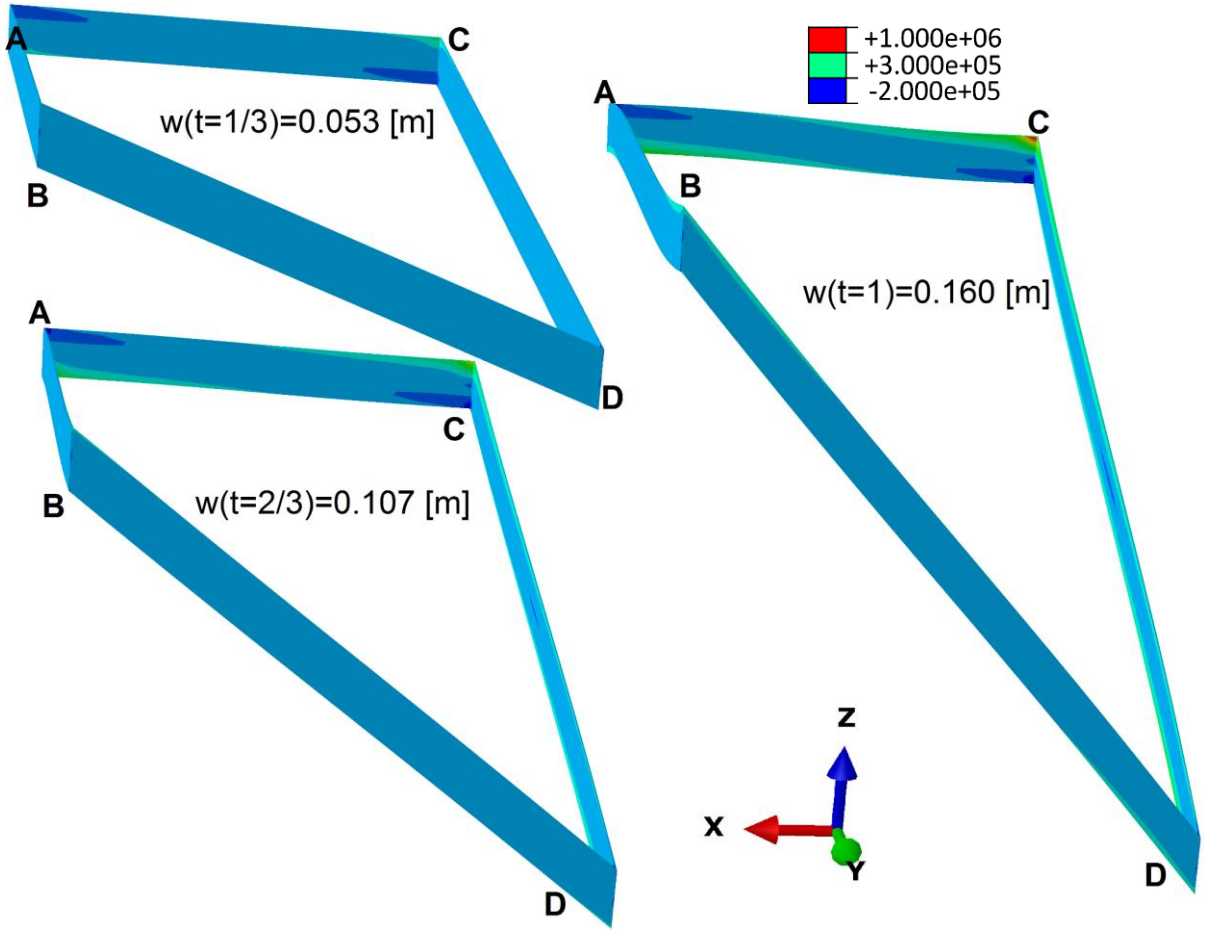

Figure 120: $\sigma_{max,pr}$ [N/m²] for the secondary seal at the time steps t=0, t=1/3, t=2/3 and t=1, double-bent support situation 1, z is upscaled 10 times

6.3.2.4 Required force for the cold bending process

In Figure 121, F is shown as a function of the enforced displacement. For the first half of the displacement, a total force of about $200\ [N]$ is required, which means that just $25\ [N]$ are required on average per centimeter for the first $8\ [cm]$. Because the curve is exponential, the IGU gets slightly stiffer with increasing deformation. For the last $8\ [cm]$, more than $43\ [N]$ are required on average per centimeter, which means that the IGU behaves more than 1.7 times stiffer. However, a total force of $547\ [N]$ means, that a group of trained workers can realize the cold bending process without machinery.

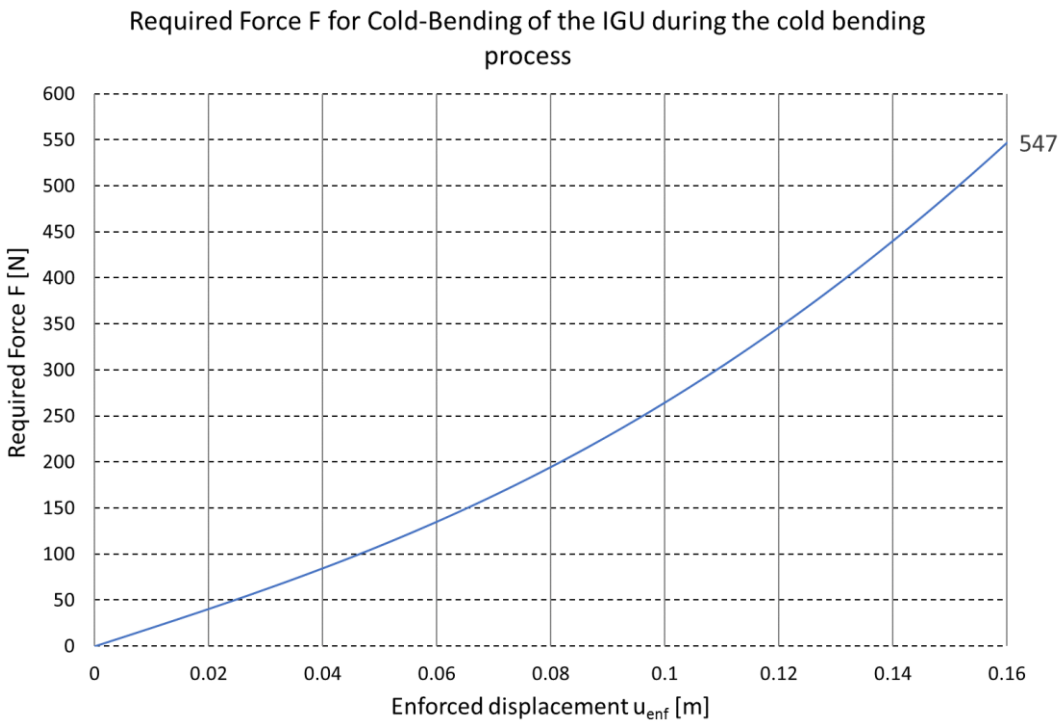

Figure 121: Reference model 1, double-bent, required force F for cold-bending of the IGU

6.3.2.5 Movement of the corners in the xy-plane

The movement of the corners B, C and D is shown in Figure 122. The movement of these corner points are examined at the same nodes where the BCs are applied. Each x-component and y-component is shown separately. In Figure 123, the movement of the corners B, C and D in the xy-plane is shown. As it is visible in Figure 122, corner B moves almost the same amount in x-direction as corner D.

Corner C moves almost the same amount in y-direction as corner D. Corner B in y-direction and corner C in x-direction almost do not move away from their origin. At $w\left(t = \frac{2}{3}\right) = 0.107\ [m]$, a turning point is visible in the curves after which the rate of movement increases over time. The movement of corner B and corner D in x-direction from over $2\ [cm]$ to almost $-10\ [cm]$ within the last third of the time step suggest a spring-back effect. Looking at Figure 123, the turnaround in the xy-movement curve for all 3 corners B, C and D is visible.

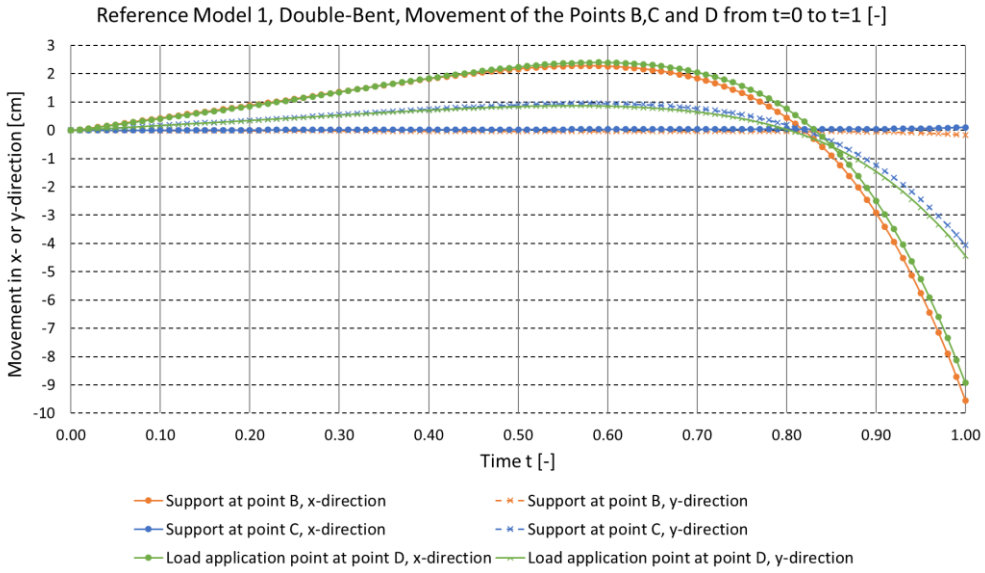

Figure 122: Reference model 1, double-bent, movement of the corners B, C and D from t=0 to t=1 [-]

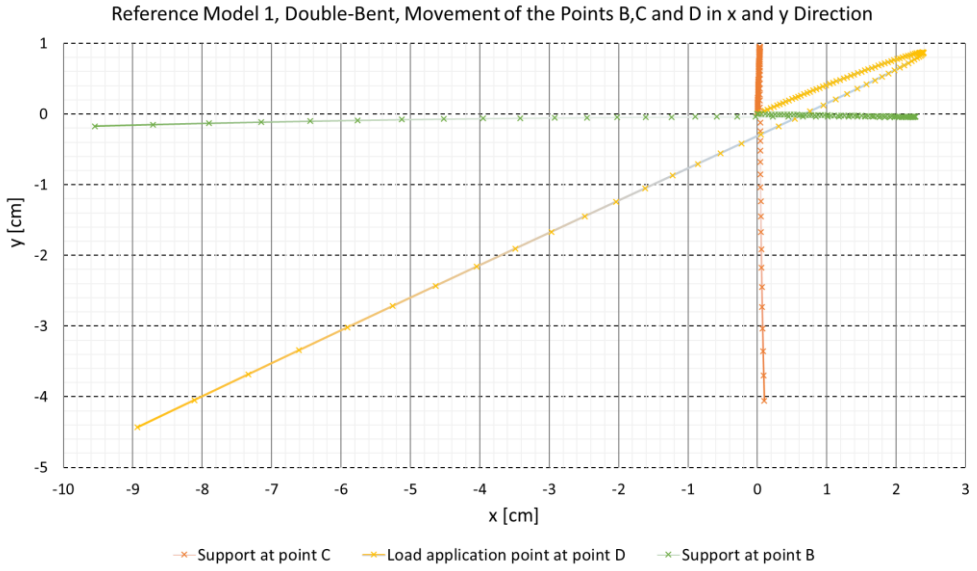

Figure 123: Reference model 1, double-bent, movement of the corners B, C and D in x- and y-direction

6.3.2.6 Distortion of the edge zone

In Figure 126 and in Figure 127, the difference from a straight line between the considered corner points and the current shape of the glass pane edge is depicted. Firstly, this gives an insight in the natural occurring double-bent shape and secondly, a substantial displacement deviation over time can be a hint for stability issues. This non-linear edge deformation is called Δu_3 whereas for the double-bent case, only the

vertical deformations are considered. Equation 6 shows how Δu_3 from a discrete set of deformation points is obtained. If $\Delta u_{3,i} < 0$, then the absolute deformation is smaller than the linear average, and if $\Delta u_{3,i} > 0$, then the absolute deformation is larger than the linear average.

Annotation to Equation 6: $\Delta u_{3,i}$ is obtained from a straight result path l and does not refer to the global coordinate system.

$$\Delta u_{3,i} = u_{3,1} + \frac{u_{3,n} - u_{3,1}}{l_n} * l_i - u_{3,i}\,, \qquad i = 1,2,\dots n \qquad \textit{Equation 6}$$

In Figure 124, which depicts Δu_3 between the corners C and D, and in Figure 125, which depicts Δu_3 between the corner B and D, an almost sinus-shaped curve is obtained and it's amplitude is increasing steadily and slightly exponential. This shows a stable deformation behavior which does not explain the drastic turnaround of point D over time in Figure 123.

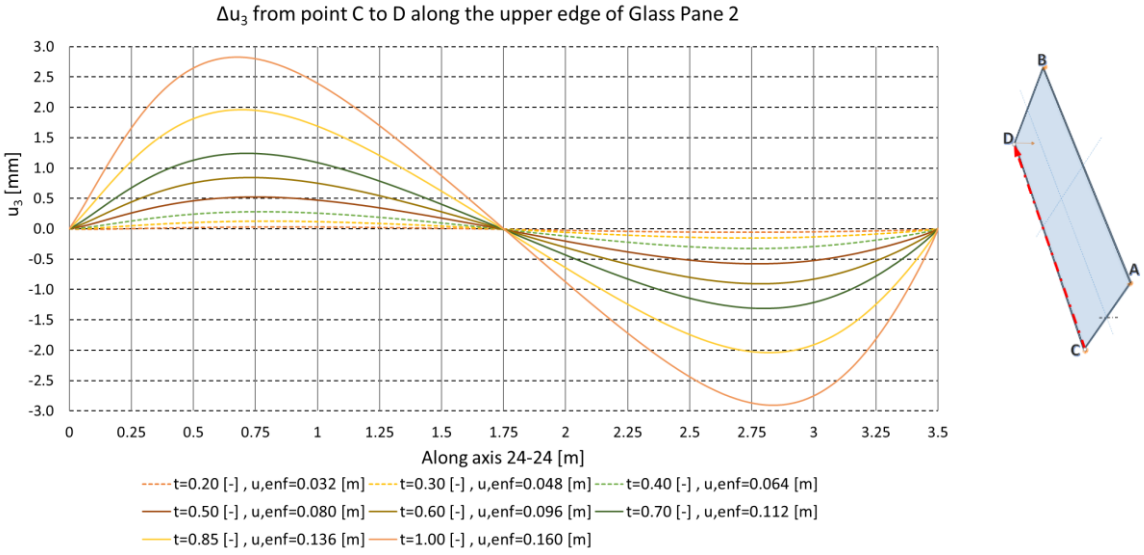

Figure 124: Reference model 1, double-bent, Δu_3 from corner C to D along the upper edge of glass pane 2

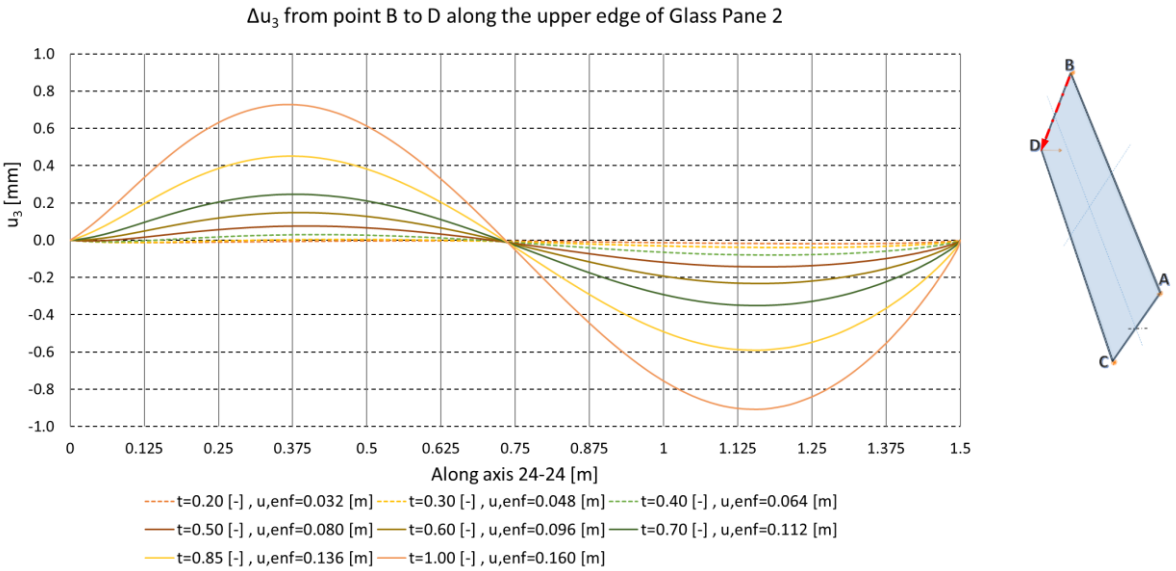

Figure 125: Reference model 1, double-bent, Δu₃ from corner B to D along the upper edge of glass pane 2

The rate of change in Δu_3, or rather its first derivative can measure the degree of warping in order to ensure optical quality of the IGU. Because from FEM calculations, a set of discrete notes is obtained, the first derivative can be approximated quite easily, which is shown in Equation 7.

Annotation to Equation 7: $\Delta u_{3,i}{}'$ is obtained *from a straight result path l and does not refer to the global coordinate system.*

$$\Delta u_{3,i}{}' = \frac{\partial \Delta u_{3,i}}{\partial l} = \frac{\Delta u_{3,i+1} - \Delta u_{3,i}}{l_{i+1} - l_i}, \qquad i = 1,2, \dots n-1 \qquad \textit{Equation 7}$$

Because the amplitude is the highest at $t = 1$, the global maximum of $\Delta u_{3,i}{}'$ will be obtained for the last time step. For example, the maximum value for $\Delta u_{3,i}{}'$ in Figure 124 is 0.94% and the minimum value for $\Delta u_{3,i}{}'$ is -0.35%. From laboratory testing or high-quality rendering, a sensible limit for $\Delta u_{3,i}{}'$ can be stipulated. However, it has to be taken into account, that this value comes only from the bending process itself and does not consider wind load, climate load and other deformation imposing effects.

In Figure 126, which depicts Δu_3 between the corners A and C, and in Figure 127, which depicts Δu_3 between the corners A and B, an atypical change of Δu_3 is visible at $t = 0.7$ which is due to stability issues. In Figure 126, the curves for Δu_3 can be described as a multiple of each other until $t = 0.7$. After that, the zero crossing shifts

significantly from about $0.15\,[m]$ to $0.375\,[m]$ and the amplitude increases significantly. At $t = 0.85$, the curve is almost parallel to the abscissa which is a sign for snap-through buckling. At $t = 1$, Δu_3 looks completely different from the previous curves which means not only, that buckling occurred, but also that the structural system of the IGU behaves different. In Figure 127, the onset of stability failure at $t = 0.70$ can be seen clearly. At $t = 0.85$, snap-through buckling can be observed like in Figure 126.

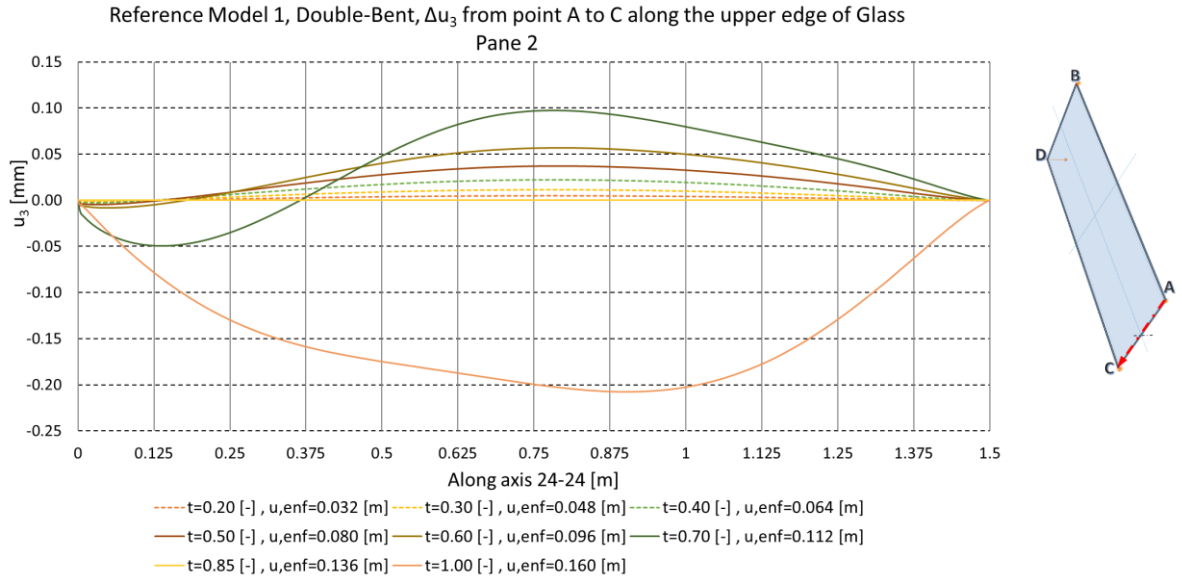

Figure 126: Reference model 1, double-bent, Δu_3 from corner A to C along the upper edge of glass pane 2

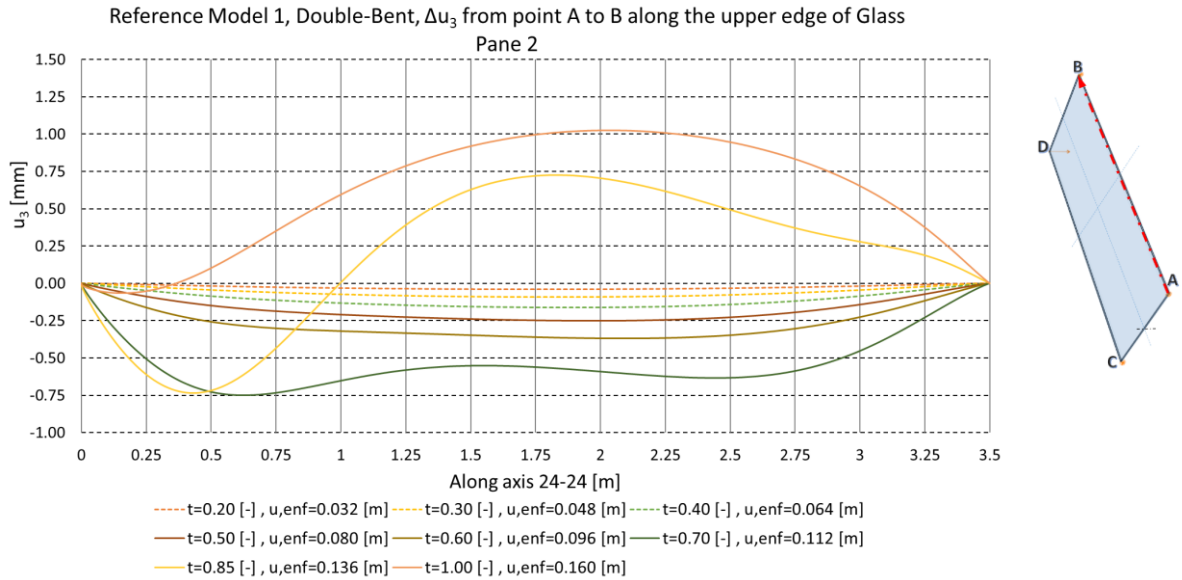

Figure 127: Reference model 1, double-bent, Δu_3 from corner A to B along the upper edge of glass pane 2

6.3.2.7 Glass pane

In this paragraph, $\sigma_{max,pr}$ and the vertical deformations u_3 in the glass are examined. Because the deformation and the stress in glass pane 2 and glass pane 1 is almost the same, the axes 22-22 and 24-24 are not described. In Figure 128, $\sigma_{max,pr}$ along axis 21-21 is depicted. The stress curve has two stress amplitudes which are about $0.2\ [m]$ away from the corner whereby the stress amplitudes seem to increase disproportionately compared to the stress in the center region. From $t > 0.5$ to $t = 1$, the stress in the center region stays constant. Looking at the corresponding u_3 in Figure 129, the maximum value of u_3 at $t = 0.5$ is $-32\ [mm]$ and at $t = 1$ is $40\ [mm]$. From this observations, it can be seen that for $t > 0.5$ the deformation is still increasing but not the stress. This is owed due to the small resilience of the IGU system which is in accordance with the disproportionate movement of the corner B and the corner C after $t > \frac{2}{3}$.

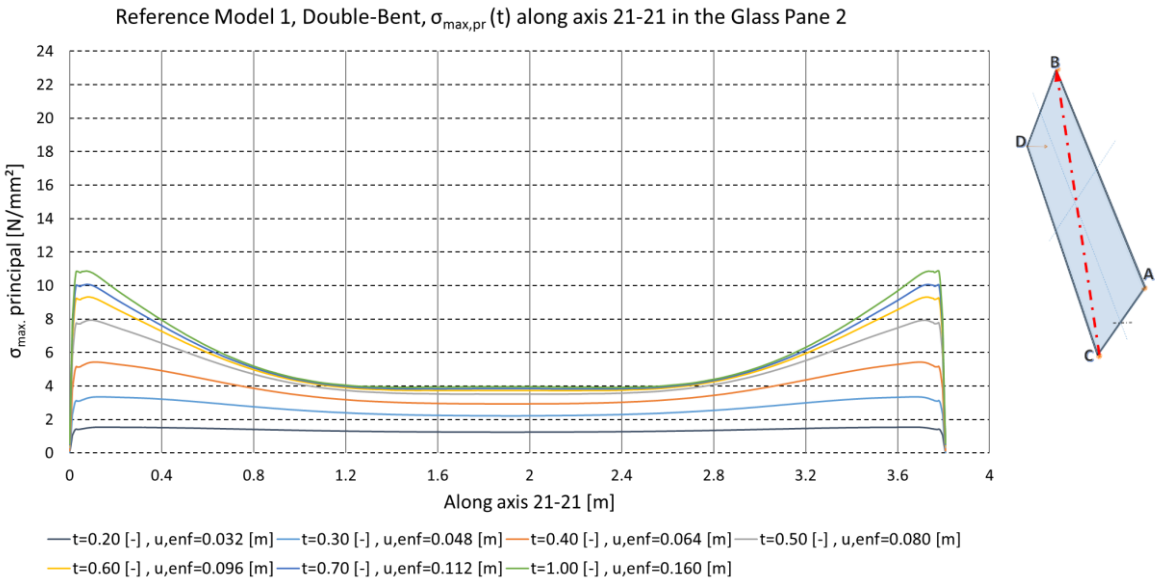

Figure 128: Reference model 1, double-bent, σmax,pr (t) along axis 21-21 in the glass pane 2

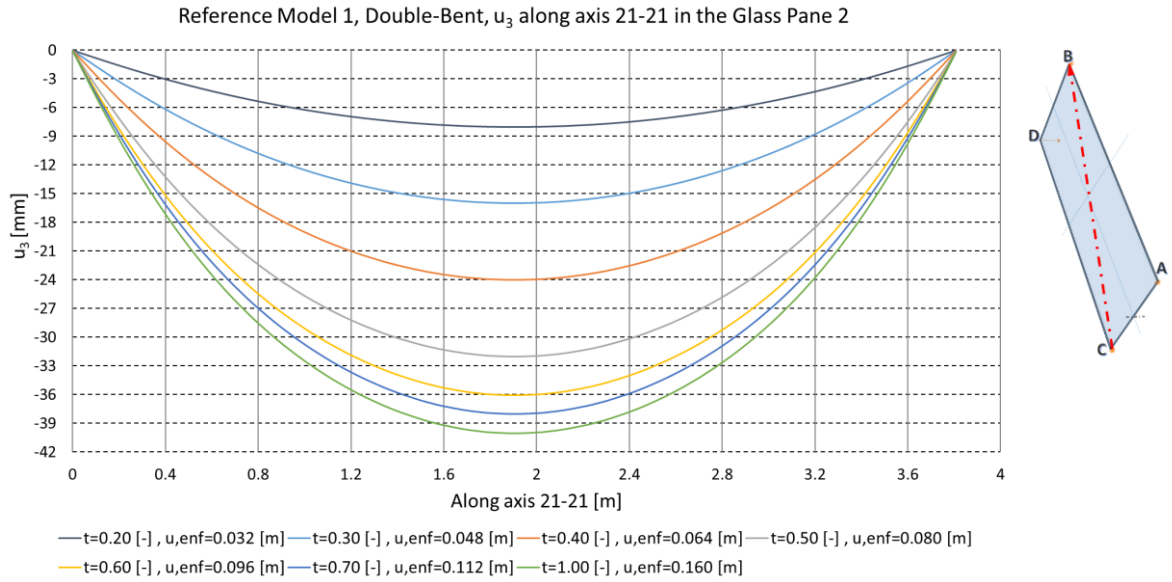

Figure 129: Reference model 1, double-bent, u_3 (t) along axis 21-21 in the glass pane 2

In Figure 130, $\sigma_{max,pr}$ along axis 23-23 is depicted. Like for axis 21-21, $\sigma_{max,pr}$ does not increase in the center region for $t > 0.5$. At $t = 0.2$, the stress is almost constant along the whole axis and increases near the corner region slightly at $t = 0.4$. The stress curve gets highly nonlinear with an increased $\sigma_{max,pr}$ near the corner regions at $t = 0.5$. For glass pane 2, $\sigma_{max,pr}$ is significant at axis 23-23 next to the support, however singularities occur next to the support region.

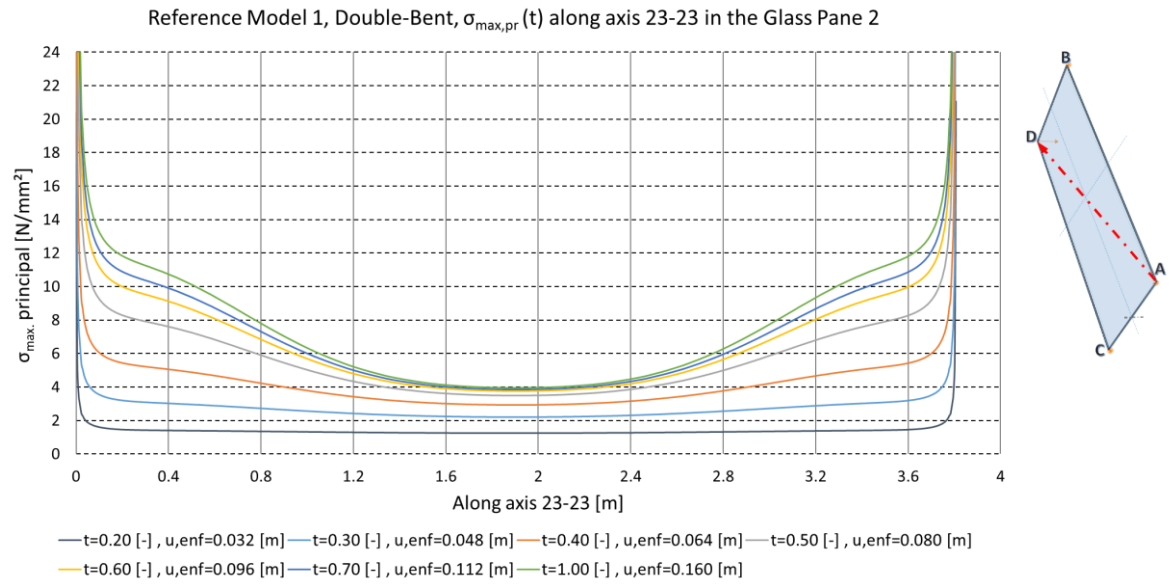

Figure 130: Reference model 1, double-bent, $\sigma_{max,pr}$ (t) along axis 23-23 in the glass pane 2

6.3.2.8 Spacer bar

In Figure 131, σ_e in the longitudinal spacer in axis 25-25 is depicted. Looking just at $t = 0.2$, $t = 0.4$, $t = 0.8$ and $t = 1$, it can be seen, that the stress curves show the same characteristics. This means, that the mechanism of load transfer of the longitudinal spacer does not change during the bending process even though this is not true for the glass panes. This is, because the spacer does not undergo buckling like the glass panes and therefore just elongates according to the imposed displacement and transfers compression forces between the glass panes. Furthermore, the stress in the center region is remarkably lower than in the corner region, resulting mainly from elongation of the spacer. Stress peaks occur at both ends of the axis whereas the spacer just yields at $t = 1$ at the front tip next to corner D which means, that the degree of utilization is low at any time step. Therefore, it can be said that the spacer is not a decisive structural component in the IGU system.

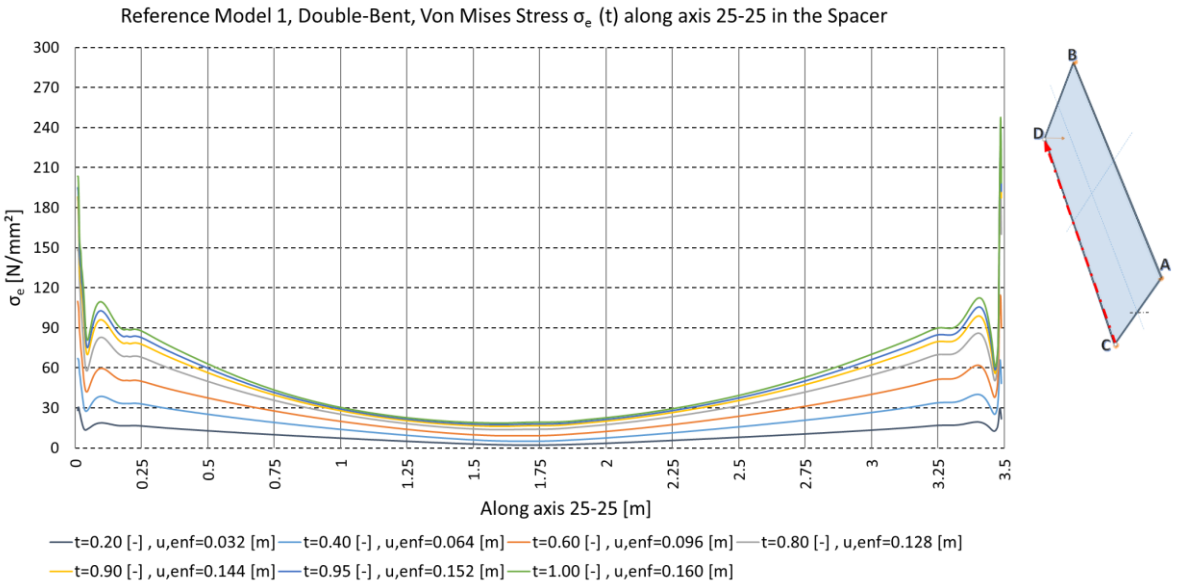

Figure 131: Reference model 1, double-bent, von Mises stress σ_e (t) along axis 25-25 in the spacer

In Figure 132, different stress components are depicted for axis 25-25 in order to show the contribution to σ_e. A dominating proportion of σ_e is owed to σ_x at advanced time steps which means that for a large deformation, the spacer has to withstand a bending moment around the z-axis. Furthermore, σ_y stays almost constant along the axis 25-25 which comes from elongation of the spacer bar. Stress component σ_{xy}, which equals the shear stress τ_{xy}, has the lowest contribution to σ_e. In addition, it has

negative values which means, that the degree of confinement in the center region is low, and that glass pane 2 is pressing onto the spacer. Next to the corner region, τ_{xy} is increased significantly which is due to a very high degree of confinement which is owed to the rigid connection between both spacers.

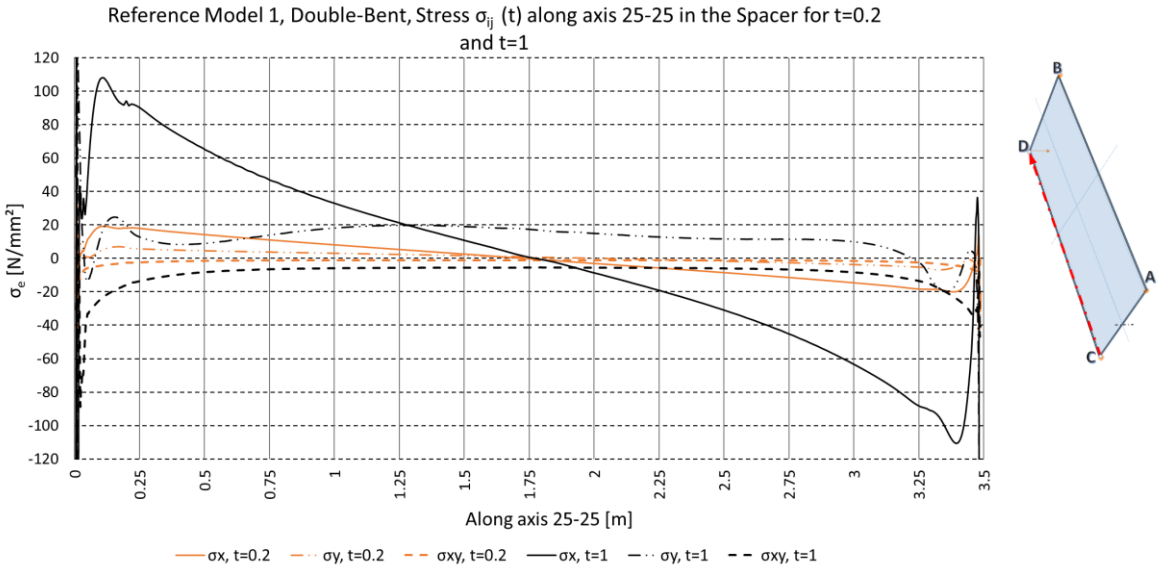

Figure 132: Reference model 1, double-bent, stress σij (t) along axis 25-25 in the spacer for t=0.2 and t=1 [-]

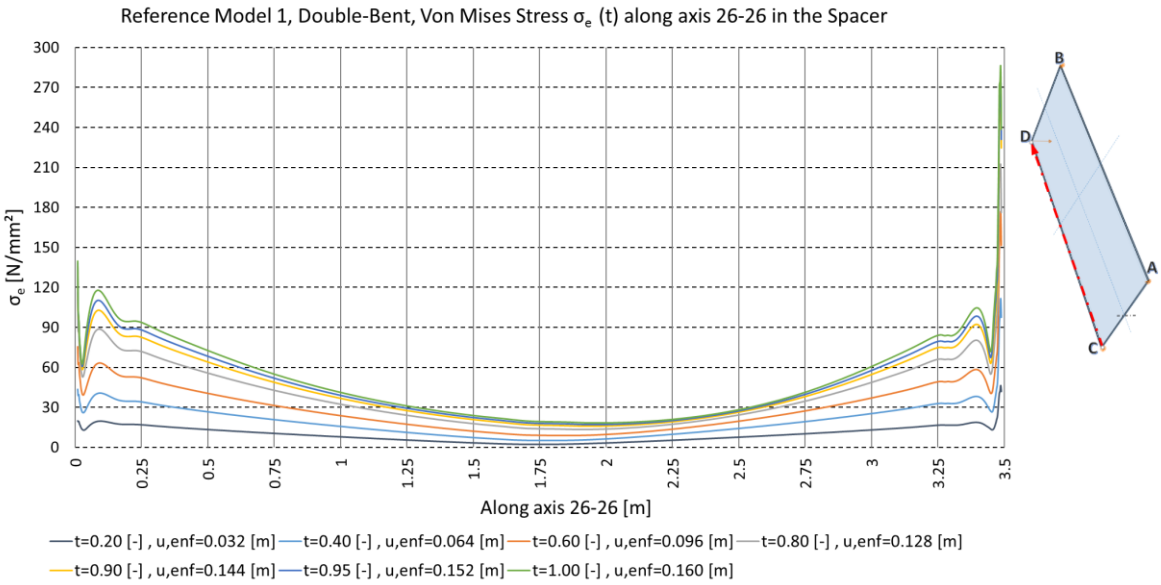

Figure 133: Reference model 1, double-bent, von Mises stress σ_e (t) along axis 26-26 in the spacer

In Figure 133, σ_e is shown for the broadside spacer along axis 26-26. All stress curves are showing the same characteristics like in axis 25-25. Compared to axis 25-25, σ_e is

slightly increased at the back tip next to corner C but is slightly decreased at the front tip next to corner D.

In Figure 134 and in Figure 135, the von Mises stresses σ_e in the broadside spacer along axis 27-27 and along axis 28-28 are shown. A stress peak occurs at the back tip next to corner B of axis 27-27 which comes from the redirection of the vertical forces into the support. Another stress peak occurs at the front tip next to corner D for axis 28-28 because of the imposed deformation. About $0.1\ [m]$ away from the tips of both axes, another stress peak is present, which is similar to the case of the longitudinal spacers, but more pronounced. This comes from the overlapping of a high stress value of σ_y and τ_{xy}. Stress component σ_y exhibits similar characteristics in the broadside spacer like σ_x in the longitudinal spacer. The global minimum for σ_e for axis 27-27 is located before $0.75\ [m]$. For axis 28-28, the global minimum is located after $0.75\ [m]$, which comes from a different bending radius for the upper glass pane and for the lower glass pane. The very same observation can be made for the longitudinal spacer.

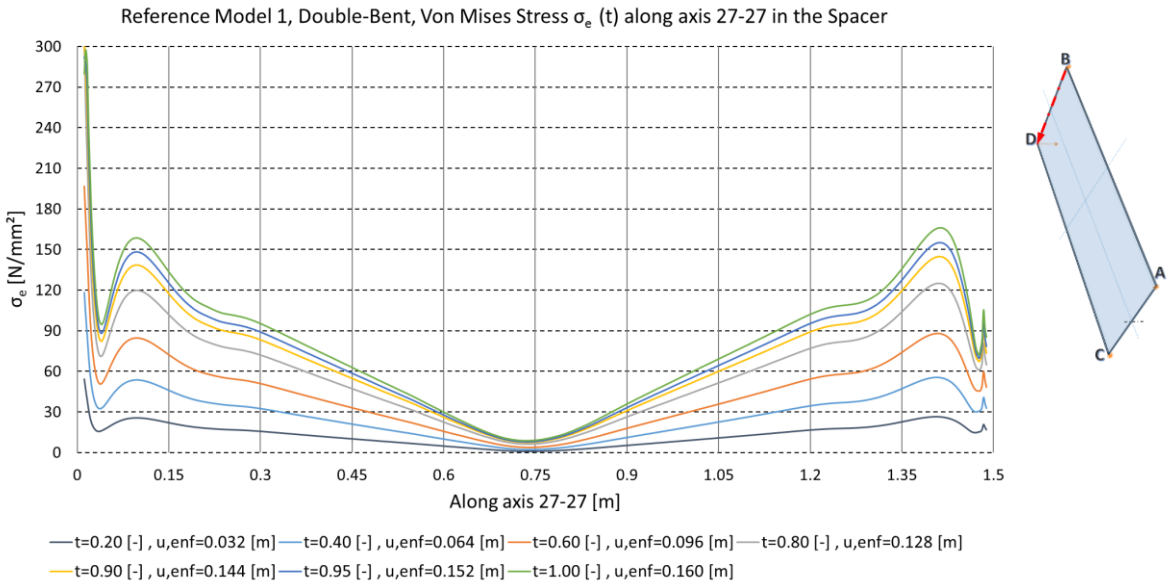

Figure 134: Reference model 1, double-bent, von Mises stress σe (t) along axis 27-27 in the spacer

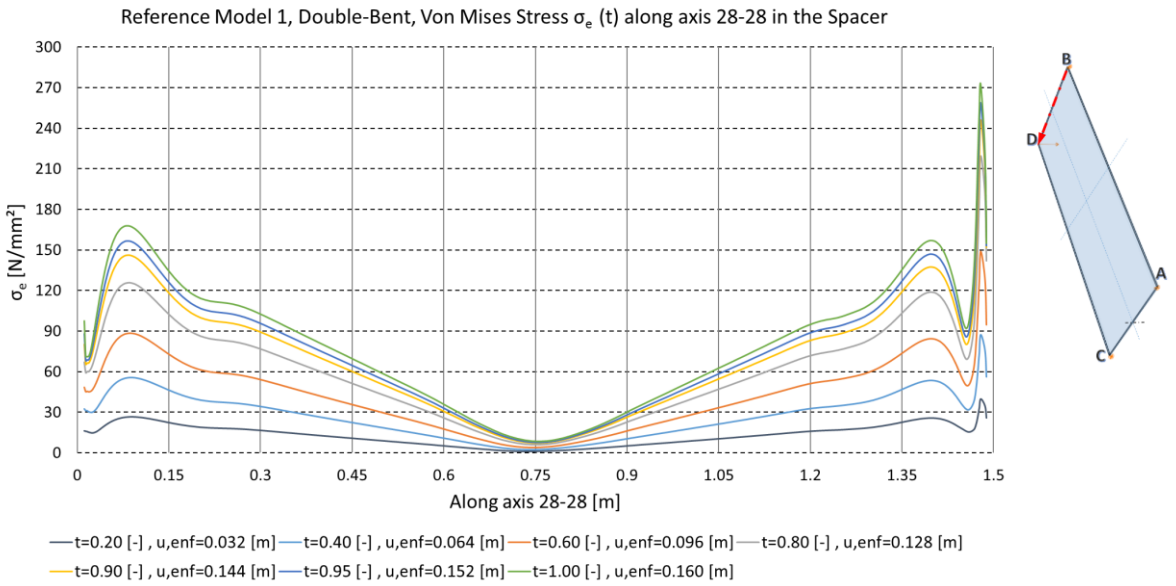

Figure 135: Reference model 1, double-bent, von Mises stress σ_e (t) along axis 28-28 in the spacer

6.3.2.9 Deformation of the edge zone

For the deformation of the secondary seal in the edge zone of the IGU, it seems to be sensible to depict the x-component $u_1(t)$ and the y-component $u_2(t)$ separately. This provides a deeper insight into the deformation behavior. As a simplification, the z-component does not get examined because it is small in comparison $u_3(t) \ll u_1(t) \wedge u_2(t)$.

In Figure 136, axis S21-S21 is depicted, which is located at the outer corner at point D. In Figure 137, axis S22-S22 is depicted, which is shifted parallel from axis 21-21 $5\ [cm]$ inwards at the longitudinal side. S23-S23, which is depicted in Figure 138, is shifted parallel from axis 21-21 $10\ [cm]$ inwards and lies next to axis S22-S22. These three axes are considered as one unit in the subsequent explanation in order to understand the edge-zone distortion at point D comprehensively.

All deformation curves of all three axes S21-S21, S22-S22 and S23-S23, have negative values in the x-direction $u_1(t) \leq 0\ [mm]$. In addition, all curves in axis S22-S22 and axis S23-S23 have positive values $u_2(t) > 0\ [mm]$. Looking at the global coordinate system, this means, that glass pane 2 slips relative to glass pane 1 along axis 23-23. Looking at the amplitudes of different time steps for all three axes, it can be observed that the amplitudes for u_1 and u_2 are almost the same. In addition, the

deformation in x-direction is about a fivefold of the deformation in y-direction. The deformation shape is always highly non-linear which indicates a complex interaction of non-linear geometry and influences from the deformation of the adjacent spacer and glass panes. Looking at all three graphs at u_1, these curves are similar and do not change their characteristic over time. Because the secondary seal is tied to both glass panes, the relative movement in u_1-direction as well as in all other directions at $z = 0\ [mm]$ and $z = 16\ [mm]$ is equal to the movement of the glass panes as well. Looking at all three graphs at u_2, the distortion of the secondary seal has a local minimum at $z = 13\ [mm]$ and a global maximum at $z = 8\ [mm]$ whereas both are turning points as well. Just looking at the deformation curves from $0 \leq z \leq 8\ [mm]$ and from $13 \leq z \leq 16\ [mm]$, the deformation can be explained from the relative slip of glass pane 2 to glass pane 1 whereby elongation from the glass panes play a subordinate role. However, the deformation curve from $8 \leq z \leq 13\ [mm]$ shows in the opposite direction, which can be explained because the silicone is tied to the spacer as well.

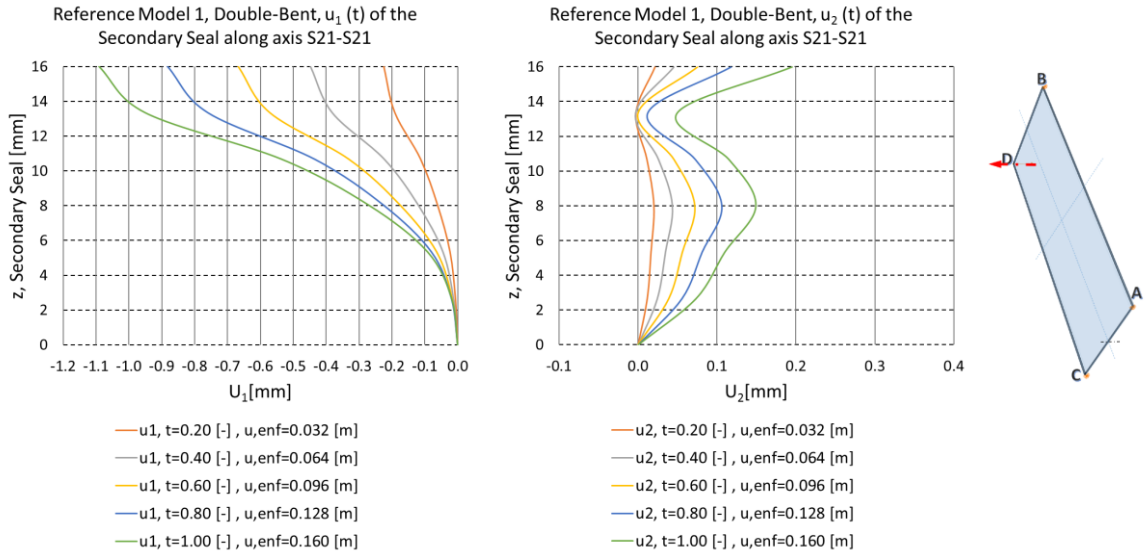

Figure 136: Reference model 1, double-bent, max. displacement (t) of the secondary seal along axis S21-S21

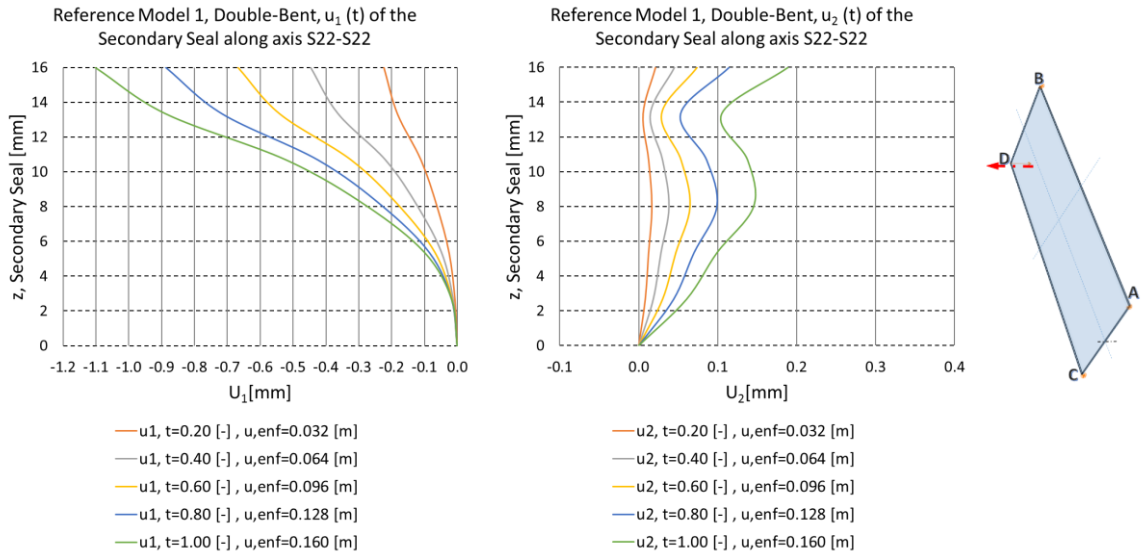

Figure 137: Reference model 1, double-bent, max. displacement (t) of the secondary seal along axis S22-S22

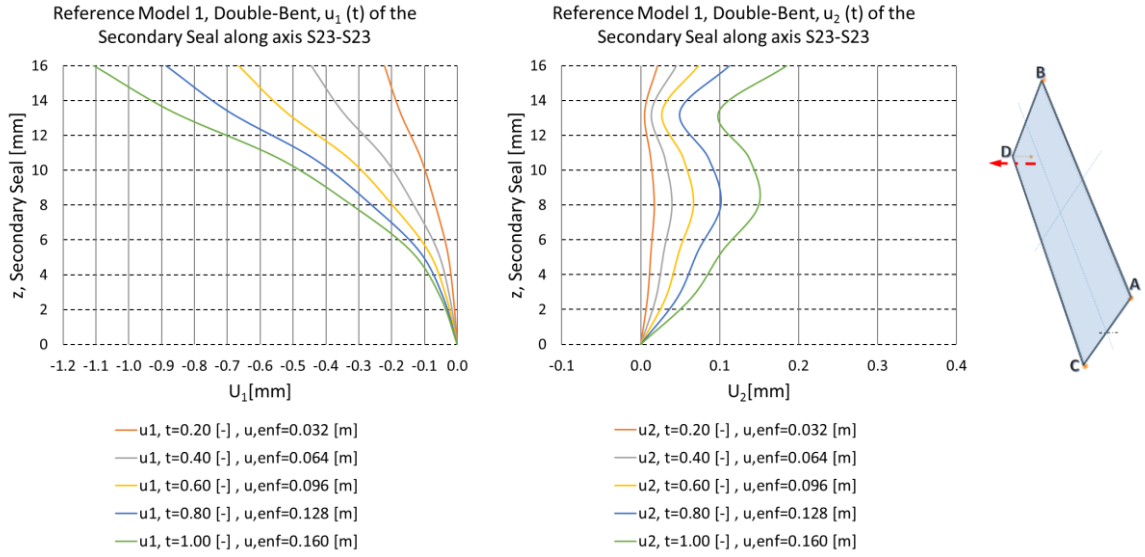

Figure 138: Reference model 1, double-bent, max. displacement (t) of the secondary seal along axis S23-S23

In Figure 139, axis S24- S24 is depicted, which is shifted parallel from axis 21-21 $5\ [cm]$ inwards at the broadside. S25- S25, which is depicted in Figure 140, is shifted parallel from axis S21- S21 $10\ [cm]$ inwards and lies next to axis S24- S24. Firstly, all three axes are considered as one unit in the subsequent explanation in order to understand the edge-zone distortion at point D comprehensively. Secondly, the axes S22-S22 and S23-S23 are also considered for the explanation at corner D. These two axes were explained on the previous pages.

Axis S24-S24, which is depicted in Figure 139 shows very similar deformation curves like the axes S21-S21, S22-S22 and S23-S23 at the longitudinal side. Axis S25-S25, which is depicted in Figure 140 has smaller values for u_2 but not for u_1 compared to axis S24-S24. For both deformation components u_1 and u_2 for axis S24-S24 and for axis S25-S25, the characteristics of the curves and values of the amplitudes are almost the same (in a range of $\pm 0.1\ [mm]$). For axis S24-24 and S25-S25, the amplitudes of u_1 at $t = 1$ are $1.1\ [mm]$ and at $t = 0.6$, they are about $0.7\ [mm]$. For axis S24-S24, the amplitude for u_2 at $t = 1$ is $0.15\ [mm]$ and for axis S24-24, it is $0.1\ [mm]$.

It is striking how all 5 axes in the vicinity of corner point D are exhibiting the same characteristics in the u_1-direction and also in the u_2-direction.

From this it can be deduced that the deformation in x-direction in the vicinity of corner D is bigger than the deformation in y-direction at any time step. This means that the deformation is affected mainly globally whereas local deformation plays a subordinate role.

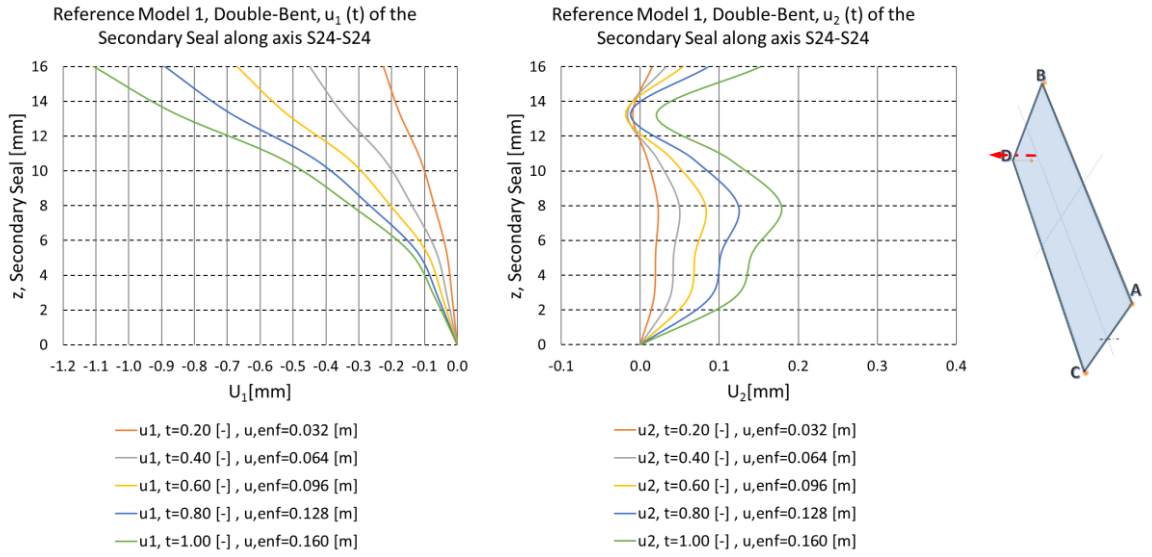

Figure 139: Reference model 1, double-bent, max. displacement (t) of the secondary seal along axis S24-S24

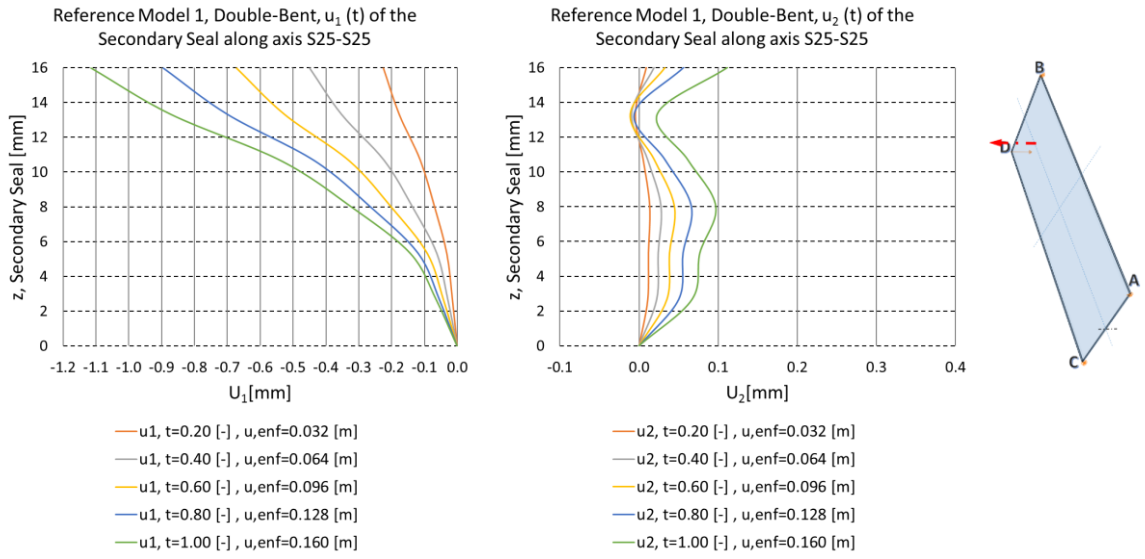

Figure 140: Reference model 1, double-bent, max. displacement (t) of the secondary seal along axis S25-S25

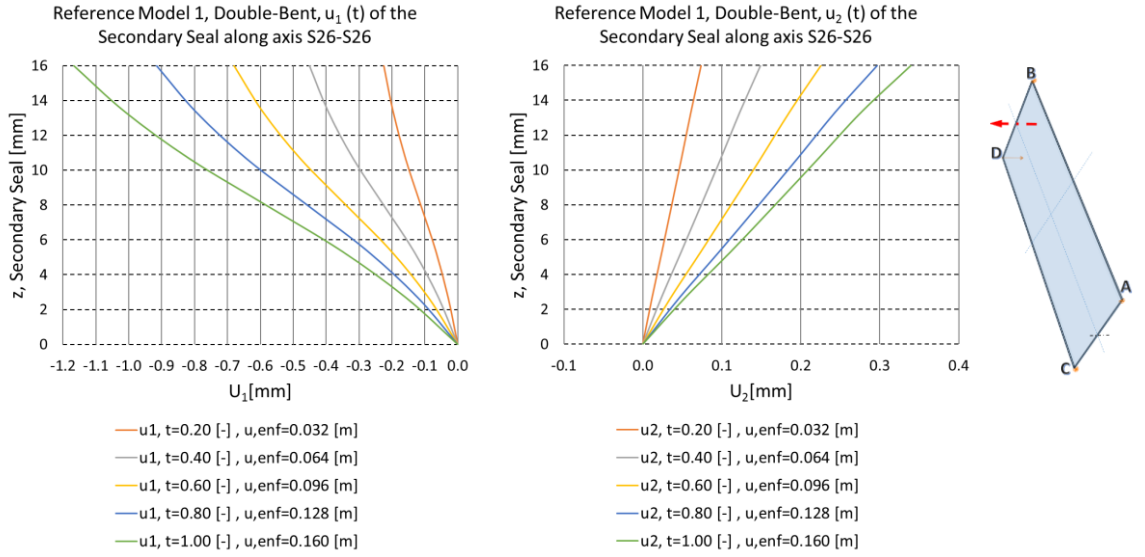

Figure 141: Reference model 1, double-bent, max. displacement (t) of the secondary seal along axis S26-S26

In Figure 142, axis S27-S27 is depicted, which is located between the corner points A and B at $\frac{l_{gp}}{2} = 1.75\ [m]$. Conspicuous are the linear deformation curves during all time steps for u_1. The amplitudes are lower than at corner point D, for $t = 1$, the maximum amplitude is $-0.9\ [mm]$ in contrast to $-1.1\ [mm]$ at corner D. In contrast to corner D, the amplitude of u_2 is four times higher for all time steps and peaks at $t = 1$ with $0.8\ [mm]$.

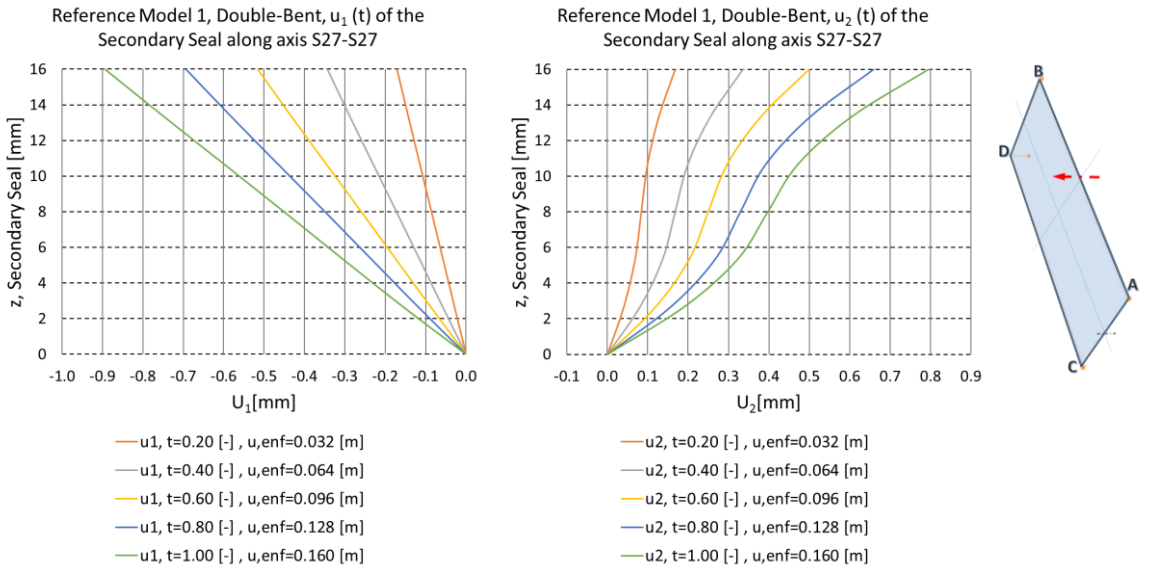

Figure 142: Reference model 1, double-bent, max. displacement (t) of the secondary seal along axis S27-S27

In Figure 143, axis S28-S28 is depicted, which is located between the corners A and C at $\frac{w_{gp}}{2} = 0.75\ [m]$. Interestingly, u_1 shows similar characteristics like u_2 in axis S27-27, and u_2 shows similar characteristics like u_1 in axis S27-S27. However, the amplitudes are smaller, at $t = 1$, $u_1 = -0.6\ [mm]$ and $u_2 = 0.35\ [mm]$. Axis S27-S27 lies at the longitudinal side. Axis S28- S28 lies at the broadside. Both axes are exhibiting they very same behavior over time. The linear characteristic is due to the slip of glass pane 2 in direction of axis 23-23 towards corner D which also happens partly to the spacer which subsequently enables a free deformation in x-direction. However, the slip along the diagonal axis 23-23 also has a component in y-direction, and because the spacer is tied to the secondary seal, the linear deformation from the glass panes is hindered which was also explained for the previous axes S21-S21 to S25-S25 and also is happening for the single-bent model which is explained in detail in subchapter 6.1.2.

In Figure 144, axis S29-S29 is depicted. Axis S29-S29 is located between the corners C and D at $\frac{l_{gp}}{2} = 1.75\ [m]$. The amplitudes for u_1 have the same values in axis S27-S27 which means, that the deformation happens unobstructed over the broadside of the center region. The deformation of u_2 is highly non-linear but has a small amplitude, which is only $0.1\ [mm]$ at $t = 1$.

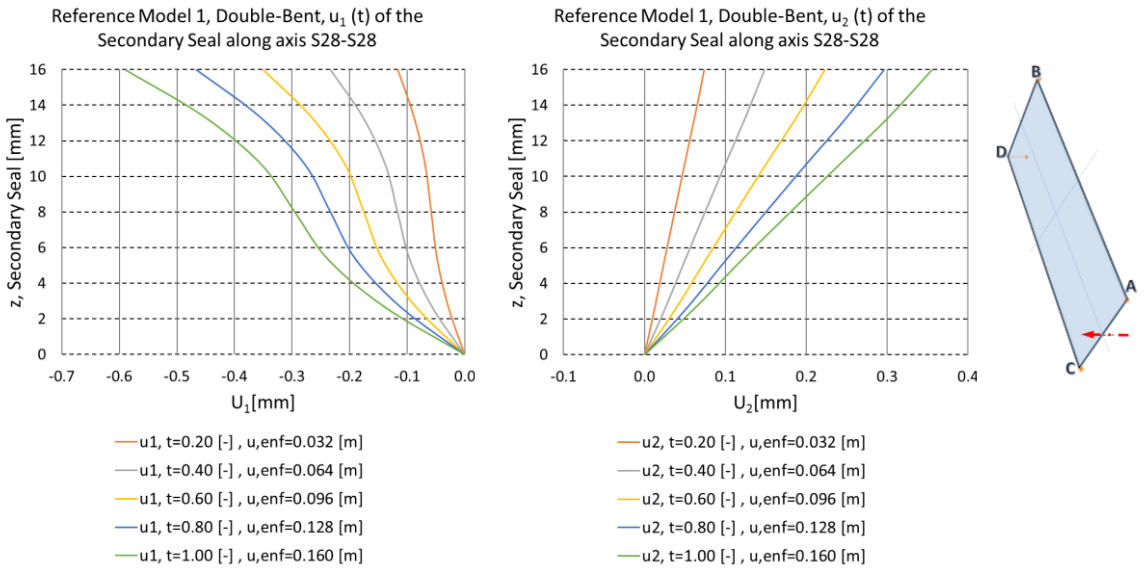

Figure 143: Reference model 1, double-bent, max. displacement (t) of the secondary seal along axis S28-S28

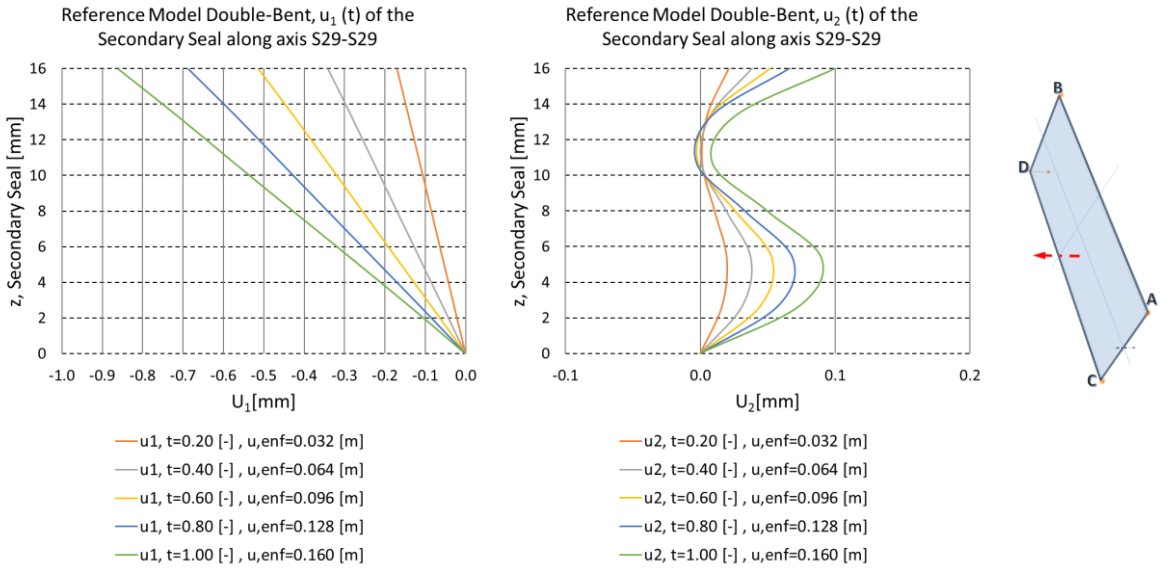

Figure 144: Reference model 1, double-bent, max. displacement (t) of the secondary seal along axis S29-S29

6.3.3 Double-bent IGU, support situation 2

For the double-bent reference model which is described in 0, the influence of the BCs is investigated for different reference models. In this subchapter, support situation 2 is subject to investigations. An overview of the BCs is provided in Figure 145. The BCs are depicted in Figure 146 for the corners A and D. In Figure 147, the BCs are depicted

for the corners B and C. In the subsequent part of this subchapter, the results from this reference model are presented.

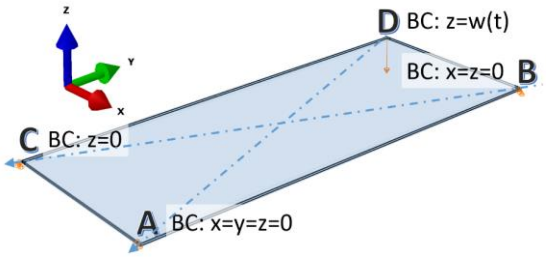

Figure 145: Schematic overview of boundary conditions for support situation 2

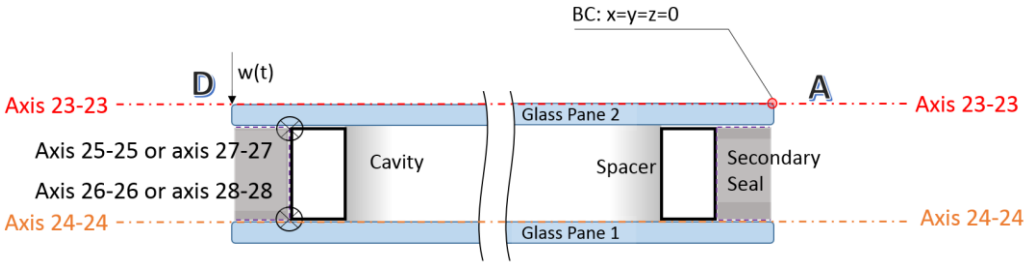

Figure 146: Schematic longitudinal section of the double-bent IGU along the diagonal 23-23, support situation 2

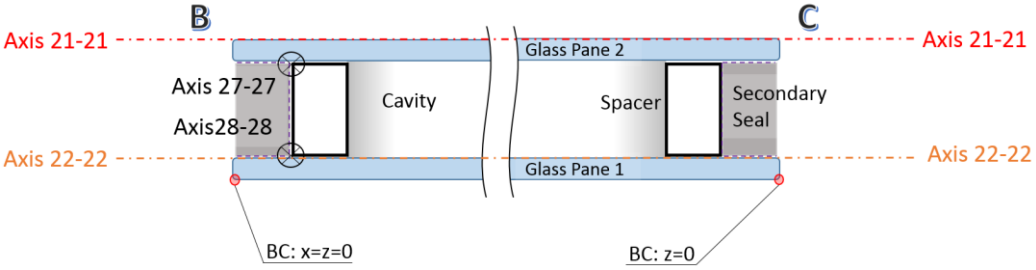

Figure 147: Schematic longitudinal section of the double-bent IGU along the diagonal 21-21, support situation 2

6.3.3.1 Required force for the cold bending process

In Figure 148, F is shown as a function of the enforced displacement. Because the support situation 2 sustains a more stable mechanical behavior than support situation 1, it gets deformed $0.277\ [m]$ for $t = 1$ instead of $0.16\ [m]$.

At $0.243\ [m]$ or rather at $t = 0.88$, where F has a value of $1112\ [N]$, a kink in the curve occurs. From $t = 0.88$ until $t = 1$, F increases linearly and finally reaches a value of $1290\ [N]$. The full time step from $t = 0$ to $t = 1$ is examined on the subsequent pages.

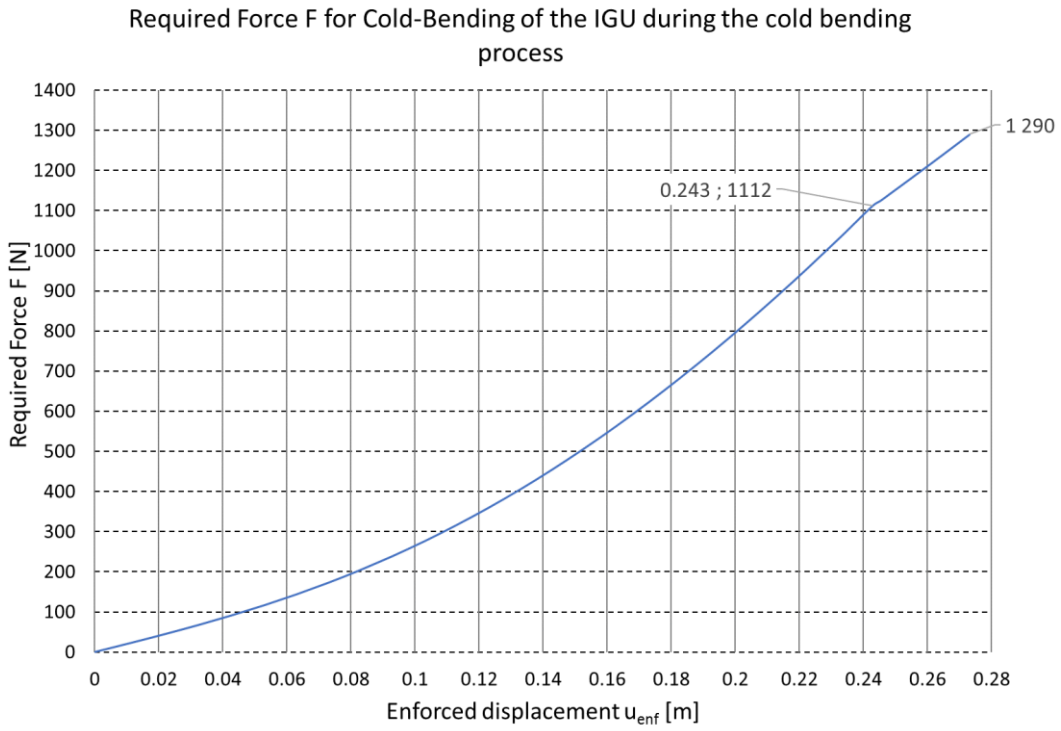

Figure 148: Reference model 2, double-bent, required force F for cold-bending of the IGU

6.3.3.2 Movement of the corners in the xy-plane

In Figure 149 and in Figure 150, the movement of the support points at corner B and corner C and the deformation point at corner D is shown with respect to time and to the global coordinate system. In Figure 149, the movement along the x-direction and the y-direction is shown separately. The deformation values in x-direction of corner D are more than three times higher than in y-direction but the maximum value stays below $2\ [cm]$ which makes it suitable for practical applications. Looking at the support points at corner B and corner C, it can be seen that the maximum values are staying well below $3\ [mm]$ at any time. Because the y-direction is not locked for the support at the corners B and C, the y-components are always higher than the x-component.

In Figure 150, the movement of all three corners is depicted in the xy-plane and shows that the movement of the corners is monotonous increasing in contrast to the support situation 1.

On the one hand, the maximum movement prevents the occurrence of significant residual stress and on the other hand, the maximum movement makes practical applications feasible which is advantageous in comparison to support situation 1.

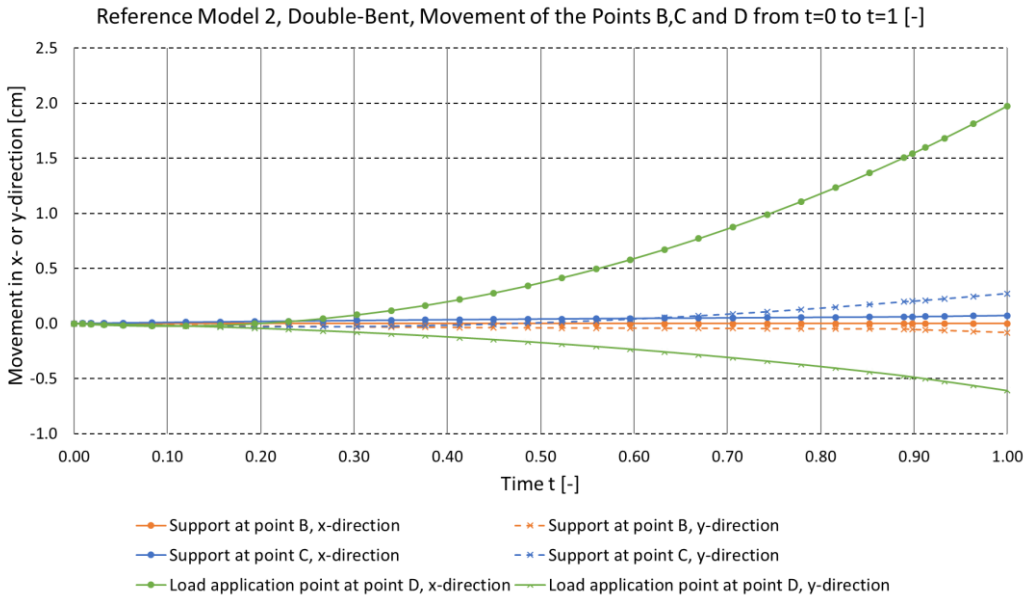

Figure 149: Reference model 2, double-bent, movement of the corners B, C and D from t=0 to t=1 [-]

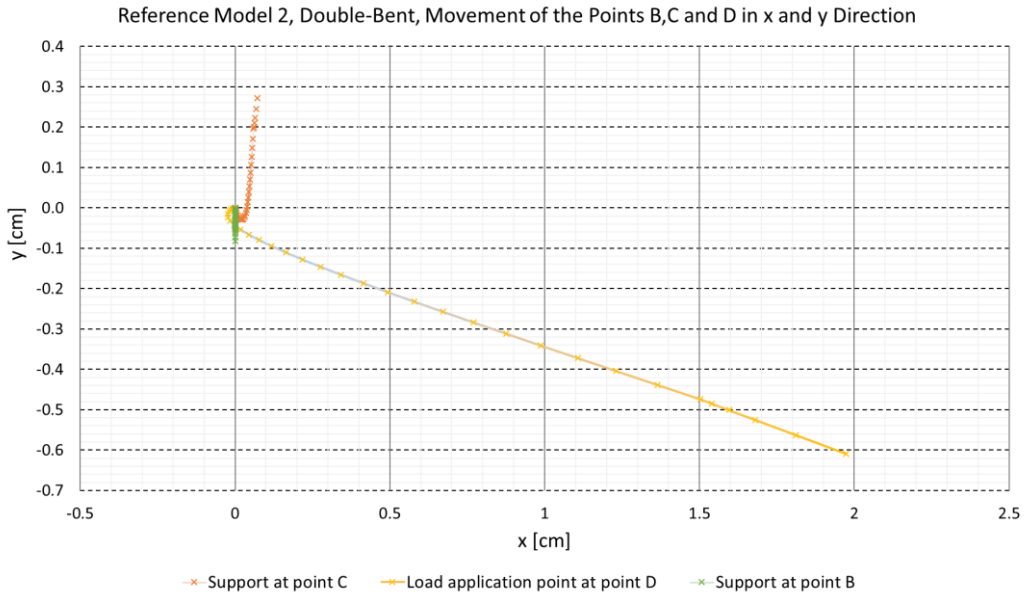

Figure 150: Reference model 2, double-bent, movement of the corners B, C and D in x- and y-direction

6.3.3.3 Distortion of the edge zone

In Figure 151 and in Figure 152, Δu_3, which is the difference from a straight line between the considered corner points and the real shape of the glass pane edge, is depicted. A more detailed explanation can be found in subchapter 6.3.2.6 for support situation 1. For $t < 0.89$ in Figure 151, Δu_3 has a zero crossing at $1.75\ [m]$ which is

exactly $\frac{l_{gp}}{2}$ and the amplitudes have almost the same values. For example, for $w(t = 0.7) = 0.194\ [m]$, the amplitudes are $4.0\ [mm]$ and $-4.1\ [mm]$. For $w(t = 0.89) = 0.247\ [m]$, the amplitudes are peaking in at $5.0\ [mm]$ and at $-5.1\ [mm]$, but more importantly, the curve is changing it's characteristic. Until $t < 0.89$, two turning points are present, one between $0.55\ [m]$ and $0.75\ [m]$ and the other one between $2.75\ [m]$ and $2.95\ [m]$, depending on the time step. But at $w(t = 0.89) = 0.247\ [m]$, two more turning points start to emerge at $1.25\ [m]$ and at $2.25\ [m]$. This means, that a critical value of imposed deformation is reached. At $w(t = 1) = 0.277\ [m]$, the curve unveils a distinct deformation shape of the IGU.

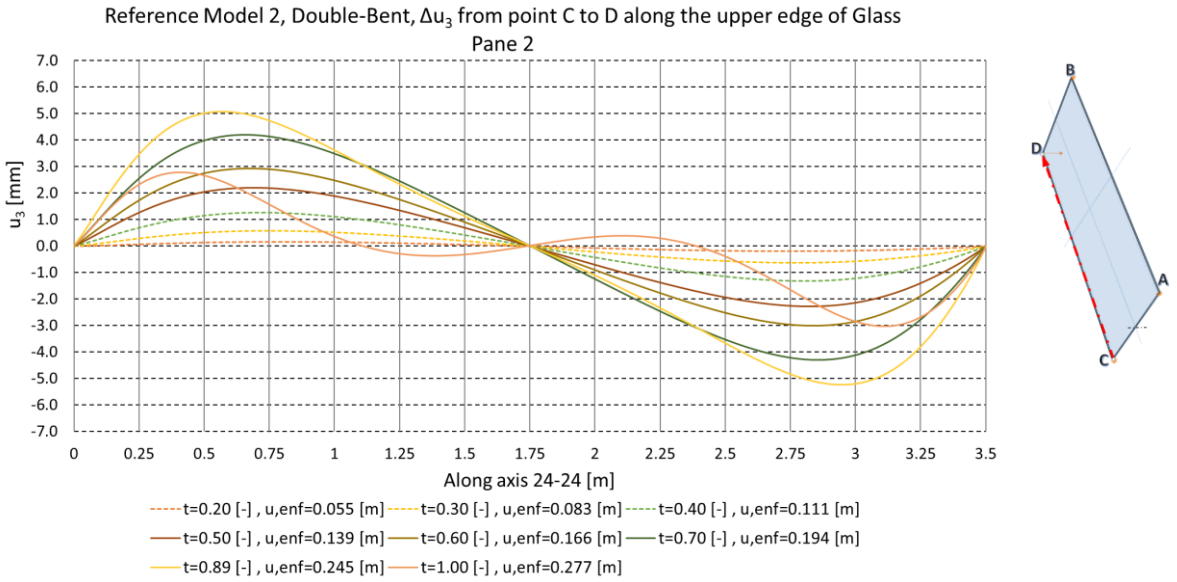

Figure 151: Reference model 2, double-bent, Δu_3 from corner C to D along the upper edge of glass pane 2

Looking at the broadside edge in Figure 152, no change in the characteristics of Δu_3 over time can be seen, but a stark increase of the maximum amplitude from $1.3\ [mm]$ at $t = 0.7$ to $5.6\ [mm]$ at $w(t = 1) = 0.277\ [m]$ is observed.

However, the zero crossing is shifting from $\frac{w_{gp}}{2}$ towards the deformation point at corner D which correlates with the significant growth of Δu_3. The maximum and minimum values of the first derivative of Δu_3, which is $\Delta u_{3,i}{}'$, are 0.92% and -0.52% at $t = 0.7$. At $w(t = 1) = 0.277\ [m]$, the maximum value increases to 1.85% and the minimum value decreases to -1.19%.

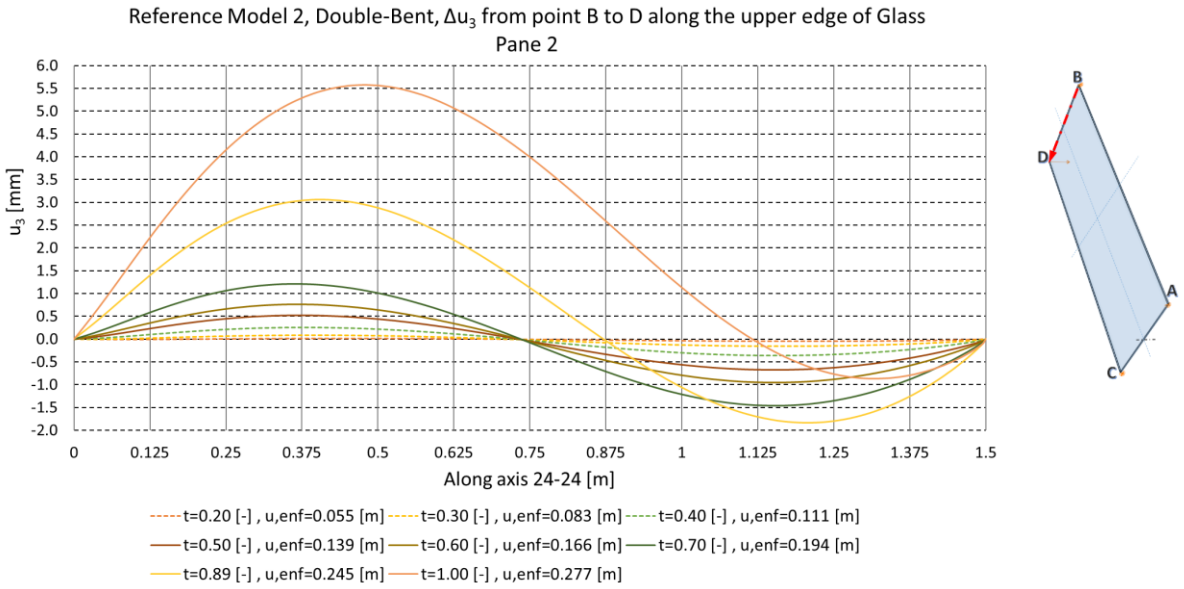

Figure 152: Reference model 2, double-bent, Δu₃ from corner B to D along the upper edge of glass pane 2

6.3.3.4 Glass pane

In the following paragraph, $\sigma_{max,pr}$ and u_3 in the glass are examined. Like for support situation 1, these values in glass pane 1 and glass pane 2 differ insignificantly, hence just the results for glass pane 2 are shown.

In Figure 153, $\sigma_{max,pr}$ along axis 21-21 is illustrated. Until $w(t = 0.7) = 0.194\ [m]$, the stress curve is symmetrical and the stress peaks at the tips of the axis have the same value, which is about $14.2\ \left[\frac{N}{mm^2}\right]$ at $w(t = 0.7) = 0.194\ [m]$. For $w(t = 0.89) = 0.247\ [m]$ and $w(t = 1) = 0.277\ [m]$ the stress curve is unsymmetrical and the maximum stress grows significantly and reaches more than $24\ \left[\frac{N}{mm^2}\right]$ at $w(t = 1) = 0.277\ [m]$. From $2.2\ [m]$ to $3.0\ [m]$, $\sigma_{max,pr}$ is $0\ \left[\frac{N}{mm^2}\right]$ which is due to a pronounced local buckling which starts having an impact at $w(t = 0.89) = 0.247\ [m]$ already.

In Figure 154, the deformation of axis 21-21 for u_3 is shown. Until $w(t = 0.7) = 0.194\ [m]$, the deformation figure is symmetrical and has a maximum value of $-48\ [mm]$ at $w(t = 0.7) = 0.194\ [m]$. At any higher time step, the deformation figure gets more unsymmetrical and the amplitude moves towards the deformation point at corner D whereas the increase of deformation grows at a little higher rate (about 8% faster) for time steps between $t = 0.7$ and $t = 1$. At $t = 1$, the maximum value is

$-74\ [mm]$. Interestingly, the amplitude of the unsymmetrical deformation curves coincides with the stress valley at $t > 0.88$ which is an indicator for buckling.

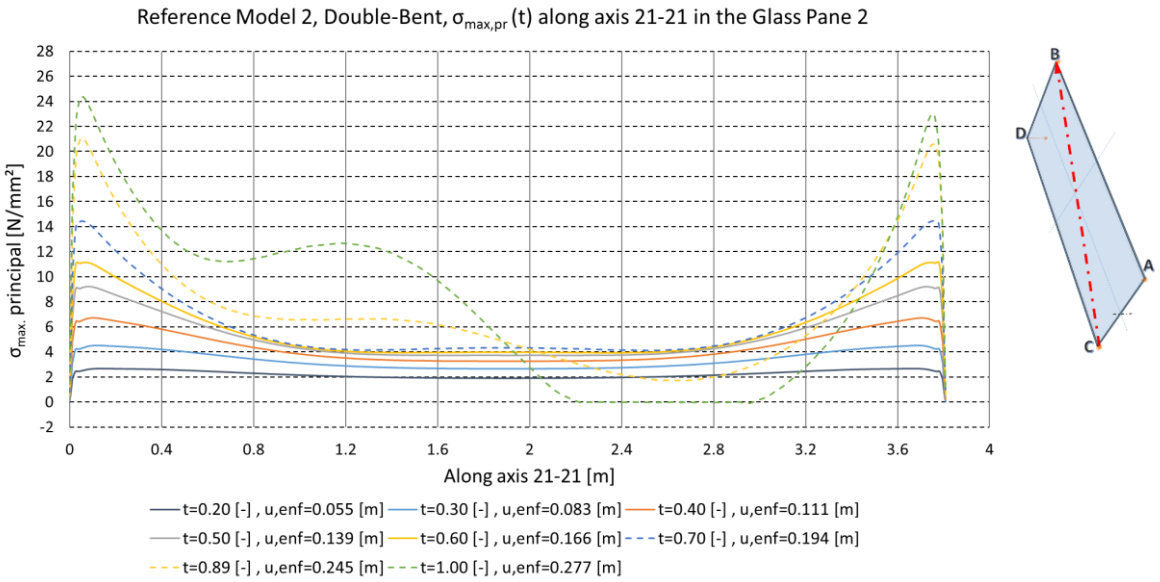

Figure 153: Reference model 2, double-bent, $\sigma_{max,pr}$ (t) along axis 21-21 in the glass pane 2

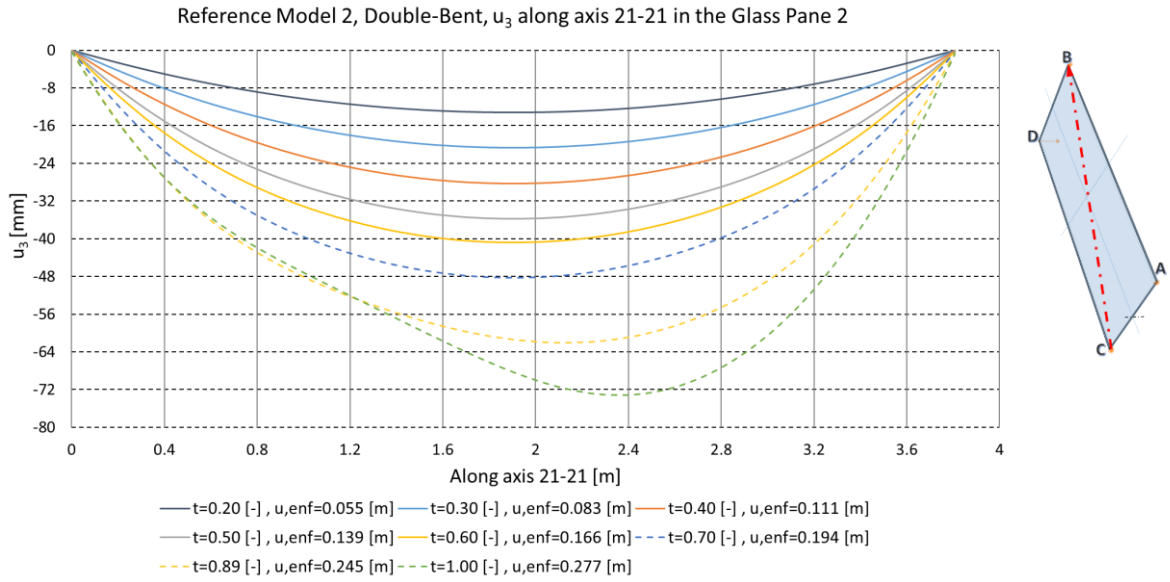

Figure 154: Reference model 2, double-bent, u_3 (t) along axis 21-21 in the glass pane 2

In Figure 155, a considerably higher stress at the tips of axis 23-23 than in the case of axis 21-21 can be seen. One reason for this is the definition of the BCs at a single point in the corners A and D at the upper side of glass pane 2. This also coincides with axis 23-23. However, it can be assumed, that the stresses indeed are higher than in the case of axis 21-21. The maximum stress for axis 23-23 is about $28\ [N/mm^2]$ for

$w(t = 0.7) = 0.194\ [m]$ and about $40\ [N/mm^2]$ for $w(t = 1) = 0.277\ [m]$. Like in the formerly examined axis 21-21, the stress curves are symmetrical until $w(t = 0.7) = 0.194\ [m]$ and then start shaping stress valleys. Moreover, this results in local buckling as well as an unsymmetrical manifestation of the stress curve.

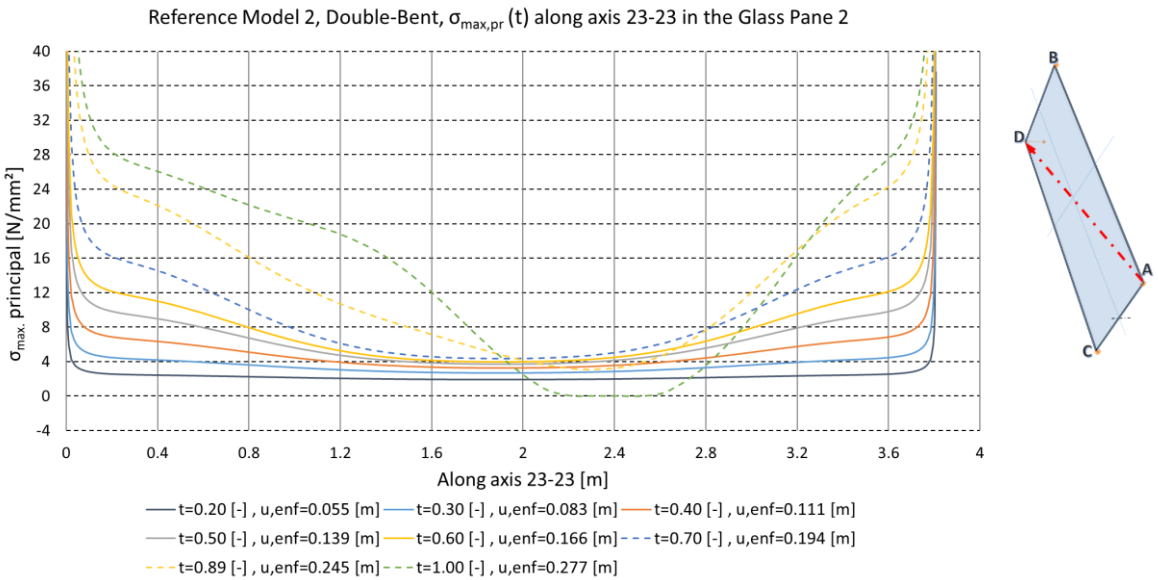

Figure 155: Reference model 2, double-bent, $\sigma_{max,pr}$ (t) along axis 23-23 in the glass pane 2

6.3.3.5 Spacer bar

In Figure 156, the von Mises stress σ_e in the longitudinal spacer along axis 26-26 is depicted. A local onset of yielding in the spacer can be seen at the front tip next to corner D at $w(t = 0.6) = 0.166\ [m]$ where σ_e is $340\ \left[\frac{N}{mm^2}\right]$. In addition, σ_e at the back tip next to corner C is $230\ \left[\frac{N}{mm^2}\right]$ which equals the yielding stress.

The maximum stress keeps increasing until $w < 0.249\ [m]$ (or rather $t < 0.9$). After that, the maximum value σ_e is not increasing anymore, but the curve is slightly changing it's shape. The significant stress of axis 26-26 occurs at the front tip next to axis D for $w > 0.249\ [m]$ and is $495\ \left[\frac{N}{mm^2}\right]$.

In Figure 157, σ_e in the broadside spacer along axis 27-27 is depicted. Compared to axis 26-26, the degrees of utilization in the center region is higher, but the maximum stress values are lower. Like in axis 26-26, σ_e does not increase for $w > 0.249\ [m]$. The maximum stress value for $w > 0.249\ [m]$ is reached at the back tip next to corner

B and is $385\ \left[\frac{N}{mm^2}\right]$. This is slightly higher than the stress at the front tip next to corner D which is $375\ \left[\frac{N}{mm^2}\right]$. Near the corner region, yielding occurs for $w > 0.222\ [m]$ (or rather $t > 0.8$) from $0.10\ [m]$ to $0.14\ [m]$ and from $1.37\ [m]$ to $1.45\ [m]$. A global minimum for σ_e is reached at $0.75\ [m]$ for $w < 0.222\ [m]$ and is shifting towards the deformation point D. It lies at $0.85\ [m]$ for $w(t = 1) = 0.277\ [m]$.

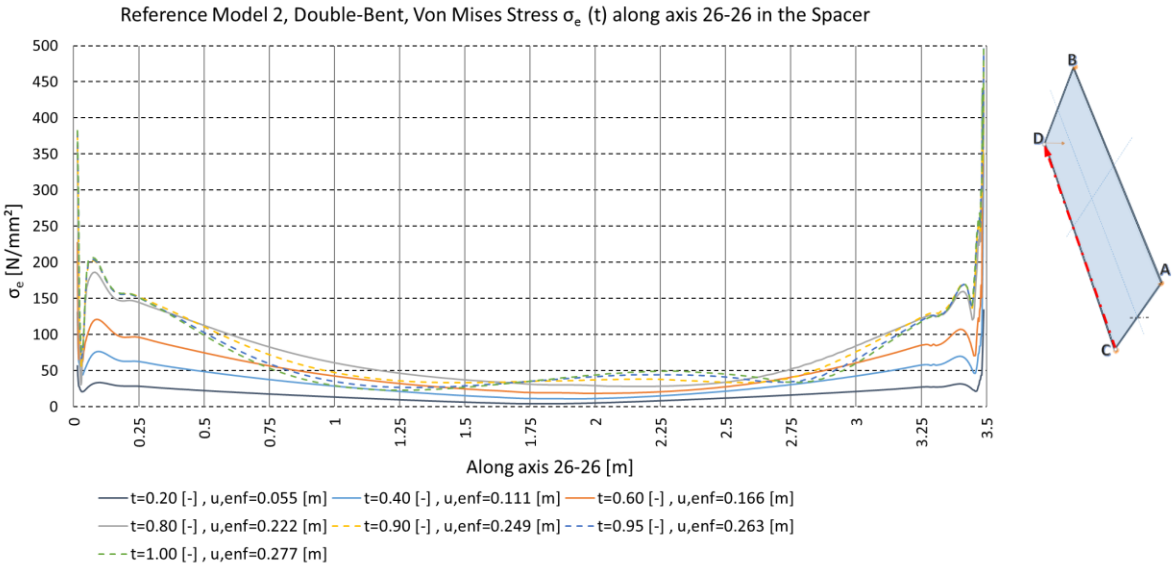

Figure 156: Reference model 2, double-bent, von Mises stress σ_e (t) along axis 26-26 in the spacer

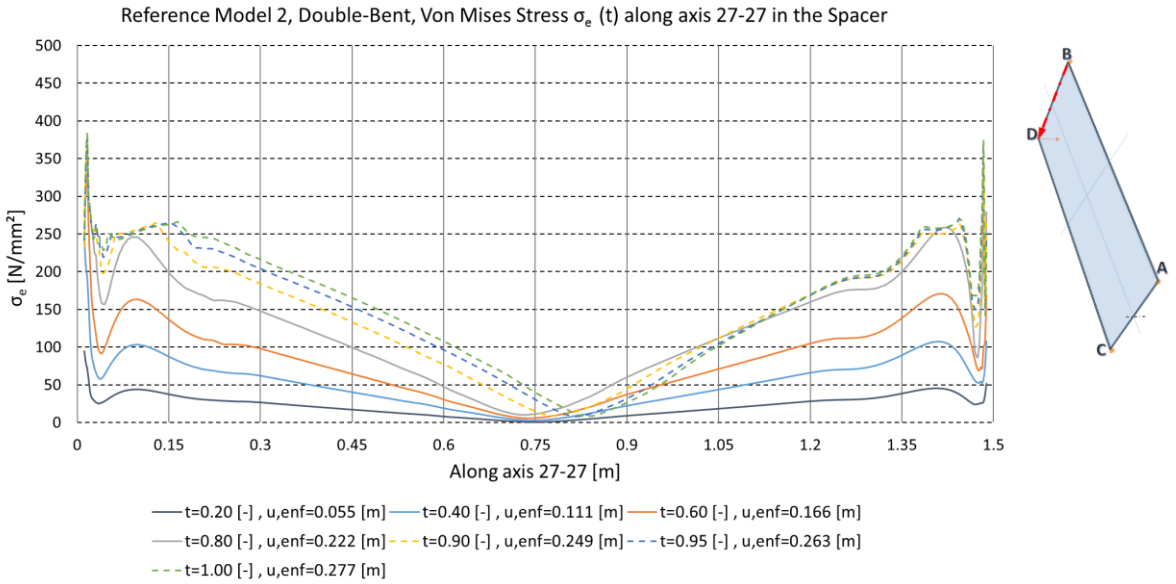

Figure 157: Reference model 2, double-bent, von Mises stress σ_e (t) along axis 27-27 in the spacer

6.3.3.6 Deformation of the edge zone

In Figure 158, Figure 159 and in Figure 160 the deformation of the secondary seal along the axes S21-S21, S26-S26 and S29-S29 is depicted. Like for all double-bent models, the deformation components $u_1(t)$ and $u_2(t)$ are depicted separately. All curves of support situation 1 and support situation 2 do have the same characteristics during all time steps. Therefore, all axes from S22-S22 to S25-S25 are omitted in this subchapter. However, the deformation values for support situation 1 are about 50% bigger than for support situation 1.

In Figure 158, the non-linear curves along axis S21-S21 appears due to the influence from the broadside and the longitudinal side of the IGU. These two spacer bars are interacting at S21-S21, where the enforced displacement is also applied. At axis S26-S26, $u_1(t)$ and $u_2(t)$ are almost linear which comes from a similar displacement of the spacer and the silicone. The edge zone at axis S26-S26 is distorted according to the glass panes unlike for $u_2(t)$ in axis S29-S29. This comes from a bigger slip of glass pane 2 on the spacer. As a consequence of the slippage, the silicone elongates next to glass pane 2 and is restrained by the spacer at the same time.

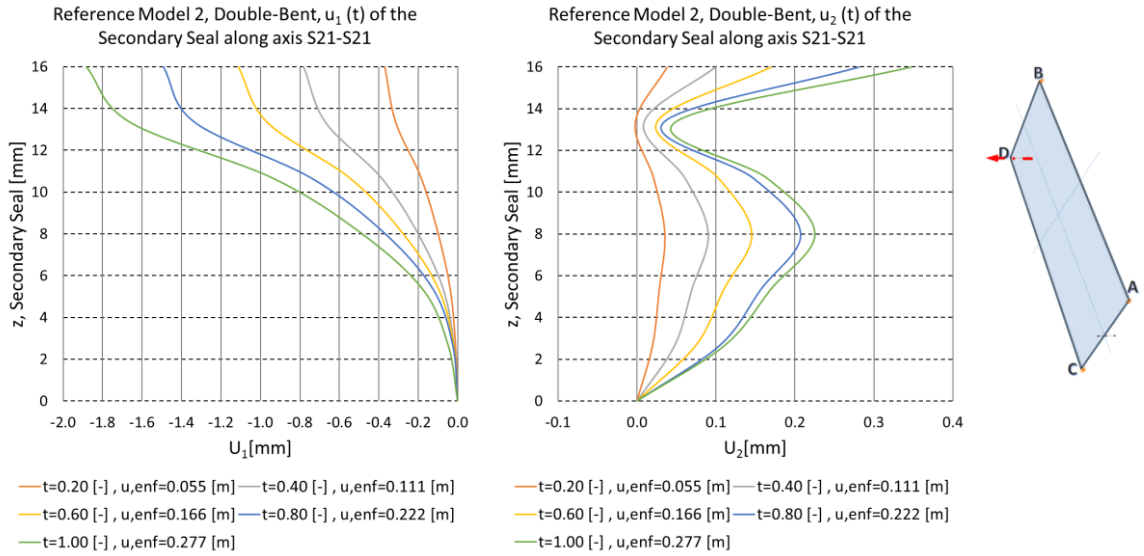

Figure 158: Reference model 2, double-bent, max. displacement (t) of the secondary seal along axis S21-S21

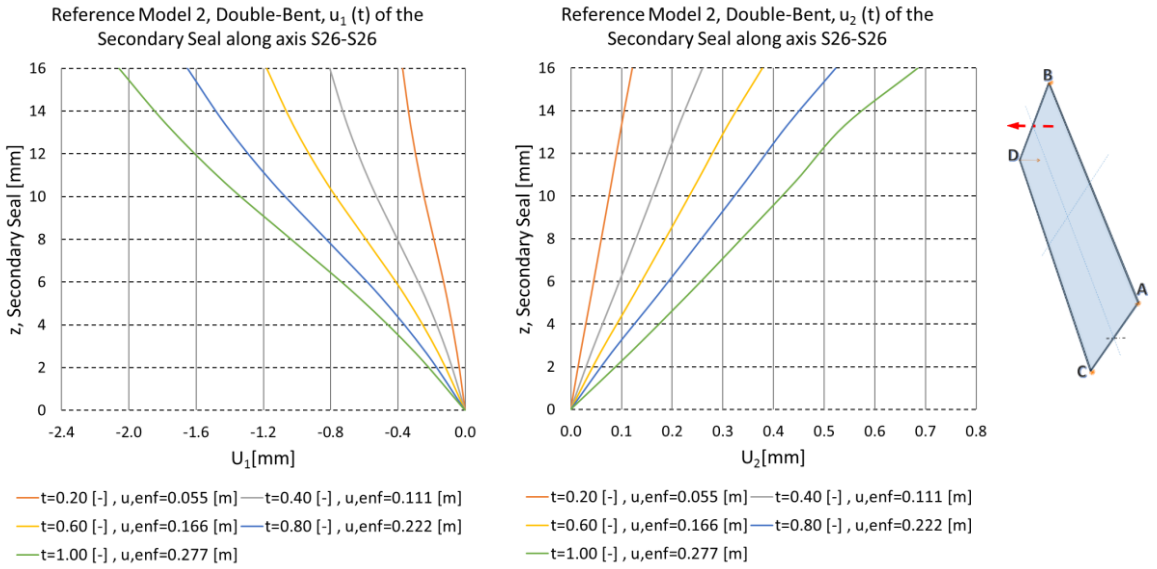

Figure 159: Reference model 2, double-bent, max. displacement (t) of the secondary seal along axis S26-S26

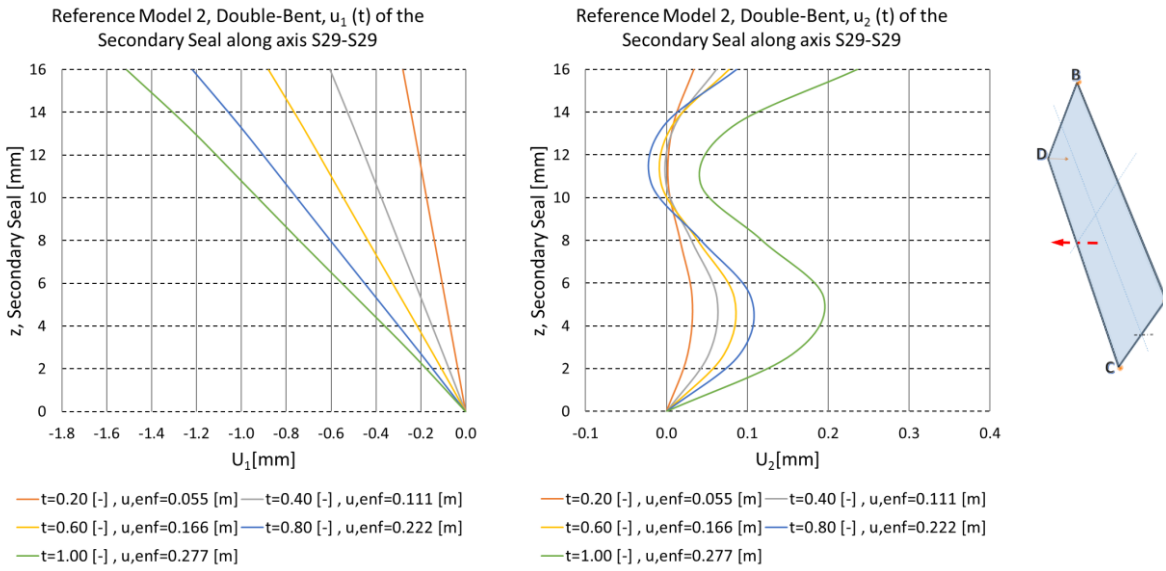

Figure 160: Reference model 2, double-bent, max. displacement (t) of the secondary seal along axis S29-S29

6.3.4 Double-bent IGU, support situation 3

For the double-bent reference model which is described in chapter 6.3, the influence of the BCs are investigated. In this subchapter, support situation 3 is subject to investigations. An overview of the BCs is provided in Figure 161. All BCs are depicted in Figure 162 for the corners A and D and in Figure 163 for the corners B and C. In the subsequent part of this subchapter, the results for this reference model are presented.

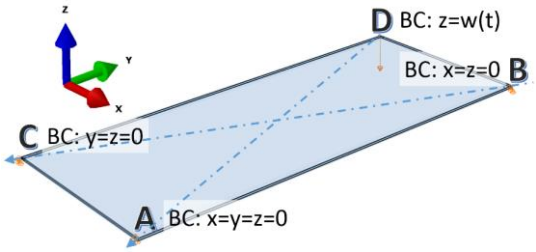

Figure 161: Schematic overview of boundary conditions for support situation 3

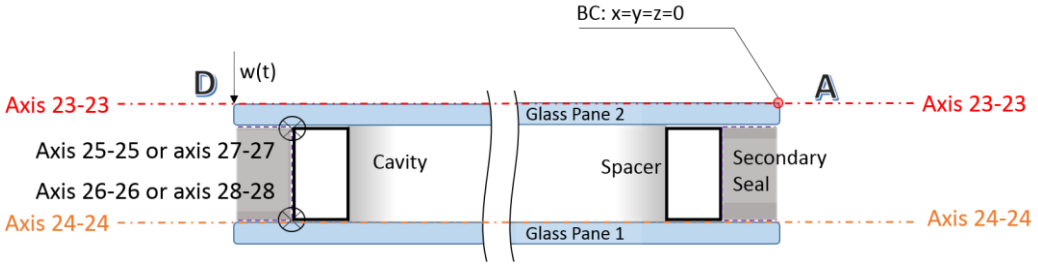

Figure 162: Schematic longitudinal section of the double-bent IGU along the diagonal 23-23, support situation 3

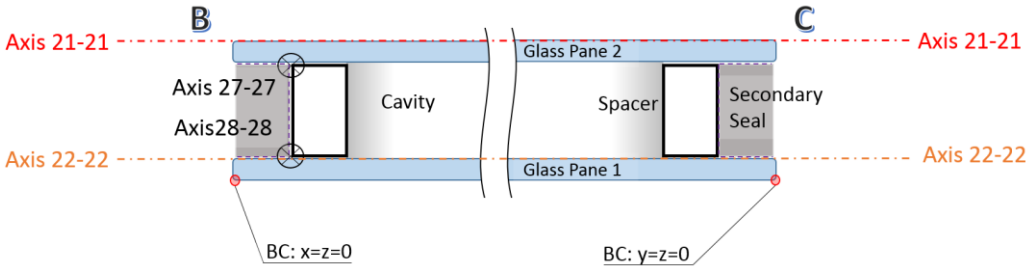

Figure 163: Schematic longitudinal section of the double-bent IGU along the diagonal 21-21, support situation 3

6.3.4.1 Required force for the cold bending process

In Figure 164, the required force F is shown as a function of the enforced displacement. Recalling the same figure for support situation 1 from subchapter 6.3.2.4 until $u_{enf} = 0.16\ [m]$, both curves are almost identical.

In addition, recalling the same figure for support situation 2 from subchapter 6.3.3.1, where both values of u_{enf} are the same, also the curve is almost the same but with the difference that in this case, the curve is completely smooth and does not have a kink. Hence, F is almost independent of this 3 support situations.

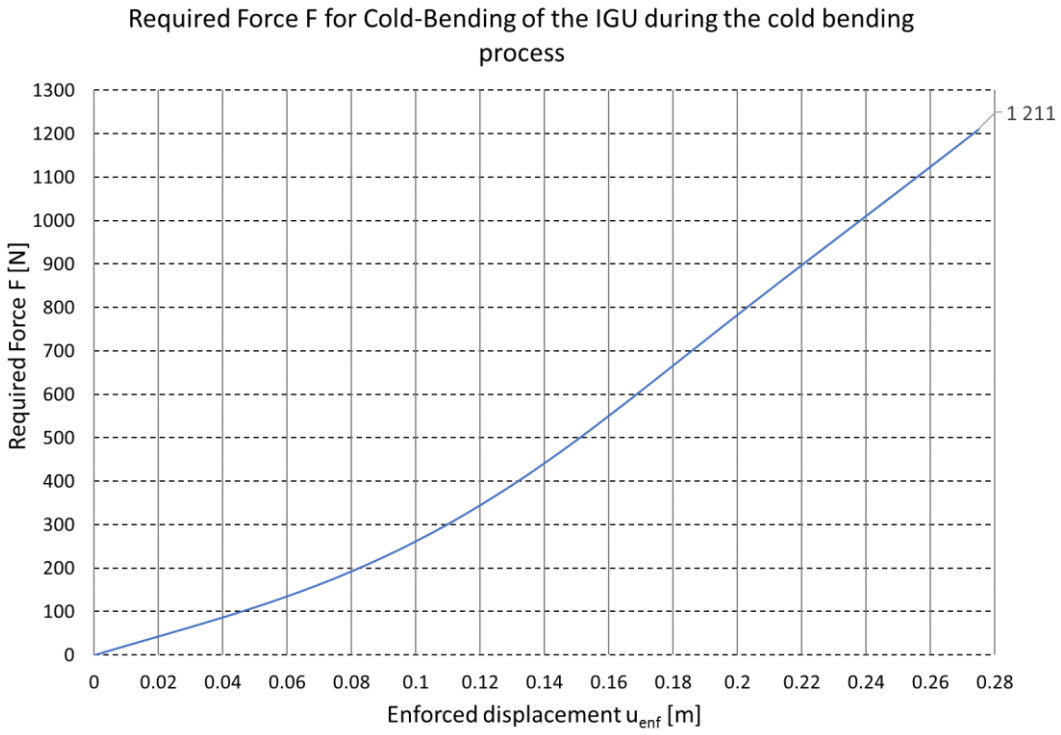

Figure 164: Reference model 3, double-bent, required force F for cold-bending of the IGU

6.3.4.2 Movement of the corners in the xy-plane

In Figure 165 and in Figure 166, the movement of the support points at the corners B and C and the deformation point at corner D is shown with respect to time and to the global coordinate system. In Figure 165, the movement along the x-direction and the y-direction are shown separately. The deformation values in x-direction of point D are more than twice as high than in y-direction, reaching a value in y-direction of about $20\ [mm]$ and in x-direction of about $10\ [mm]$. The maximum values for the support points at corner B and corner C are increasing insignificantly and are approaching a peak of about $\pm 1\ [mm]$ for $w(t = 1) = 0.277\ [m]$.

In Figure 166, the movement of all three corner points is depicted in the xy-plane. A striking similarity of the corners B and C according to their degree of freedom is visible whilst point D is wandering in the xy-plane with an almost constant $\frac{x}{y}$ ratio of $\frac{1}{2}$. Hence, support situation 3 ensures a stable configuration during the cold-bending process.

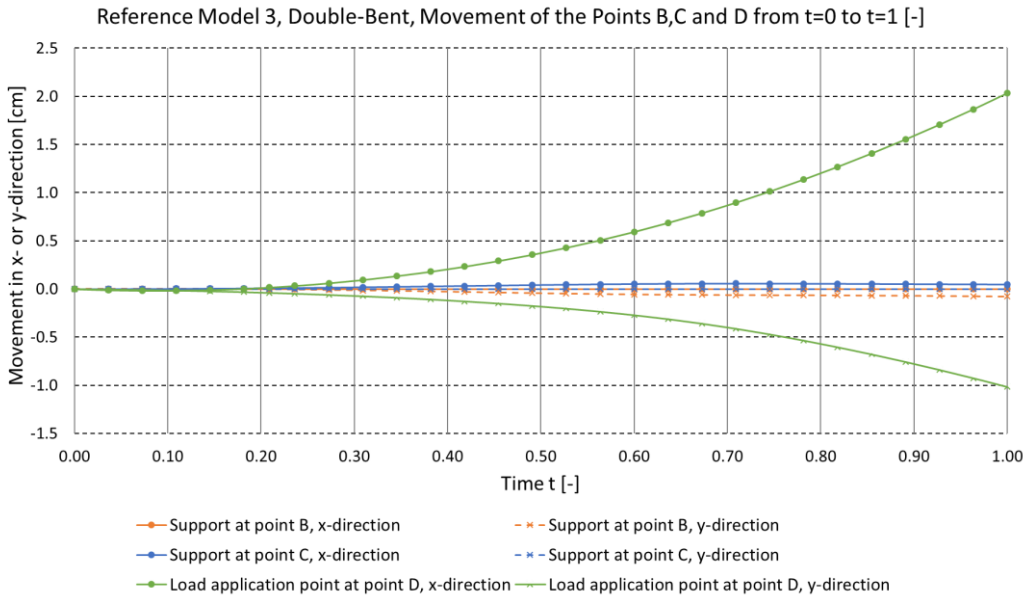

Figure 165: Reference model 3, double-bent, movement of the corners B, C and D from t=0 to t=1 [-]

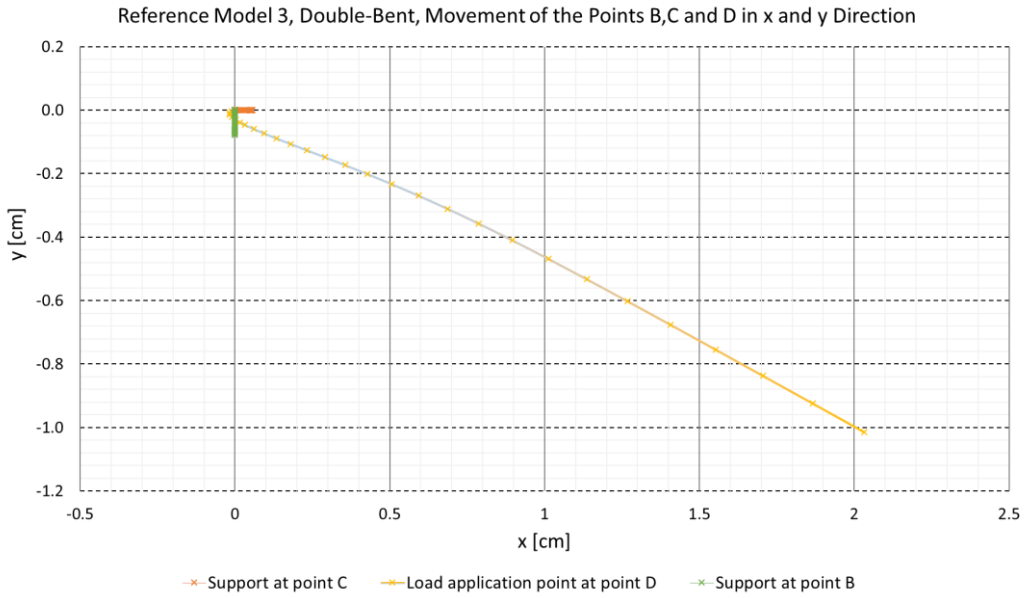

Figure 166: Reference model 3, double-bent, movement of the cornrs B, C and D in x- and y-direction

6.3.4.3 Distortion of the edge zone

In Figure 167, Δu_3, which is the difference from a straight line between the corner points C and D and the real shape of the glass pane edge, is depicted. A more detailed explanation about Δu_3 and $\Delta u_3'$ can be found in subchapter 6.3.2 for support situation 1. All other 3 edges do have smaller amplitudes for Δu_3 and thus are not depicted.

Firstly, until $t = 0.4$, Δu_3 has relatively small values, the amplitude at $w(t = 0.4) = 0.111\ [m]$ is $\pm 2\ [mm]$. After that, the amplitudes as well as the whole curve starts to increase exponentially, with an amplitude for $w(t = 0.6) = 0.166\ [m]$ of $-6\ [mm]$ and for $w(t = 1) = 0.277\ [m]$ of $-32\ [mm]$.

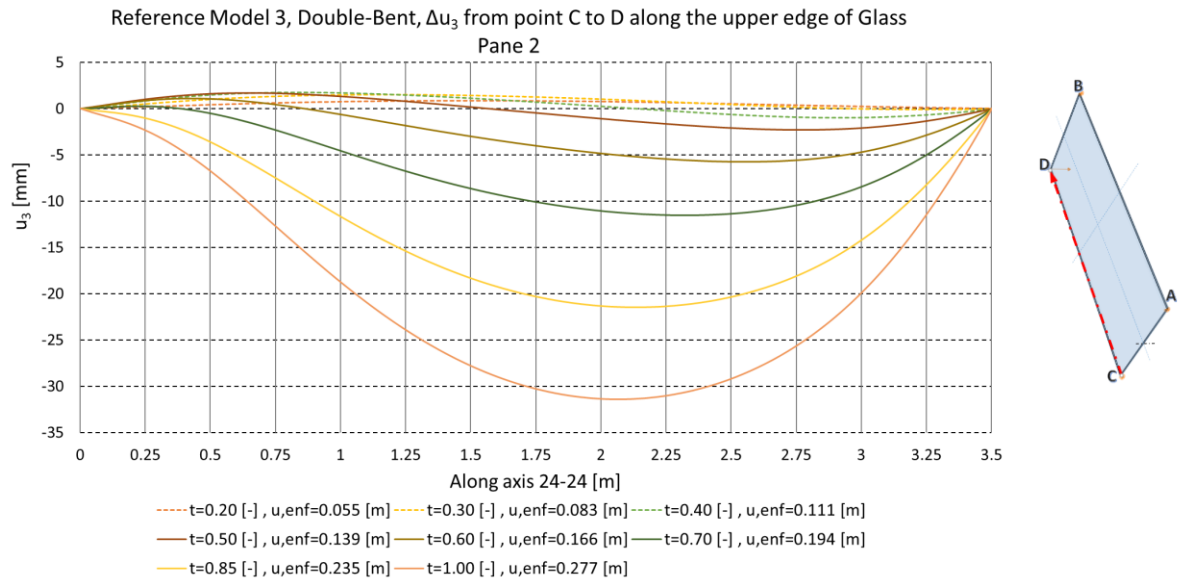

Figure 167: Reference model 3, double-bent, Δu₃ from corner C to corner D along the upper edge of glass pane 2

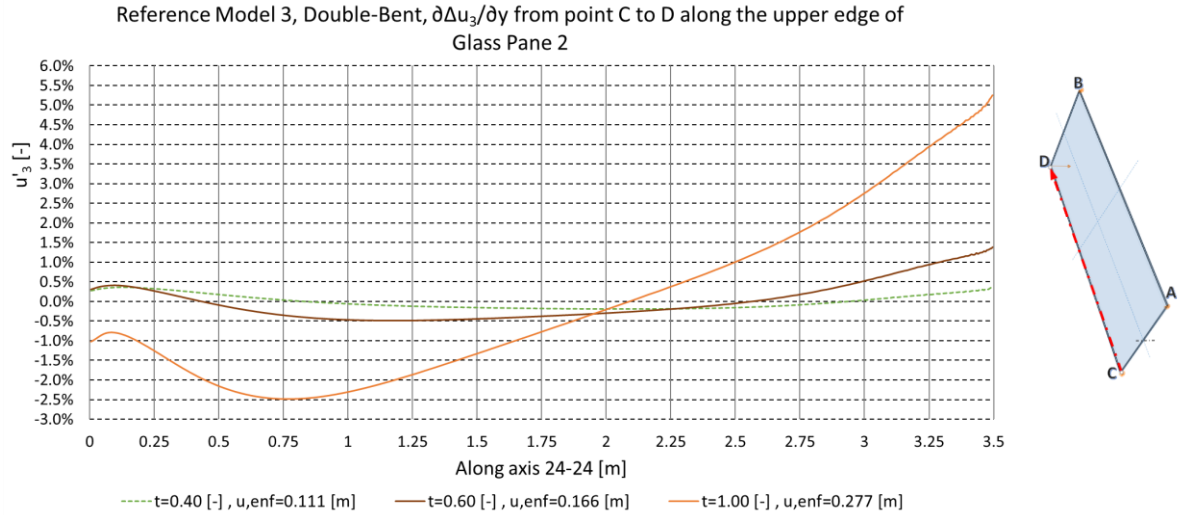

Figure 168: Reference model 3, double-bent, Δu'₃ from corner C to corner D along the upper edge of glass pane 2

In Figure 168, the curves for $\Delta u_3{}'$ for $w(t = 0.4) = 0.111\ [m]$, $w(t = 0.6) = 0.166\ [m]$ and $w(t = 1) = 0.277\ [m]$ are shown. It can be seen, that the rate of distortion along the edge of the IGU is increased by about a factor of four from $w(t = 0.6) = 0.166\ [m]$ to $w(t = 1) = 0.277\ [m]$ which means that the edge zone gets "softer". The reason for

this is serious plasticization in the broadside spacer which can be seen in Figure 176. However, the stress in the spacer is well beyond its ultimate limit which is explained on the next pages in more depth. It is important to recognize that, unlike for the other support situations, no local buckling occurs.

In Figure 169, an illustration of a non-linear edge deformation for the final time step along edge $\overline{AB}$ is shown. This edge deformation occurs due to the statically over-determined support situation.

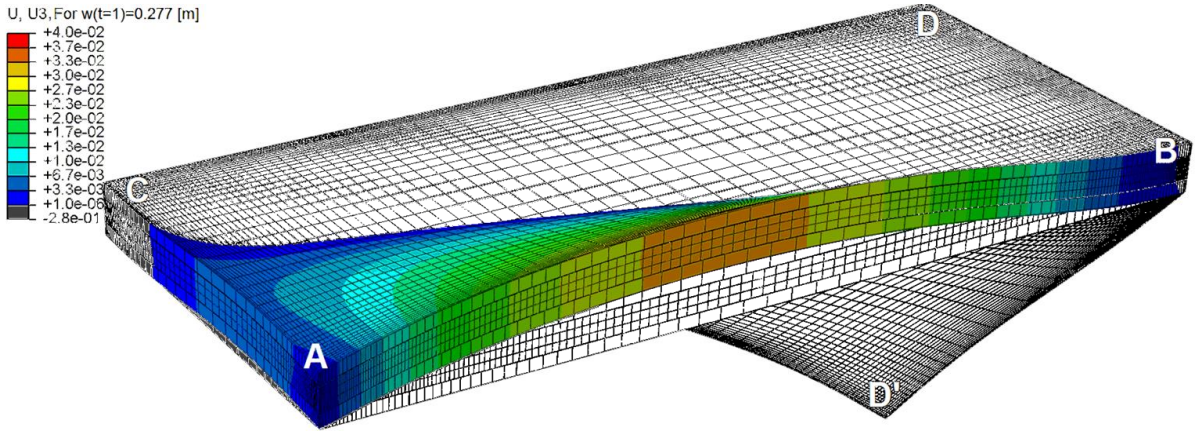

Figure 169: An illustration of a non-linear edge deformation for t=1 along edge $\overline{AB}$, z is upscaled 10 times

6.3.4.4 Glass pane

In Figure 170, $\sigma_{max,pr}$ along the axis 21-21 is depicted. For any time step, the stress curves are almost symmetric. Until $w(t = 0.5) = 0.139\ [m]$, the stress curves do have a minimum in the center region. This starts to change for $w(t = 0.6) = 0.166\ [m]$ when the stress also increases in the center region. The reason for this is that the stress from the diagonal $\overline{AD}$ adds up in the center region after $w(t = 0.5) = 0.139\ [m]$ at a substantial level. The glass between the diagonal $\overline{BC}$ restrains it's elongation which leads to increased stress. As a consequence, a higher growth of deformation per time step t after $t = 0.5$ must be endured next to D.

In Figure 171, the deformation of axis 21-21 for u_3 is shown, which helps to understand the stress curves in Figure 170. The shape of the deformation curves is staying the same over time. The growth of the deformation curves per time step is slowing down over time. This can be shown for example for the amplitude. The value of the amplitude at $w(t = 0.2) = 0.055\ [m]$ is $-15\ [mm]$, at $w(t = 0.4) = 0.111\ [m]$ it is $-30\ [mm]$ and at $w(t = 0.6) = 0.166\ [m]$ is $-37\ [mm]$. For $t > 0.6$, the amplitude of u_3 peaks in at a

plateau in the center region of the curve. The position of the deformation plateau in axis 21-21 coincides with an increased stress and can be seen in Figure 170.

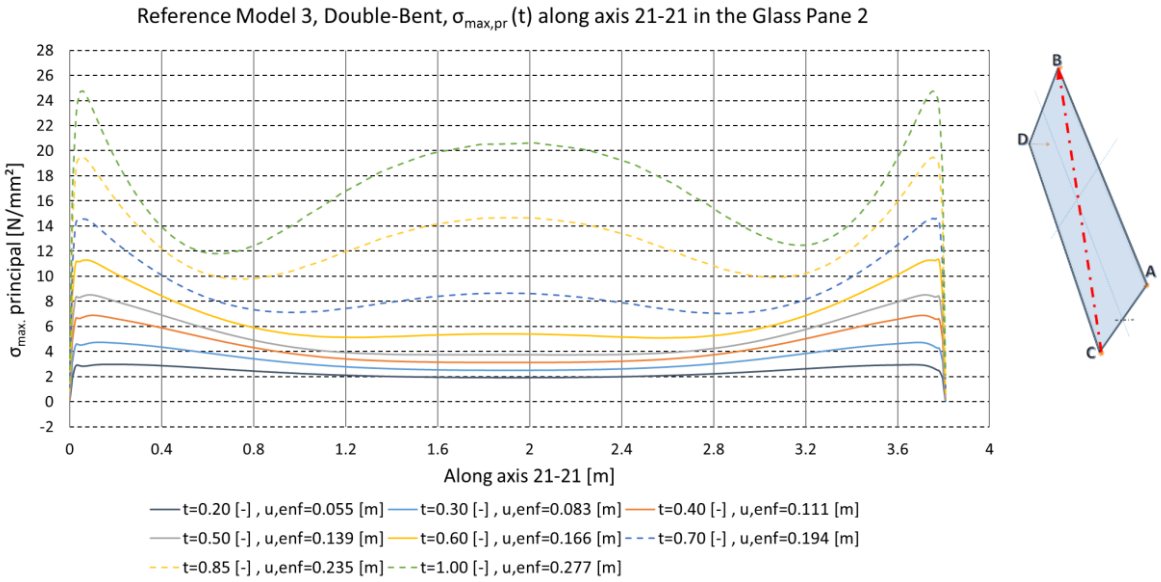

Figure 170: Reference model 3, double-bent, $\sigma_{max,pr}$ (t) along axis 21-21 in the glass pane 2

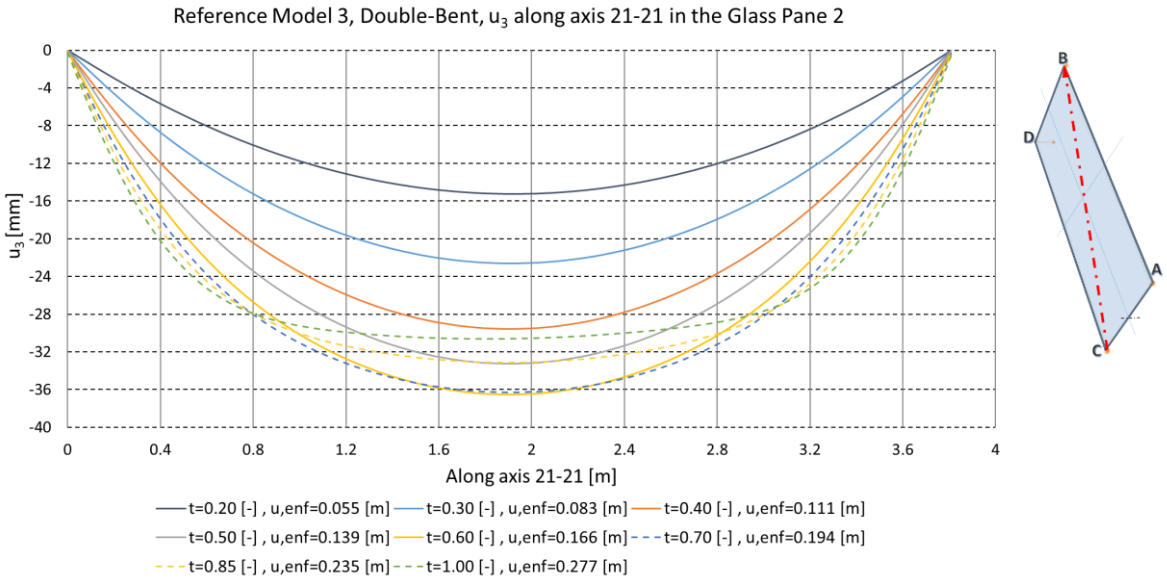

Figure 171: Reference model 3, double-bent, u_3 (t) along axis 21-21 in the glass pane 2

In Figure 172, $\sigma_{max,pr}$ along axis 23-23 is depicted. Like $\sigma_{max,pr}$ along axis 21-21, the stress is almost symmetrical, but slightly increased towards the deformation point at corner D. Also like in axis 21-21, $\sigma_{max,pr}$ increases in the center region for $t > 0.6$, but for earlier time steps, a global minimum is existing in the center region. At $w(t = 0.2) =$

$0.055\ [m]$, $\sigma_{max,pr}$ is almost constant at a low level, which is about $3\ \left[\frac{N}{mm^2}\right]$. Stress singularities are present at the back tip next to corner A and at the front tip next to corner D. Despite these issues, it can be stated that the stress in this axis is significant and has a value of roughly $40\ \left[\frac{N}{mm^2}\right]$ for $t = 1$.

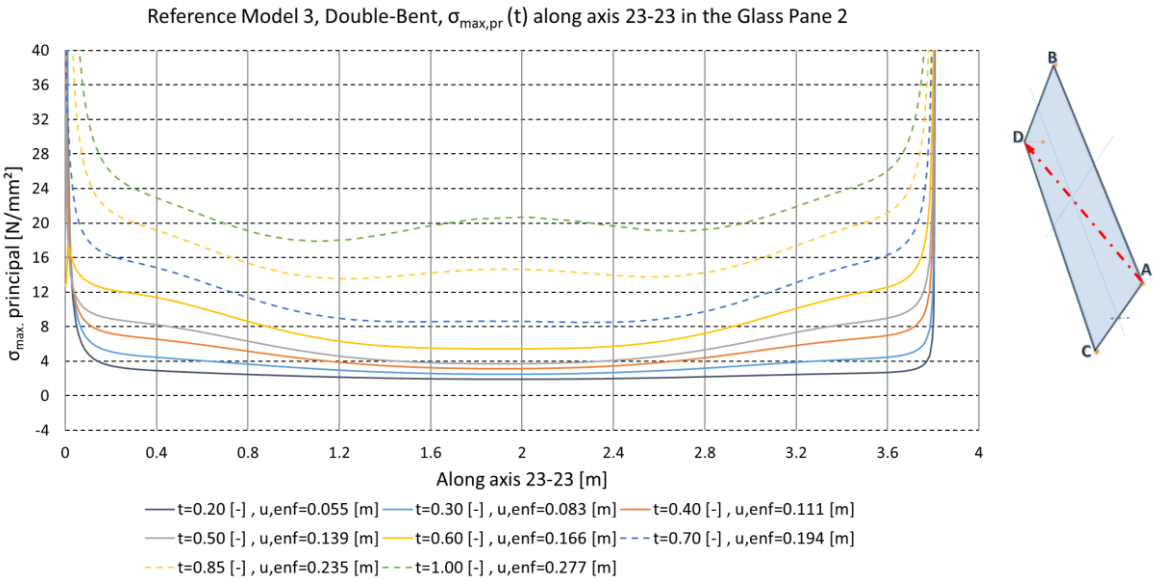

Figure 172: Reference model 3, double-bent, $\sigma_{max,pr}$ (t) along axis 23-23 in the glass pane 2

In Figure 173, the absolute maximum values of the true principal strain $\varepsilon_{true,pr,abs}$ are depicted for time step $w(t = 0.6) = 0.166\ [m]$ and $w(t = 1) = 0.277\ [m]$ for the bottom surface of glass pane 1 and for the top surface of glass pane 2. For $t = 0.6$, between the corners B and C along the diagonal 21-21, the dominating strain is negative which means that this diagonal undergoes compression. Next to the corners A and D, all $\varepsilon_{true,pr} > 0$, therefore tension is dominating. For $t = 1$ at the bottom surface of glass pane 1, the compression along axis 21-21 is clearly dominating. For the bottom surface of glass pane 1 at $t = 0.6$ and at $t = 1$ and for the top surface of glass pane 2 at $t = 0.6$, the distribution of $\max|\varepsilon_{true,pr}|$ is symmetrical. For the top surface of glass pane 2 at $t = 1$, the distribution of $\varepsilon_{true,abs} > 0$ is unsymmetrical because tension is increased towards corner D (due to yielding of the spacers). More specifically, along diagonal $\overline{AD}$, it can be seen that the upper half of the diagonal towards corner D undergoes more tension which results in increased stress $\sigma_{max,pr}$ towards corner D in Figure 172.

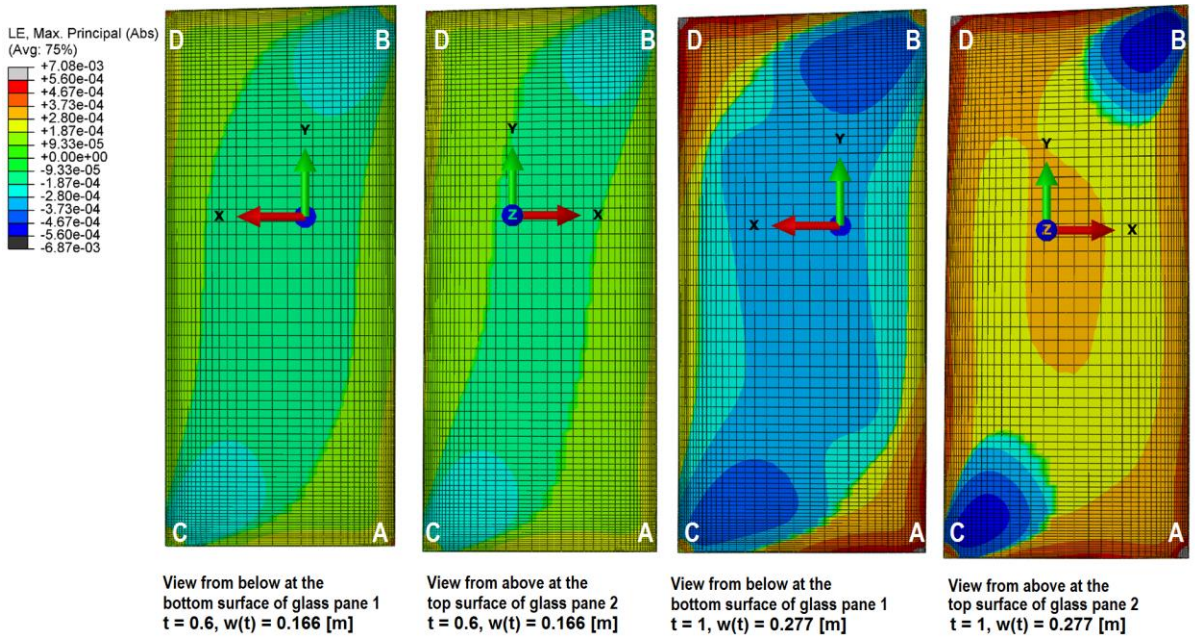

Figure 173: Reference model 3, double-bent, $\varepsilon_{true,pr,abs}$

6.3.4.5 Spacer bar

In Figure 175, σ_e in the longitudinal spacer in axis 26-26 is shown. For $w(t = 0.2) = 0.055\ [m]$ to $w(t = 0.6) = 0.166\ [m]$ the stress curves do have a minimum at $2\ [m]$ which stays constant over time with a value of $15\ [N/mm^2]$. For $t > 0.6$, the minimum is moving backwards to corner C and lies at $0.8\ [m]$. For $w(t = 1) = 0.277\ [m]$, the stress increases towards the front tip of axis 26-26 next to corner D at the same amount per time for each stress function. For $w(t = 0.95) = 0.263\ [m]$, the spacer starts plasticizing already at $3.35\ [m]$. However, at both ends of the axis, the spacer yields from time step $t \geq 0.6$ on. A more detailed view of the stress distribution and the yielding areas of the spacer at corner D is illustrated in Figure 174.

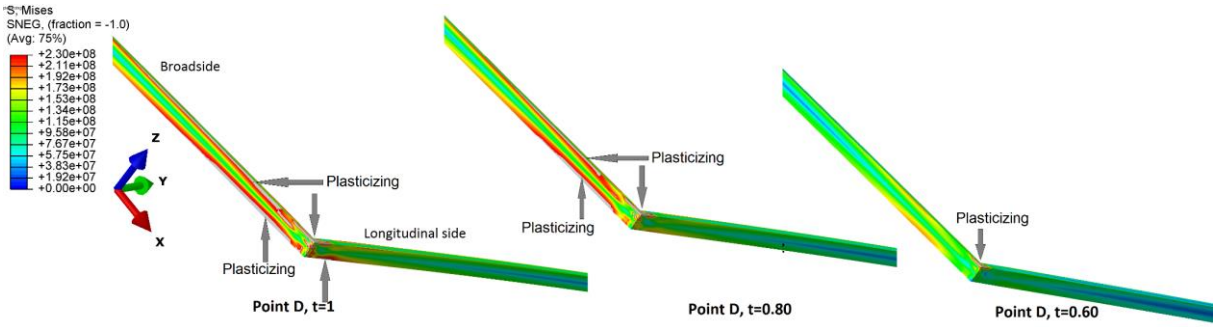

Figure 174: Reference model 3, double-nemt, von Mises stress σ_e in the corner D as a sequence for t=1, t=0.8 and t=0.6 (grey areas are plasticizing)

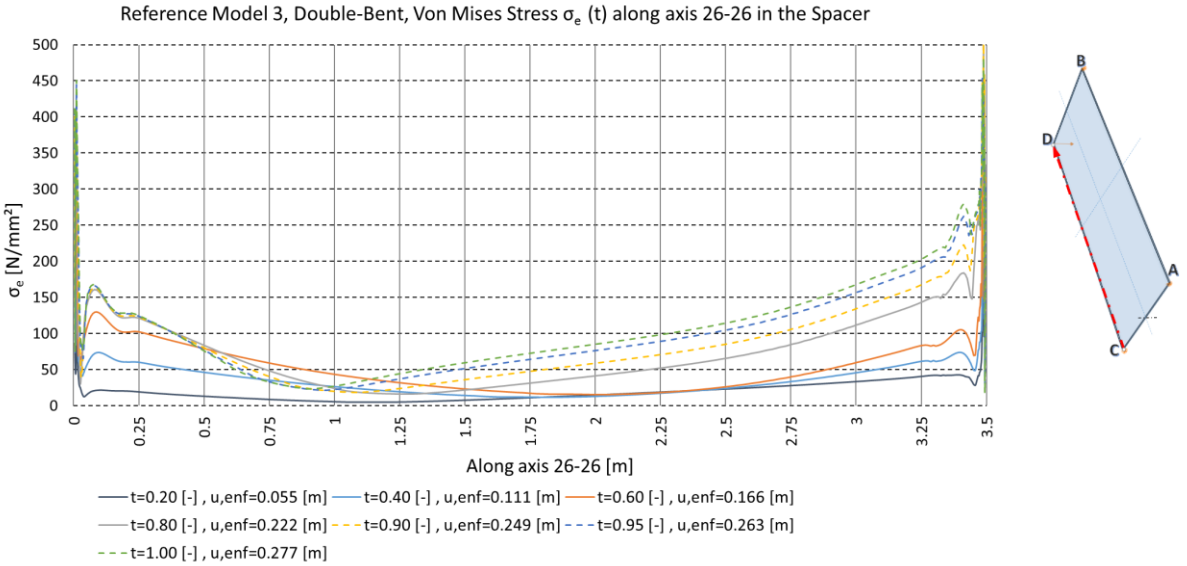

Figure 175: Reference model 3, double-bent, von Mises stress σ_e (t) along axis 26-26 in the spacer

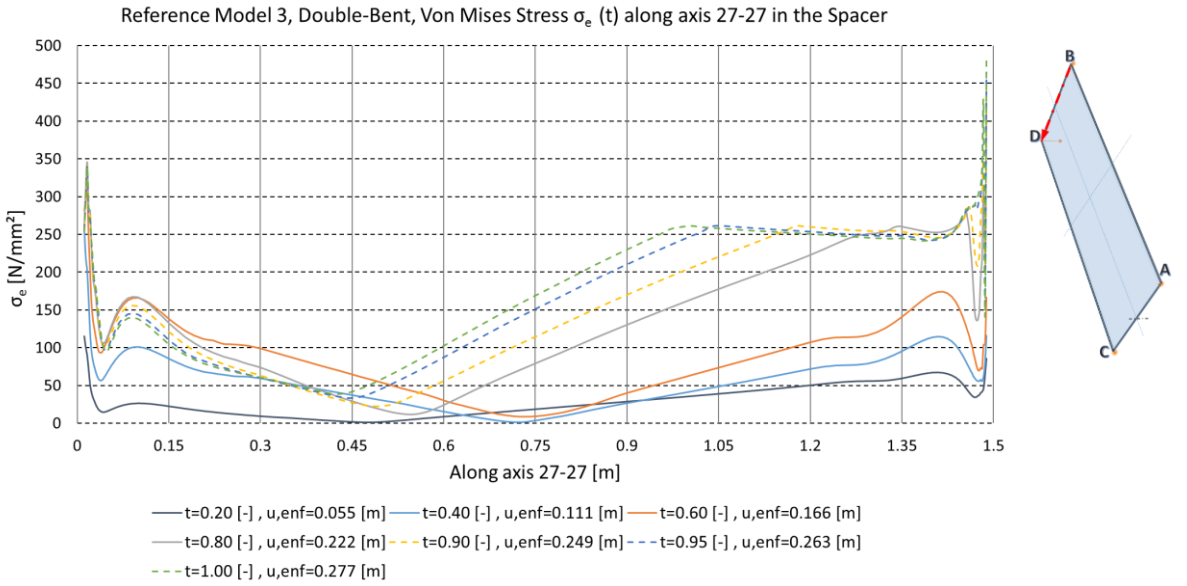

Figure 176: Reference model 3, double-bent, von Mises stress σ_e (t) along axis 27-27 in the spacer

In Figure 176, σ_e is yielding for $w(t = 0.4) = 0.111\ [m]$ at the back tip of axis 27-27 next to corner B. At the front tip next to corner D, the onset of yielding can be observed at $w(t = 0.8) = 0.222\ [m]$. In contrast to the longitudinal spacer, the plasticizing area is much bigger and reaches from $1\ [m]$ to $1.4885\ [m]$ of the spacer. At $t > 0.8$, σ_e outside the corner region ranges from values between $250\ \left[\frac{N}{mm^2}\right]$ and $275\ \left[\frac{N}{mm^2}\right]$ and reaches a maximum of almost $500\ [N/mm^2]$ at the front tip at $w(t = 0.9) = 0.249\ [m]$.

6.3.4.6 Deformation of the edge zone

As shown in Figure 177, the deformation of the secondary seal along the axis S21-S21 is depicted. Both deformation components $u_1(t)$ and $u_2(t)$ are shown separately. All deformation curves are non-linear whereas $u_1(t)$ grows with a declining rate over time and $u_2(t)$ grows with an increasing rate over time. Both components increase over the height z from zero on. Whilst $u_1(t)$ increases until it reaches a turning point at $z = 13\ [mm]$ where it does not change it's amplitude anymore (within a range of $\pm 0.05[mm]$), $u_2(t)$ has two turning points. The first turning point of $u_2(t)$ is located at $z = 8\ [mm]$ and the second one at $z = 13\ [mm]$. This comes from a pronounced slip of glass pane 2 in y-direction on the spacer where it cannot transfer any shear force. At the same time, below $z = 13\ [mm]$, the spacer holds the secondary seal back. In addition, the deformation in x-direction has higher total values which lead to non-linear distortion along axis S21-S21.

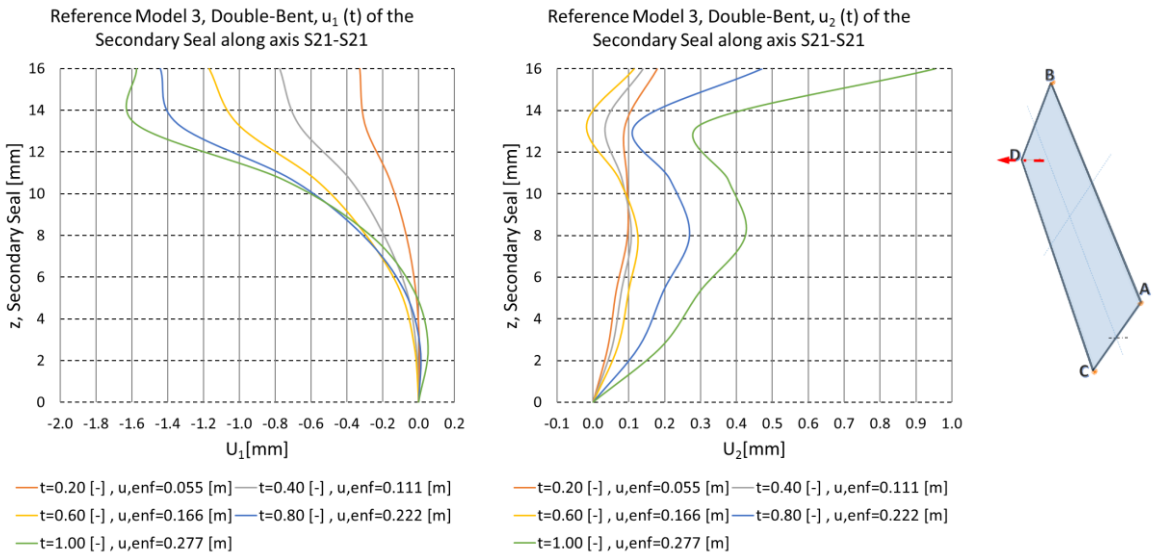

Figure 177: Reference model 3, double-bent, max. displacement (t) of the secondary seal along axis S21-S21

6.3.5 Discussion of the results for the different support situations

In this subchapter, the most important findings from the case study in chapter 6.3 are summed up for each support situation separately. For the subsequent parameter study in chapter 6.4, the best support situation possible, which is support situation 3, is chosen.

Support situation 1

The imposed deformation for support situation 1 is $0.16\ [m]$ because for higher deformations, the finite element model undergoes numerical instabilities. Furthermore, at an imposed movement of about $0.106\ [m]$, the IGU starts to rotate in the opposite direction around the z-axis. Moreover, the growth of rotation of the IGU around the z-axis per time step increases exponentially.

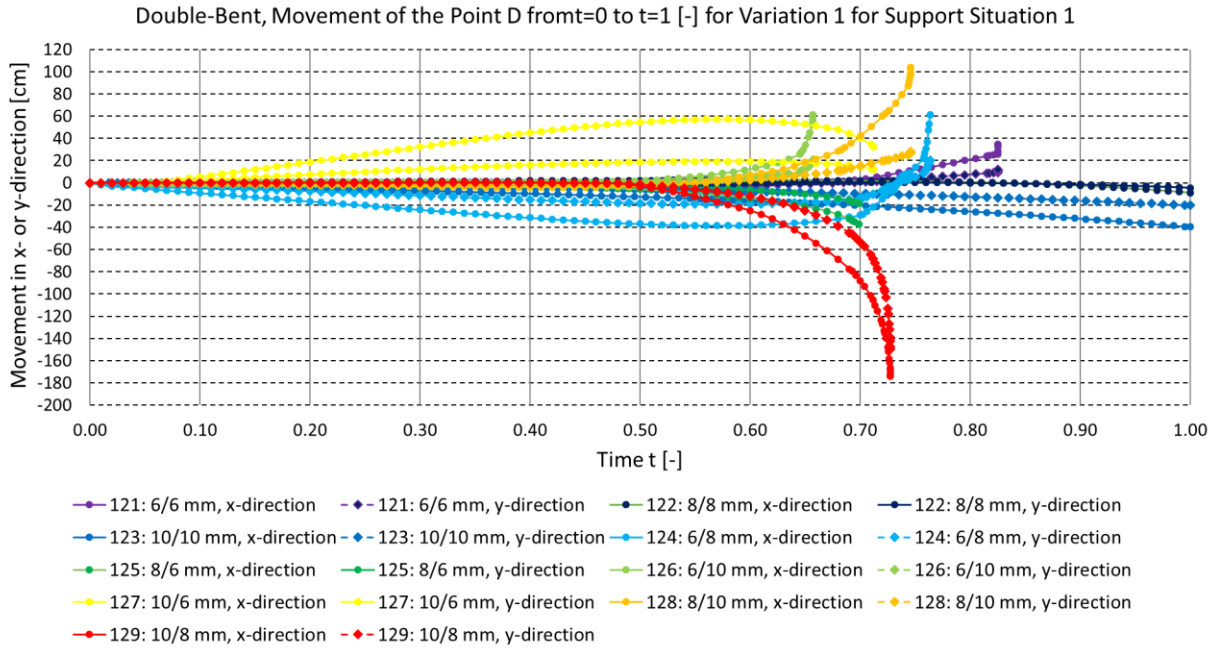

Figure 178: Double-Bent, Movement of the point D from t=0 to t=1 [-] for variation 1 for support situation 1

In Figure 178, an extract of a conducted parameter study with support situation 1 is shown. For this, IGUs with different pane thicknesses for glass pane 1 and glass pane 2 are modeled. The pane thickness is either $6\ [mm]$, $8\ [mm]$ or $10\ [mm]$ which gives 9 possible combinations. Due to the supports at the corners B $(z = 0)$ and D $(z = 0)$, a very high rotation around the z-axis was observed. This makes support situation 1

for most applications unsuitable. Therefore, the parameter study in chapter 6.4 will not be conducted with support situation 1. However, the order of magnitude of stresses and strains of any double-bent IGU is similar apart from stability problems caused by unsuitable support situations. This can be seen for support situation 2 in subchapter 6.3.3 and for support situation 3 in subchapter 6.3.4.

Support situation 2

The imposed deformation for support situation 2 is $0.277\ [m]$. If the deformation is bigger than that, then the yielding area in the stainless steel spacers expands unacceptably. Therefore, the stainless steel spacer limits the maximum double-bent deformation. The imposed deformation reaches a critical value at $w = 0.246\ [m]$ where local buckling occurs in the glass panes and also in the longitudinal spacer between corner C and D. At $w = 0.277\ [m]$, local buckling is clearly visible, but does not lead to a failure in the overall IGU. However, it can be assumed that local buckling has to be avoided because the IGU must also endure additional variable loads.

Support situation 3

The imposed deformation for support situation 3 is $0.277\ [m]$ like for support situation 2. If the deformation is bigger than $0.277\ [m]$, then the yielding area in the stainless steel spacer expands unacceptably like in support situation 2. For an imposed deformation bigger than $0.166\ [m]$, membrane stresses in the glass panes start to have a significant influence on the mechanical behavior. The big advantage over the other two support situations is that the maximum distortion in the glass pane is limited which can be important to ensure optical quality. Membrane stresses which lead to reduced deformations increase the maximum principal stresses. Despite this disadvantage, the significant stress in the glass leaves enough remaining potential for variable loads. The spacers in the corner region exhibit a bigger yielding region than for the other two support situations which can only be limited by restricting the maximum imposed deformation. Unlike support situation 1, no numerical instabilities occur and unlike support situation 2, no local buckling occurs from cold bending. Therefore, support situation 3 is the most appropriate support situation for the parameter study in chapter 6.4.

6.4 Parameter study: Double-bent IGU

Based on the case studies in chapter 6.3, the reference model from subchapter 6.3.4 with support situation 3 is chosen for a parameter study in this chapter. The reason for this is that support situation 3 shows to be stable during the bending process and does not undergo local buckling. Also important is the fact, that the material utilization leaves sufficient remaining potential for variable loads.

In order to restrict the extent of this work, some conclusions from the single-bent parameter study in chapter 6.1 haven been adopted.

Therefore, variation 2 (the parameter 22X; width of cavity h, double-bent) and variation 3 (parameter 32X; Young's modulus E, double-bent) are not subject of investigation.

In addition, variation 4 (parameter 42X; stainless steel and aluminum spacer) is not of interest because aluminum is not ductile enough to withstand the cold bending process. Furthermore, just the final time step $t = 1$ is shown.

All conditions - for example BCs, interaction properties, constraints and so forth have been adopted from the reference model with support situation 3, unless they are utilized as a parameter value.

In subchapter 6.4.1, the thickness of glass pane 1 $t_{gp,1}$ and of glass pane 2 $t_{gp,2}$ is varied. The glass thickness $t_{gp,i}$ is either $6\,[mm]$, $8\,[mm]$ or $10\,[mm]$ like for the single-bent parameter study. All 9 possible combinations for a double-paned IGU are taken into account. The associated designations are 121 to 129 whereat 122 coincides with the double-bent reference model. The enforced deformation at the final time step $t = 1$ is $w(t = 1) = u_{enf} = 0.277\,[m]$.

In subchapter 6.4.2, the length of the double-bent IGU l_{gp} is being varied from $1.50\,[m]$ to $7.00\,[m]$ which leads to a variation of the aspect ratio within a range of $\frac{1}{1} \leq \frac{l_{gp}}{w_{gp}} \leq \frac{14}{3}$. The associated designations are 522 to 529. The model 526 does not coincide with the reference model unlike for 516 because $w(t = 1) = u_{enf} = 0.20\,[m]$ instead of $w(t = 1) = u_{enf} = 0.277\,[m]$. The reason for this is that, for small IGUs with a length of $l_{gp} < 3\,[m]$, the distortion from the imposed deformation would be otherwise too high.

Annotation: *5.2.1 is associated with a length of 0.75 [m] like in the single-bent case for 5.1.1 but has been omitted because it is not comparable due to too high deformation values*.

6.4.1 Thickness of the glass pane - Variation 1

In this subchapter, a parameter study about the influence of the thickness of the glass pane on the overall double-bent IGU system is carried out. The following glass thicknesses $t_{gp,i}$ are considered: $6\ [mm]$, $8\ [mm]$ and $10\ [mm]$. Because the IGU is double-glazed, there are 9 possibilities to combine the glass pane thicknesses. All associated designations for the models and the allocated glass thicknesses can be seen from the listing in Table 17.

Double-Bent	6 mm		8 mm		10 mm	
121.	1	2				
122			1	2		
123					1	2
124	1		2			
125	2		1			
126	1				2	
127	2				1	
128			1		2	
129			2		1	

Table 17: Variation 12: Thickness of the glass panes

6.4.1.1 Required force for the cold bending process

In Figure 179, the required force F for cold-bending of the IGU from $w(t=0)=0\ [m]$ to $w(t=1)=0.277\ [m]$ is depicted. The curve function does not depend on the thickness of glass pane 1 $t_{gp,1}$ and glass pane 2 $t_{gp,2}$ but on the sum of both $t_{gp,1}+t_{gp,2}$.

Each curve is determined mainly by the moment of inertia of the IGU. The contribution of the stainless steel spacer to the moment of inertia around the x-axis is more than

2.5% for model (121: 6/6 [mm]) but decreases to 0.6% for model (123: 10/10 [mm])[14]. Therefore, the characteristics of the curve do slightly change. For instance, for model (121: 6/6 [mm]), the curve increases almost linear from about $w = 0.12\ [m]$ to $w = 0.277\ [m]$. For model (123: 10/10 [mm]), the curve increases almost linear from about $w = 0.18\ [m]$ to $w = 0.277\ [m]$.

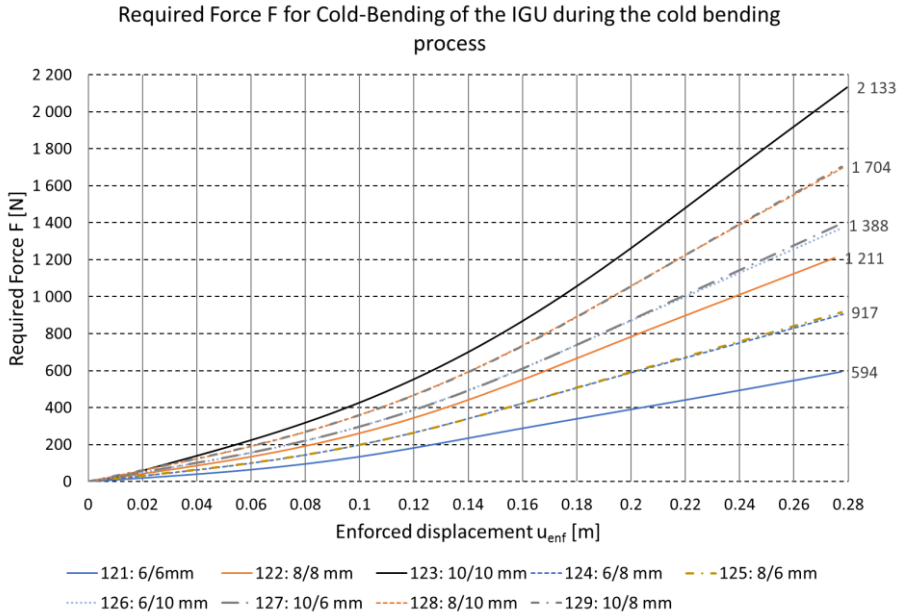

Figure 179: Double-bent model for variation 1, required force F for cold-bending of the IGU

6.4.1.2 Movement of the corners in the xy-plane

In order to assess the movement of corner D, the x-direction and the y-direction are examined. The movement of corner D is examined at the same node where the boundary conditions (BCs) for the enforced displacement $w(t)$ are applied. From Figure 180, a similar increase over time for all models can be observed. In comparison to each other, all IGUs with a smaller sum of $t_{gp,1} + t_{gp,2}$ do exhibit a slightly larger movement in the xy-plane $\left(\sqrt{x(t)^2 + y(t)^2}\right)$ over time.

Therefore it can be stated that the thickness of the glass panes do not have a significant influence on the movement of the corner points.

[14] This is estimated by $\frac{I_{x-x,spacer}}{I_{x-x,spacer}+I_{x-x,glass}+I_{x-x,silicone}} * 100\ [\%]$ with $\frac{704\ [mm^4]}{27051\ [mm^4]} * 100$ for (121: 6/6 [mm]) and $\frac{704\ [mm^4]}{125051\ [mm^4]} * 100$ for (123: 10/10 [mm]) like in subchapter 6.2.4.1.

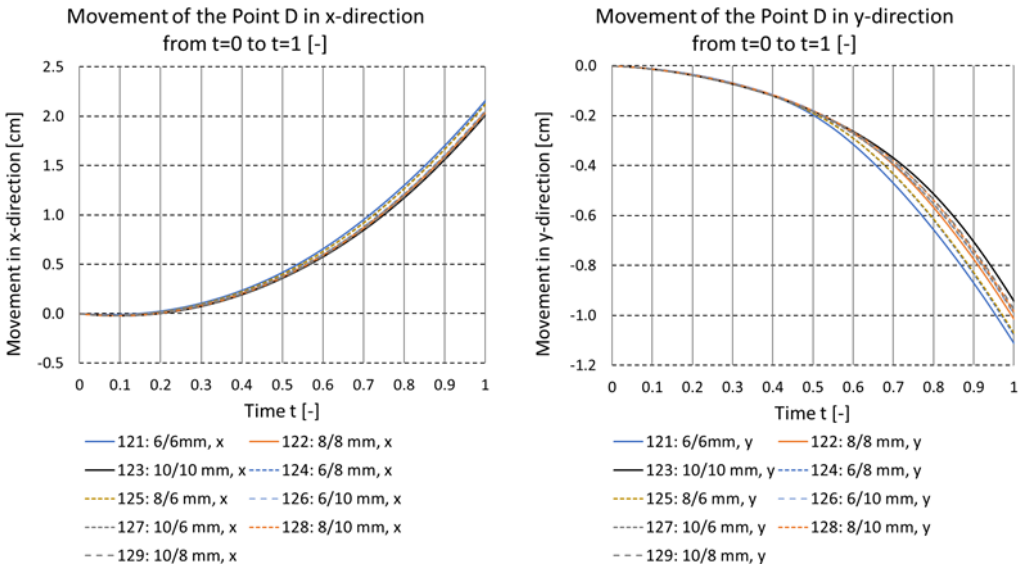

Figure 180: Double-bent model for variation 1, movement of the corner D in the xy-plane from t=0 to t=1 [-]

6.4.1.3 Distortion of the edge zone

In Figure 181, the non-linear edge deformation Δu_3 along $\overline{CD}$ is depicted. In Figure 182, Δu_3 along $\overline{BD}$ it is depicted. In both cases, the result path lies at the upper edge of glass pane 2.

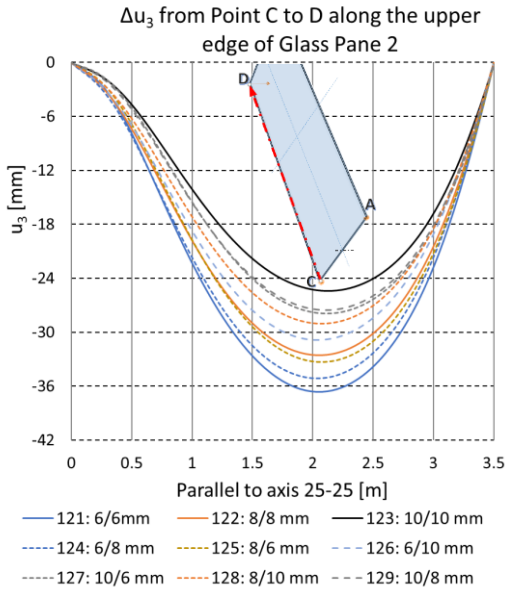

Figure 181: Double-bent model for variation 1, Δu_3 from corner C to D along the upper edge of glass pane 2

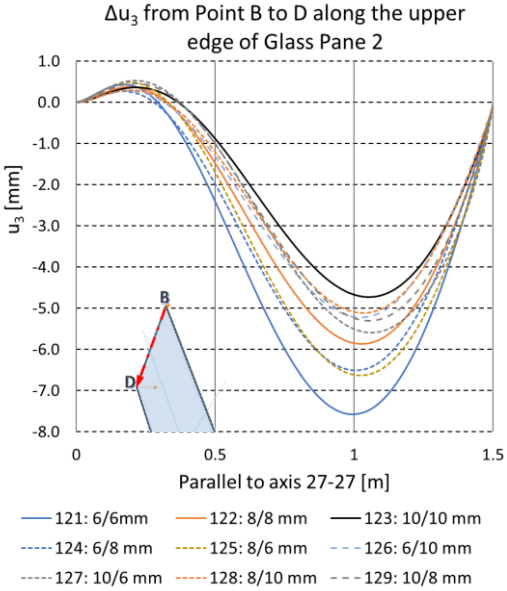

Figure 182: Double-bent model for variation 1, Δu_3 from corner B to D along the upper edge of glass pane 2

Along $\overline{CD}$, model (123: 10/10 [mm]) has an amplitude of $-25\ [mm]$. For model (121: 6/6 [mm]), the amplitude is $-37\ [mm]$ which is an increase of about 48% compared to model (123: 10/10 [mm]). Along $\overline{BD}$ for model (123: 10/10 [mm]), the amplitude is $-4.5\ [mm]$. For model (121: 6/6 [mm]) the amplitude is $-7.5\ [mm]$ which is an increase of about 67% compared to model (123: 10/10 [mm]). Model (123: 10/10 [mm]) has the lowest amplitude and the variation (121: 6/6 [mm]) has the highest amplitude. From this it can be seen, that the deformation gets bigger for a smaller pane thickness. All curves do have the same characteristics which means that the load transfer in the IGU does not change.

6.4.1.4 Glass pane

In Figure 183, $\sigma_{max,pr}$ along axis 22-22 in glass pane 1 is depicted. In the edge region, stress peaks occur due to singularities. Despite numerical singularities, increased stresses have to be expected in the vicinity of the corner region. There, $\sigma_{max,pr}$ is about $32\ \left[\frac{N}{mm^2}\right]$ for model (123: 10/10 [mm]) and $24\ \left[\frac{N}{mm^2}\right]$ for model (121: 6/6 [mm]). Increased stresses in the center region at $1.90\ [m]$ are the highest for (127: 10/6 [mm]) with a value of $23\ \left[\frac{N}{mm^2}\right]$ and the lowest for (126: 6/10 [mm]) with a value of $16\ \left[\frac{N}{mm^2}\right]$. It can be observed, that a greater ratio of $\frac{t_{gp,1}}{t_{gp,2}}$ leads to a greater stress gradient along axis 22-22 for the thicker one of both glass panes. Moreover, $\sigma_{max,pr}$ in the center region at $1.90\ [m]$ can be significant for the thicker of both glass panes if the ratio of $\frac{t_{gp,1}}{t_{gp,2}}$ is high.

In Figure 184, the deformation curves of axis 22-22 for u_3 are depicted. The curves exhibit a deformation plateau in the center region which coincides with the increased stresses. For a thinner t_{gp}, the deformation plateau is more pronounced than for thicker t_{gp}. For instance, for model (123: 10/10 [mm]), no deformation plateau is apparent. It can be assumed, that the membrane stresses in a smaller t_{gp} have a bigger effect which lead to a deformation plateau and an increase in $\sigma_{max,pr}$.

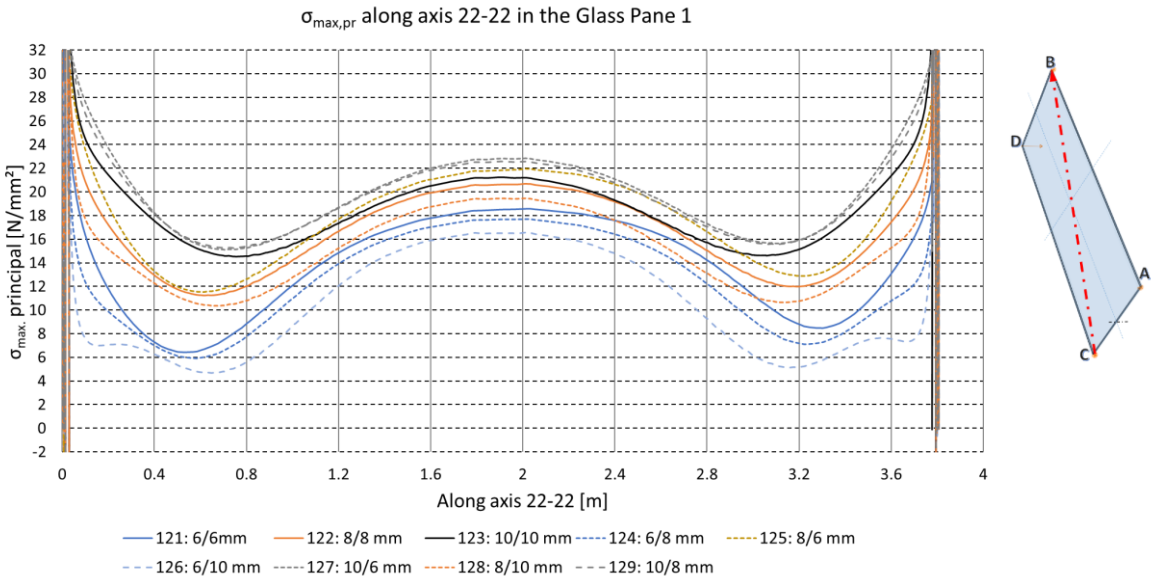

Figure 183: Double-bent model for variation 1, $\sigma_{max,pr}$. along axis 22-22 in the glass pane 1

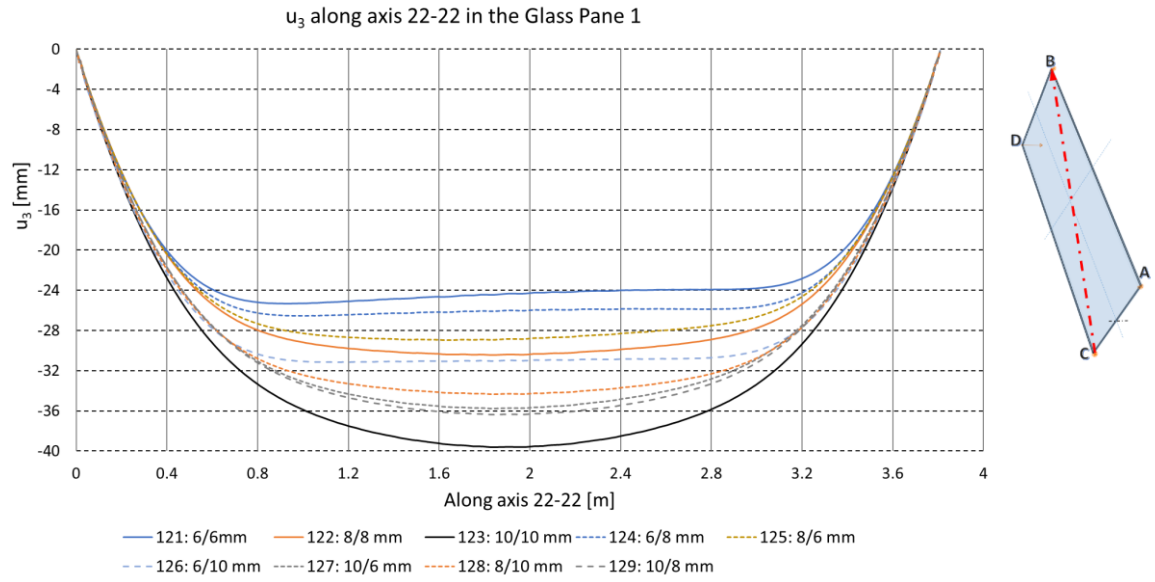

Figure 184: Double-bent model for variation 1, u_3 along axis 22-22 in the glass pane 1

In Figure 185, $\sigma_{max,pr}$ along axis 24-24 is shown. At $0.25\ [m]$ and at $3.55\ [m]$, stress peaks occur. In the center region, a cusp-shaped stress peak is present. For all series with $t_{gp,1} = 10\ [mm]$, the significant stress is about $28\ \left[\frac{N}{mm^2}\right]$. For all series with $t_{gp,1} = 8\ [mm]$, the significant stress is about $23\ \left[\frac{N}{mm^2}\right]$. For all series with $t_{gp,1} = 6\ [mm]$, the significant stress is about $18\ \left[\frac{N}{mm^2}\right]$. Like for axis 22-22, $\sigma_{max,pr}$ in axis 24-24 reaches the highest values for (127: 10/6 [mm]) and decreases for all models with

a smaller ratio $\frac{t_{gp,1}}{t_{gp,2}}$ until (126: 6/10 [mm]). It can be observed, that for $t_{gp,1} > t_{gp,2}$, the stress in $t_{gp,1}$ is higher. Furthermore, it can be deduced that the stress in $t_{gp,2}$ is higher for $t_{gp,1} < t_{gp,2}$.

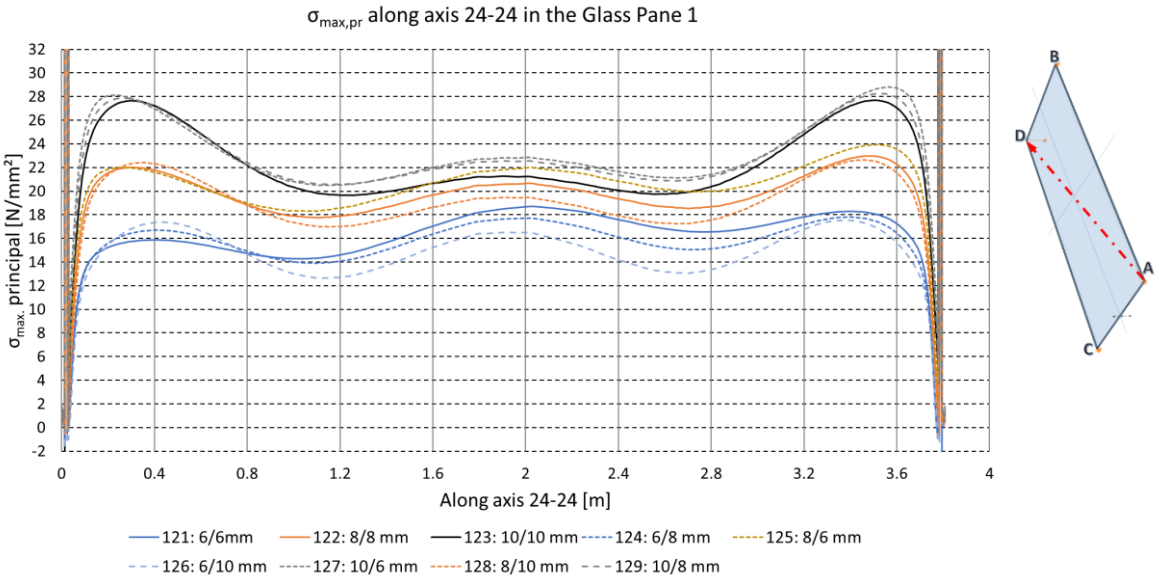

Figure 185: Double-bent model for variation 1, $\sigma_{max,pr}$. along axis 24-24 in the glass pane 1

In Figure 186, the corresponding deformations to Figure 185 in axis 24-24 are shown. In each case, $u_3 > 0$ has a zero crossing between $1.2\ [m]$ and $1.5\ [m]$. Thinner glass panes have a higher positive amplitude and their zero crossing is nearer to corner D. Hence, they also have the highest deformation gradient $\frac{\partial u_3}{\partial 24-24}$ for the same enforced displacement. The biggest absolute difference for the positive amplitude occurs between model (121: 6/6 [mm]) and model (123: 10/10 [mm]) and is $13\ [mm]$. In addition, model (121: 6/6 [mm]) has the highest deformation gradient and model (123: 10/10 [mm]) has the lowest deformation gradient.

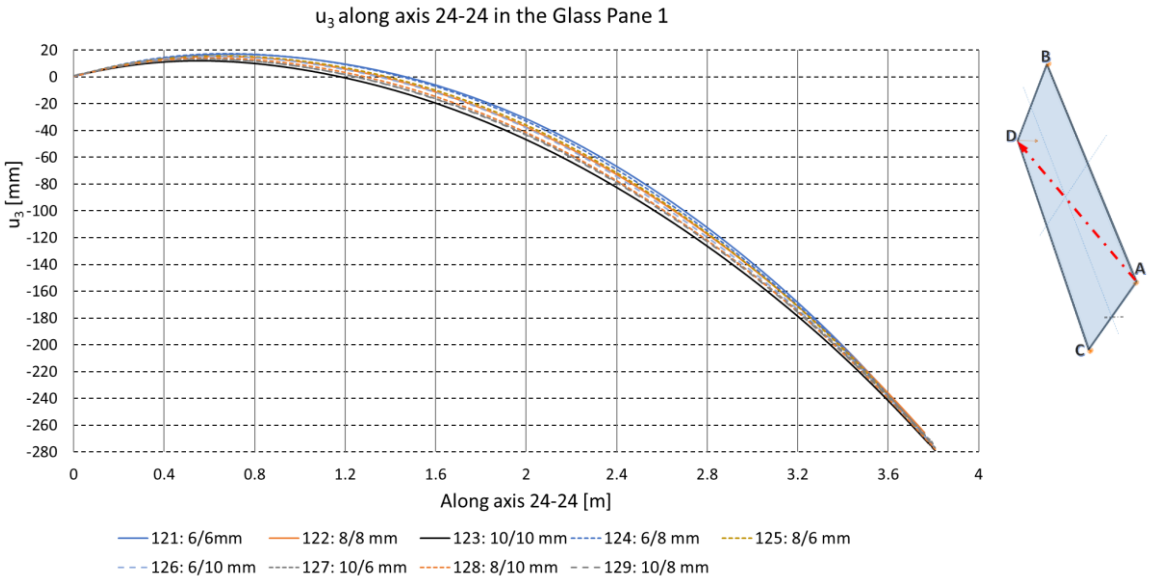

Figure 186: Double-bent model for variation 1, u_3 along axis 24-24 in the glass pane 1

6.4.1.5 Spacer bar

In Figure 187, the von Mises stress σ_e is illustrated for the longitudinal spacer along axis 26-26. In Figure 188, σ_e is illustrated for the broadside spacer along axis 27-27. In both cases, σ_e reaches higher values for a smaller t_{gp}. The stress in the longitudinal spacer is at the back end next to corner C higher for a high t_{gp}. This relationship turns around between $0.75\ [m]$ and $1.20\ [m]$. After that, σ_e increases towards corner D until the spacer undergoes plasticization for all models from $3.35\ [m]$ to $3.49\ [m]$. Like in the longitudinal spacer, a turnaround point in the stress curves of the broadside spacer is evident. In this case, the turnaround point occurs after $0.40\ [m]$ for model (121: 6/6 [mm]) and after $0.55\ [m]$ for model (123: 10/10 [mm]). In axis 27-27, the spacer undergoes plasticization from $0.8\ [m]$ to the front end at corner D for (121: 6/6 [mm]). For model (123: 10/10 [mm]), plasticization occurs from $1.0\ [m]$ on. Along the plastifying area in axis 27-27, σ_e reaches a stress plateau which has a value of about $255\ [N/mm^2]$ for all series.

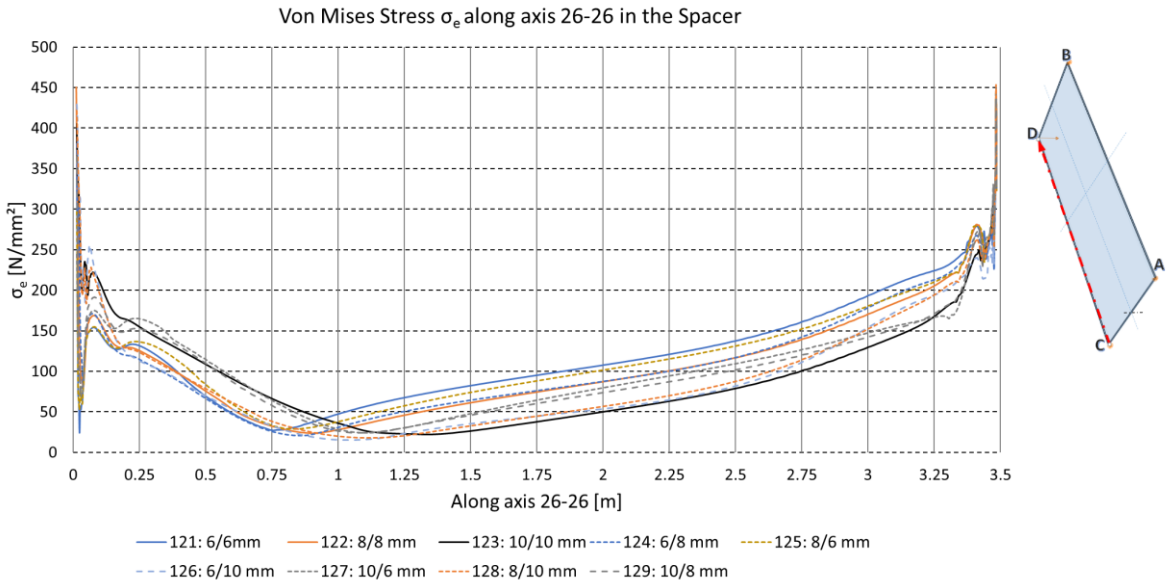

Figure 187: Double-bent model for variation 1, von Mises stress σ_e along axis 26-26 in the spacer

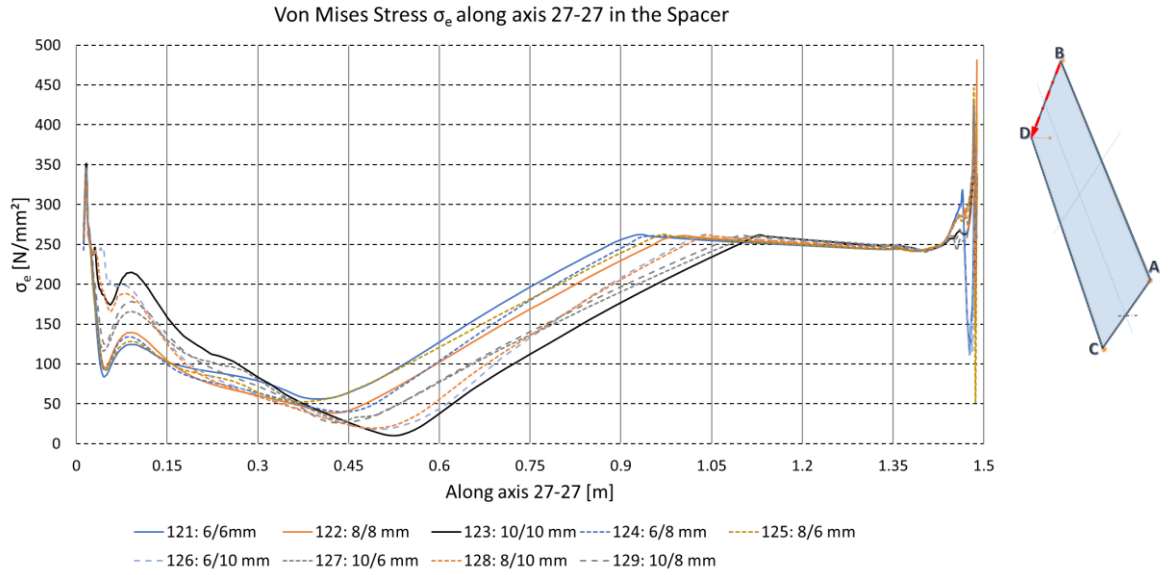

Figure 188: Double-bent model for variation 1, von Mises stress σ_e along axis 27-27 in the spacer

In Figure 189, the stresses σ_{xx} (coincides with the global x-direction) and σ_{yy} (coincides with the global y-direction) are depicted for model (122: 8/8 [mm]) at corner D. For the last time step at $w(t = 1) = 0.277\ [m]$, the stress in the edge of the spacer is above the yielding point of the stainless steel which is $230\ \left[\frac{N}{mm^2}\right]$. At time step $t = \frac{2}{3}$ at $w(t = \frac{2}{3}) = 0.185\ [m]$, the stress is already increased in the lower and upper edge

zone. If it is required, a reduction of the imposed deformation can reduce the plasticizing area in the spacer to a large degree.

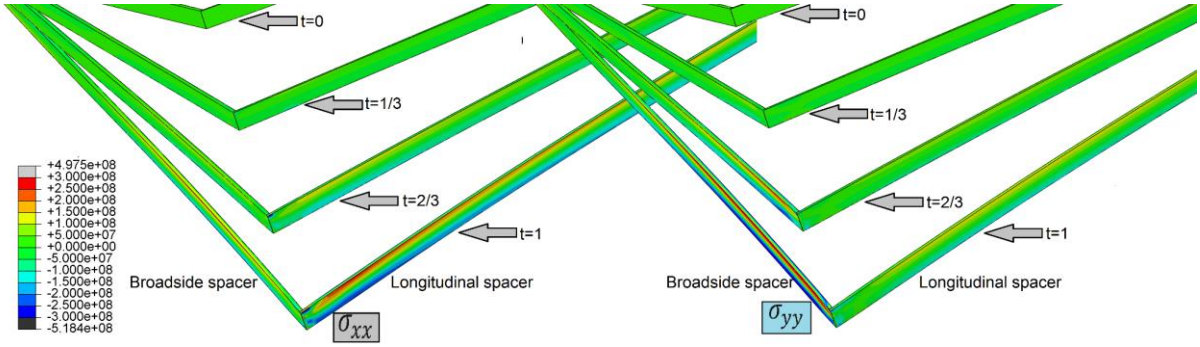

Figure 189: Double-bent model for variation 5, σ_{xx} and σ_{yy} for different time steps

6.4.1.6 Deformation of the edge zone

In Figure 190, axis S26-S26 is depicted. For u_1, all deformation curves are the same if deviations in a range of $\pm 0.01\ [mm]$ are neglected. The shear displacement $\Delta\alpha$ is approximately 12.5% and the maximum deformation at $z = 16\ [mm]$ is approximately $-2\ [mm]$. For u_2, the deformation curves are depending on $t_{gp,i}$. Curves for a $t_{gp,i} = 10\ [mm]$ have an increased amplitude in comparison to all other models. For example, the amplitude is $0.35\ [mm]$ for model (123:10/10 [mm]) and $0.24\ [mm]$ for model (127: 10/6 [mm]). The smallest maximum amplitude is $0.07\ [mm]$ for model (121: 6/6 [mm]).

In Figure 191, axis S29-S29 is depicted. For u_1, the biggest deformation value occurs for model (123: 10/10 [mm]) and is -1.4 [mm]. The smallest maximum deformation value occurs for model (121: 6/6 [mm]) and is -1.2 [mm]. The characteristics of all deformation curves are the same like for u_1 in axis S26-S26.

Putting the deformation at $w(t = 1) = 0.277\ [m]$ for axis S26-S26 and axis S29-S29 into a common context, then both are exhibiting a steadily increasing amplitude of u_1 in the negative x-direction for a bigger $t_{gp,i}$. This indicates a uniform deformation of the edge zone of the IGU. In contrast to u_1, u_2 does not increase steadily but instead has two turning points. These two turning points are intensively pronounced along axis S29-S29. This indicates, that glass pane 2 is slipping onto the spacer forward by a larger amount than the rest of the IGU. The deformation of u_1 is always higher than u_2. Both deformation components are pointing towards the negative direction of x or y.

Axis S21-S21 was not examined in this subchapter because it's amplitudes are not significant. Furthermore, the values in axis S21-S21 does not differ from the reference model in subchapter 6.3.4.

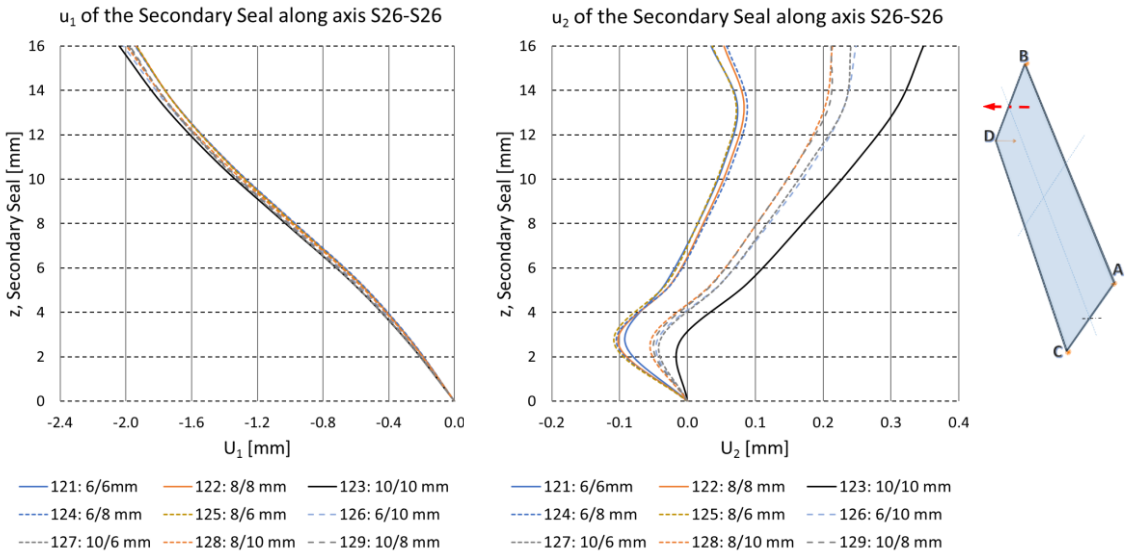

Figure 190: Double-bent model for variation 1, max. displacement of the secondary seal along axis S26-S26

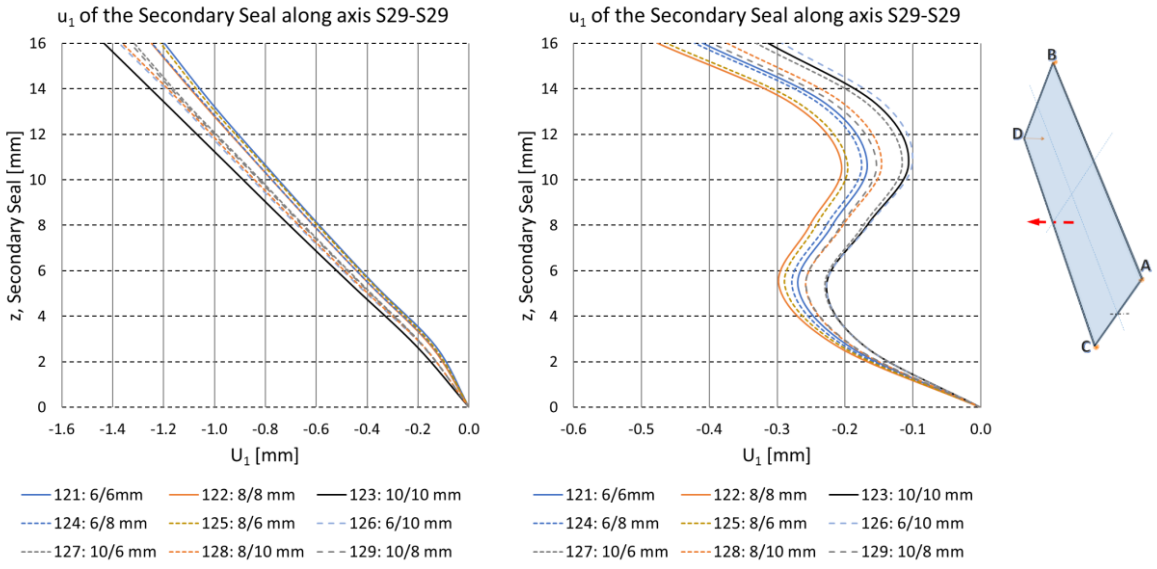

Figure 191: Double-bent model for variation 1, max. displacement of the secondary seal along axis S29-S29

6.4.2 Aspect ratio - Variation 5

In this subchapter, a parameter study about the influence of the aspect ratio on the overall behavior of the double-bent IGU system is carried out. Different aspect ratios are obtained by varying the total length l_{gp} of the IGU. The width w_{gp} of the IGU stays constant during the whole parameter study. The enforced displacement $u_{enf} = w(t = 1) = 0.20\ [m]$ has the same value for all models. The following lengths of the IGU l_{gp} are considered: $1.50\ [m]$, $2.00\ [m]$, $2.50\ [m]$, $3.00\ [m]$, $3.50\ [m]$, $4.67\ [m]$, $5.83\ [m]$ and $7.00\ [m]$. The different models are also listed in Table 18 and are also depicted as a schematic longitudinal section in Figure 192.

Double-Bent	1.50 m	2.00 m	2.50 m	3.00 m	3.50 m	4.67 m	5.83 m	7.00 m
522	X							
523		X						
524			X					
525				X				
526					X			
527						X		
528							X	
529								X

Table 18: Variation 52: Different aspect ratios of the IGU

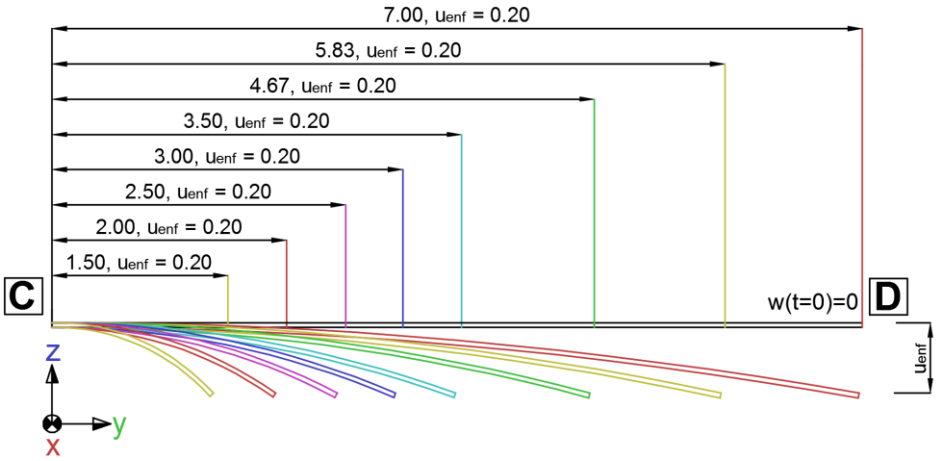

Figure 192: Variation 52: Different aspect ratios of the IGU, values in the sketch in meters

6.4.2.1 Required force for the cold bending process

The required force F for cold-bending of the IGU from $w(t=0)=0\ [m]$ to $w(t=1)=0.20[m]=u_{enf}$ is depicted in Figure 193. The highest value for F at $w(t=1)=0.20\ [m]$ is required for model (522: 1.5 [m]) and is $1841\ [N]$. F declines with a longer l_{gp} and is just $302\ [N]$ for a l_{gp} of $7.00\ [m]$. Recalculating the required moment M for cold bending with a simplified relationship $M=F*l_{gp}$ reveals that $M=2.8\ [kNm]$ within a wide range of $1.5\leq l_{gp}\leq 3.5$. Furthermore, M steadily decreases for $l_{gp}>3.5\ [m]$ until $M=2.1\ [kNm]$ for $l_{gp}=7.00\ [m]$. Hence, a big lever arm has a small influence for $l_{gp}>3.5\ [m]$ on F. Also interesting is the fact, that after $w(t=0.5)=0.10\ [m]$, the increase of the average gradient of force per displacement is about 1.6 times higher for any l_{gp}. For example, model (529: 7.00 [m]) has an average "force per displacement" gradient of $11.6\ [N/cm]$ for the first $10\ [cm]$. For the last $10\ [cm]$, it has an average gradient of $18.6\ [N/cm]$, which is 1.6 times higher.

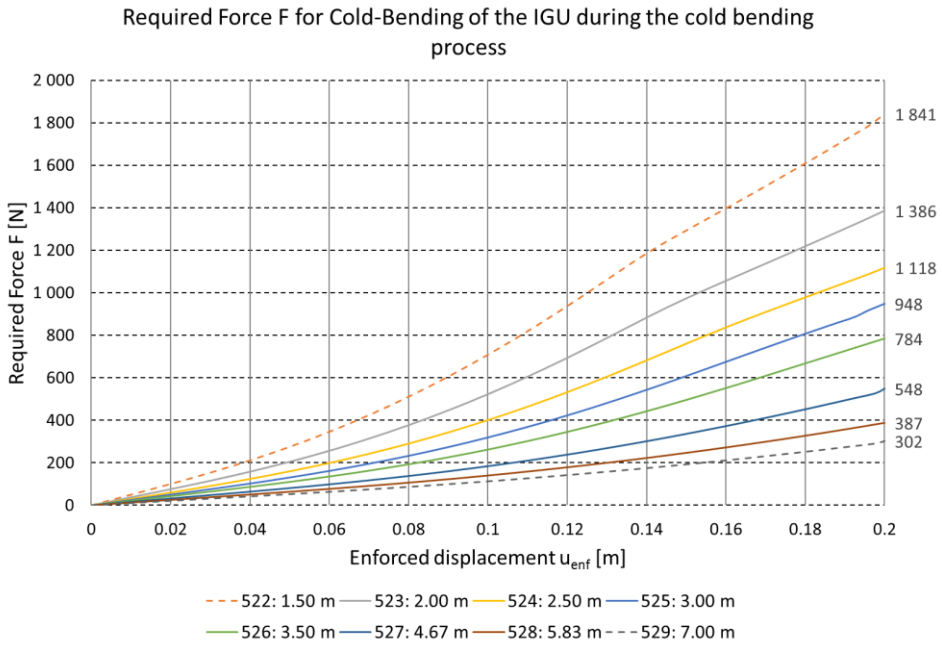

Figure 193: Double-bent model for variation 5, required force F for cold-bending of the IGU

Note that for the reference model and for the parameter study in subchapter 6.4.1, $w(t=1)=0.277[m]=u_{enf}$ but this value had to be lowered in order to get comparable results also for the models (522: 1.50 [m]) and (523: 2.00 [m]). These models undergo numerical instabiities for $w>0.25\ [m]$. (521: 0.75 [m]) with an IGU

length of $l_{gp} = 0.75\ [m]$ is excluded for the double-bent case because for $w > 0.16\ [m]$ it is numerically unstable.

6.4.2.2 Movement of the corners in the xy-plane

In order to assess the movement of corner D, the x-direction and the y-direction are examined, which is depicted in Figure 194. The movement of corner D is examined at the same node where the boundary condition (BC) for the imposed displacement $w(t)$ is applied.

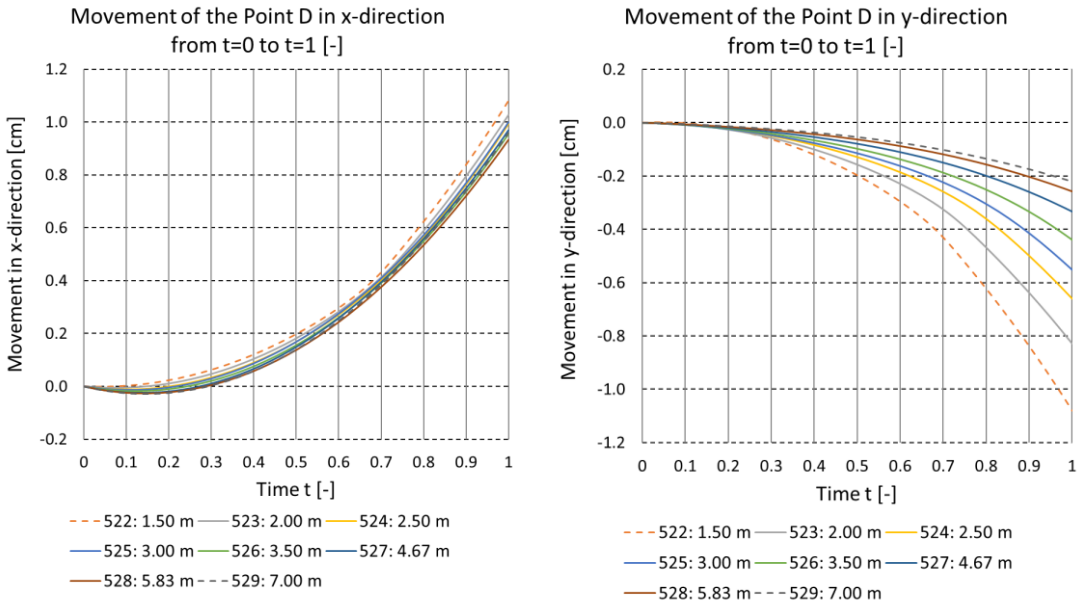

Figure 194: Double-bent model for variation 5, movement of the corner D in the xy-plane from t=0 to t=1 [-]

For u_1, the deformation curves show to be independent from the aspect ratio. Recall from subchapter 6.4.1, that the curves in x-direction are also independent from $t_{gp,i}$. As a consequence, only u_1 increases according to a growing $w(t)$ and the rate of growth depend only on the support situation. For u_2, the deformation curves are increasing accordingly to a high aspect ratio (or a small l_{gp}). Within the xy-plane, the movement of corner D compared to the corners A, B and C is the largest. This is not only true for the last time step but for all time steps.

6.4.2.3 Glass pane

In Figure 195, $\sigma_{max,pr}$ along axis 22-22 is depicted. In the middle of the diagonal, which is at $\frac{1}{2}\sqrt{l_{gp}^2 + w_{gp}^2}$ ($w_{gp} = 1.50\ [m]$), a stress peak occurs for all models $1.50 \leq l_{gp} \leq 4.67\ [m]$. Left and right to the stress peak, a stress valley is present. The position of the minimum stress value in axis 22-22 is roughly at $\frac{1}{4}\sqrt{l_{gp}^2 + 2.25}$ and at $\frac{3}{4}\sqrt{l_{gp}^2 + 2.25}$. This is more accurate for models with a higher l_{gp} because the influence of the edge region gets smaller. For model (522: 1.50 [m]), the minimum value is $12\left[\frac{N}{mm^2}\right]$ and the maximum value is $25.9\left[\frac{N}{mm^2}\right]$. Calculating the ratio between $\max(\sigma_{max,pr})$and $\min(\sigma_{max,pr})$ for model (522: 1.50 [m]) gives a value of 2.16[15]. This characteristic value gives an insight of the influence from membrane stress. This ratio decreases steadily for models with a longer l_{gp} and is 1.05 for model (527: 4.67 [m]). The models (528: 5.83 [m]) and (529: 7.00 [m]) do not have a stress peak which means, that no membrane stress is present.

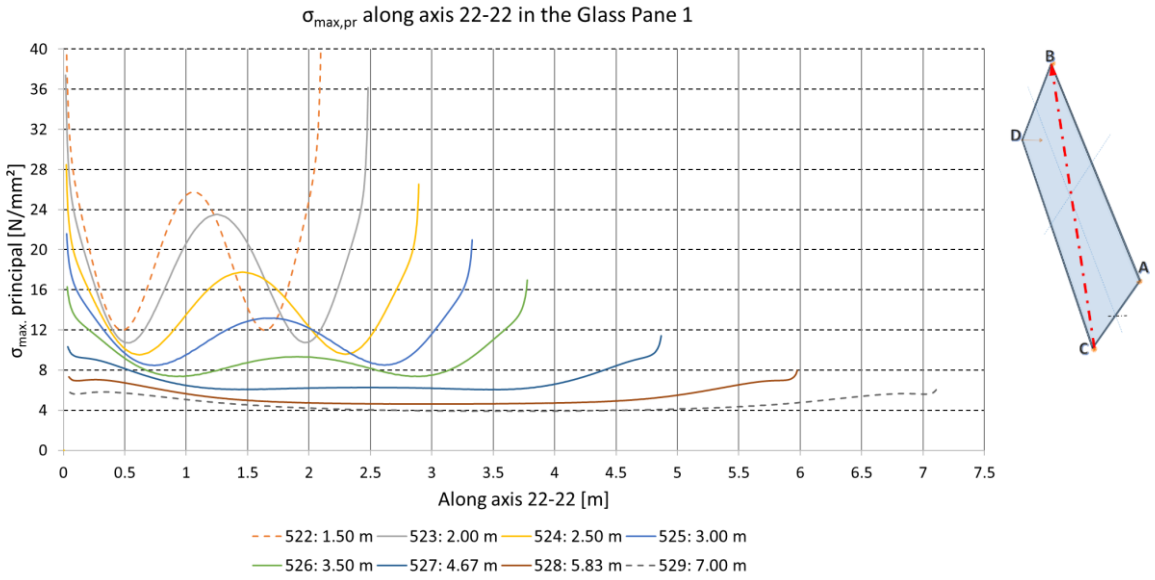

Figure 195: Double-bent model for variation 5, double-bent, $\sigma_{max,pr}$ along axis 22-22 in the glass pane 1

In Figure 196, the vertical displacement u_3 along axis 22-22 is depicted. The maximum amplitude of deformation is increasing monotonously. For model (522: 1.50 [m]), u_3 is

[15] The ratio is calculated for a maximum principal stress which exists in the boundaries $\frac{1}{4}\sqrt{l_{gp}^2 + 2.25} \leq \max(\sigma_{max,pr}(22-22))/(\min(\sigma_{max,pr}(22-22))) \leq \frac{3}{4}\sqrt{l_{gp}^2 + 2.25}$

$-28.3\ [mm]$ and for model (529: 7.00 [m]), u_3 is $-37.6\ [mm]$ which is 33% higher. The deformation amplitude between (522: 1.50 [m]) and (523: 2.00 [m]) is only 0.8% increased. From model (528: 5.83 [m]) to (529: 7.00 [m]), u_3 increases only 0.2%. As it is visible, u_3 increases significantly for $2.50 \leq l_{gp} \leq 4.67\ [m]$ or rather for an aspect ratio of $\frac{5}{3} \leq \frac{l_{gp}}{w_{gp}} \leq \frac{28}{9}$. Exceeding this limits leads to an insignificant change of maximum deformation in axis 22-22. It is assumable, that membrane stresses have a substantial effect on the deformation for small aspect ratios. For an increasing aspect ratio, the influence of the membrane stresses is declining and does not have a noticeable effect for $\frac{l_{gp}}{w_{gp}} > \frac{28}{9}$ anymore which is in accordance with $\sigma_{max,pr}$.

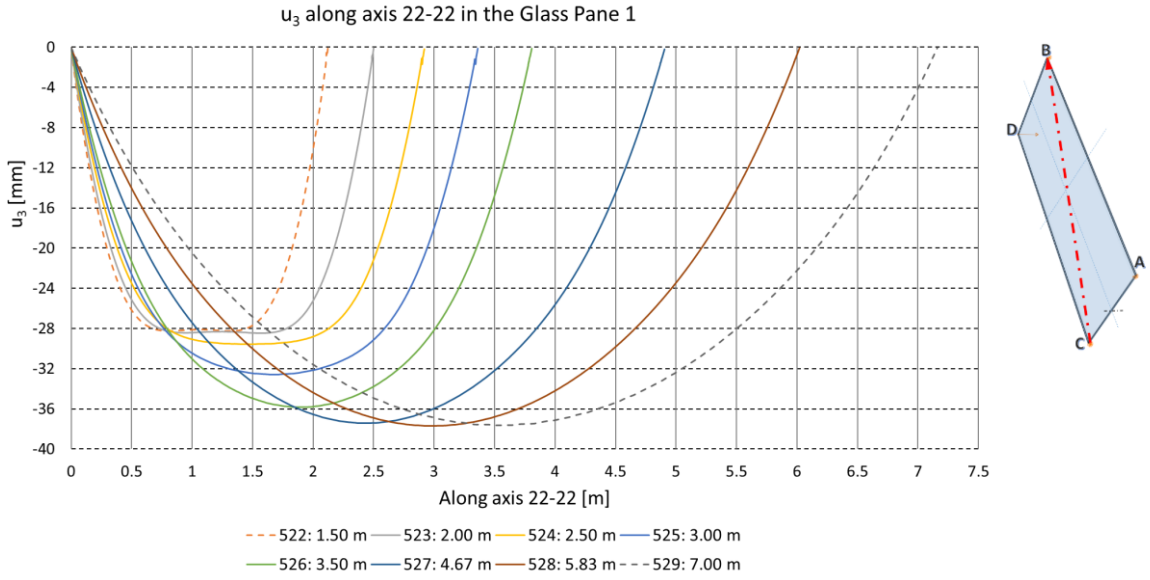

Figure 196: Double-bent model for variation 5, double-bent, u_3 along axis 22-22 in the glass pane 1

In Figure 197, $\sigma_{max,pr}$ along axis 24-24 is depicted. The stress curve increases from corner A on until it reaches a stress peak. This stress peak is located for all models before $\frac{1}{3}\sqrt{l_{gp}^2 + 2.25}$. For all models, $\sigma_{max,pr}$ reaches a local minimum at $\frac{1}{2}\sqrt{l_{gp}^2 + 2.25}$. Comparing the maximum values $\sigma_{max,pr}$ of axis 22-22 and axis 24-24 leads to two observations. Firstly, the maximum values in axis 22-22 are higher if the corner region is taken into account. However, $\sigma_{max,pr}$ in the corner region can be reduced by a soft intermediate layer between the support and the glass which is not considered in this work. Secondly, if the stress peaks at the corners C and B in axis 22-22 are excluded then $\sigma_{max,pr}$ in axis 24-24 is always higher.

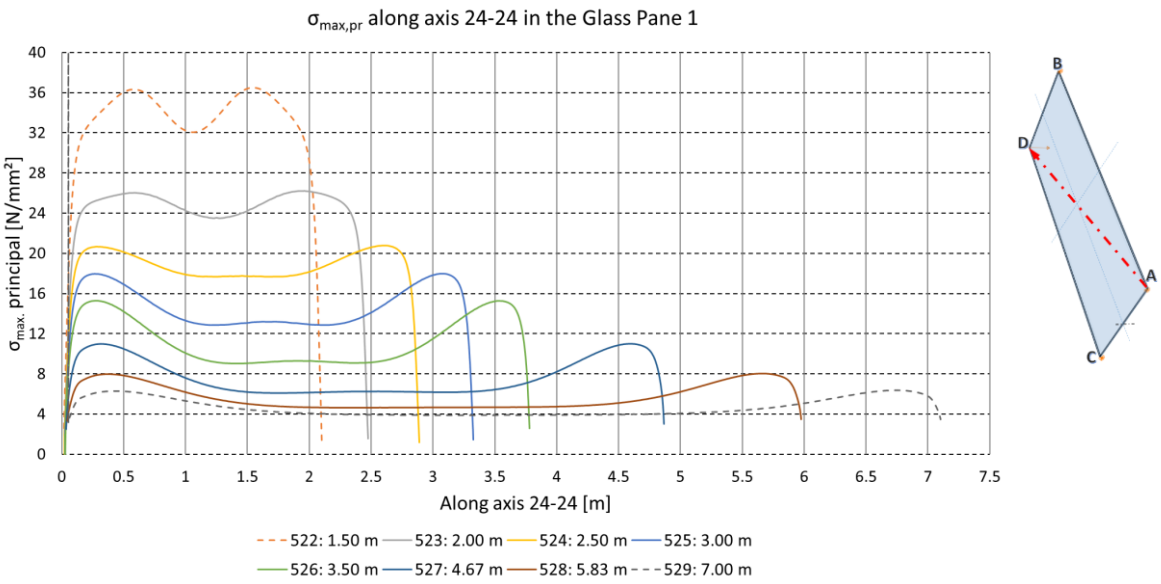

Figure 197: Double-bent model for variation 5, double-bent, $\sigma_{max,pr}$ along axis 24-24 in the glass pane 1

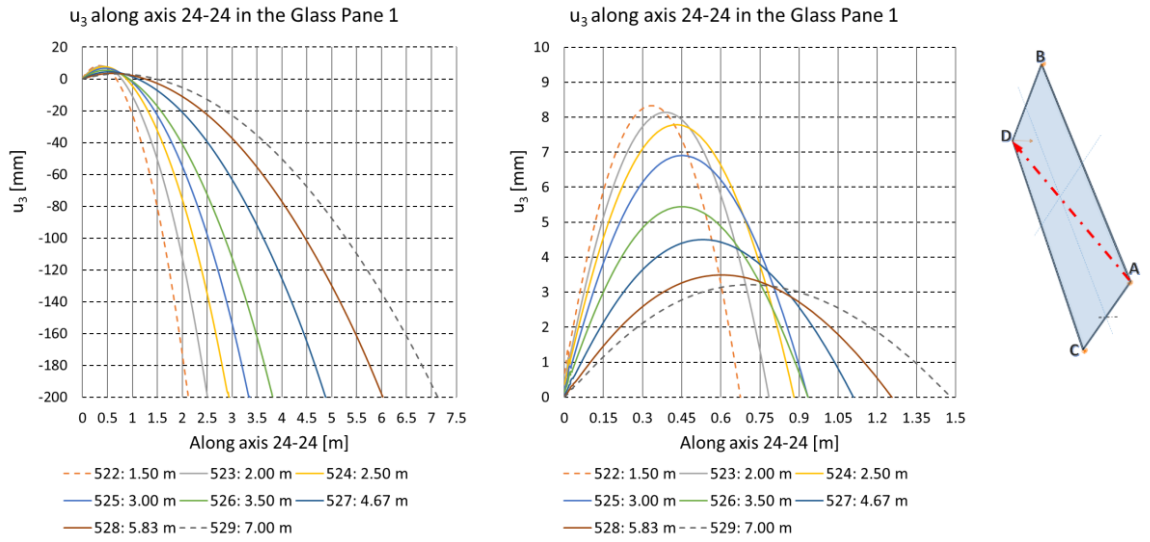

Figure 198: Double-bent model for variation 5, u_3 along axis 24-24 in the glass pane 1

In Figure 198, the vertical deformation u_3 is depicted along axis 24-24 from $0\ [m]$ to $\sqrt{l_{gp}^2 + 2.25}\ [m]$ ($w_{gp} = 1.50\ [m]$) on the left side and from $0\ [m]$ to $1.50\ [m]$ on the right side. The bending figure is smooth for all models and all curves are exhibiting the same characteristics. A close-up view in Figure 198 on the right side unveils a bigger difference between the curves. The smaller l_{gp} is, the higher is the amplitude at the turning point. The maximum amplitude is $8.2\ [mm]$ at $0.33\ [m]$ for model (522: 1.50 [m]). The turning point moves along axis 24-24 towards point D and gets smaller for a

longer l_{gp} and is $3.2\ [mm]$ at $0.69\ [m]$ for model (529: 7.00 [m]). The zero crossing lies at $0.67\ [m]$ for model (522: 1.50 [m]) and moves forward to $1.49\ [m]$ for model (529: 7.00 [m]). If the position of the turning point at axis 24-24 is called "a", then the zero crossing is always located approximately at $2a$, but never after $2a$. Therefore, the maximum gradient along axis 24-24 occurs for the smallest $\sqrt{l_{gp}^2 + 2.25}$ or rather for the shortest diagonal. This relationship between a high aspect ratio and a high deformation gradient has to be taken into account, when examining the admissible distortion and hence optical quality of a double-bent IGU.

6.4.2.4 Spacer bar

In Figure 199, the von Mises stress σ_e in the spacer along axis 26-26 is depicted. At $0.0065\ [m]$ and at $l_{gp} - \left(\underbrace{0.0065}_{w_{sp}} + \underbrace{0.005}_{w_{ss}}\right)\ [m]$, stress peaks which are caused by numerical singularities are present. A global stress minimum occurs between $\frac{1}{3} l_{gp}$ and $\frac{2}{3} l_{gp}$ which is $40\ \left[\frac{N}{mm^2}\right]$ for model (522: 1.50 [m]) and declines for longer spacers. For model (529: 7.00 [m]), σ_e is $11\ \left[\frac{N}{mm^2}\right]$. A stress peak occurs at $0 < \max(\sigma_e)_1 < \frac{1}{3} l_{gp}$ and a second stress peak occurs at $\frac{2}{3} l_{gp} < \max(\sigma_e)_2 < l_{gp}$. For all models within a range of $1.50 \leq l_{gp} \leq 3.00\ [m]$, the significant stress comes from the second stress peak $\max(\sigma_e)_2$. For all models within a range of $3.50 \leq l_{gp} \leq 7.00\ [m]$, the significant stress comes from the first stress peak $\max(\sigma_e)_1$. All models within a range of $1.50 \leq l_{gp} \leq 2.50\ [m]$ undergo yielding in the spacer. In general, it can be stated that the higher the aspect ratio $\frac{l_{gp}}{w_{gp}}$ is, the lower the significant stress in the longitudinal spacer is.

In Figure 200, the von Mises stress σ_e in the spacer along axis 27-27 is depicted. At $0.0115\ [m]$, all spacers are yielding except for model (528: 5.83 [m]) and for model (529: 7.00 [m]). At $1.4885\ [m]$, all spacers are yielding except for model (527: 4.67 [m]), (528: 5.83 [m]) and (529: 7.00 [m]).

Between $\frac{1}{3} w_{gp} < w_{gp}(27-27) < \frac{1}{2} w_{gp}$, a global stress minimum in all spacers is present. All models have an extended plasticizing area which is shorter for a higher

aspect ratio $\frac{l_{gp}}{w_{gp}}$. For example, the plasticizing area ranges from $1\ [m]$ up to $1.4885\ [m]$ for (522: 1.50 [m]).

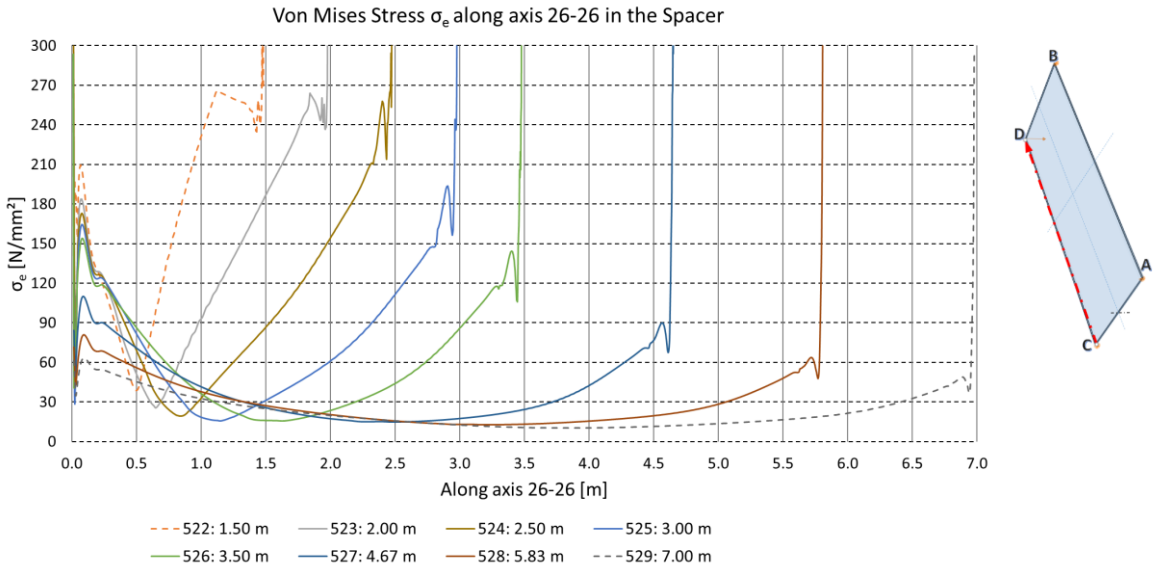

Figure 199: Double-bent model for variation 5, von Mises stress σ_e along axis 26-26 in the spacer

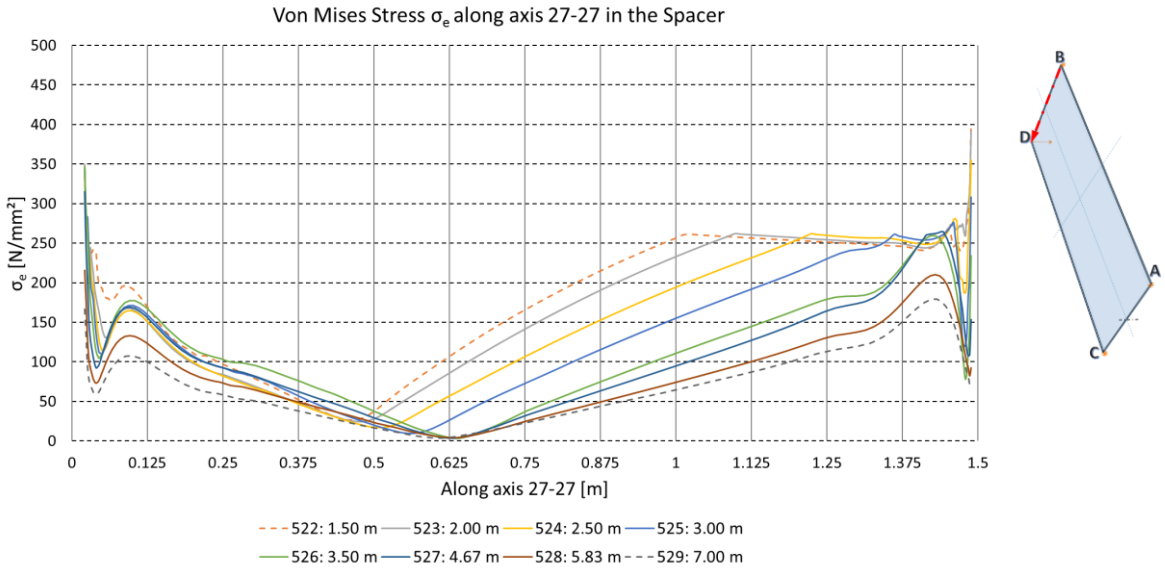

Figure 200: Double-bent model for variation 5, von Mises stress σ_e along axis 27-27 in the spacer

6.4.2.5 Deformation of the edge zone

Figure 201 shows u_1 and u_2 in axis S26-S26. The shear deformation for u_1 increases from (522: 1.50 [m]) to (529: 7.00 [m]) in the negative x-direction. For the curve (522: 1.50 [m]), two turning points are visible. They diminish gradually in accordance with

an increasing l_{gp}. For u_2, the maximum amplitude is the highest for (522: 1.50 [m]) and decreases gradually with an increasing l_{gp}. Both deformation components u_1 and u_2 are deforming in the same direction like in variation 1 but the deformation values differ in a wider range.

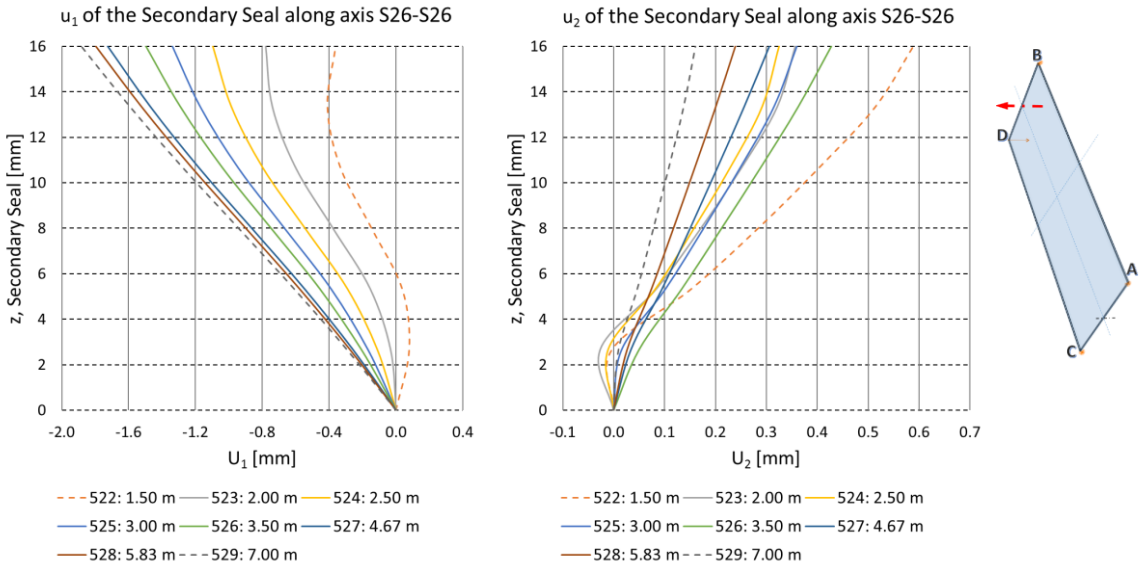

Figure 201: Double-bent model for variation 5, max. displacement of the secondary seal along axis S26-S26

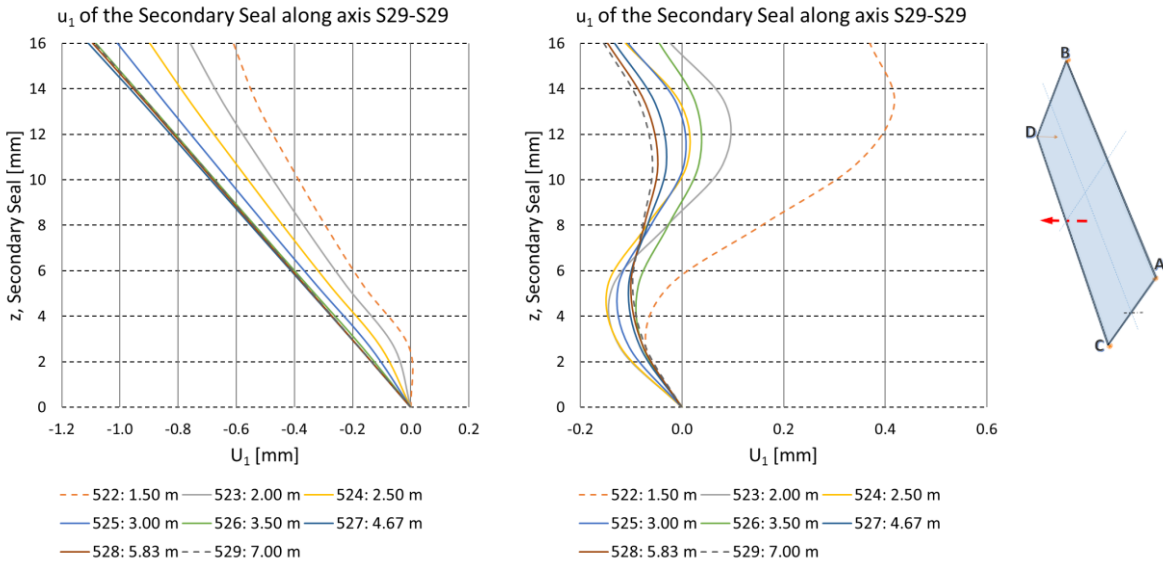

Figure 202: Double-bent model for variation 5, max. displacement of the secondary seal along axis S29-S29

Axis S29-S29 in Figure 202 shows u_1 and u_2. The maximum shear deformation in u_1 increases from $-0.6\ [mm]$ for (522: 1.50 [m]) to $-1.1\ [mm]$ for (529: 7.00 [m]). The shear deformation in u_2 differs slightly for all models except for (522: 1.50 [m]) which

has a maximum amplitude of $0.4\ [m]$. Compared to u_1, u_2 has two pronounced turning points which was also the case in variation 1.

6.4.3 Discussion of the results for the double-bent IGU

In this subchapter, the most important findings from the double-bent parameter study in chapter 6.4 are summed up. For parameter variation 1 and 5, the influence of the current parameter is described for the glass panes, the spacers and the secondary seal. An overarching summary is provided along with the conclusions in chapter 7. Based on the findings in chapter 6.3, variation 2, 3 and 4 were not performed for the double-bent IGU.

Thickness of the glass pane - Variation 1

The absolute displacement of the IGU in the xy-plane is almost the same for all glass panes. The biggest values for the movement of the loaded corner D in the xy-plane are roughly $2\ [cm]$ in x-direction and $-1\ [cm]$ in y-direction at an imposed deformation of $0.277\ [m]$.

Obviously, glass pane 1 and glass pane 2 cannot deform remarkably different from each other along the edge of the IGU. As a result, the sum of the thickness of both glass panes determines the maximum deformation. If the sum of the thickness of both glass panes increases, then the deformation decreases. Along the edge $\overline{CD}$, the absolute maximum value for the smallest sum, which is $12\ [mm]$, gives a maximum deformation of $37\ [mm]$.

For the biggest sum, which is $20\ [mm]$, the maximum deformation is $25\ [mm]$. The influence of different pane thicknesses for the two glass panes is not significant.

The maximum principal stresses in the glass pane increases outside the corner regions due to membrane stresses which at the same time limit the deformations. For thin glass panes, the membrane stresses do clearly inhibit the deformations along diagonal $\overline{BC}$. The significant stress occurs in the thicker glass pane like in the single-bent model. The membrane stresses in the middle of any diagonal axis in the thicker glass pane can be significant. For thick glass panes in general, the stress at the static

support can be significant. Unlike for variation 1 in the single-bent case, the position of the maximum stress in the (thicker) glass pane cannot be predicted.

The von Mises stress in the spacer next to the thicker glass pane is lower than next to the thinner glass pane. If both glass panes have the same pane thickness, then the significant stress along the upper side next to glass pane 2 and along the lower side next to glass pane 1 are almost the same. If the pane thickness is increased, then the stress values are increasing next to the static supports. In contrast to that, the stress is decreasing next to the corner (corner D) where the controlled deformation is applied.

The deformation of the secondary seal in x-direction is roughly about 5 times bigger than in y-direction. The contribution of the z-direction (vertical direction) is negligible. For the deformation in x-direction, the dependency on the pane thickness is small (and the deformation in x-direction is increased for a smaller pane thickness). For the deformation in y-direction, the dependency on the pane thickness is significant. The deformation in y-direction tends to be higher if the thicker glass pane is glass pane 2. If the pane thicknesses are the same, then the deformation grows with thicker glass panes.

Aspect ratio - Variation 5

Corner D has the biggest absolute displacement values in x-direction and in y-direction (and obviously - from the imposed deformation - also the biggest absolute value in z-direction). The movement in the x-direction is almost the same for all aspect ratios and is about $1\ [cm]$. In contrast to that, the movement in the y-direction is bigger for a smaller length of the IGU and decreases from about $-1.1\ [cm]$ for an IGU length of $1.50\ [m]$ to $-0.2\ [cm]$ for an IGU length of $7.00\ [m]$. Interestingly, the movements in both directions have the same values for an aspect ratio of $1/1$ (or for an IGU length of $1.50\ [m]$). The maximum principal stress in the glass pane is practically the same for both glass panes. The significant stress occurs along either the diagonal $\overline{AD}$ or the diagonal $\overline{BC}$. A membrane effect is noticeable for aspect ratios in a range from $5/3$ to $28/9$ (length over width of the IGU). The maximum stress for an aspect ratio of $1/1$ is $36\ [N/mm^2]$ and decreases to about $6\ [N/mm^2]$ for an aspect ratio of $14/3$.

The von Mises stress in the broadside spacer $\overline{BD}$ is significant for all aspect ratios. The broadside spacer undergoes yielding outside the corner region next to the deformation point D. For a smaller aspect ratio, the yielding area gets bigger. For an aspect ratio of $35/9$ or bigger, the broadside spacer does not yield. Furthermore, for an aspect ratio of $35/9$ or bigger, no spacer starts yielding outside the corner region. For smaller aspect ratios, the stress in the longitudinal spacer CD increases. Next to the deformation point D, all spacers start to yield. Outside of the corner region next to corner D, the longitudinal spacer starts to yield for an aspect ratio lower or equal to $5/3$.

The deformation of the secondary seal in the y-direction is smallest for the smallest aspect ratio $1/1$ and highest for the highest aspect ratio $14/3$. However, for aspect ratios in a range of $5/3$ to $28/9$, no obvious deformation pattern is visible. This is within the range where membrane stresses have a significant influence on the glass panes.

The deformation of the edge zone in the x-direction grows with bigger aspect ratios. The significant shear displacement (in x-direction) is about 11% for an aspect ratio of $14/3$ and decreases to about 4% for an aspect ratio of $1/1$.

7 Conclusions

In this work, different cold-bent insulating glass units (IGU) were examined with the finite element method. The numerical investigations can be divided into two main parts. Firstly, single-bent IGUs which are bent on an arc-shaped subconstruction which has a constant radius were analyzed. Secondly, double-bent IGUs which are statically supported at three corners and are displaced out-of-plane at the fourth corner were examined.

From a numerically point of view, the IGU model can be split up into three main parts. These three main parts are (1) two broadside spacers and two longitudinal spacers, (2) two monolithic glass panes and (3) a circumferential secondary seal. The primary seal (butyl strip) increases numerical instability and the need for exceptional calculation expenses. In addition, the primary seal has no mechanical contribution to the IGU and hence is neglected.

Spacers which are made out of stainless steel show to be suitable because of the high ductility of the material. During the cold bending process, an onset of yielding can be observed in the corner region of the spacers. The plasticizing in the corners stays locally limited if the deformation is increased further. At a certain deformation value, the plasticizing area starts to expand. Therefore, the spacers limit the feasible deformation of IGUs. Aluminum spacers are not ductile enough because they are reaching their ultimate strength in the corner region already for small deformations. In the corner region, high strains and pressures must be endured by the spacers and the secondary seal. This can also lead to local buckling of aluminum spacers. Outside the corner region, the spacers' stress is - as a general rule - below half of the yield stress.

Because the spacer reaches first a crucial stress level, it limits the possible deformation. Based on this restriction, the critical values in the glass panes are well below the material resistance. A low material utilization is indispensable in order to bear variable loads during the service life. However, if it is necessary to reduce the stress in the glass for a given deformation, then the pane thickness has to be reduced. For a double-glazed insulating glass, the significant maximum principal stresses occur in the thicker of both glass panes. If both glass panes do have the same pane thickness, then the maximum stress values are practically the same. If only one pane

thickness of both glass panes is reduced, then the significant stress in the thicker glass pane does almost not change.

The circumferential secondary seal, which is made out of structural silicone, ensures air tightness of the IGU. Structural silicones are able to withstand high deformations which makes them a suitable material for cold bending. The shear displacement of the secondary seal usually exceeds 10% before the maximum feasible deformation due to yielding of the spacer is reached. For the single-bent model with a length of $3.50\ [m]$ and a width of $1.50\ [m]$, the shear deformation can be as high as 17% if both glass panes have a thickness of $10\ [mm]$. For the double-bent model with the same dimensions, the shear deformation can be as high as 13%. Around the corners where the longitudinal spacer and the broadside spacer are joined, the structural silicone undergoes an engineering strain which can exceed 80% locally. A stiffer silicone can reduce the strain outside the corner regions but is not able to reduce the shear displacement to an appreciable level. Therefore, it is important to use a structural silicone which can meet the required properties under a certain permanent degree of strain during the whole service live.

In general, single-bent IGUs are not sensitive to different boundary conditions (BCs) and do not undergo local stability problems. On the contrary, double-bent IGUs are sensitive to different BCs. If the double-bent IGU has a statically determinate support configuration, then the IGU is susceptible to local buckling and deformation along the edge of the glass panes. If the double-bent IGU is statically over-determined, then the mechanical behavior is stable for larger deformations. Furthermore, in case of statically over-determined double-bent IGUs, membrane stresses are present in relatively thin glass panes and prevent a perfectly anticlastic shape. This can be an issue regarding the optical quality.

8 Outlook

The scope of this work is restricted to the mechanical behavior during the cold bending process. For a practical application, a subsequent examination under decisive variable loads and alternating loads is vitally important. Furthermore, laboratory testing must be done in order to verify the accuracy of the numerical results.

In order to meet safety standards, laminated safety glass is often required for building facades. Therefore, laminated safety glass as a component of an insulating glass unit (IGU) has to be examined. Also of interest is the investigation of triple-glazed insulating glass units. In addition, quadruple-glazed insulating glass could be subject of investigations.

For single-bent glass, the influence of the subconstruction should be examined. For this, the width and thickness as well as the Young's modulus should be investigated with and without an elastic interlayer. Important is also the change of mechanical stress in the IGU in dependency of different constant bending radii. In addition, sinusoidal-shaped subconstructions can give interesting results such as reduced stresses.

For double-bent glass, different boundary conditions have a significant influence on the mechanical behavior. Therefore, a wide range of different boundary conditions should be examined. Furthermore, the warping of the surface should be examined in order to ensure optical quality.

Several improvements can be made for more accurate numerical results. However, complexity and calculation expenses are increasing in order to obtain more accurate results.

The secondary seal, which is made out of silicone, should be modeled with a hyperelastic material model. This can give a better insight in the strain distribution around the corner region.

Moreover, all 4 spacers (2 longitudinal spacers and 2 broadside spacers) should be modeled as one piece in order to avoid slave-master interactions. This can improve the accuracy in the corner region and the numerical stability of the overall model. It can be advantageous to investigate the mechanical behavior of spacer bars with a certain bending radius in the corner of an IGU in order to avoid yielding. Of course, the

bending radius leads to a bigger silicone joint in the corners which might be an aesthetic issue.

In addition, the primary seal, which is made out of butyl, could be modeled. This avoids the necessity of a slave-master interaction between the spacer and the glass pane. Because butyl is very soft and flexible, the master-slave interaction must allow to separate the glass pane from the spacer. As a consequence, this leads to an open cavity which impairs the stability of fluid elements. This can be an issue when putting a distributed load onto a glass pane and the underlying glass pane(s) do not get the right proportion of load. Because the butyl strip is relatively soft, the shear distortion is expected to be big. As a result, the finite element distortion of the primary seal will escalate after a certain deformation is reached. A mesh refining algorithm can provide a possible solution in order to avoid mesh distortion. However, the huge difference in the stiffness of the materials of the IGU leads to an ill-conditioned stiffness matrix. As a result, it can be necessary to apply numerical coupling-methods between different parts of the IGU.

Considering long-term effects such as creeping and aging of the plastics are important. This pertains the interlayer in the laminated glass, the primary seal and the secondary seal. Furthermore, temperature during the service live and in case of fire should be examined. In addition, the gas loss effect should be estimated when calculating the long-term effects. However, to obtain reliable material values can be a challenge. In this case, laboratory testing should accompany the numerical simulations.

Finally, standardized manufacturing and design procedures for a cold-bent insulating glass unit should be derived from the research. The goal should be to provide simplified relationships which enable a fast, reliable and economical structural design. Eventually, standardization can be achieved in order to avoid individual approvals from local authorities.

9 Lists

9.1 List of Tables

9.2 List of Figures

9.3 List of Equations

10 Bibliography

10.1 Books, journals and conference papers

[1] J. Salo, „Modern safety glazing - demand, challenge and opportunity," Tamglass Singapore Pte. Ltd., Singapore, 2005.

[2] Steffen Schäfer, Michael Elstner, „Starke Kurven," Deutsches Architektenblatt, 31 8 2010.

[3] Eva Scheideler, Markus Broich, Michael Elstner, „Anwendung von thermisch gebogenem Glas im Bauwesen," Ernst & Sohn, Berlin, 2012.

[4] H. Schober, Transparent Shells: Form, Topology, Structure, Ernst & Sohn, 2015, pp. 150-151.

[7] Stefan Peters, Stephan Engelsmann, Christoph Dengler, „seele Glasbrücke: Eine gläserne Brückenkonstruktion aus kaltverformten Glas," Bautechnik, Bd. 91, Nr. 12, 2014.

[8] M. Saksala, „Extraordinary Shapes with Ordinary Costs," Glass Processing Days, Tampere, 2005.

[9] W. Wittwer, „Triple Glazing - Challenges and Solutions," Glass Performance Days, Tampere, 2011.

[10] M. Baitinger, „Zur Bemessung von SL-belasteten Anschlüssen im konstruktiven Glasbau," RWTH Aachen University, Aachen, 2009.

[11] Manfred Hegger, Volker Auch-Schwelk, Matthias Fuchs, Thorsten Rosenkranz, Construction Materials Manual, Basel: Birkhäuser - Publishers for Architecture, Part of the Springer Science+Business Media, 2006.

[14] Bernhard Weller, Philipp Krampe, Michael Engelmann, „Prüfung vorgespannter, gebogener Gläser," Ernst & Sohn, Berlin, 2012.

[15] M. Feldmann, R. Kasper and various other, „Guidance for European Structural Design of Glass Components," Joint Research Centre, Ispra, 2014.

[16] Kondrad Zilch, Claus Jürgen Diederichs, Rolf Katzenbach, Klaus J. Beckmann, Handbuch für Bauingenieure, 2. Auflage Hrsg., Springer, 2012.

[17] Deutscher Beton- und Bautechnikverein E.V. (Various Authors), Beispiele zur Bemessung nach Eurocode 2, Band 1: Hochbau, Köln: Ernst & Sohn, 2011.

[18] M. Haldimann, „Fracture Strength of Structural Glass Elements - Analytical and Numerical Modelling, Testing and Design," École polytechnique fédérale de Lausanne, Lausanne, 2006.

[19] Shawn M. Allan, Morgana L. Fall, Inessa Baranova, Holly S. Shulman, Autoclave-Free Radio Frequency Lamination for Armor and other Transparent Windows, Troy (State New York): Ceralink Inc.

[21] Meenu Teotia, R.K. Soni, „Polymer Interlayers for Glass Lamination - A Review," International Journal of Science and Research (IJSR), Bd. 3, Nr. 8, pp. 1264-1270, 1 8 2014.

[23] S. Van Den Bergh, R. Hart, B. Petter Jelle, A. Gustavsen, „Window Spacers and Edge Seals in Insulating Glass Units: A State-of-the-Art Review and Future Perspectives," Energy and Buildings 58, pp. 263-280, 1 1 2013.

[24] A. Hagl, „Experimental and Numerical Analysis of Edge Seal Spacers of Insulated Glass Units for Structural Sealant Glazing Applications," Challenging Glass 3 – Conference on Architectural and Structural Applications of Glass, 1 6 2012.

[25] K. Kunal, M. Paluch, C. M. Roland, J. E. Puskas, Y. Chen, A. P. Sokolov, „Polyisobutylene: A Most Unusual Polymer," Journal of Polymer Science: Part B: Polymer Physics, Vol. 46, pp. 1390-1399, 10 4 2008.

[26] J. Baker, „IGMA Spacer Thermal Performance Study," WESTLab Canada, Ottawa, 2005.

[27] L. Jacob, „Curtain Wall Systems Design with an Emphasis on Structural Silicone," in Glass Processing Days, Tampere, 2001.

[28] J. Wurm, Glas als Tragwerk, Entwurf und Konstruktion selbsttragender Hüllen, Basel: Springer Science+Business Media, 2007.

[29] H. S. Norville, „The effect of interlayer thickness on laminated glass strength," Glass Processing Days, Tampere, 1997.

[32] Bernhard Weller, Christiane Kothe, Michael Kothe, Jan Wünsch, „Thermo Mechanical Behaviour of Polymeric Interlayer Materials," in Glass Performance Days, Tampere, 2009.

[33] A. H. Elmahdy, „Improved spacer bar design enhances window performance," NRC Publications Archive, Ottawa, 2004.

[34] Bjorn Peter Jelle, Andrew Hynd, Arild Gustavsen, Dariush Arasteh, Howdy Goudey, Robert Hart, „Fenestration of today and tomorrow: A state-of-the-art review and future research opportunities," Solar Energy Materials & Solar Cells, Bd. 96, pp. 1-28, 2012.

[35] A. Elmahdy, „Effects of Improved Spacer Bar Design on Window Performance," Construction Technology Update, Bd. 58, 9 2003.

[36] Seung-Yeong Song, Jae-Hun Jo, Myoung-Souk Yeo, Young-Don Kim, Kyoo-Dong Song, „Evaluation of inside surface condensation in double glazing window system with insulation spacer: A case study of residential complex," Building and Environment, Bd. 42, pp. 940-950, 2007.

[38] G. Unger, „The Thermoplastic Edge Seal System - A New Insulating Glass Generation," in Glas Processing Days, 1999.

[39] G. Schmidt, „Sealants for IG Units, Performance Parameters and Requirements," in Glass Processing Days, Tampere, 1997.

[40] Dan Hoffmeyer, Carl Axel Lorentzen, „Substitution of SF6-gas in Double Glazings Sound-Insulating Windows – without Greenhouse Gas," in Glass Processing Days 2003, Tampere, 2005.

[41] Brian Hubbs, Peng, James Higgins, „Glazing Failures and Ways to Prevent Them," in 30th RCI International Convention and Trade Show, Vancouver, 2015.

[42] G. Finch, „Argon Gas Fill & Insulated Glass Units," RDH Technical Bulletin, Vancouver, 2008.

[43] R. Ernst, „Gas Fillings of IG Units," FDR Design, Inc., Buffalo, Minnesota, 2016.

[46] J. Neugebauer, „Climatic loads in curved insulated glasses," in Challenging Glass, Conference on Architectural and Structural Applications of Glass, Delft, 2008.

[47] S. L. Meisel, „Role of desiccants, Complex subject made easy," Glass Magazine, pp. 98-102, 1 9 2005.

[48] G. Winstanley, „The Fogging of I.G.Units in Stick and Curtain Wall Installations," Glass Performance Days, Tampere, 2009.

[49] Rolf Kochs, „Condensate risks pertaining to inner surfaces of insulating glass units," in Glass Performance Days, Tampere, 2013.

[50] Jerome Klosowski, Andreas T. Wolf, Sealants in Construction, 2nd Edition Hrsg., Boca Raton, Florida: CRC Press, Taylor & Francis Group, LLC, 2016.

[51] Mick Eekhout, Dries Staaks, „Cold Deformation of Glass," Octatube Space Structures, Delft, 2005.

[52] B. Beer, „Structural Silicone Sealed Cold-Bent Glass - High-Rise Projects Experience Leading to a New Design Concept," Glass Performance Days, Tampere, 2015.

[54] Christian Louter, Freek Bos, Jan Belis, Jean-Paul Lebet, „Challenging Glass 4," in COST Action TU0905 Final Conference, Lausanne, 2014.

[55] Tihemo Fildhuth, Jan Knippers, „Geometrie und Tragverhalten von doppelt gekrümmten Ganzglasschalen aus kalt verformten Glaslaminaten," Stahlbau Spezial, pp. 31-44, 2011.

[56] S. M. G. R.-C. Laura Galuppi, „Buckling phenomena in double curved cold-bent glass," International Journal of Non-Linear Mechanics, Bd. 64, pp. 70-84, 2014.

[57] F. Doebbel, „Bemessung elastischer Klebefugen in kaltverformten SSG-Einheiten," Sika Services AG, Zurich, 2016.

[58] N. Baldassini, „Glass and Geometry," Glass Processing Days, Tampere, 2005.

[61] Vladimir Marinov, Peter Lenk, „Optimising quadrilateral free-form grids for panelisation with cold-bent glass," Glass Performance Days, Tampere, 2013.

[62] Johann Sischka, René Ziegler, Benjamin Schneider, „Beyond Boundaries - Exploring Geometric Complexity," Glass Performance Days, 2011, 2011.

[63] Michael Eigensatz, Alexander Schiftner, „Case Studies in Optimization of Glass-panelized Architectural Freeform Designs," Glass Performance Days, 2011, 2011.

[64] Johannes Wallner, Helmut Pottmann, „Geometric Computing for Freeform Architecture," Journal of Mathematics in Industry, Berlin, Germany, 2011.

[65] Ömer Bucak, Markus Feldmann, Ruth Kasper, Martin Bues, Marcus Illguth, „Das Bauprodukt "warm gebogenes Glas" - Prüfverfahren, Festigkeiten und Qualitätssicherung," Stahlbau Spezial, Bd. Konstruktiver Glasbau, pp. 23-28, 2009.

[66] Christian Schuler, Michael Elstner, Marcus Illguth, Sonja Stief, Alexander Lorenz, „Einsatz von gebogenem Glas im Bauwesen," Stahlbau, Bd. 81, Nr. 3, pp. 190-196, 2012.

[67] Bundesverband Flachglas (Various authors), „Leitfaden für thermisch gebogenes Glas im Bauwesen," Bundesverband Flachglas, Troisdorf, 2011.

[68] J. Neugebauer, „Applications for curved glass in buildings," Journal of Facade Design and Engineering, Bd. 2, pp. 67-83, 22 12 2014.

[69] Geralt Siebert, Iris Maniatis, „Tragende Bauteile aus Glas Grundlagen, Konstruktion, Bemessung, Beispiele," Bd. 2, Berlin, Ernst & Sohn, 2012.

[70] Graham Dodd, Sebastian Thieme, „Comparison of curved glass and cold bent panels," in Glass Performance Days, Tampere, 2007.

[71] Ulrich Breuninger, Martin Stumpf, „Cold bent Arches of laminated Glass," Herrmann und Partner, Stuttgart, 2005.

[72] B. Kassnel–Henneberg, „Purely structural glass building envelopes," seele sedak GmbH & Co. KG, Tampere, 2011.

[73] G. R.-C. Laura Galuppi, „Cold-lamination-bending of glass: Sinusoidal is better than circular," ScienceDirect, Parma, 2015.

[74] Laura Galuppi, Gianni Royer-Carfagni, „Rheology of cold-lamination-bending for curved glazing," Engineering Structures, Bd. 61, pp. 140-142, 7 2 2014.

[75] Thiemo Fildhuth, Jan Knippers, „Permanent Strain Measurement Inside of Cold Bent Glass Laminates," in Glass Performance Days, Tampere, 2013.

[76] Jan Belis, Bart Inghelbrecht, Rudy Van Impe, Dieter Callewaert, „Cold bending of laminated glass panels," Bd. 52, Nr. 1/2, 2007.

[77] J. Neugebauer, „Gekrümmte Isoliergläser," Glasbau 1. Auflage, pp. 112-122, 2012.

[78] Keith Besserud, Matt Bergers, Andrew J. Black & Co., „Durability of Cold-Bent Insulating-Glass Units," Journal of ASTM International, Bd. 9, Nr. 3, pp. 1-25, 2012.

[79] M. Wißling, „Kleben von Stahl mit Stahl und Glas mit Stahl FE-Simulationen, Anwendungen, Perspektiven," Stahlbau, Bd. 73, Nr. 6, pp. 438-440, 2004.

[80] P. Kurzweil, Chemie Grundlagen, Aufbauwissen, Anwendungen und Experimente, Bd., Wiesbaden: Springer Fachmedien, 2015.

[81] Bernhard Weller, Michael Kothe, Felix Nicklisch, Thomas Schadow, Silke Tasche, Iris Vogt, Jan Wunsch, „Kleben im konstruktiven Glasbau," Ernst und Sohn, Berlin, 2011.

[82] Stefan Böhm, K. Dilger, „Kurzbeschreibung zum Forschungsantrag Einsatz geklebter Punkthalter für Glasfassaden," Institut für Füge- und Schweißtechnik, TU Braunschweig, Braunschweig.

[83] Greg Dean, Louise Crocker, „The Use of Finite Element Methods for Design with Adhesives," Measurement Good Practice Guide, Bd. 48, 2001.

[84] Bruce Duncan, Louise Crocker, Jeannie Urquhart, Elena Arranz, Richard Mera and Bill Broughton, „FAILURE OF FLEXIBLE ADHESIVE JOINTS," National Physical Laboratory UK, Teddington, 2001.

[86] G. Habenicht, Kleben Grundlagen, Technologien, Anwendungen, 6. Auflage Hrsg., Wörthsee/Steinebach: Springer, 2012.

[88] J. W. Bernhard Weller, „Determination of Curing for Transparent Epoxy Resin Adhesives," Glass Performance Days, Tampere, 2011.

[89] Bernhard Weller, Michael Kothe, Robert Laborge, Jan Wünsch, „Structural Sealants - Uni-Axial Mechanical," Technische Universität Dresden, Institute of Building Construction, Dresden, 2010.

[90] A.K. Dhaliwal, J.N. Hay, „The characterization of polyvinyl butyral by thermal analysis," Thermochimica Acta, Bd. 391, pp. 245-255, 30 1 2002.

[91] K. Puller, „Untersuchung des Tragverhaltens von in die Zwischenschicht von Verbundglas integrierten Lasteinleitungselementen," in Dissertation, Stuttgart, 2012.

[93] P. Steinke, Finite-Elemente-Methode, Rechnergestützte Einführung, Berlin: Springer-Verlag, 2015.

[94] F. U. Mathiak, Die Methode der finiten Elemente (FEM), Einführung und Grundlagen, Neubrandenburg: Hochschule Neubrandenburg, 2010.

[95] Thomas Rüberg, Jürgen Zechner, Introduction to Finite Element Method, Graz: Graz University of Technology, 2009.

[96] Herbert Goering, Hans-Görg Roos, Lutz Tobiska, Die Finite-Elemente-Methode für Anfänger, Weinheim: WILEY-VCH Verlag, 2010.

[97] T.-P. Fries, „Lecture Notes from Finite Element Methode," Graz University of Technology, Graz, 2015.

[98] B. Klein, FEM, Grundlagen und Anwendungen der Finite-Element-Methode im Maschinen- und Fahrzeugbau, Wiesbaden: Springer Fachmedien, 2015.

[99] F. Wellershoff, M. Förch, „Principal strains in foam spacer systems of curved double glazed units under climatic loads," in Challenging Glass 4 & COST Action TU0905 Final Conference, Hamburg, Germany, 2014.

[100] Cambridge University Engineering Department, „Marerials Data Book," 2003.

[104] R. Spiegelberg, Numerische Untersuchung zum Kaltiegen von Dünnglas, Graz: Graz University of Technology, 2016.

[105] T. Fildhuth, „Design and Monitoring of Cold Bent Lamination-Stabilised Glass," Universität Stuttgart, Stuttgart, 2015.

[106] J. Neugebauer, „Spring stifness of the edge sealing in curved insulated glass units," Glass Performance Days, Tampere, Finland, 2011.

10.2 Standards

[12] „Glas im Bauwesen - Konstruktiver Glasbau, Teil 1: Grundlagen,"

(Austrian Standard) ÖNORM B3716-1, 2013.

[13] „Glas im Bauwesen - Bemessung und Konstruktionsregeln - Teil 1: Begriffe und allgemeine Grundlagen,“

(German Standard) DIN 18008-1, 2010.

[44] „Glass in building - Insulating glass units - Part 3: Long term test method and requirements for gas leakage rate and for gas concentration tolerances,“

(European Standard) EN 1279-3, 2003.

[45] "Glas im Bauwesen - Konstruktiver Glasbau,"

(Austrian Standard) in ÖNORM B3716, 2013.

[53] „Standard Specification for Bent Glass,“

(International Standard) ASTM C1464, 2011.

[85] „Adhesives - Designation of main failure patterns,“

(International Standard) ISO 10365, 1992.

[87] „Glass in building - Insulation glass units - Part 4: Methods of test for the physical attributes of edge seals,“

(European Standard) EN 1279-4, 2002.

[101] „Stainless steels - Technical delivery conditions for sheet/plate and strip of corrosion resisting steels for general purposes,“

(European Standard) EN 10088-2, 2014.

[102] „Eurocode 3: Design of steel structures - Part 1-1: General rules and rules for buildings,“ in

(European Standard) EN 1993-1-1, 2005.

[103] „Eurocode 9: Design of aluminium structures - Part 1-1: General structural rules,“ in

(European Standard) EN 1999-1-1, 2009.

[107] „Glass in Building - Design and construction rules,“

(German Standard) DIN 18008, 2010.

10.3 Patents

[30] P. Henricus, K. Wolfgang, S. Gunther und V. M. R. Hubertus, „Thermoplastic Polyurethane and use Thereof“.

International Patent JP2006169536 (A), 2006.

[31] C. A. S. David M. Rinehart.

USA Patent US7334371 B2, 2008.

10.4 Online sources

[5] E. Levin, „Steel Institute of New York,“ 20 3 2016. [Online]. [Access date: March-3-2016]. Available:

http://siny.org/projects/

[6] „OpenBuildings,“ 2016 3 2016. [Online]. [Access date: March-3-2016]. Available:

http://openbuildings.com/buildings/strasbourg-railway-station-profile-41811.

[20] „Flat Glass,“ Asahi Glass Co., Ltd., [Online]. [Access date: April-21-2016]. Available:

http://www.agc.com/english/products/products_01.html.

[22] Glass for Europe Team, „Glass for Europe,“ [Online]. [Access date: February-21-2016]. Available:

http://www.glassforeurope.com/en/products/main-types-of-glass.php.

[37] Quanex Building Products, [Online]. [Access date: February-14-2016]. Available:

https://www.quanex.com/Products/Residential/Insulating-Glass-Systems/Single-Seal-Spacers.aspx.

[59] M. Altmann, „Worcester Polytechnic Institute,“ [Online]. [Access date: January-20-2016]. Available:
http://web.cs.wpi.edu/~matt/courses/cs563/talks/nurbs.html.

[60] Hongxin Zhang, JieqingFeng, „Zhejiang University,“ [Online]. [Access date: January-31-2016]. Available:

http://www.cad.zju.edu.cn/home/zhx/GM/010/00-subd1.pdf.

[92] Kuraray (Various Authors), „glasslaminatingsolutions.kuraray.com [Online]. [Access date: March-8-2016]. Available: http://glasslaminatingsolutions.kuraray.com/fileadmin/user_upload/technical_information/downloads/sentryglas/150129_Kuraray_TM_Datenblatt_SG.pdf.

[108] „Glass and Glazing Standards for the Building Industry,“ [Online]. [Access date: May-3-2016]. Available:

http://www.astm.org/BOOKSTORE/COMPS/PDFS/GLASSCMP_TOC.pdf.

11 Annex

11.1 Convergence study

Firstly, different element types are varied for the single-bent model which are depicted in Figure 203 and in Figure 204. Secondly, the edge-zone is subject of a convergence study which can be seen in Figure 205 and in Figure 206.

In Figure 203, the results along axis 7-7 for the single-bent model are depicted for different FE types. In this case, the model is clamped along axis 7-7 $x = y = z = m_{x-x} = m_{y-y} = m_{z-z} = 0$. The FE type "quadratic" which is depicted as a blue line was chosen for the numerical investigations. The mesh size is described in the subchapter 6.1.1. Striking is the difference between linear FEs and quadratic FEs. However, such a big difference occurs only along axis 7-7. For a finer FE, a higher maximum principal stress can be observed. From this can be decuded that shear locking occurs along axis 7-7. In order to avoid shear locking, quadratic elements are chosen.

In Figure 204, the same results as in Figure 203 are depicted along axis 3-3 from $0\ [m]$ to $0.10\ [m]$. A great difference in the results next to axis 7-7 can be seen for linear and quadratic FEs.

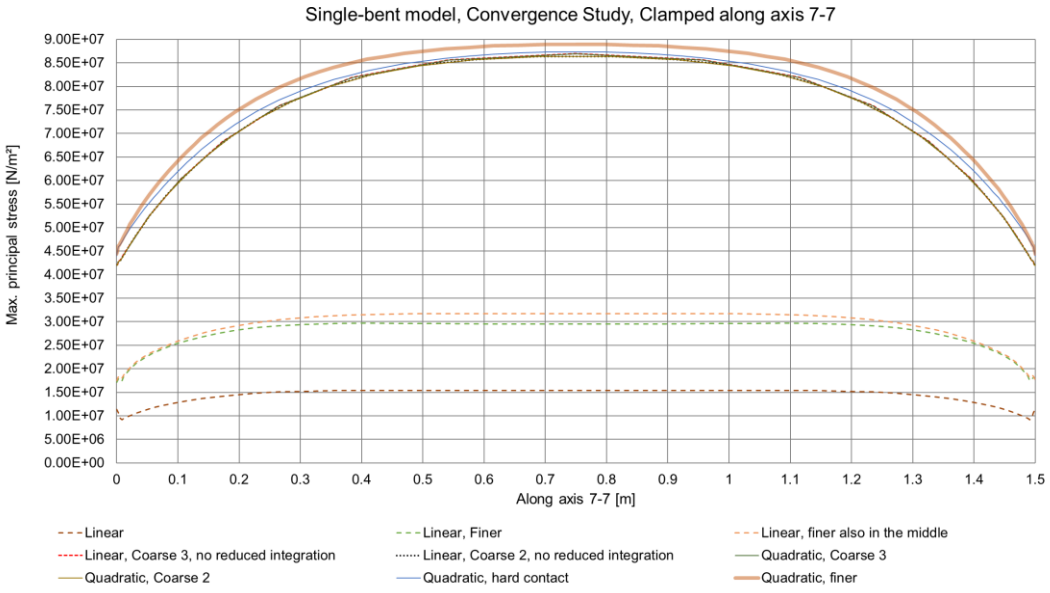

Figure 203: Single-bent model, convergence study, axis 7-7, clamped along axis 7-7, r=10

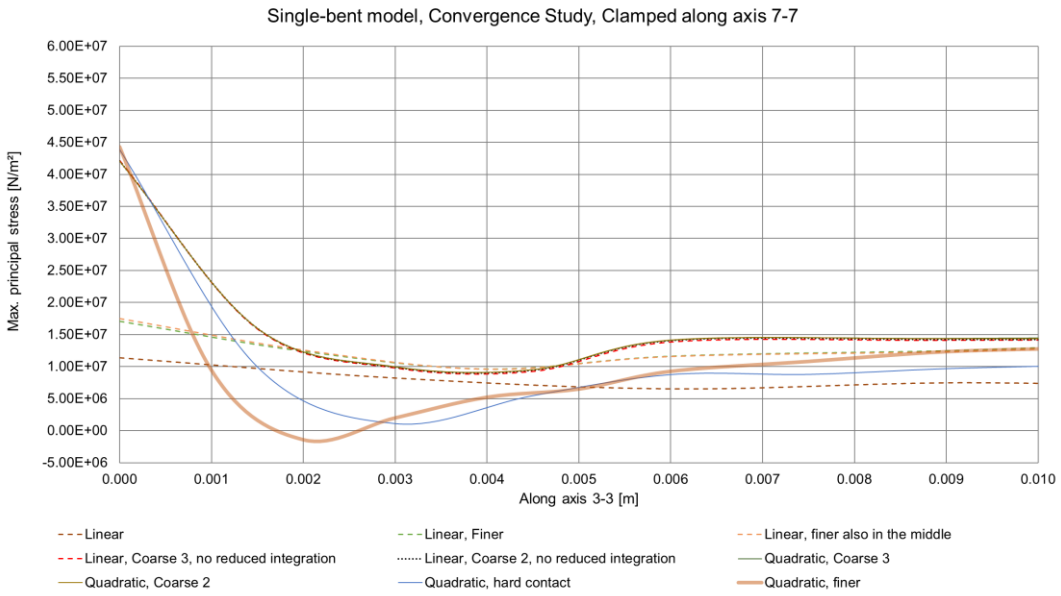

Figure 204: Single-bent model, convergence study, axis 3-3, clamped along axis 7-7, r=10

In Figure 205, Δu_3 is depicted for the secondary seal along the longitudinal side parallel to axis 3-3 from 0 [m] to 3.5 [m] and along the broadside parallel to axis 8-8 from $0.0\ [m]$ to $1.5\ [m]$. From the previous investigations it is known that only quadratic elements are appropriate. Therefore, a convergence study with three different mesh sizes is carried out and $|\Delta u_3|$ is examined. $|\Delta u_3|$ is the absolute difference between u_3 from the upper edge of the secondary seal next to glass pane 2 (next to axis 3-3) and u_3 from the lower edge of the secondary seal next to glass pane 1 (next to axis 1-1). The previous chosen quadratic mesh "quad 1" seems appropriate again (blue) whereas the finest quadratic mesh is "quad 2" but the calculation time doubles for "quad 2".

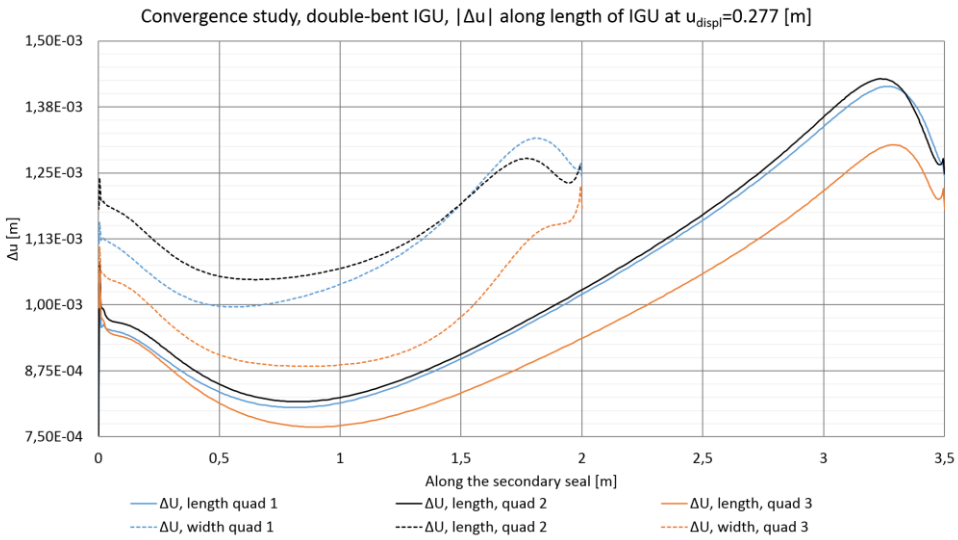

Figure 205: Double-bent model, convergence study, $|\Delta u_3|$ along l_{gp}

In Figure 206, a convergence study for the deformation of the secondary seal along axis S21-S21 is carried out. The radius of the single-bent reference model is $r = 10\ [m]$ in this case. It can be seen, that all investigated mesh sizes and element types are appropriate for a qualitative assessment. Because no hyperelastic material model is used, an accuracy below $\pm 0.1\ [mm]$ is not realistic.

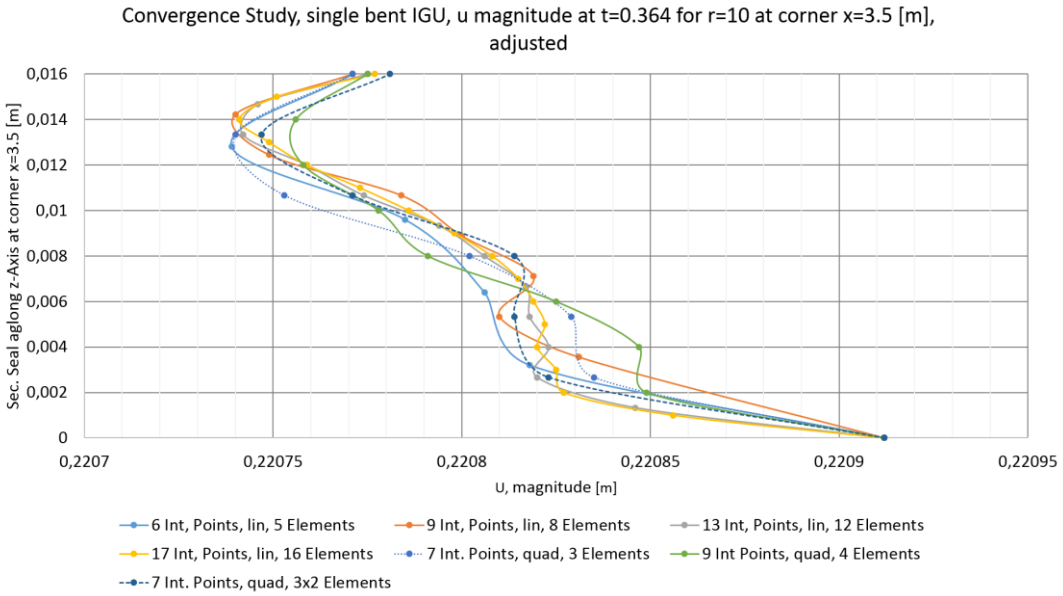

Figure 206: Double-bent model, convergence study, u magnitude at S21-S21

11.2 Empiric relationship

In this section, it is shown, how the empiric relationship of **Equation 5** in subchapter 6.2.2.1 is obtained, which can be easily reproduced by two nested loops in for example Matlab or Java.

Firstly, all $F(t=1)$ from 1.1.1 to 1.1.9 are set into a non-linear relationship with the thickness of both glass panes. Two arbitrary chosen fitting exponents a and b are introduced such as that a third fitting constant c as a function of them is obtained

$$c_i = \frac{F_i(t=1)}{t_{gp,1,i}^{a,i} + t_{gp,2,i}^{b,i}}; i = 1,2, \dots n = 9 \qquad \textit{Equation 8}$$

Secondly, all constants c_i are summed up in such a way that ε_j is obtained, whereas ε yields a minimum deviation for the $j-th$ try by the right adjustment or rather guess of a and b

$$\varepsilon_j = \sqrt{\frac{1}{n}\sum_{i=1}^{n} c_i}; j = 1,2, \dots m \qquad \textit{Equation 9}$$

Thirdly, ε_j is used to estimate the maximum error of the force F which the empiric formula prognosticates such as that the maximum error ΔF is a minimum

$$\Delta F_j = \max |F_i(t=1) - \varepsilon_j\left(t_{gp,1,i}^{a,j} + t_{gp,2,i}^{b,j}\right)| \qquad \textit{Equation 10}$$

This three steps have to be repeated j -times in order to find a minimum between the maximum deviation of ΔF and F. Obviously, this can be done by adjusting the fitting exponents a and b as long as $j \equiv m$.

This yields **Equation 5** which is $F = 5.508\left(t_{gp,1,i}^{2.25} + t_{gp,2,i}^{2.45}\right)$.

Of course, more digits and variables can be taken into consideration in order to improve the accuracy and to make it more versatile which seems not worthwhile in this case. In addition, an extension of the formula can also to lead an incomprehensible equation which might give unpredictable results for special values.

11.3 Python input script for Abaqus

If this is the printed version, then the code can be found on the accompanying CD, if this is the digital version, then the code can be found in the subsequent part of this chapter. Due to the vast quantity of result data, it is not possible to provide them. If necessary, the numerical model can be reproduced with the aid of the provided script and the software Abaqus and must then be calculated.

The python input script can also be invoked by the QR-code in Figure 207.

Figure 207: QR-code for python input script

```
# ------------------------------------------------------------------------------------------------------------------------
# Author: Franz N. Polzl
# Graz Technical University of Technology, Institute for Building Construction, 2017
# hochbau@tugraz.at
# Open source code, commercial use is prohibited
# ------------------------------------------------------------------------------------------------------------------------

class startAll():
    from abaqus import *
    from abaqusConstants import *
    import regionToolset
    import datetime
    import math
    session.viewports['Viewport: 1'].setValues(displayedObject=None)

    # USER*HAS*TO*EDIT*BELOW*****************************************************************************
    calculation             = int(0)     # Start the calculation with 1
    CPU_in_use              = int(4)     # Cores of the CPU which are available
    max_Memory              = int(90)    # Memory which is available
    # USER*HAS*TO*EDIT*ABOVE*****************************************************************************

    # ---------------------------------------------------------------------------------------------
    # Create the model
    # Width spacer and width secSeal are equal to thicknessCavity

    # USER*HAS*TO*EDIT*BELOW*****************************************************************************
    # Geometry
    thicknessGlassPane1     = 0.012   # Lower pane interacting with the subconstruction
    thicknessGlassPane2     = 0.008   # Upper pane in case of double glazing
    thicknessGlassPane3     = 0.006   # Upper pane in case of triple glazing, set zero to ignore
    thicknessGlassPane4     = 0.012   # Upper pane in case of quadruple glazing, set zero to ignore
    thicknessCavity         = 0.012   # Cavity between thicknessGlassPane(i) and thicknessGlassPane(i+1)
    thicknessSecSeal        = 0.005
    heightSpacer            = 0.0065  # Outer side of the shell element
    thicknessSpacer         = 0.00018# Shell and sheet thickness of the spacer
```

```
widthPane                = 1
lengthPane               = 3.50
widthSubConstr           = 0.04    # Width of the subconstruction
thicknessSubConstr       = 0.01    # Shell thickness of the subconstruction
radiusSubConstr          = 12      # Constant radius of the subconstruction
displacementTwo          = -0.22   # Displacement for double bending

# Material
# Give the Young's modulus and the Poisson's ratio for linear-elastic analysis
youngsGlass              = 70e9
youngsSecSeal            = 2e6
youngsSpacer             = 189e9
youngsSubConstr          = 210e9
poissGlass               = 0.23
poissSecSeal             = 0.48
poissSpacer              = 0.305
poissSubConstr           = 0.30
yieldStressSpacer        = 2.3e8

#Cavity properties
ambientPressureCavity   = 101300# Ambient pressure
molecularWeightCavity   = 0.0034 # Molecular weight of the gas in the cavity
magnitudePressureLoad = 0        # Pressure load on the undeformed glass pane either 0 or not

# For one-way bending, choose lengthPane gets curved - do not change that to widthPane
# instead change your input values
arcLength                = lengthPane
oneWay                   = int(1)      # 1=One-way, 2=Biaxial, 3=No bending

# For any parameter variation, define the variables or fixed values on the right side
fStep                    = int(1)      # Step size of the for loop
minfIncrement            = int(1)      # Lower boundary of the for loop
maxfIncrement            = int(6)      # Upper boundary of the for loop
fIncrement               = widthPane
# USER*HAS*TO*EDIT*ABOVE*****************************************************************************

from abaqus import *
from abaqusConstants import *
import regionToolset
import datetime
import math
session.viewports['Viewport: 1'].setValues(displayedObject=None)
# ----------------------------------------------------------------------------------------

# ----------------------------------------------------------------------------------------
# Check the input parameters
# if oneWay<1 or oneWay>2:
    # raise ValueError('The input value in oneWay is not valid')
if calculation!=0 | calculation!=1:
    raise ValueError('The input value in calculation is not valid')
if CPU_in_use==0 | CPU_in_use>999:
    raise ValueError('The input value in CPU_in_use is not valid')
if max_Memory<0 or max_Memory>100:
    raise ValueError('The input value in max_Memory is not valid')
if thicknessGlassPane1<-1e-12 or thicknessGlassPane1>1e999 or thicknessGlassPane1==0:
    raise ValueError('The input value in thicknessGlassPane1 is not valid')
if thicknessGlassPane2<-1e-12 or thicknessGlassPane2>1e999 or thicknessGlassPane2==0:
    raise ValueError('The input value in thicknessGlassPane2 is not valid')
if thicknessGlassPane3<-1e-12 or thicknessGlassPane3>1e999:
    raise ValueError('The input value in thicknessGlassPane3 is not valid')
if thicknessGlassPane4<-1e-12 or thicknessGlassPane4>1e999:
    raise ValueError('The input value in thicknessGlassPane4 is not valid')
if ((thicknessGlassPane4>-1e-12 or thicknessGlassPane4<1e999)& (thicknessGlassPane3<-1e-12 or
thicknessGlassPane3>1e999)):
    raise ValueError('The input value in thicknessGlassPane3 and/or 4 is not valid')
print(thicknessCavity)
```

```
    if thicknessCavity<-1e-12 or thicknessCavity>1e999 or thicknessCavity==0:
        raise ValueError('The input value in thicknessCavity is not valid')
    if thicknessSecSeal<-1e-12 or thicknessSecSeal>1e999 or thicknessSecSeal==0:
        raise ValueError('The input value in thicknessSecSeal is not valid')
    if heightSpacer<-1e-12 or heightSpacer>1e999 or heightSpacer==0:
        raise ValueError('The input value in heightSpacer is not valid')
    if thicknessSpacer<1e-12 or thicknessSpacer>heightSpacer/2 or thicknessSpacer>(thicknessSecSeal/2):
        raise ValueError('The input value in thicknessSpacer is not valid')
    if widthPane<1e-12 or widthPane>1e999 or widthPane<(2*(thicknessSecSeal+thicknessSpacer)):
        raise ValueError('The input value in widthPane is not valid')
    if lengthPane<1e-12 or lengthPane>1e999 or lengthPane<(2*(thicknessSecSeal+thicknessSpacer)):
        raise ValueError('The input value in lengthPane is not valid')
    if (widthSubConstr<1e-12 or widthSubConstr>1e999 or widthSubConstr>(lengthPane/2)
    or widthSubConstr==0)&(oneWay==1):
        raise ValueError('The input value in widthSubConstr is not valid')
    if (thicknessSubConstr<-1e-12 or thicknessSubConstr>1e999 or thicknessSubConstr==0
        or widthSubConstr<(thicknessSecSeal+heightSpacer))&(oneWay==1):
        raise ValueError('The input value in thicknessSubConstr is not valid')
    if oneWay==0:
        # For partition purposes
        widthSubConstr=widthSubConstr+heightSpacer
    if (radiusSubConstr<-1e-12 or radiusSubConstr>1e999 or radiusSubConstr==0)&(oneWay==1):
        raise ValueError('The input value in radiusSubConstr is not valid')
    if youngsGlass<-1e-12 or youngsGlass>1e999 or youngsGlass==0:
        raise ValueError('The input value in youngsGlass is not valid')
    if youngsSecSeal<-1e-12 or youngsSecSeal>1e999 or youngsSecSeal==0:
        raise ValueError('The input value in youngsSecSeal is not valid')
    if youngsSpacer<-1e-12 or youngsSpacer>1e999 or youngsSpacer==0:
        raise ValueError('The input value in youngsSpacer is not valid')
    if (youngsSubConstr<-1e-12 or youngsSubConstr>1e999 or youngsSubConstr==0)&(oneWay==1):
        raise ValueError('The input value in youngsSubConstr is not valid')
    if poissGlass<-1e-12 or poissGlass>0.4999:
        raise ValueError('The input value in poissGlass is not valid')
    if poissSecSeal<-1e-12 or poissSecSeal>0.4999:
        raise ValueError('The input value in poissSecSeal is not valid')
    if poissSpacer<-1e-12 or poissSpacer>0.4999:
        raise ValueError('The input value in poissSpacer is not valid')
    if (poissSubConstr<-1e-12 or poissSubConstr>0.4999)&(oneWay==1):
        raise ValueError('The input value in poissSubConstr is not valid')

    # ----------------------------------------------------------------------------------

    # Start the loop where the parameter study is evaluated
    for fIncrement in xrange(minfIncrement,maxfIncrement+1,fStep):

        if 'Model-1' in mdb.models.keys():
            mdb.models.changeKey(fromName='Model-1', toName='ParameterStudy' +
            repr(fIncrement))

        mdb.Model(modelType=STANDARD_EXPLICIT, name='ParameterStudy' + repr(fIncrement))
        glassModel = mdb.models['ParameterStudy' + repr(fIncrement)]

        # USER*HAS*TO*EDIT*BELOW*****************************************************************
        # For any parameter variation, redefine the variable fIncrement on the left side
        # For example it should look like this: parameterVariable = fIncrement
        #widthPane = fIncrement
        #uselessVariable = fIncrement
        # USER*HAS*TO*EDIT*ABOVE*****************************************************************

        import sketch
        import part

        # ----------------------------------------------------------------------------------
        # Create the geometry of the IGU

        # a1) Sketch the glass pane section
```

```
    glassPane = glassModel.ConstrainedSketch(name='GlassPaneSke', sheetSize=lengthPane*2)
    glassPane.rectangle(point1=(0,0), point2=(widthPane,lengthPane))

    # a2) Sketch the secondary seal section
    secSeal = glassModel.ConstrainedSketch(name='SecSealSketch',sheetSize=lengthPane*2)
    secSeal.rectangle(point1=(0,0), point2=(widthPane,lengthPane))
    secSealGG = secSeal.geometry
    secSeal.offset(distance=thicknessSecSeal, objectList=(secSealGG[2], secSealGG[3],
    secSealGG[4], secSealGG[5]), side=LEFT)

    # a3) Sketch the short spacer section
    shortSpacer = glassModel.ConstrainedSketch(name='ShortSpacerSketch', sheetSize=lengthPane*2)
    shortSpacer.rectangle(point1=(0.0, 0.0), point2=(thicknessCavity, heightSpacer))

    # a4) Sketch the long spacer section
    longSpacer = glassModel.ConstrainedSketch(name='LongSpacerSketch', sheetSize=lengthPane*2)
    longSpacer.rectangle(point1=(0.0, 0.0), point2=(thicknessCavity, heightSpacer))

    if oneWay == 1:
        # a5) Sketch the subConstruction
        subconstruction = glassModel.ConstrainedSketch(name='SubconstructionSketch',
        sheetSize=lengthPane*4)
        angleSubCon=arcLength/radiusSubConstr
        lowerAngleSubCon=math.pi/2-angleSubCon
        xPoint2=math.cos(lowerAngleSubCon)*radiusSubConstr
        yPoint2=math.sin(lowerAngleSubCon)*radiusSubConstr
        subconstruction.ArcByCenterEnds(center=(0.0, 0.0), point1=(0.0, radiusSubConstr),
        point2=(xPoint2,yPoint2), direction=CLOCKWISE)

    # b1-1) Create a 3D deformable part named "GlassPane1" by extruding the sketch
    glassPanePart1=glassModel.Part(name='GlassPanePart1', dimensionality=THREE_D,
    type=DEFORMABLE_BODY)
    glassPanePart1.BaseSolidExtrude(sketch=glassPane, depth=thicknessGlassPane1)

    # b1-2) Create a 3D deformable part named "GlassPane2" by extruding the sketch
    glassPanePart2=glassModel.Part(name='GlassPanePart2', dimensionality=THREE_D,
    type=DEFORMABLE_BODY)
    glassPanePart2.BaseSolidExtrude(sketch=glassPane, depth=thicknessGlassPane2)

    if thicknessGlassPane3>1e-12:
        # b1-3) Create a 3D deformable part named "GlassPane3" by extruding the sketch
        glassPanePart3=glassModel.Part(name='GlassPanePart3', dimensionality=THREE_D,
        type=DEFORMABLE_BODY)
        glassPanePart3.BaseSolidExtrude(sketch=glassPane, depth=thicknessGlassPane3)

        if thicknessGlassPane4>1e-12:
            # b1-4) Create a 3D deformable part named "GlassPane4" by extruding the sketch
            glassPanePart4=glassModel.Part(name='GlassPanePart4', dimensionality=THREE_D,
            type=DEFORMABLE_BODY)
            glassPanePart4.BaseSolidExtrude(sketch=glassPane, depth=thicknessGlassPane4)

    # b2-1) Create a 3D deformable part named "secSeal" by extruding the sketch
    secSealPart=glassModel.Part(name='SecSealPart', dimensionality=THREE_D,
    type=DEFORMABLE_BODY)
    secSealPart.BaseSolidExtrude(sketch=secSeal, depth=thicknessCavity)

    # b3-1) Create a 3D deformable part named "shortSpacer" by extruding the sketch
    shortSpacerPart=glassModel.Part(name='ShortSpacerPart', dimensionality=THREE_D,
    type=DEFORMABLE_BODY)
    shortSpacerPart.BaseShellExtrude(sketch=shortSpacer,
    depth=lengthPane-2*thicknessSecSeal)
    # shortSpacerPart=glassModel.Part(name='ShortSpacerPart', dimensionality=THREE_D,
    # type=DEFORMABLE_BODY)
    # shortSpacerPart.BaseShellExtrude(sketch=shortSpacer,
    # depth=widthPane-2*thicknessSecSeal)

```

```
234.
235.    # b4) Create a 3D deformable part named "longSpacer" by extruding the sketch
236.    longSpacerPart=glassModel.Part(name='LongSpacerPart', dimensionality=THREE_D,
237.    type=DEFORMABLE_BODY)
238.    longSpacerPart.BaseShellExtrude(sketch=longSpacer, depth=widthPane-2*thicknessSecSeal)
239.    # longSpacerPart=glassModel.Part(name='LongSpacerPart', dimensionality=THREE_D,
240.    # type=DEFORMABLE_BODY)
241.    # longSpacerPart.BaseShellExtrude(sketch=longSpacer, depth=lengthPane-2*thicknessSecSeal)
242.
243.
244.    if oneWay == 1:
245.        # b5) Create a 3D deformable part named "subconstruction" by extruding the sketch
246.        subconstructionPart=glassModel.Part(name='SubconstructionPart',
247.        dimensionality=THREE_D, type=DEFORMABLE_BODY)
248.        subconstructionPart.BaseShellExtrude(sketch=subconstruction, depth=widthSubConstr)
249.
250.    # ----------------------------------------------------------------------------------
251.    # Create material
252.
253.    import material
254.
255.    # Linear-elastic glass
256.    glassMaterial = glassModel.Material(name='Glass')
257.    glassMaterial.Elastic(table=((youngsGlass, poissGlass), ))
258.
259.    # Linar-elastic secondary seal
260.    secSealMaterial = glassModel.Material(name='SecondarySeal')
261.    secSealMaterial.Elastic(table=((youngsSecSeal, poissSecSeal), ))
262.
263.    # Linar-elastic spacer
264.    spacerMaterial = glassModel.Material(name='SpacerMaterial')
265.    spacerMaterial.Elastic(table=((youngsSpacer, poissSpacer), ))
266.
267.    # #Ideal-plastic part of the spacer with one point
268.    # mdb.models['ParameterStudy' + repr(fIncrement)].materials['SpacerMaterial'].Plastic(table=((
269.    # yieldStressSpacer, 0.0), ))
270.
271.    #From EN 10088-2:2014 (D) page 19 Stainless steel 1.4301
272.    mdb.models['ParameterStudy' + repr(fIncrement)].materials['SpacerMaterial'].Plastic(table=((
273.    230000000.0, 0.0), (260000000.0, 0.01), (600000000.0, 0.45)))
274.
275.    if oneWay == 1:
276.        # Linar-elastic subconstruction
277.        subConstrMaterial = glassModel.Material(name='Subconstruction')
278.        subConstrMaterial.Elastic(table=((youngsSubConstr, poissSubConstr), ))
279.
280.    # ----------------------------------------------------------------------------------
281.    # Create solid section and assign the parts to it
282.
283.    import section
284.    #
285.
286.    # Create a section for the glass pane
287.    glassPaneSection = glassModel.HomogeneousSolidSection(name='GlassPaneSection',
288.    material='Glass')
289.
290.    # Create a section for the secondary seal
291.    secSealSection = glassModel.HomogeneousSolidSection(name='SecondarySealSection',
292.    material='SecondarySeal')
293.
294.    # Create a section for the spacer
295.    spacerSection = glassModel.HomogeneousShellSection(name='SpacerMaterialSection',
296.    material='SpacerMaterial',thickness=thicknessSpacer)
297.
298.    if oneWay == 1:
299.        # Create a section for the subconstruction
```

```
            subConstrSection = glassModel.HomogeneousShellSection(name='SubconstructionSection',
            material='Subconstruction',thickness=thicknessSubConstr)

        # Assign the glass pane 1 to the specific section
        glassRegion1 = (glassPanePart1.cells,)
        glassPanePart1.SectionAssignment(region=glassRegion1, sectionName='GlassPaneSection')

        # Assign the glass pane 2 to the specific section
        glassRegion2 = (glassPanePart2.cells,)
        glassPanePart2.SectionAssignment(region=glassRegion2, sectionName='GlassPaneSection')

        if thicknessGlassPane3>1e-12:
            # Assign the glass pane 3 to the specific section
            glassRegion3 = (glassPanePart3.cells,)
            glassPanePart3.SectionAssignment(region=glassRegion3, sectionName='GlassPaneSection')

            if thicknessGlassPane4 >1e-12:
                # Assign the glass pane 4 to the specific section
                glassRegion4 = (glassPanePart4.cells,)
                glassPanePart4.SectionAssignment(region=glassRegion4, sectionName='GlassPaneSection')

        # Assign the secondary seal to the specific section
        secSealRegion = (secSealPart.cells,)
        secSealPart.SectionAssignment(region=secSealRegion, sectionName='SecondarySealSection')

        # Assign the short spacer to the specific section
        shortSpacerRegion = mdb.models['ParameterStudy' + repr(fIncrement)].parts['ShortSpacerPart']
        f = shortSpacerRegion.faces
        faces = f.getSequenceFromMask(mask=('[#3ff ]', ), )
        region = shortSpacerRegion.Set(faces=faces, name='Set-1')
        shortSpacerPart.SectionAssignment(region=region, sectionName=
        'SpacerMaterialSection',offset=0.0, offsetType=TOP_SURFACE, offsetField='',
        thicknessAssignment=FROM_SECTION)

        # Assign the long spacer to the specific section
        longSpacerRegion = mdb.models['ParameterStudy' + repr(fIncrement)].parts['LongSpacerPart']
        f = longSpacerRegion.faces
        faces = f.getSequenceFromMask(mask=('[#3fff ]', ), )
        region = longSpacerRegion.Set(faces=faces, name='Set-1')
        longSpacerPart.SectionAssignment(region=region, sectionName='SpacerMaterialSection',
        offset=0.0, offsetType=TOP_SURFACE, offsetField='',
        thicknessAssignment=FROM_SECTION)

        if oneWay == 1:
            # Assign the subConstruction to the specific section
            subConstrRegion = mdb.models['ParameterStudy' + repr(fIncrement)].parts['SubconstructionPart']
            f = subConstrRegion.faces
            faces = f.getSequenceFromMask(mask=('[#7fff ]', ), )
            region = subConstrRegion.Set(faces=faces, name='Set-1')
            subconstructionPart.SectionAssignment(region=region, sectionName='SubconstructionSection',
                offset=0.0, offsetType=BOTTOM_SURFACE, offsetField='',
                thicknessAssignment=FROM_SECTION)

        # ----------------------------------------------------------------------------------
        # Create partitions

        # Create partition secondary seal
        p = mdb.models['ParameterStudy' + repr(fIncrement)].parts['SecSealPart']
        f1 = p.faces
        p.DatumPlaneByOffset(plane=f1[5], flip=SIDE1, offset=0.0)
        #---
        f = p.faces
        p.DatumPlaneByOffset(plane=f[0], flip=SIDE2, offset=widthSubConstr)
        #---
        f1 = p.faces
        p.DatumPlaneByOffset(plane=f1[7], flip=SIDE2, offset=0.0)
```

```
366.        #---
367.        f = p.faces
368.        p.DatumPlaneByOffset(plane=f[2], flip=SIDE2, offset=widthSubConstr)
369.        #---
370.        f1 = p.faces
371.        p.DatumPlaneByOffset(plane=f1[6], flip=SIDE2, offset=0.0)
372.        #---
373.        f = p.faces
374.        p.DatumPlaneByOffset(plane=f[4], flip=SIDE2, offset=0.0)
375.        #---
376.        c = p.cells
377.        pickedCells = c.getSequenceFromMask(mask=('[#1 ]', ), )
378.        d1 = p.datums
379.        p.PartitionCellByDatumPlane(datumPlane=d1[5], cells=pickedCells)
380.        #---
381.        c = p.cells
382.        pickedCells = c.getSequenceFromMask(mask=('[#1 ]', ), )
383.        d = p.datums
384.        p.PartitionCellByDatumPlane(datumPlane=d[6], cells=pickedCells)
385.        #---
386.        c = p.cells
387.        pickedCells = c.getSequenceFromMask(mask=('[#e ]', ), )
388.        d1 = p.datums
389.        p.PartitionCellByDatumPlane(datumPlane=d1[8], cells=pickedCells)
390.        #---
391.        c = p.cells
392.        pickedCells = c.getSequenceFromMask(mask=('[#7 ]', ), )
393.        d = p.datums
394.        p.PartitionCellByDatumPlane(datumPlane=d[7], cells=pickedCells)
395.        #---
396.        c = p.cells
397.        pickedCells = c.getSequenceFromMask(mask=('[#49 ]', ), )
398.        d1 = p.datums
399.        p.PartitionCellByDatumPlane(datumPlane=d1[3], cells=pickedCells)
400.        #---
401.        c = p.cells
402.        pickedCells = c.getSequenceFromMask(mask=('[#3 ]', ), )
403.        d = p.datums
404.        p.PartitionCellByDatumPlane(datumPlane=d[4], cells=pickedCells)
405.
406.        f = p.faces
407.        p.DatumPlaneByOffset(plane=f[56], flip=SIDE1, offset=0.0065)
408.        #---
409.        f1 = p.faces
410.        p.DatumPlaneByOffset(plane=f1[40], flip=SIDE1, offset=0.0065)
411.        #---
412.        c = p.cells
413.        pickedCells = c.getSequenceFromMask(mask=('[#20 ]', ), )
414.        d = p.datums
415.        p.PartitionCellByDatumPlane(datumPlane=d[16], cells=pickedCells)
416.        #---
417.        c = p.cells
418.        pickedCells = c.getSequenceFromMask(mask=('[#100 ]', ), )
419.        d1 = p.datums
420.        p.PartitionCellByDatumPlane(datumPlane=d1[16], cells=pickedCells)
421.        #---
422.        c = p.cells
423.        pickedCells = c.getSequenceFromMask(mask=('[#1 ]', ), )
424.        d = p.datums
425.        p.PartitionCellByDatumPlane(datumPlane=d[15], cells=pickedCells)
426.        #---
427.        c = p.cells
428.        pickedCells = c.getSequenceFromMask(mask=('[#100 ]', ), )
429.        d1 = p.datums
430.        p.PartitionCellByDatumPlane(datumPlane=d1[15], cells=pickedCells)
431.
```

```
#---
f = p.faces
p.DatumPlaneByOffset(plane=f[75], flip=SIDE1, offset=0.0065)
#---
f1 = p.faces
p.DatumPlaneByOffset(plane=f1[77], flip=SIDE1, offset=0.0065)
#---
c = p.cells
pickedCells = c.getSequenceFromMask(mask=('[#2000 ]', ), )
d = p.datums
p.PartitionCellByDatumPlane(datumPlane=d[22], cells=pickedCells)
c = p.cells
pickedCells = c.getSequenceFromMask(mask=('[#2000 ]', ), )
d1 = p.datums
p.PartitionCellByDatumPlane(datumPlane=d1[22], cells=pickedCells)
#---
c = p.cells
pickedCells = c.getSequenceFromMask(mask=('[#80 ]', ), )
d = p.datums
p.PartitionCellByDatumPlane(datumPlane=d[21], cells=pickedCells)
#---
c = p.cells
pickedCells = c.getSequenceFromMask(mask=('[#80 ]', ), )
d1 = p.datums
p.PartitionCellByDatumPlane(datumPlane=d1[21], cells=pickedCells)

# Create partitions on one end of ShortSpacerPart
partNShortSpacerPart = mdb.models['ParameterStudy' + repr(fIncrement)].parts['ShortSpacerPart']
vvShortSpacerPart = partNShortSpacerPart.vertices
partNShortSpacerPart.DatumPointByOffset(point=vvShortSpacerPart[6],
vector=(0.0, 0.0, -1*heightSpacer))
vv1ShortSpacerPart = partNShortSpacerPart.vertices
partNShortSpacerPart.DatumPointByOffset(point=vv1ShortSpacerPart[4],
vector=(0.0, 0.0, -1*heightSpacer))
partNShortSpacerPart.DatumPointByOffset(point=vvShortSpacerPart[1],
vector=(0.0, 0.0, -1*heightSpacer))
partNShortSpacerPart.DatumPointByOffset(point=vv1ShortSpacerPart[0],
vector=(0.0, 0.0, -1*heightSpacer))
fNSpacerPart = partNShortSpacerPart.faces
pickedFaces = fNSpacerPart.getSequenceFromMask(mask=('[#1 ]', ), )
vvShortSpacerPart, dNShortSpacerPart=partNShortSpacerPart.vertices, partNShortSpacerPart.datums
partNShortSpacerPart.PartitionFaceByShortestPath(point1=dNShortSpacerPart[6],
point2=dNShortSpacerPart[5], faces=pickedFaces)
fNSpacerPart = partNShortSpacerPart.faces
pickedFaces = fNSpacerPart.getSequenceFromMask(mask=('[#4 ]', ), )
vv1ShortSpacerPart,dd1ShortSpacerPart=partNShortSpacerPart.vertices,partNShortSpacerPart.datums
partNShortSpacerPart.PartitionFaceByShortestPath(point1=dd1ShortSpacerPart[5],
point2=dd1ShortSpacerPart[4], faces=pickedFaces)
pickedFaces = fNSpacerPart.getSequenceFromMask(mask=('[#10 ]', ), )
partNShortSpacerPart.PartitionFaceByShortestPath(point1=dNShortSpacerPart[4],
point2=dNShortSpacerPart[3], faces=pickedFaces)
f1SpacerPart = partNShortSpacerPart.faces
partNShortSpacerPart.RemoveFaces(faceList = f1SpacerPart[4:5], deleteCells=False)
pickedFaces = fNSpacerPart.getSequenceFromMask(mask=('[#20 ]', ), )
partNShortSpacerPart.PartitionFaceByShortestPath(point1=dd1ShortSpacerPart[6],
point2=dd1ShortSpacerPart[3], faces=pickedFaces)

# Create partitions on the other end of ShortSpacerPart
partNShortSpacerPart.DatumPointByOffset(point=vvShortSpacerPart[9],
vector=(0.0, 0.0, heightSpacer))
vv1ShortSpacerPart = partNShortSpacerPart.vertices
partNShortSpacerPart.DatumPointByOffset(point=vv1ShortSpacerPart[8],
vector=(0.0, 0.0, heightSpacer))
vvShortSpacerPart = partNShortSpacerPart.vertices
partNShortSpacerPart.DatumPointByOffset(point=vvShortSpacerPart[6],
vector=(0.0, 0.0, heightSpacer))
```

```
partNShortSpacerPart.DatumPointByOffset(point=vv1ShortSpacerPart[5],
vector=(0.0, 0.0, heightSpacer))
pickedFaces = fNSpacerPart.getSequenceFromMask(mask=('[#8 ]', ), )
partNShortSpacerPart.PartitionFaceByShortestPath(point1=dNShortSpacerPart[12],
point2=dNShortSpacerPart[13], faces=pickedFaces)
pickedFaces = fNSpacerPart.getSequenceFromMask(mask=('[#8 ]', ), )
partNShortSpacerPart.PartitionFaceByShortestPath(point1=dd1ShortSpacerPart[13],
point2=dd1ShortSpacerPart[14], faces=pickedFaces)
pickedFaces = fNSpacerPart.getSequenceFromMask(mask=('[#8 ]', ), )
partNShortSpacerPart.PartitionFaceByShortestPath(point1=dNShortSpacerPart[14],
point2=dNShortSpacerPart[15], faces=pickedFaces)
pickedFaces = fNSpacerPart.getSequenceFromMask(mask=('[#200 ]', ), )
partNShortSpacerPart.PartitionFaceByShortestPath(point1=dd1ShortSpacerPart[12],
point2=dd1ShortSpacerPart[15], faces=pickedFaces)
partNShortSpacerPart.RemoveFaces(faceList = fNSpacerPart[2:3], deleteCells=False)

 # Create partitions on LongSpacerPart
p = mdb.models['ParameterStudy' + repr(fIncrement)].parts['LongSpacerPart']
v1 = p.vertices
p.DatumPointByOffset(point=v1[6], vector=(0.0, 0.0, -1*heightSpacer))
#---
v = p.vertices
p.DatumPointByOffset(point=v[0], vector=(0.0, 0.0, -1*heightSpacer))
#---
p.DatumPointByOffset(point=v1[4], vector=(0.0, 0.0, -1*heightSpacer))
#---
p.DatumPointByOffset(point=v[1], vector=(0.0, 0.0, -1*heightSpacer))
#---
p.DatumPointByOffset(point=v1[6], vector=(-1*(widthSubConstr-thicknessSecSeal), 0.0, 0.0))
#---
p.DatumPointByOffset(point=v[6], vector=(0.0, 0.0, -1*(widthSubConstr-thicknessSecSeal)))
#---
p.DatumPointByOffset(point=v1[4], vector=(0.0, 0.0, -1*(widthSubConstr-thicknessSecSeal)))
#---
p.DatumPointByOffset(point=v[1], vector=(0.0, 0.0, -1*(widthSubConstr-thicknessSecSeal)))
#---
p.DatumPointByOffset(point=v1[0], vector=(0.0, 0.0, -1*(widthSubConstr-thicknessSecSeal)))
#---
p.DatumPointByOffset(point=v[2], vector=(0.0, 0.0, heightSpacer))
#---
p.DatumPointByOffset(point=v1[3], vector=(0.0, 0.0, heightSpacer))
#---
p.DatumPointByOffset(point=v[5], vector=(0.0, 0.0, heightSpacer))
#---
p.DatumPointByOffset(point=v1[7], vector=(0.0, 0.0, heightSpacer))
#---
p.DatumPointByOffset(point=v[2], vector=(0.0, 0.0, (widthSubConstr-thicknessSecSeal)))
#---
p.DatumPointByOffset(point=v1[3], vector=(0.0, 0.0, (widthSubConstr-thicknessSecSeal)))
#---
p.DatumPointByOffset(point=v[5], vector=(0.0, 0.0, (widthSubConstr-thicknessSecSeal)))
#---
p.DatumPointByOffset(point=v1[7], vector=(0.0, 0.0, (widthSubConstr-thicknessSecSeal)))
#---
f = p.faces
pickedFaces = f.getSequenceFromMask(mask=('[#2 ]', ), )
v, e1, d1 = p.vertices, p.edges, p.datums
p.PartitionFaceByShortestPath(point1=d1[16], point2=d1[18], faces=pickedFaces)
#---
f = p.faces
pickedFaces = f.getSequenceFromMask(mask=('[#1 ]', ), )
v1, e, d = p.vertices, p.edges, p.datums
p.PartitionFaceByShortestPath(point1=d[12], point2=d[14], faces=pickedFaces)
#---
f = p.faces
pickedFaces = f.getSequenceFromMask(mask=('[#10 ]', ), )
```

```
564.    v, e1, d1 = p.vertices, p.edges, p.datums
565.    p.PartitionFaceByShortestPath(point1=d1[18], point2=d1[19], faces=pickedFaces)
566.    #---
567.    f = p.faces
568.    pickedFaces = f.getSequenceFromMask(mask=('[#1 ]', ), )
569.    v1, e, d = p.vertices, p.edges, p.datums
570.    p.PartitionFaceByShortestPath(point1=d[14], point2=d[15], faces=pickedFaces)
571.    #---
572.    f = p.faces
573.    pickedFaces = f.getSequenceFromMask(mask=('[#20 ]', ), )
574.    v, e1, d1 = p.vertices, p.edges, p.datums
575.    p.PartitionFaceByShortestPath(point1=d1[10], point2=d1[9], faces=pickedFaces)
576.    #---
577.    f = p.faces
578.    pickedFaces = f.getSequenceFromMask(mask=('[#40 ]', ), )
579.    v1, e, d = p.vertices, p.edges, p.datums
580.    p.PartitionFaceByShortestPath(point1=d[6], point2=d[5], faces=pickedFaces)
581.    #---
582.    f = p.faces
583.    pickedFaces = f.getSequenceFromMask(mask=('[#100 ]', ), )
584.    v, e1, d1 = p.vertices, p.edges, p.datums
585.    p.PartitionFaceByShortestPath(point1=d1[9], point2=d1[8], faces=pickedFaces)
586.    #---
587.    f = p.faces
588.    pickedFaces = f.getSequenceFromMask(mask=('[#200 ]', ), )
589.    v1, e, d = p.vertices, p.edges, p.datums
590.    p.PartitionFaceByShortestPath(point1=d[5], point2=d[3], faces=pickedFaces)
591.    #---
592.    f = p.faces
593.    pickedFaces = f.getSequenceFromMask(mask=('[#100 ]', ), )
594.    v, e1, d1 = p.vertices, p.edges, p.datums
595.    p.PartitionFaceByShortestPath(point1=d1[10], point2=d1[11], faces=pickedFaces)
596.    #---
597.    f = p.faces
598.    pickedFaces = f.getSequenceFromMask(mask=('[#1 ]', ), )
599.    v1, e, d = p.vertices, p.edges, p.datums
600.    p.PartitionFaceByShortestPath(point1=d[6], point2=d[4], faces=pickedFaces)
601.    #---
602.    f = p.faces
603.    pickedFaces = f.getSequenceFromMask(mask=('[#2000 ]', ), )
604.    v, e1, d1 = p.vertices, p.edges, p.datums
605.    p.PartitionFaceByShortestPath(point1=d1[11], point2=d1[8], faces=pickedFaces)
606.    #---
607.    f = p.faces
608.    pickedFaces = f.getSequenceFromMask(mask=('[#1 ]', ), )
609.    v1, e, d = p.vertices, p.edges, p.datums
610.    p.PartitionFaceByShortestPath(point1=d[4], point2=d[3], faces=pickedFaces)
611.    #---
612.    f = p.faces
613.    pickedFaces = f.getSequenceFromMask(mask=('[#1000 ]', ), )
614.    v, e1, d1 = p.vertices, p.edges, p.datums
615.    p.PartitionFaceByShortestPath(point1=d1[16], point2=d1[17], faces=pickedFaces)
616.    #---
617.    f = p.faces
618.    pickedFaces = f.getSequenceFromMask(mask=('[#2000 ]', ), )
619.    v1, e, d = p.vertices, p.edges, p.datums
620.    p.PartitionFaceByShortestPath(point1=d[12], point2=d[13], faces=pickedFaces)
621.    #---
622.    f = p.faces
623.    pickedFaces = f.getSequenceFromMask(mask=('[#20000 ]', ), )
624.    v, e1, d1 = p.vertices, p.edges, p.datums
625.    p.PartitionFaceByShortestPath(point1=d1[17], point2=d1[19], faces=pickedFaces)
626.    #---
627.    f = p.faces
628.    pickedFaces = f.getSequenceFromMask(mask=('[#40000 ]', ), )
629.    v1, e, d = p.vertices, p.edges, p.datums
```

```
630.    p.PartitionFaceByShortestPath(point1=d[13], point2=d[15], faces=pickedFaces)
631.    session.viewports['Viewport: 1'].partDisplay.setValues(renderStyle=SHADED)
632.    #---
633.    f = p.faces
634.    p.RemoveFaces(faceList = f[16:17], deleteCells=False)
635.    #---
636.    f1 = p.faces
637.    p.RemoveFaces(faceList = f1[14:15], deleteCells=False)
638.    #---
639.    f = p.faces
640.    p.RemoveFaces(faceList = f[16:17], deleteCells=False)
641.    #---
642.    f1 = p.faces
643.    p.RemoveFaces(faceList = f1[15:16], deleteCells=False)
644.    #---
645.    f = p.faces
646.    p.RemoveFaces(faceList = f[6:7], deleteCells=False)
647.    #---
648.    f1 = p.faces
649.    p.RemoveFaces(faceList = f1[11:12], deleteCells=False)
650.
651.    #Create the datum planes for the glass pane 1
652.    p = mdb.models['ParameterStudy' + repr(fIncrement)].parts['GlassPanePart1']
653.    f = p.faces
654.    p.DatumPlaneByOffset(plane=f[1], flip=SIDE2, offset=thicknessSecSeal)
655.    ##---
656.    f1 = p.faces
657.    p.DatumPlaneByOffset(plane=f1[2], flip=SIDE2, offset=thicknessSecSeal)
658.    f = p.faces
659.    p.DatumPlaneByOffset(plane=f[2], flip=SIDE2,
660.    offset=thicknessSecSeal+heightSpacer)
661.    ##---
662.    f1 = p.faces
663.    p.DatumPlaneByOffset(plane=f1[1], flip=SIDE2,
664.    offset=thicknessSecSeal+heightSpacer)
665.    f = p.faces
666.    p.DatumPlaneByOffset(plane=f[0], flip=SIDE2, offset=thicknessSecSeal)
667.    ##---
668.    f1 = p.faces
669.    p.DatumPlaneByOffset(plane=f1[3], flip=SIDE2, offset=thicknessSecSeal)
670.    ##---
671.    f = p.faces
672.    p.DatumPlaneByOffset(plane=f[0], flip=SIDE2,
673.    offset=thicknessSecSeal+heightSpacer)
674.    #---
675.    f1 = p.faces
676.    p.DatumPlaneByOffset(plane=f1[3], flip=SIDE2,
677.    offset=thicknessSecSeal+heightSpacer)
678.    #---
679.    f = p.faces
680.    p.DatumPlaneByOffset(plane=f[0], flip=SIDE2, offset=widthSubConstr)
681.    #---
682.    f1 = p.faces
683.    p.DatumPlaneByOffset(plane=f1[2], flip=SIDE2, offset=widthSubConstr)
684.    c = p.cells
685.    pickedCells = c.getSequenceFromMask(mask=('[#1 ]', ), )
686.    d = p.datums
687.    p.PartitionCellByDatumPlane(datumPlane=d[4], cells=pickedCells)
688.    #---
689.    c = p.cells
690.    pickedCells = c.getSequenceFromMask(mask=('[#1 ]', ), )
691.    d1 = p.datums
692.    p.PartitionCellByDatumPlane(datumPlane=d1[5], cells=pickedCells)
693.    #---
694.    c = p.cells
695.    pickedCells = c.getSequenceFromMask(mask=('[#1 ]', ), )
```

```
696.        d = p.datums
697.        p.PartitionCellByDatumPlane(datumPlane=d[12], cells=pickedCells)
698.        #---
699.        c = p.cells
700.        pickedCells = c.getSequenceFromMask(mask=('[#f ]', ), )
701.        d1 = p.datums
702.        p.PartitionCellByDatumPlane(datumPlane=d1[3], cells=pickedCells)
703.        #---
704.        c = p.cells
705.        pickedCells = c.getSequenceFromMask(mask=('[#f0 ]', ), )
706.        d = p.datums
707.        p.PartitionCellByDatumPlane(datumPlane=d[6], cells=pickedCells)
708.        #---
709.        c = p.cells
710.        pickedCells = c.getSequenceFromMask(mask=('[#f00 ]', ), )
711.        d1 = p.datums
712.        p.PartitionCellByDatumPlane(datumPlane=d1[8], cells=pickedCells)
713.        #---
714.        c = p.cells
715.        pickedCells = c.getSequenceFromMask(mask=('[#f ]', ), )
716.        d = p.datums
717.        p.PartitionCellByDatumPlane(datumPlane=d[10], cells=pickedCells)
718.        #---
719.        c = p.cells
720.        pickedCells = c.getSequenceFromMask(mask=('[#24442 ]', ), )
721.        d1 = p.datums
722.        p.PartitionCellByDatumPlane(datumPlane=d1[7], cells=pickedCells)
723.        #---
724.        c = p.cells
725.        pickedCells = c.getSequenceFromMask(mask=('[#847 ]', ), )
726.        d = p.datums
727.        p.PartitionCellByDatumPlane(datumPlane=d[9], cells=pickedCells)
728.        #---
729.        c = p.cells
730.        pickedCells = c.getSequenceFromMask(mask=('[#108a8 ]', ), )
731.        d1 = p.datums
732.        p.PartitionCellByDatumPlane(datumPlane=d1[11], cells=pickedCells)
733.
734.        #Create the datum planes for the glass pane 2
735.        p = mdb.models['ParameterStudy' + repr(fIncrement)].parts['GlassPanePart2']
736.        f = p.faces
737.        p.DatumPlaneByOffset(plane=f[1], flip=SIDE2, offset=thicknessSecSeal)
738.        ##---
739.        f1 = p.faces
740.        p.DatumPlaneByOffset(plane=f1[2], flip=SIDE2, offset=thicknessSecSeal)
741.        f = p.faces
742.        p.DatumPlaneByOffset(plane=f[2], flip=SIDE2,
743.        offset=thicknessSecSeal+heightSpacer)
744.        ##---
745.        f1 = p.faces
746.        p.DatumPlaneByOffset(plane=f1[1], flip=SIDE2,
747.        offset=thicknessSecSeal+heightSpacer)
748.        f = p.faces
749.        p.DatumPlaneByOffset(plane=f[0], flip=SIDE2, offset=thicknessSecSeal)
750.        ##---
751.        f1 = p.faces
752.        p.DatumPlaneByOffset(plane=f1[3], flip=SIDE2, offset=thicknessSecSeal)
753.        ##---
754.        f = p.faces
755.        p.DatumPlaneByOffset(plane=f[0], flip=SIDE2,
756.        offset=thicknessSecSeal+heightSpacer)
757.        #---
758.        f1 = p.faces
759.        p.DatumPlaneByOffset(plane=f1[3], flip=SIDE2,
760.        offset=thicknessSecSeal+heightSpacer)
761.        #---
```

```
762.        f = p.faces
763.        p.DatumPlaneByOffset(plane=f[0], flip=SIDE2, offset=widthSubConstr)
764.        #---
765.        f1 = p.faces
766.        p.DatumPlaneByOffset(plane=f1[2], flip=SIDE2, offset=widthSubConstr)
767.        c = p.cells
768.        pickedCells = c.getSequenceFromMask(mask=('[#1 ]', ), )
769.        d = p.datums
770.        p.PartitionCellByDatumPlane(datumPlane=d[4], cells=pickedCells)
771.        #---
772.        c = p.cells
773.        pickedCells = c.getSequenceFromMask(mask=('[#1 ]', ), )
774.        d1 = p.datums
775.        p.PartitionCellByDatumPlane(datumPlane=d1[5], cells=pickedCells)
776.        #---
777.        c = p.cells
778.        pickedCells = c.getSequenceFromMask(mask=('[#1 ]', ), )
779.        d = p.datums
780.        p.PartitionCellByDatumPlane(datumPlane=d[12], cells=pickedCells)
781.        #---
782.        c = p.cells
783.        pickedCells = c.getSequenceFromMask(mask=('[#f ]', ), )
784.        d1 = p.datums
785.        p.PartitionCellByDatumPlane(datumPlane=d1[3], cells=pickedCells)
786.        #---
787.        c = p.cells
788.        pickedCells = c.getSequenceFromMask(mask=('[#f0 ]', ), )
789.        d = p.datums
790.        p.PartitionCellByDatumPlane(datumPlane=d[6], cells=pickedCells)
791.        #---
792.        c = p.cells
793.        pickedCells = c.getSequenceFromMask(mask=('[#f00 ]', ), )
794.        d1 = p.datums
795.        p.PartitionCellByDatumPlane(datumPlane=d1[8], cells=pickedCells)
796.        #---
797.        c = p.cells
798.        pickedCells = c.getSequenceFromMask(mask=('[#f ]', ), )
799.        d = p.datums
800.        p.PartitionCellByDatumPlane(datumPlane=d[10], cells=pickedCells)
801.        #---
802.        c = p.cells
803.        pickedCells = c.getSequenceFromMask(mask=('[#24442 ]', ), )
804.        d1 = p.datums
805.        p.PartitionCellByDatumPlane(datumPlane=d1[7], cells=pickedCells)
806.        #---
807.        c = p.cells
808.        pickedCells = c.getSequenceFromMask(mask=('[#847 ]', ), )
809.        d = p.datums
810.        p.PartitionCellByDatumPlane(datumPlane=d[9], cells=pickedCells)
811.        #---
812.        c = p.cells
813.        pickedCells = c.getSequenceFromMask(mask=('[#108a8 ]', ), )
814.        d1 = p.datums
815.        p.PartitionCellByDatumPlane(datumPlane=d1[11], cells=pickedCells)
816.
817.        if thicknessGlassPane3>1e-12:
818.            #Create the datum planes for the glass pane 3
819.            p = mdb.models['ParameterStudy' + repr(fIncrement)].parts['GlassPanePart3']
820.            f = p.faces
821.            p.DatumPlaneByOffset(plane=f[1], flip=SIDE2, offset=thicknessSecSeal)
822.            ##---
823.            f1 = p.faces
824.            p.DatumPlaneByOffset(plane=f1[2], flip=SIDE2, offset=thicknessSecSeal)
825.            f = p.faces
826.            p.DatumPlaneByOffset(plane=f[2], flip=SIDE2,
827.            offset=thicknessSecSeal+heightSpacer)
```

```
##---
f1 = p.faces
p.DatumPlaneByOffset(plane=f1[1], flip=SIDE2,
offset=thicknessSecSeal+heightSpacer)
f = p.faces
p.DatumPlaneByOffset(plane=f[0], flip=SIDE2, offset=thicknessSecSeal)
##---
f1 = p.faces
p.DatumPlaneByOffset(plane=f1[3], flip=SIDE2, offset=thicknessSecSeal)
##---
f = p.faces
p.DatumPlaneByOffset(plane=f[0], flip=SIDE2,
offset=thicknessSecSeal+heightSpacer)
#---
f1 = p.faces
p.DatumPlaneByOffset(plane=f1[3], flip=SIDE2,
offset=thicknessSecSeal+heightSpacer)
#---
f = p.faces
p.DatumPlaneByOffset(plane=f[0], flip=SIDE2, offset=widthSubConstr)
#---
f1 = p.faces
p.DatumPlaneByOffset(plane=f1[2], flip=SIDE2, offset=widthSubConstr)
c = p.cells
pickedCells = c.getSequenceFromMask(mask=('[#1 ]', ), )
d = p.datums
p.PartitionCellByDatumPlane(datumPlane=d[4], cells=pickedCells)
#---
c = p.cells
pickedCells = c.getSequenceFromMask(mask=('[#1 ]', ), )
d1 = p.datums
p.PartitionCellByDatumPlane(datumPlane=d1[5], cells=pickedCells)
#---
c = p.cells
pickedCells = c.getSequenceFromMask(mask=('[#1 ]', ), )
d = p.datums
p.PartitionCellByDatumPlane(datumPlane=d[12], cells=pickedCells)
#---
c = p.cells
pickedCells = c.getSequenceFromMask(mask=('[#f ]', ), )
d1 = p.datums
p.PartitionCellByDatumPlane(datumPlane=d1[3], cells=pickedCells)
#---
c = p.cells
pickedCells = c.getSequenceFromMask(mask=('[#f0 ]', ), )
d = p.datums
p.PartitionCellByDatumPlane(datumPlane=d[6], cells=pickedCells)
#---
c = p.cells
pickedCells = c.getSequenceFromMask(mask=('[#f00 ]', ), )
d1 = p.datums
p.PartitionCellByDatumPlane(datumPlane=d1[8], cells=pickedCells)
#---
c = p.cells
pickedCells = c.getSequenceFromMask(mask=('[#f ]', ), )
d = p.datums
p.PartitionCellByDatumPlane(datumPlane=d[10], cells=pickedCells)
#---
c = p.cells
pickedCells = c.getSequenceFromMask(mask=('[#24442 ]', ), )
d1 = p.datums
p.PartitionCellByDatumPlane(datumPlane=d1[7], cells=pickedCells)
#---
c = p.cells
pickedCells = c.getSequenceFromMask(mask=('[#847 ]', ), )
d = p.datums
```

```
894.            p.PartitionCellByDatumPlane(datumPlane=d[9], cells=pickedCells)
895.            #---
896.            c = p.cells
897.            pickedCells = c.getSequenceFromMask(mask=('[#108a8 ]', ), )
898.            d1 = p.datums
899.            p.PartitionCellByDatumPlane(datumPlane=d1[11], cells=pickedCells)
900.
901.            if thicknessGlassPane4 >1e-12:
902.              #Create the datum planes for the glass pane 2
903.              p = mdb.models['ParameterStudy' + repr(fIncrement)].parts['GlassPanePart4']
904.              f = p.faces
905.              p.DatumPlaneByOffset(plane=f[1], flip=SIDE2, offset=thicknessSecSeal)
906.              ##---
907.              f1 = p.faces
908.              p.DatumPlaneByOffset(plane=f1[2], flip=SIDE2, offset=thicknessSecSeal)
909.              f = p.faces
910.              p.DatumPlaneByOffset(plane=f[2], flip=SIDE2,
911.              offset=thicknessSecSeal+heightSpacer)
912.              ##---
913.              f1 = p.faces
914.              p.DatumPlaneByOffset(plane=f1[1], flip=SIDE2,
915.              offset=thicknessSecSeal+heightSpacer)
916.              f = p.faces
917.              p.DatumPlaneByOffset(plane=f[0], flip=SIDE2, offset=thicknessSecSeal)
918.              ##---
919.              f1 = p.faces
920.              p.DatumPlaneByOffset(plane=f1[3], flip=SIDE2, offset=thicknessSecSeal)
921.              ##---
922.              f = p.faces
923.              p.DatumPlaneByOffset(plane=f[0], flip=SIDE2,
924.              offset=thicknessSecSeal+heightSpacer)
925.              #---
926.              f1 = p.faces
927.              p.DatumPlaneByOffset(plane=f1[3], flip=SIDE2,
928.              offset=thicknessSecSeal+heightSpacer)
929.              #---
930.              f = p.faces
931.              p.DatumPlaneByOffset(plane=f[0], flip=SIDE2, offset=widthSubConstr)
932.              #---
933.              f1 = p.faces
934.              p.DatumPlaneByOffset(plane=f1[2], flip=SIDE2, offset=widthSubConstr)
935.              c = p.cells
936.              pickedCells = c.getSequenceFromMask(mask=('[#1 ]', ), )
937.              d = p.datums
938.              p.PartitionCellByDatumPlane(datumPlane=d[4], cells=pickedCells)
939.              #---
940.              c = p.cells
941.              pickedCells = c.getSequenceFromMask(mask=('[#1 ]', ), )
942.              d1 = p.datums
943.              p.PartitionCellByDatumPlane(datumPlane=d1[5], cells=pickedCells)
944.              #---
945.              c = p.cells
946.              pickedCells = c.getSequenceFromMask(mask=('[#1 ]', ), )
947.              d = p.datums
948.              p.PartitionCellByDatumPlane(datumPlane=d[12], cells=pickedCells)
949.              #---
950.              c = p.cells
951.              pickedCells = c.getSequenceFromMask(mask=('[#f ]', ), )
952.              d1 = p.datums
953.              p.PartitionCellByDatumPlane(datumPlane=d1[3], cells=pickedCells)
954.              #---
955.              c = p.cells
956.              pickedCells = c.getSequenceFromMask(mask=('[#f0 ]', ), )
957.              d = p.datums
958.              p.PartitionCellByDatumPlane(datumPlane=d[6], cells=pickedCells)
959.              #---
```

```
            c = p.cells
            pickedCells = c.getSequenceFromMask(mask=('[#f00 ]', ), )
            d1 = p.datums
            p.PartitionCellByDatumPlane(datumPlane=d1[8], cells=pickedCells)
            #---
            c = p.cells
            pickedCells = c.getSequenceFromMask(mask=('[#f ]', ), )
            d = p.datums
            p.PartitionCellByDatumPlane(datumPlane=d[10], cells=pickedCells)
            #---
            c = p.cells
            pickedCells = c.getSequenceFromMask(mask=('[#24442 ]', ), )
            d1 = p.datums
            p.PartitionCellByDatumPlane(datumPlane=d1[7], cells=pickedCells)
            #---
            c = p.cells
            pickedCells = c.getSequenceFromMask(mask=('[#847 ]', ), )
            d = p.datums
            p.PartitionCellByDatumPlane(datumPlane=d[9], cells=pickedCells)
            #---
            c = p.cells
            pickedCells = c.getSequenceFromMask(mask=('[#108a8 ]', ), )
            d1 = p.datums
            p.PartitionCellByDatumPlane(datumPlane=d1[11], cells=pickedCells)

        if oneWay == 1:
            p = mdb.models['ParameterStudy' + repr(fIncrement)].parts['SubconstructionPart']
            v = p.vertices
            p.DatumPointByOffset(point=v[2], vector=(0.0, 0.0, thicknessSecSeal))
            ##---
            v1, d = p.vertices, p.datums
            p.DatumPointByOffset(point=d[3], vector=(0.0, 0.0, heightSpacer))
            ##---
            v, d1 = p.vertices, p.datums
            p.DatumPointByOffset(point=v[3], vector=(0.0, 0.0, thicknessSecSeal))
            ##---
            v1, d = p.vertices, p.datums
            p.DatumPointByOffset(point=d[5], vector=(0.0, 0.0, heightSpacer))

            alpha1=thicknessSecSeal/radiusSubConstr
            alpha2=lengthPane/radiusSubConstr
            alpha3=alpha2-alpha1
            alpha4=math.pi/2-alpha3
            length=math.cos(alpha4)*radiusSubConstr
            height=math.sin(alpha4)*radiusSubConstr
            p.DatumPointByCoordinate(coords=(length, height, 0.0))
            p.DatumPointByCoordinate(coords=(length, height, widthSubConstr))

            alpha1=(thicknessSecSeal+heightSpacer)/radiusSubConstr
            alpha2=lengthPane/radiusSubConstr
            alpha3=alpha2-alpha1
            alpha4=math.pi/2-alpha3
            length=math.cos(alpha4)*radiusSubConstr
            height=math.sin(alpha4)*radiusSubConstr
            p.DatumPointByCoordinate(coords=(length, height, 0.0))
            p.DatumPointByCoordinate(coords=(length, height, widthSubConstr))

            alpha1=thicknessSecSeal/radiusSubConstr
            alpha4=math.pi/2-alpha1
            length=math.cos(alpha4)*radiusSubConstr
            height=math.sin(alpha4)*radiusSubConstr
            p.DatumPointByCoordinate(coords=(length, height, 0.0))
            p.DatumPointByCoordinate(coords=(length, height, widthSubConstr))

            alpha1=(thicknessSecSeal+heightSpacer)/radiusSubConstr
            alpha4=math.pi/2-alpha1
```

```
        length=math.cos(alpha4)*radiusSubConstr
        height=math.sin(alpha4)*radiusSubConstr
        p.DatumPointByCoordinate(coords=(length, height, 0.0))
        p.DatumPointByCoordinate(coords=(length, height, widthSubConstr))

        p = mdb.models['ParameterStudy' + repr(fIncrement)].parts['SubconstructionPart']
        f = p.faces
        pickedFaces = f.getSequenceFromMask(mask=('[#1 ]', ), )
        v, e, d = p.vertices, p.edges, p.datums
        p.PartitionFaceByShortestPath(point1=d[8], point2=d[7], faces=pickedFaces)
        #---
        f = p.faces
        pickedFaces = f.getSequenceFromMask(mask=('[#2 ]', ), )
        v1, e1, d1 = p.vertices, p.edges, p.datums
        p.PartitionFaceByShortestPath(point1=d1[10], point2=d1[9], faces=pickedFaces)
        #---
        f = p.faces
        pickedFaces = f.getSequenceFromMask(mask=('[#7 ]', ), )
        v, e, d = p.vertices, p.edges, p.datums
        p.PartitionFaceByShortestPath(point1=d[5], point2=d[3], faces=pickedFaces)
        #---
        f = p.faces
        pickedFaces = f.getSequenceFromMask(mask=('[#22 ]', ), )
        v1, e1, d1 = p.vertices, p.edges, p.datums
        p.PartitionFaceByShortestPath(point1=d1[11], point2=d1[12], faces=pickedFaces)
        #---
        f = p.faces
        pickedFaces = f.getSequenceFromMask(mask=('[#88 ]', ), )
        v, e, d = p.vertices, p.edges, p.datums
        p.PartitionFaceByShortestPath(point1=d[13], point2=d[14], faces=pickedFaces)
        #---
        f = p.faces
        pickedFaces = f.getSequenceFromMask(mask=('[#1aa ]', ), )
        v1, e1, d1 = p.vertices, p.edges, p.datums
        p.PartitionFaceByShortestPath(point1=d1[6], point2=d1[4], faces=pickedFaces)

    # ----------------------------------------------------------------------------------
    # Create the assembly

        import assembly

        a1 = mdb.models['ParameterStudy' + repr(fIncrement)].rootAssembly
        a1.DatumCsysByDefault(CARTESIAN)
        p = mdb.models['ParameterStudy' + repr(fIncrement)].parts['GlassPanePart1']
        a1.Instance(name='GlassPanePart1-1', part=p, dependent=ON)
        #---
        p = mdb.models['ParameterStudy' + repr(fIncrement)].parts['SecSealPart']
        a1.Instance(name='SecSealPart-1', part=p, dependent=ON)
        #---
        a1.translate(instanceList=('SecSealPart-1', ), vector=(0.0, 0.0, thicknessGlassPane1))
        #---
        p = mdb.models['ParameterStudy' + repr(fIncrement)].parts['LongSpacerPart']
        a1.Instance(name='LongSpacerPart-1', part=p, dependent=ON)
        #---
        a1.rotate(instanceList=('LongSpacerPart-1', ), axisPoint=(0.0, 0.0, 0.0),
            axisDirection=(0.0, thicknessSecSeal, 0.0), angle=-90.0)
        #---
        a1.translate(instanceList=('LongSpacerPart-1', ), vector=(widthPane-thicknessSecSeal, thicknessSecSeal, thicknessGlassPane1))
        #---
        p = mdb.models['ParameterStudy' + repr(fIncrement)].parts['LongSpacerPart']
        a1.Instance(name='LongSpacerPart-2', part=p, dependent=ON)
        #---
        a1.rotate(instanceList=('LongSpacerPart-2', ), axisPoint=(0.0, 0.0, 0.0),
            axisDirection=(0.0, thicknessSecSeal, 0.0), angle=-180.0)
        #---
        a1.rotate(instanceList=('LongSpacerPart-2', ), axisPoint=(0.0, 0.0, 0.0),
```

```
1092.         axisDirection=(0.0, thicknessSecSeal, 0.0), angle=90.0)
1093.     #---
1094.     a1.rotate(instanceList=('LongSpacerPart-2', ), axisPoint=(0.0, 0.0, 0.0),
1095.         axisDirection=(-1*thicknessCavity, 0.0, 0.0), angle=180.0)
1096.     #---
1097.     a1.translate(instanceList=('LongSpacerPart-2', ), vector=(0.0, 0.0, thicknessGlassPane1+thicknessCavity))
1098.     #---
1099.     a1.translate(instanceList=('LongSpacerPart-2', ), vector=(widthPane-thicknessSecSeal, lengthPane-thicknessSecSeal, 0.0))
1100.     #---
1101.     p = mdb.models['ParameterStudy' + repr(fIncrement)].parts['ShortSpacerPart']
1102.     a1.Instance(name='ShortSpacerPart-1', part=p, dependent=ON)
1103.     #---
1104.     a1.rotate(instanceList=('ShortSpacerPart-1', ), axisPoint=(0.0, 0.0, 0.0),
1105.         axisDirection=(0.016, 0.0, 0.0), angle=-90.0)
1106.     #---
1107.     a1.rotate(instanceList=('ShortSpacerPart-1', ), axisPoint=(0.0, 0.0, 0.0),
1108.         axisDirection=(0.0, thicknessCavity, 0.0), angle=90.0)
1109.     #---
1110.     a1.translate(instanceList=('ShortSpacerPart-1', ), vector=(0.0, 0.0, thicknessGlassPane1+thicknessCavity))
1111.     #---
1112.     a1.translate(instanceList=('ShortSpacerPart-1', ), vector=(widthPane-thicknessSecSeal, thicknessSecSeal, 0.0))
1113.     #---
1114.     p = mdb.models['ParameterStudy' + repr(fIncrement)].parts['ShortSpacerPart']
1115.     a1.Instance(name='ShortSpacerPart-2', part=p, dependent=ON)
1116.     #---
1117.     a1.rotate(instanceList=('ShortSpacerPart-2', ), axisPoint=(0.0, 0.0, 0.0),
1118.         axisDirection=(thicknessCavity, 0.0, 0.0), angle=-90.0)
1119.     #---
1120.     a1.rotate(instanceList=('ShortSpacerPart-2', ), axisPoint=(0.0, 0.0, 0.0),
1121.         axisDirection=(0.0, thicknessCavity, 0.0), angle=-90.0)
1122.     #---
1123.     a1.translate(instanceList=('ShortSpacerPart-2', ), vector=(0.0, 0.0, thicknessGlassPane1))
1124.     #---
1125.     a1.translate(instanceList=('ShortSpacerPart-2', ), vector=(thicknessSecSeal, thicknessSecSeal, 0.0))
1126.     #---
1127.     p = mdb.models['ParameterStudy' + repr(fIncrement)].parts['GlassPanePart2']
1128.     a1.Instance(name='GlassPanePart2-1', part=p, dependent=ON)
1129.     i1 = mdb.models['ParameterStudy' + repr(fIncrement)].rootAssembly.allInstances['GlassPanePart1-1']
1130.     a1.translate(instanceList=('GlassPanePart2-1', ), vector=(0.0, 0.0, thicknessGlassPane1+thicknessCavity))
1131.     a = mdb.models['ParameterStudy' + repr(fIncrement)].rootAssembly
1132.
1133.     if oneWay == 1:
1134.         p = mdb.models['ParameterStudy' + repr(fIncrement)].parts['SubconstructionPart']
1135.         a.Instance(name='SubconstructionPart-1', part=p, dependent=ON)
1136.         a = mdb.models['ParameterStudy' + repr(fIncrement)].rootAssembly
1137.         a.rotate(instanceList=('SubconstructionPart-1', ), axisPoint=(0.0, 0.0, 0.0),
1138.             axisDirection=(0.0, thicknessSecSeal, 0.0), angle=90.0)
1139.         a = mdb.models['ParameterStudy' + repr(fIncrement)].rootAssembly
1140.         a.rotate(instanceList=('SubconstructionPart-1', ), axisPoint=(0.0, 0.0, 0.0),
1141.             axisDirection=(thicknessSecSeal, 0.0, 0.0), angle=90.0)
1142.         a = mdb.models['ParameterStudy' + repr(fIncrement)].rootAssembly
1143.         a.translate(instanceList=('SubconstructionPart-1', ), vector=(0.0, 0.0, -radiusSubConstr))
1144.
1145.         a.Instance(name='SubconstructionPart-2', part=p, dependent=ON)
1146.         a.rotate(instanceList=('SubconstructionPart-2', ), axisPoint=(0.0, 0.0, 0.0),
1147.             axisDirection=(0.0, thicknessSecSeal, 0.0), angle=90.0)
1148.         a = mdb.models['ParameterStudy' + repr(fIncrement)].rootAssembly
1149.         a.rotate(instanceList=('SubconstructionPart-2', ), axisPoint=(0.0, 0.0, 0.0),
1150.             axisDirection=(thicknessSecSeal, 0.0, 0.0), angle=90.0)
1151.         a = mdb.models['ParameterStudy' + repr(fIncrement)].rootAssembly
1152.         a.translate(instanceList=('SubconstructionPart-2', ), vector=(0.0, 0.0, -radiusSubConstr))
1153.
1154.         a = mdb.models['ParameterStudy' + repr(fIncrement)].rootAssembly
1155.         alpha3=math.pi/2-arcLength/radiusSubConstr
1156.         doubleAlpha2=2*math.atan((1-math.sin(alpha3))/cos(alpha3))
1157.         alpha3DEG=alpha3*180/pi
```

```
        doubleAlpha2DEG=doubleAlpha2*180/pi
        a.rotate(instanceList=('SubconstructionPart-2', ), axisPoint=(0.0, 0.0, 0.0),
            axisDirection=(thicknessSecSeal, 0.0, 0.0), angle=doubleAlpha2DEG)
        a = mdb.models['ParameterStudy' + repr(fIncrement)].rootAssembly
        a.rotate(instanceList=('SubconstructionPart-2', ), axisPoint=(0.0, 0.0, 0.0),
            axisDirection=(0.0, 0.0, thicknessGlassPane1), angle=-180.0)
        a = mdb.models['ParameterStudy' + repr(fIncrement)].rootAssembly
        a.translate(instanceList=('SubconstructionPart-2', ), vector=(widthSubConstr, 0.0, 0.0))
        a = mdb.models['ParameterStudy' + repr(fIncrement)].rootAssembly
        a.translate(instanceList=('SubconstructionPart-2', ), vector=(widthPane-widthSubConstr, 0.0, 0.0))
        a = mdb.models['ParameterStudy' + repr(fIncrement)].rootAssembly
        a.translate(instanceList=('SubconstructionPart-2', ), vector=(0.0, math.cos(alpha3)*radiusSubConstr,
            (math.sin(alpha3)-1)*radiusSubConstr))

    if thicknessGlassPane3>1e-12:
        translate3=thicknessCavity*1+thicknessGlassPane2
        p = mdb.models['ParameterStudy' + repr(fIncrement)].parts['SecSealPart']
        a1.Instance(name='SecSealPart-1-23', part=p, dependent=ON)
        #---
        a1.translate(instanceList=('SecSealPart-1-23', ), vector=(0.0, 0.0, thicknessGlassPane1+translate3))
        #---
        p = mdb.models['ParameterStudy' + repr(fIncrement)].parts['LongSpacerPart']
        a1.Instance(name='LongSpacerPart-23', part=p, dependent=ON)
        #---
        a1.rotate(instanceList=('LongSpacerPart-23', ), axisPoint=(0.0, 0.0, 0.0),
            axisDirection=(0.0, thicknessSecSeal, 0.0), angle=-90.0)
        #---
        a1.translate(instanceList=('LongSpacerPart-23', ), vector=(widthPane-thicknessSecSeal, thicknessSecSeal, thicknessGlassPane1+translate3))
        #---
        p = mdb.models['ParameterStudy' + repr(fIncrement)].parts['LongSpacerPart']
        a1.Instance(name='LongSpacerPart-2-23', part=p, dependent=ON)
        #---
        a1.rotate(instanceList=('LongSpacerPart-2-23', ), axisPoint=(0.0, 0.0, 0.0),
            axisDirection=(0.0, thicknessSecSeal, 0.0), angle=-180.0)
        #---
        a1.rotate(instanceList=('LongSpacerPart-2-23', ), axisPoint=(0.0, 0.0, 0.0),
            axisDirection=(0.0, thicknessSecSeal, 0.0), angle=90.0)
        #---
        a1.rotate(instanceList=('LongSpacerPart-2-23', ), axisPoint=(0.0, 0.0, 0.0),
            axisDirection=(-1*thicknessCavity, 0.0, 0.0), angle=180.0)
        #---
        a1.translate(instanceList=('LongSpacerPart-2-23', ), vector=(0.0, 0.0, thicknessGlassPane1+thicknessCavity))
        #---
        a1.translate(instanceList=('LongSpacerPart-2-23', ), vector=(widthPane-thicknessSecSeal, lengthPane-thicknessSecSeal, translate3))
        #---
        p = mdb.models['ParameterStudy' + repr(fIncrement)].parts['ShortSpacerPart']
        a1.Instance(name='ShortSpacerPart-1-23', part=p, dependent=ON)
        #---
        a1.rotate(instanceList=('ShortSpacerPart-1-23', ), axisPoint=(0.0, 0.0, 0.0),
            axisDirection=(0.016, 0.0, 0.0), angle=-90.0)
        #---
        a1.rotate(instanceList=('ShortSpacerPart-1-23', ), axisPoint=(0.0, 0.0, 0.0),
            axisDirection=(0.0, thicknessCavity, 0.0), angle=90.0)
        #---
        a1.translate(instanceList=('ShortSpacerPart-1-23', ), vector=(0.0, 0.0, thicknessGlassPane1+thicknessCavity))
        #---
        a1.translate(instanceList=('ShortSpacerPart-1-23', ), vector=(widthPane-thicknessSecSeal, thicknessSecSeal, translate3))
        #---
        p = mdb.models['ParameterStudy' + repr(fIncrement)].parts['ShortSpacerPart']
        a1.Instance(name='ShortSpacerPart-2-23', part=p, dependent=ON)
        #---
        a1.rotate(instanceList=('ShortSpacerPart-2-23', ), axisPoint=(0.0, 0.0, 0.0),
            axisDirection=(thicknessCavity, 0.0, 0.0), angle=-90.0)
        #---
        a1.rotate(instanceList=('ShortSpacerPart-2-23', ), axisPoint=(0.0, 0.0, 0.0),
            axisDirection=(0.0, thicknessCavity, 0.0), angle=-90.0)
```

```
        #---
        a1.translate(instanceList=('ShortSpacerPart-2-23', ), vector=(0.0, 0.0, thicknessGlassPane1))
        #---
        a1.translate(instanceList=('ShortSpacerPart-2-23', ), vector=(thicknessSecSeal, thicknessSecSeal, translate3))

        p = mdb.models['ParameterStudy' + repr(fIncrement)].parts['GlassPanePart3']
        a1.Instance(name='GlassPanePart3-1', part=p, dependent=ON)
        i1 = mdb.models['ParameterStudy' + repr(fIncrement)].rootAssembly.allInstances['GlassPanePart3-1']
        a1.translate(instanceList=('GlassPanePart3-1', ), vector=(0.0, 0.0, thicknessGlassPane1+thicknessCavity+translate3))
        a = mdb.models['ParameterStudy' + repr(fIncrement)].rootAssembly

        if thicknessGlassPane4>1e-12:
            translate4=thicknessCavity*2+thicknessGlassPane2+thicknessGlassPane3
            p = mdb.models['ParameterStudy' + repr(fIncrement)].parts['SecSealPart']
            a1.Instance(name='SecSealPart-1-34', part=p, dependent=ON)
            #---
            a1.translate(instanceList=('SecSealPart-1-34', ), vector=(0.0, 0.0, thicknessGlassPane1+translate4))
            #---
            p = mdb.models['ParameterStudy' + repr(fIncrement)].parts['LongSpacerPart']
            a1.Instance(name='LongSpacerPart-34', part=p, dependent=ON)
            #---
            a1.rotate(instanceList=('LongSpacerPart-34', ), axisPoint=(0.0, 0.0, 0.0),
                axisDirection=(0.0, thicknessSecSeal, 0.0), angle=-90.0)
            #---
            a1.translate(instanceList=('LongSpacerPart-34', ), vector=(widthPane-thicknessSecSeal, thicknessSecSeal, thicknessGlassPane1+translate4))
            #---
            p = mdb.models['ParameterStudy' + repr(fIncrement)].parts['LongSpacerPart']
            a1.Instance(name='LongSpacerPart-2-34', part=p, dependent=ON)
            #---
            a1.rotate(instanceList=('LongSpacerPart-2-34', ), axisPoint=(0.0, 0.0, 0.0),
                axisDirection=(0.0, thicknessSecSeal, 0.0), angle=-180.0)
            #---
            a1.rotate(instanceList=('LongSpacerPart-2-34', ), axisPoint=(0.0, 0.0, 0.0),
                axisDirection=(0.0, thicknessSecSeal, 0.0), angle=90.0)
            #---
            a1.rotate(instanceList=('LongSpacerPart-2-34', ), axisPoint=(0.0, 0.0, 0.0),
                axisDirection=(-1*thicknessCavity, 0.0, 0.0), angle=180.0)
            #---
            a1.translate(instanceList=('LongSpacerPart-2-34', ), vector=(0.0, 0.0, thicknessGlassPane1+thicknessCavity))
            #---
            a1.translate(instanceList=('LongSpacerPart-2-34', ), vector=(widthPane-thicknessSecSeal, lengthPane-thicknessSecSeal, translate4))
            #---
            p = mdb.models['ParameterStudy' + repr(fIncrement)].parts['ShortSpacerPart']
            a1.Instance(name='ShortSpacerPart-1-34', part=p, dependent=ON)
            #---
            a1.rotate(instanceList=('ShortSpacerPart-1-34', ), axisPoint=(0.0, 0.0, 0.0),
                axisDirection=(0.016, 0.0, 0.0), angle=-90.0)
            #---
            a1.rotate(instanceList=('ShortSpacerPart-1-34', ), axisPoint=(0.0, 0.0, 0.0),
                axisDirection=(0.0, thicknessCavity, 0.0), angle=90.0)
            #---
            a1.translate(instanceList=('ShortSpacerPart-1-34', ), vector=(0.0, 0.0, thicknessGlassPane1+thicknessCavity))
            #---
            a1.translate(instanceList=('ShortSpacerPart-1-34', ), vector=(widthPane-thicknessSecSeal, thicknessSecSeal, translate4))
            #---
            p = mdb.models['ParameterStudy' + repr(fIncrement)].parts['ShortSpacerPart']
            a1.Instance(name='ShortSpacerPart-2-34', part=p, dependent=ON)
            #---
            a1.rotate(instanceList=('ShortSpacerPart-2-34', ), axisPoint=(0.0, 0.0, 0.0),
                axisDirection=(thicknessCavity, 0.0, 0.0), angle=-90.0)
            #---
            a1.rotate(instanceList=('ShortSpacerPart-2-34', ), axisPoint=(0.0, 0.0, 0.0),
                axisDirection=(0.0, thicknessCavity, 0.0), angle=-90.0)
            #---
            a1.translate(instanceList=('ShortSpacerPart-2-34', ), vector=(0.0, 0.0, thicknessGlassPane1))
            #---
```

```
        a1.translate(instanceList=('ShortSpacerPart-2-34', ), vector=(thicknessSecSeal, thicknessSecSeal, translate4))

        p = mdb.models['ParameterStudy' + repr(fIncrement)].parts['GlassPanePart4']
        a1.Instance(name='GlassPanePart4-1', part=p, dependent=ON)
        i1 = mdb.models['ParameterStudy' + repr(fIncrement)].rootAssembly.allInstances['GlassPanePart4-1']
        a1.translate(instanceList=('GlassPanePart4-1', ), vector=(0.0, 0.0, thicknessGlassPane1+thicknessCavity+translate4))
        a = mdb.models['ParameterStudy' + repr(fIncrement)].rootAssembly

# ------------------------------------------------------------------------------------------

initialIncInp=0.01              # Between 1e-20 and 1e-1
minIncInp=0.0000001                 # Discard calculation if residuum is below
maxIncInp=0.01                  # Between initialInc and 1
timePeriod=1                    # Full calculation step = 1
nlgeom=ON                       # Should be always on

# Create the step AppyLoad
mdb.models['ParameterStudy' + repr(fIncrement)].StaticStep(name='ApplyLoad', previous='Initial',
description='Static step ', initialInc=initialIncInp, minInc=minIncInp, maxInc=maxIncInp, nlgeom=ON)

# Interaction property between spacer and glass pane
mdb.models['ParameterStudy' + repr(fIncrement)].ContactProperty('InteractionSpacerGlass')
mdb.models['ParameterStudy' + repr(fIncrement)].interactionProperties['InteractionSpacerGlass'].TangentialBehavior(
    formulation=FRICTIONLESS)
mdb.models['ParameterStudy' + repr(fIncrement)].interactionProperties['InteractionSpacerGlass'].NormalBehavior(
    pressureOverclosure=HARD, allowSeparation=ON,
    constraintEnforcementMethod=DEFAULT)

# ------------------------------------------------------------------------------------------
# Create all constraints

tieTolerance=0.0001

# Create all constraints

#Constraint SecSeal-All 12
a = mdb.models['ParameterStudy' + repr(fIncrement)].rootAssembly
s1 = a.instances['GlassPanePart1-1'].faces
side1Faces1 = s1.getSequenceFromMask(mask=(
    '[#10040040 #4220100 #80400010 #21012480 #404820 ]', ), )
s2 = a.instances['LongSpacerPart-2'].faces
side1Faces2 = s2.getSequenceFromMask(mask=('[#2033 ]', ), )
s3 = a.instances['ShortSpacerPart-1'].faces
side1Faces3 = s3.getSequenceFromMask(mask=('[#209 ]', ), )
s4 = a.instances['ShortSpacerPart-2'].faces
side1Faces4 = s4.getSequenceFromMask(mask=('[#209 ]', ), )
s5 = a.instances['LongSpacerPart-1'].faces
side1Faces5 = s5.getSequenceFromMask(mask=('[#2033 ]', ), )
s6 = a.instances['GlassPanePart2-1'].faces
side1Faces6 = s6.getSequenceFromMask(mask=(
    '[#4080080 #1848080 #24900020 #42400020 #800041 ]', ), )
region1=a.Surface(side1Faces=side1Faces1+side1Faces2+side1Faces3+side1Faces4+\
    side1Faces5+side1Faces6, name='m_Surf-14')
a = mdb.models['ParameterStudy' + repr(fIncrement)].rootAssembly
s1 = a.instances['SecSealPart-1'].faces
side1Faces1 = s1.getSequenceFromMask(mask=(
    '[#ad6e3ad6 #e2e1dcb5 #c18de2e1 #f ]', ), )
region2=a.Surface(side1Faces=side1Faces1, name='s_Surf-14')
mdb.models['ParameterStudy' + repr(fIncrement)].Tie(name='Tie-SecSeal', master=region1,
    slave=region2, positionToleranceMethod=COMPUTED, adjust=ON,
    tieRotations=ON, thickness=ON)

# Create constraint Tie between the spacers itselves in the corner
a = mdb.models['ParameterStudy' + repr(fIncrement)].rootAssembly
e1 = a.instances['LongSpacerPart-2'].edges
edges1 = e1.getSequenceFromMask(mask=('[#d214e080 #3 ]', ), )
```

```
    e2 = a.instances['LongSpacerPart-1'].edges
    edges2 = e2.getSequenceFromMask(mask=('[#d214e080 #3 ]', ), )
    region1=a.Set(edges=edges1+edges2, name='m_Set-1')
    e1 = a.instances['ShortSpacerPart-1'].edges
    edges1 = e1.getSequenceFromMask(mask=('[#3ea26c0 ]', ), )
    e2 = a.instances['ShortSpacerPart-2'].edges
    edges2 = e2.getSequenceFromMask(mask=('[#3ea26c0 ]', ), )
    region2=a.Set(edges=edges1+edges2, name='s_Set-1')
    mdb.models['ParameterStudy' + repr(fIncrement)].Tie(name='Tie_SpacerSpacer', master=region1,
        slave=region2, positionToleranceMethod=SPECIFIED, positionTolerance=tieTolerance,
        adjust=ON, tieRotations=ON, thickness=ON)

    if thicknessGlassPane3>1e-12:
        # Create all constraints in case of a 3rd glass pane

        # Create constraint Tie between GlassPane2 and all Spacers LongSpacerPart and ShortSpacerPart
        a = mdb.models['ParameterStudy' + repr(fIncrement)].rootAssembly
        s1 = a.instances['GlassPanePart2-1'].faces
        side1Faces1 = s1.getSequenceFromMask(mask=(
            '[#80008100 #10400020 #10002480 #8000000 #2 ]', ), )
        region1=a.Surface(side1Faces=side1Faces1, name='m_Surf-1-23')
        s1 = a.instances['ShortSpacerPart-2-23'].faces
        side1Faces1 = s1.getSequenceFromMask(mask=('[#c4 ]', ), )
        s2 = a.instances['LongSpacerPart-23'].faces
        side1Faces2 = s2.getSequenceFromMask(mask=('[#4c ]', ), )
        s3 = a.instances['LongSpacerPart-2-23'].faces
        side1Faces3 = s3.getSequenceFromMask(mask=('[#980 ]', ), )
        s4 = a.instances['ShortSpacerPart-1-23'].faces
        side1Faces4 = s4.getSequenceFromMask(mask=('[#112 ]', ), )
        region2=a.Surface(side1Faces=side1Faces1+side1Faces2+side1Faces3+side1Faces4,
            name='s_Surf-1-23')
        mdb.models['ParameterStudy' + repr(fIncrement)].SurfaceToSurfaceContactStd(name='Contact_GlassPane2_Spacer-23', #---
        createStepName='Initial', master=region1, slave=region2,
        sliding=FINITE, thickness=ON, interactionProperty='InteractionSpacerGlass',
        adjustMethod=NONE, initialClearance=OMIT, datumAxis=None, clearanceRegion=None)

        # Create constraint Tie between GlassPane2 and SecSealPart
        a = mdb.models['ParameterStudy' + repr(fIncrement)].rootAssembly
        s1 = a.instances['GlassPanePart2-1'].faces
        side1Faces1 = s1.getSequenceFromMask(mask=(
            '[#10040040 #4220100 #80400010 #21012480 #404820 ]', ), )
        region1=a.Surface(side1Faces=side1Faces1, name='m_Surf-3-23')
        s1 = a.instances['SecSealPart-1-23'].faces
        side1Faces1 = s1.getSequenceFromMask(mask=('[#9022090 #40c09014 #8c00a1 #8 ]',
        ), )
        region2=a.Surface(side1Faces=side1Faces1, name='s_Surf-3-23')
        mdb.models['ParameterStudy' + repr(fIncrement)].Tie(name='Tie_GlassPane2_SecS-23', master=region1,
            slave=region2, positionToleranceMethod=SPECIFIED, positionTolerance=tieTolerance,
            adjust=ON, tieRotations=ON, thickness=ON)

        # Create constraint Tie between GlassPane3 and all Spacers LongSpacerPart and ShortSpacerPart
        a = mdb.models['ParameterStudy' + repr(fIncrement)].rootAssembly
        s1 = a.instances['GlassPanePart3-1'].faces
        side1Faces1 = s1.getSequenceFromMask(mask=(
            '[#20010400 #20000009 #100 #4900 #10400 ]', ), )
        region1=a.Surface(side1Faces=side1Faces1, name='m_Surf-5-23')
        s1 = a.instances['ShortSpacerPart-1-23'].faces
        side1Faces1 = s1.getSequenceFromMask(mask=('[#c4 ]', ), )
        s2 = a.instances['LongSpacerPart-2-23'].faces
        side1Faces2 = s2.getSequenceFromMask(mask=('[#4c ]', ), )
        s3 = a.instances['LongSpacerPart-23'].faces
        side1Faces3 = s3.getSequenceFromMask(mask=('[#980 ]', ), )
        s4 = a.instances['ShortSpacerPart-2-23'].faces
        side1Faces4 = s4.getSequenceFromMask(mask=('[#112 ]', ), )
        mdb.models['ParameterStudy' + repr(fIncrement)].SurfaceToSurfaceContactStd(name='Contact_GlassPane3_Spacer-23', #----
        createStepName='Initial', master=region1, slave=region2,
```

```
1422.         sliding=FINITE, thickness=ON, interactionProperty='InteractionSpacerGlass',
1423.         adjustMethod=NONE, initialClearance=OMIT, datumAxis=None, clearanceRegion=None)
1424.
1425.         # Create constraint Tie between GlassPane3 and SecSealPart
1426.         a = mdb.models['ParameterStudy' + repr(fIncrement)].rootAssembly
1427.         s1 = a.instances['GlassPanePart3-1'].faces
1428.         side1Faces1 = s1.getSequenceFromMask(mask=(
1429.             '[#4080080 #1848080 #24900020 #42400020 #800041 ]', ), )
1430.         region1=a.Surface(side1Faces=side1Faces1, name='m_Surf-7-23')
1431.         s1 = a.instances['SecSealPart-1-23'].faces
1432.         side1Faces1 = s1.getSequenceFromMask(mask=(
1433.             '[#20480a02 #a2210881 #100c240 #4 ]', ), )
1434.         region2=a.Surface(side1Faces=side1Faces1, name='s_Surf-7-23')
1435.         mdb.models['ParameterStudy' + repr(fIncrement)].Tie(name='Tie_GlassPane3_SecS-23', master=region1,
1436.             slave=region2, positionToleranceMethod=SPECIFIED, positionTolerance=tieTolerance,
1437.             adjust=ON, tieRotations=ON, thickness=ON)
1438.
1439.         # Create constraint Tie between all Spacers-23 and SecSealPart-23
1440.         a = mdb.models['ParameterStudy' + repr(fIncrement)].rootAssembly
1441.         s1 = a.instances['SecSealPart-1-23'].faces
1442.         side1Faces1 = s1.getSequenceFromMask(mask=('[#84241044 #4420 #c0012000 #3 ]',
1443.             ), )
1444.         region1=a.Surface(side1Faces=side1Faces1, name='m_Surf-9-23')
1445.         s1 = a.instances['LongSpacerPart-2-23'].faces
1446.         side1Faces1 = s1.getSequenceFromMask(mask=('[#2033 ]', ), )
1447.         s2 = a.instances['ShortSpacerPart-2-23'].faces
1448.         side1Faces2 = s2.getSequenceFromMask(mask=('[#209 ]', ), )
1449.         s3 = a.instances['LongSpacerPart-23'].faces
1450.         side1Faces3 = s3.getSequenceFromMask(mask=('[#2033 ]', ), )
1451.         s4 = a.instances['ShortSpacerPart-1-23'].faces
1452.         side1Faces4 = s4.getSequenceFromMask(mask=('[#209 ]', ), )
1453.         region2=a.Surface(side1Faces=side1Faces1+side1Faces2+side1Faces3+side1Faces4,
1454.             name='s_Surf-9-23')
1455.         mdb.models['ParameterStudy' + repr(fIncrement)].Tie(name='Tie_Spacer_SecS-23', master=region1,
1456.             slave=region2, positionToleranceMethod=SPECIFIED, positionTolerance=tieTolerance,
1457.             adjust=ON, tieRotations=ON, thickness=ON)
1458.         mdb.models['ParameterStudy' + repr(fIncrement)].constraints['Tie_Spacer_SecS-23'].swapSurfaces()
1459.
1460.         # Create constraint Tie between the spacers itselves in the corner
1461.         a = mdb.models['ParameterStudy' + repr(fIncrement)].rootAssembly
1462.         e1 = a.instances['LongSpacerPart-2-23'].edges
1463.         edges1 = e1.getSequenceFromMask(mask=('[#d214e080 #3 ]', ), )
1464.         e2 = a.instances['LongSpacerPart-23'].edges
1465.         edges2 = e2.getSequenceFromMask(mask=('[#d214e080 #3 ]', ), )
1466.         region1=a.Set(edges=edges1+edges2, name='m_Set-1-23')
1467.         e1 = a.instances['ShortSpacerPart-1-23'].edges
1468.         edges1 = e1.getSequenceFromMask(mask=('[#3ea26c0 ]', ), )
1469.         e2 = a.instances['ShortSpacerPart-2-23'].edges
1470.         edges2 = e2.getSequenceFromMask(mask=('[#3ea26c0 ]', ), )
1471.         region2=a.Set(edges=edges1+edges2, name='s_Set-1-23')
1472.         mdb.models['ParameterStudy' + repr(fIncrement)].Tie(name='Tie_SpacerSpacer-23', master=region1,
1473.             slave=region2, positionToleranceMethod=SPECIFIED, positionTolerance=tieTolerance,
1474.             adjust=ON, tieRotations=ON, thickness=ON)
1475.
1476.         if thicknessGlassPane4>1e-12:
1477.             # Create all constraints in case of a 4th glass pane
1478.
1479.             # Create constraint Tie between GlassPane2 and all Spacers LongSpacerPart and ShortSpacerPart
1480.             a = mdb.models['ParameterStudy' + repr(fIncrement)].rootAssembly
1481.             s1 = a.instances['GlassPanePart3-1'].faces
1482.             side1Faces1 = s1.getSequenceFromMask(mask=(
1483.                 '[#80008100 #10400020 #10002480 #8000000 #2 ]', ), )
1484.             region1=a.Surface(side1Faces=side1Faces1, name='m_Surf-1-34')
1485.             s1 = a.instances['ShortSpacerPart-2-34'].faces
1486.             side1Faces1 = s1.getSequenceFromMask(mask=('[#c4 ]', ), )
1487.             s2 = a.instances['LongSpacerPart-34'].faces
```

```
side1Faces2 = s2.getSequenceFromMask(mask=('[#4c ]', ), )
s3 = a.instances['LongSpacerPart-2-34'].faces
side1Faces3 = s3.getSequenceFromMask(mask=('[#980 ]', ), )
s4 = a.instances['ShortSpacerPart-1-34'].faces
side1Faces4 = s4.getSequenceFromMask(mask=('[#112 ]', ), )
region2=a.Surface(side1Faces=side1Faces1+side1Faces2+side1Faces3+side1Faces4,
    name='s_Surf-1-34')
mdb.models['ParameterStudy' + repr(fIncrement)].SurfaceToSurfaceContactStd(name='Contact_GlassPane3_Spacer-34', #--
createStepName='Initial', master=region1, slave=region2,
sliding=FINITE, thickness=ON, interactionProperty='InteractionSpacerGlass',
adjustMethod=NONE, initialClearance=OMIT, datumAxis=None, clearanceRegion=None)

# Create constraint Tie between GlassPane4 and SecSealPart
a = mdb.models['ParameterStudy' + repr(fIncrement)].rootAssembly
s1 = a.instances['GlassPanePart3-1'].faces
side1Faces1 = s1.getSequenceFromMask(mask=(
    '[#10040040 #4220100 #80400010 #21012480 #404820 ]', ), )
region1=a.Surface(side1Faces=side1Faces1, name='m_Surf-3-34')
s1 = a.instances['SecSealPart-1-34'].faces
side1Faces1 = s1.getSequenceFromMask(mask=('[#9022090 #40c09014 #8c00a1 #8 ]',
), )
region2=a.Surface(side1Faces=side1Faces1, name='s_Surf-3-34')
mdb.models['ParameterStudy' + repr(fIncrement)].Tie(name='Tie_GlassPane3_SecS-34', master=region1,
    slave=region2, positionToleranceMethod=SPECIFIED, positionTolerance=tieTolerance,
    adjust=ON, tieRotations=ON, thickness=ON)

# Create constraint Tie between GlassPane4 and all Spacers LongSpacerPart and ShortSpacerPart
a = mdb.models['ParameterStudy' + repr(fIncrement)].rootAssembly
s1 = a.instances['GlassPanePart4-1'].faces
side1Faces1 = s1.getSequenceFromMask(mask=(
    '[#20010400 #20000009 #100 #4900 #10400 ]', ), )
region1=a.Surface(side1Faces=side1Faces1, name='m_Surf-5-34')
s1 = a.instances['ShortSpacerPart-1-34'].faces
side1Faces1 = s1.getSequenceFromMask(mask=('[#c4 ]', ), )
s2 = a.instances['LongSpacerPart-2-34'].faces
side1Faces2 = s2.getSequenceFromMask(mask=('[#4c ]', ), )
s3 = a.instances['LongSpacerPart-34'].faces
side1Faces3 = s3.getSequenceFromMask(mask=('[#980 ]', ), )
s4 = a.instances['ShortSpacerPart-2-34'].faces
side1Faces4 = s4.getSequenceFromMask(mask=('[#112 ]', ), )
region2=a.Surface(side1Faces=side1Faces1+side1Faces2+side1Faces3+side1Faces4,
    name='s_Surf-5-34')
mdb.models['ParameterStudy' + repr(fIncrement)].SurfaceToSurfaceContactStd(name='Contact_GlassPane4_Spacer-34', #----
createStepName='Initial', master=region1, slave=region2,
sliding=FINITE, thickness=ON, interactionProperty='InteractionSpacerGlass',
adjustMethod=NONE, initialClearance=OMIT, datumAxis=None, clearanceRegion=None)

# Create constraint Tie between GlassPane4 and SecSealPart
a = mdb.models['ParameterStudy' + repr(fIncrement)].rootAssembly
s1 = a.instances['GlassPanePart4-1'].faces
side1Faces1 = s1.getSequenceFromMask(mask=(
    '[#4080080 #1848080 #24900020 #42400020 #800041 ]', ), )
region1=a.Surface(side1Faces=side1Faces1, name='m_Surf-7-34')
s1 = a.instances['SecSealPart-1-34'].faces
side1Faces1 = s1.getSequenceFromMask(mask=(
    '[#20480a02 #a2210881 #100c240 #4 ]', ), )
region2=a.Surface(side1Faces=side1Faces1, name='s_Surf-7-34')
mdb.models['ParameterStudy' + repr(fIncrement)].Tie(name='Tie_GlassPane4_SecS-34', master=region1,
    slave=region2, positionToleranceMethod=SPECIFIED, positionTolerance=tieTolerance,
    adjust=ON, tieRotations=ON, thickness=ON)

# Create constraint Tie between all Spacers-34 and SecSealPart-34
a = mdb.models['ParameterStudy' + repr(fIncrement)].rootAssembly
s1 = a.instances['SecSealPart-1-34'].faces
side1Faces1 = s1.getSequenceFromMask(mask=('[#84241044 #4420 #c0012000 #3 ]',
    ), )
```

```
            region1=a.Surface(side1Faces=side1Faces1, name='m_Surf-9-34')
            s1 = a.instances['LongSpacerPart-2-34'].faces
            side1Faces1 = s1.getSequenceFromMask(mask=('[#2033 ]', ), )
            s2 = a.instances['ShortSpacerPart-2-34'].faces
            side1Faces2 = s2.getSequenceFromMask(mask=('[#209 ]', ), )
            s3 = a.instances['LongSpacerPart-34'].faces
            side1Faces3 = s3.getSequenceFromMask(mask=('[#2033 ]', ), )
            s4 = a.instances['ShortSpacerPart-1-34'].faces
            side1Faces4 = s4.getSequenceFromMask(mask=('[#209 ]', ), )
            region2=a.Surface(side1Faces=side1Faces1+side1Faces2+side1Faces3+side1Faces4,
                name='s_Surf-9-34')
            mdb.models['ParameterStudy' + repr(fIncrement)].Tie(name='Tie_Spacer_SecS-34', master=region1,
                slave=region2, positionToleranceMethod=SPECIFIED, positionTolerance=tieTolerance,
                adjust=ON, tieRotations=ON, thickness=ON)
            mdb.models['ParameterStudy' + repr(fIncrement)].constraints['Tie_Spacer_SecS-34'].swapSurfaces()

            #Create constraint Tie between the spacers itselves in the corner
            a = mdb.models['ParameterStudy' + repr(fIncrement)].rootAssembly
            e1 = a.instances['LongSpacerPart-2-34'].edges
            edges1 = e1.getSequenceFromMask(mask=('[#d214e080 #3 ]', ), )
            e2 = a.instances['LongSpacerPart-34'].edges
            edges2 = e2.getSequenceFromMask(mask=('[#d214e080 #3 ]', ), )
            region1=a.Set(edges=edges1+edges2, name='m_Set-1-34')
            e1 = a.instances['ShortSpacerPart-1-34'].edges
            edges1 = e1.getSequenceFromMask(mask=('[#3ea26c0 ]', ), )
            e2 = a.instances['ShortSpacerPart-2-34'].edges
            edges2 = e2.getSequenceFromMask(mask=('[#3ea26c0 ]', ), )
            region2=a.Set(edges=edges1+edges2, name='s_Set-1-34')
            mdb.models['ParameterStudy' + repr(fIncrement)].Tie(name='Tie_SpacerSpacer-34', master=region1,
                slave=region2, positionToleranceMethod=SPECIFIED, positionTolerance=tieTolerance,
                adjust=ON, tieRotations=ON, thickness=ON)

        # ----------------------------------------------------------------------------------------
        # Create gas filling

        # Fluid cavity property
        mdb.models['ParameterStudy' + repr(fIncrement)].FluidCavityProperty(name='CavityGas',
        definition=PNEUMATIC, molecularWeight=molecularWeightCavity)

        # Create a reference point for cavity 12
        a = mdb.models['ParameterStudy' + repr(fIncrement)].rootAssembly
        refPoint1=a.ReferencePoint(point=(thicknessSecSeal+heightSpacer+0.002, thicknessSecSeal+heightSpacer+0.002,
            thicknessGlassPane1+0.002))

        if thicknessGlassPane3>1e-12:
            #Create a reference point for cavity 23
            a = mdb.models['ParameterStudy' + repr(fIncrement)].rootAssembly
            refPoint2=a.ReferencePoint(point=(thicknessSecSeal+heightSpacer+0.002, thicknessSecSeal+heightSpacer+0.002,
            thicknessGlassPane1+0.002+thicknessCavity+thicknessGlassPane2))

            if thicknessGlassPane4>1e-12:
                #Create a reference point for cavity 34
                a = mdb.models['ParameterStudy' + repr(fIncrement)].rootAssembly
                refPoint3=a.ReferencePoint(point=(thicknessSecSeal+heightSpacer+0.002,
                thicknessSecSeal+heightSpacer+0.002, thicknessGlassPane1+0.002+thicknessCavity
                +thicknessGlassPane2+thicknessCavity+thicknessGlassPane3))

        #a = mdb.models['ParameterStudy' + repr(fIncrement)].rootAssembly
        a = mdb.models['ParameterStudy' + repr(fIncrement)].rootAssembly
        #r1 = a.referencePoints

        # Cavity gass filling 12
        r1 = a.referencePoints

        if thicknessGlassPane3==0:
            if oneWay == 1:
```

```
            refPoints1=(r1[24], )
        if oneWay == 2:
            refPoints1=(r1[20], )
    if thicknessGlassPane3>1e-12 and thicknessGlassPane4==0:
        if oneWay == 1:
            refPoints1=(r1[47], )
        if oneWay == 2:
            refPoints1=(r1[43], )
    if thicknessGlassPane4>1e-12 and thicknessGlassPane3>1e-12:
        if oneWay == 1:
            refPoints1=(r1[71], )
        if oneWay == 2:
            refPoints1=(r1[67], )

    #if oneWay == 1:
    #   refPoints1=(r1[24], )
    #if oneWay == 2:
    #   refPoints1=(r1[20], )

    region1=a.Set(referencePoints=refPoints1, name='Set-6')
    s1 = a.instances['GlassPanePart1-1'].faces
    side1Faces1 = s1.getSequenceFromMask(mask=('[#800 #4 #2000000 ]', ), )
    s2 = a.instances['ShortSpacerPart-2'].faces
    side1Faces2 = s2.getSequenceFromMask(mask=('[#20 ]', ), )
    s3 = a.instances['LongSpacerPart-1'].faces
    side1Faces3 = s3.getSequenceFromMask(mask=('[#1600 ]', ), )
    s4 = a.instances['LongSpacerPart-2'].faces
    side1Faces4 = s4.getSequenceFromMask(mask=('[#1600 ]', ), )
    s5 = a.instances['ShortSpacerPart-1'].faces
    side1Faces5 = s5.getSequenceFromMask(mask=('[#20 ]', ), )
    s6 = a.instances['GlassPanePart2-1'].faces
    side1Faces6 = s6.getSequenceFromMask(mask=('[#2000 #0 #4800 ]', ), )
    region2=a.Surface(side1Faces=side1Faces1+side1Faces2+side1Faces3+side1Faces4+\
        side1Faces5+side1Faces6, name='Surf-9')

    mdb.models['ParameterStudy' + repr(fIncrement)].FluidCavity(name='GasFilling',
        createStepName='Initial', cavityPoint=region1, cavitySurface=region2,
        interactionProperty='CavityGas', ambientPressure=ambientPressureCavity)

    a = mdb.models['ParameterStudy' + repr(fIncrement)].rootAssembly
    r1 = a.referencePoints
    #refPoints1=(r1[24], )
    region1=a.Set(referencePoints=refPoints1, name='Set-6')
    s1 = a.instances['GlassPanePart2-1'].faces
    side1Faces1 = s1.getSequenceFromMask(mask=('[#800 #4 ]', ), )
    region2=a.Surface(side1Faces=side1Faces1, name='Surf-10')
    mdb.models['ParameterStudy' + repr(fIncrement)].FluidCavity(name='Int-5',
        createStepName='Initial', cavityPoint=region1, cavitySurface=region2,
        interactionProperty='CavityGas')

    region1=a.Set(referencePoints=refPoints1, name='Set-3-12')
    s1 = a.instances['LongSpacerPart-1'].faces
    side1Faces1 = s1.getSequenceFromMask(mask=('[#1600 ]', ), )
    s2 = a.instances['ShortSpacerPart-2'].faces
    side1Faces2 = s2.getSequenceFromMask(mask=('[#20 ]', ), )
    s3 = a.instances['GlassPanePart1-1'].faces
    side1Faces3 = s3.getSequenceFromMask(mask=('[#800 #4 #2000000 ]', ), )
    s4 = a.instances['LongSpacerPart-2'].faces
    side1Faces4 = s4.getSequenceFromMask(mask=('[#1600 ]', ), )
    s5 = a.instances['ShortSpacerPart-1'].faces
    side1Faces5 = s5.getSequenceFromMask(mask=('[#20 ]', ), )
    s6 = a.instances['GlassPanePart2-1'].faces
    side1Faces6 = s6.getSequenceFromMask(mask=('[#2000 #0 #4800 ]', ), )
    region2=a.Surface(side1Faces=side1Faces1+side1Faces2+side1Faces3+side1Faces4+\
        side1Faces5+side1Faces6, name='cavitysurface-12')

```

```
1686.     mdb.models['ParameterStudy' + repr(fIncrement)].FluidCavity(name='CavityInteraction12',
1687.         createStepName='Initial', cavityPoint=region1, cavitySurface=region2,
1688.         interactionProperty='CavityGas', ambientPressure=ambientPressureCavity)
1689.
1690.     if thicknessGlassPane3>1e-12 and thicknessGlassPane4==0:
1691.         # Cavity gass filling 23
1692.         #r1 = a.referencePoints
1693.         if thicknessGlassPane3>1e-12 and thicknessGlassPane4==0:
1694.             if oneWay == 1:
1695.                 refPoints2=(r1[48], )
1696.             if oneWay == 2:
1697.                 refPoints2=(r1[44], )
1698.         if thicknessGlassPane4>1e-12 and thicknessGlassPane3>1e-12:
1699.             if oneWay == 1:
1700.                 refPoints2=(r1[72], )
1701.             if oneWay == 2:
1702.                 refPoints2=(r1[68], )
1703.
1704.         region1=a.Set(referencePoints=refPoints2, name='Set-3-23')
1705.         s1 = a.instances['LongSpacerPart-23'].faces
1706.         side1Faces1 = s1.getSequenceFromMask(mask=('[#1600 ]', ), )
1707.         s2 = a.instances['ShortSpacerPart-2-23'].faces
1708.         side1Faces2 = s2.getSequenceFromMask(mask=('[#20 ]', ), )
1709.         s3 = a.instances['GlassPanePart2-1'].faces
1710.         side1Faces3 = s3.getSequenceFromMask(mask=('[#800 #4 #2000000 ]', ), )
1711.         s4 = a.instances['LongSpacerPart-2-23'].faces
1712.         side1Faces4 = s4.getSequenceFromMask(mask=('[#1600 ]', ), )
1713.         s5 = a.instances['ShortSpacerPart-1-23'].faces
1714.         side1Faces5 = s5.getSequenceFromMask(mask=('[#20 ]', ), )
1715.         s6 = a.instances['GlassPanePart3-1'].faces
1716.         side1Faces6 = s6.getSequenceFromMask(mask=('[#2000 #0 #4800 ]', ), )
1717.         region2=a.Surface(side1Faces=side1Faces1+side1Faces2+side1Faces3+side1Faces4+\
1718.             side1Faces5+side1Faces6, name='cavitysurface-23')
1719.
1720.         mdb.models['ParameterStudy' + repr(fIncrement)].FluidCavity(name='CavityInteraction23',
1721.             createStepName='Initial', cavityPoint=region1, cavitySurface=region2,
1722.             interactionProperty='CavityGas', ambientPressure=ambientPressureCavity)
1723.
1724.     if thicknessGlassPane4>1e-12 and thicknessGlassPane3>1e-12:
1725.         # Cavity gass filling 23
1726.         #r1 = a.referencePoints
1727.         #if thicknessGlassPane3>1e-12 and thicknessGlassPane4==0:
1728.         #   refPoints2=(r1[57], )
1729.         if thicknessGlassPane4>1e-12 and thicknessGlassPane3>1e-12:
1730.             if oneWay == 1:
1731.                 refPoints2=(r1[72], )
1732.             if oneWay == 2:
1733.                 refPoints2=(r1[68], )
1734.
1735.         region1=a.Set(referencePoints=refPoints2, name='Set-3-23')
1736.         s1 = a.instances['LongSpacerPart-23'].faces
1737.         side1Faces1 = s1.getSequenceFromMask(mask=('[#1600 ]', ), )
1738.         s2 = a.instances['ShortSpacerPart-2-23'].faces
1739.         side1Faces2 = s2.getSequenceFromMask(mask=('[#20 ]', ), )
1740.         s3 = a.instances['GlassPanePart2-1'].faces
1741.         side1Faces3 = s3.getSequenceFromMask(mask=('[#800 #4 #2000000 ]', ), )
1742.         s4 = a.instances['LongSpacerPart-2-23'].faces
1743.         side1Faces4 = s4.getSequenceFromMask(mask=('[#1600 ]', ), )
1744.         s5 = a.instances['ShortSpacerPart-1-23'].faces
1745.         side1Faces5 = s5.getSequenceFromMask(mask=('[#20 ]', ), )
1746.         s6 = a.instances['GlassPanePart3-1'].faces
1747.         side1Faces6 = s6.getSequenceFromMask(mask=('[#2000 #0 #4800 ]', ), )
1748.         region2=a.Surface(side1Faces=side1Faces1+side1Faces2+side1Faces3+side1Faces4+\
1749.             side1Faces5+side1Faces6, name='cavitysurface-23')
1750.
1751.         mdb.models['ParameterStudy' + repr(fIncrement)].FluidCavity(name='CavityInteraction23',
```

```
1752.             createStepName='Initial', cavityPoint=region1, cavitySurface=region2,
1753.             interactionProperty='CavityGas', ambientPressure=ambientPressureCavity)
1754.
1755.         # Cavity gass filling 34
1756.         #r1 = a.referencePoints
1757.         if oneWay == 1:
1758.             refPoints3=(r1[73], )
1759.         if oneWay == 2:
1760.             refPoints3=(r1[69], )
1761.
1762.         region1=a.Set(referencePoints=refPoints3, name='Set-3-34')
1763.         s1 = a.instances['LongSpacerPart-34'].faces
1764.         side1Faces1 = s1.getSequenceFromMask(mask=('[#1600 ]', ), )
1765.         s2 = a.instances['ShortSpacerPart-2-34'].faces
1766.         side1Faces2 = s2.getSequenceFromMask(mask=('[#20 ]', ), )
1767.         s3 = a.instances['GlassPanePart3-1'].faces
1768.         side1Faces3 = s3.getSequenceFromMask(mask=('[#800 #4 #2000000 ]', ), )
1769.         s4 = a.instances['LongSpacerPart-2-34'].faces
1770.         side1Faces4 = s4.getSequenceFromMask(mask=('[#1600 ]', ), )
1771.         s5 = a.instances['ShortSpacerPart-1-34'].faces
1772.         side1Faces5 = s5.getSequenceFromMask(mask=('[#20 ]', ), )
1773.         s6 = a.instances['GlassPanePart4-1'].faces
1774.         side1Faces6 = s6.getSequenceFromMask(mask=('[#2000 #0 #4800 ]', ), )
1775.         region2=a.Surface(side1Faces=side1Faces1+side1Faces2+side1Faces3+side1Faces4+\
1776.             side1Faces5+side1Faces6, name='cavitysurface-34')
1777.
1778.         mdb.models['ParameterStudy' + repr(fIncrement)].FluidCavity(name='CavityInteraction34',
1779.             createStepName='Initial', cavityPoint=region1, cavitySurface=region2,
1780.             interactionProperty='CavityGas', ambientPressure=ambientPressureCavity)
1781.
1782.     # ----------------------------------------------------------------------------------
1783.     # Create interaction with the subconstruction
1784.     if oneWay == 1:
1785.         mdb.models['ParameterStudy' + repr(fIncrement)].ContactProperty('ContactSubconstructrion')
1786.         mdb.models['ParameterStudy' + repr(fIncrement)].interactionProperties['ContactSubconstructrion'].TangentialBehavior(
1787.         formulation=FRICTIONLESS)
1788.
1789.         a = mdb.models['ParameterStudy' + repr(fIncrement)].rootAssembly
1790.         s1 = a.instances['SubconstructionPart-1'].faces
1791.         side2Faces1 = s1.getSequenceFromMask(mask=('[#7fff ]', ), )
1792.         s2 = a.instances['SubconstructionPart-2'].faces
1793.         side2Faces2 = s2.getSequenceFromMask(mask=('[#7fff ]', ), )
1794.         region1=a.Surface(side2Faces=side2Faces1+side2Faces2, name='m_Surf-31')
1795.         s1 = a.instances['GlassPanePart1-1'].faces
1796.         side1Faces1 = s1.getSequenceFromMask(mask=(
1797.             '[#24000000 #21848089 #24904920 #42404920 #810441 ]', ), )
1798.         region2=a.Surface(side1Faces=side1Faces1, name='s_Surf-31')
1799.
1800.         mdb.models['ParameterStudy' + repr(fIncrement)].SurfaceToSurfaceContactStd(
1801.             name='InteractrionSubconstruction', createStepName='Initial',
1802.             master=region1, slave=region2, sliding=FINITE, enforcement=SURFACE_TO_SURFACE,
1803.             thickness=OFF, contactTracking=TWO_CONFIG,
1804.             interactionProperty='ContactSubconstructrion', adjustMethod=NONE,
1805.             initialClearance=OMIT, datumAxis=None, clearanceRegion=None, tied=OFF,
1806.             bondingSet=None)
1807.
1808.         #Hard contact subconstruction
1809.         mdb.models['ParameterStudy' + repr(fIncrement)].interactionProperties['ContactSubconstructrion'].NormalBehavior(
1810.         pressureOverclosure=HARD,  allowSeparation=OFF,
1811.         constraintEnforcementMethod=DEFAULT)
1812.
1813.     # Create the interaction between the spacer 12 and the glass pane 2
1814.     a = mdb.models['ParameterStudy' + repr(fIncrement)].rootAssembly
1815.     s1 = a.instances['GlassPanePart2-1'].faces
1816.     side1Faces1 = s1.getSequenceFromMask(mask=(
1817.         '[#20010400 #20000009 #100 #4900 #10400 ]', ), )
```

```
    region1=a.Surface(side1Faces=side1Faces1, name='m_Surf-5')
    s1 = a.instances['ShortSpacerPart-1'].faces
    side1Faces1 = s1.getSequenceFromMask(mask=('[#c4 ]', ), )
    s2 = a.instances['LongSpacerPart-2'].faces
    side1Faces2 = s2.getSequenceFromMask(mask=('[#4c ]', ), )
    s3 = a.instances['ShortSpacerPart-2'].faces
    side1Faces3 = s3.getSequenceFromMask(mask=('[#112 ]', ), )
    s4 = a.instances['LongSpacerPart-1'].faces
    side1Faces4 = s4.getSequenceFromMask(mask=('[#980 ]', ), )
    region2=a.Surface(side1Faces=side1Faces1+side1Faces2+side1Faces3+side1Faces4,
        name='s_Surf-5')
    mdb.models['ParameterStudy' + repr(fIncrement)].SurfaceToSurfaceContactStd(name='GlassSpacer2',
        createStepName='Initial', master=region1, slave=region2, sliding=FINITE,
        thickness=ON, interactionProperty='InteractionSpacerGlass',
        adjustMethod=NONE, initialClearance=OMIT, datumAxis=None,
        clearanceRegion=None)

    mdb.models['ParameterStudy' + repr(fIncrement)].interactionProperties['InteractionSpacerGlass'].tangentialBehavior.setValues(
        formulation=FRICTIONLESS)
    mdb.models['ParameterStudy' + repr(fIncrement)].interactionProperties['InteractionSpacerGlass'].normalBehavior.setValues(
        pressureOverclosure=HARD,  allowSeparation=ON,
        constraintEnforcementMethod=DEFAULT)
    mdb.models['ParameterStudy' + repr(fIncrement)].interactions['GlassSpacer2'].setValues(
        initialClearance=OMIT, adjustMethod=TOLERANCE, sliding=FINITE,
        enforcement=SURFACE_TO_SURFACE, thickness=OFF, contactTracking=TWO_CONFIG,
        tied=OFF, adjustTolerance=tieTolerance, bondingSet=None)

    # Create the interaction between the spacer 12 and the glass pane 1
    a = mdb.models['ParameterStudy' + repr(fIncrement)].rootAssembly
    s1 = a.instances['GlassPanePart1-1'].faces
    side1Faces1 = s1.getSequenceFromMask(mask=(
        '[#80008100 #10400020 #10002480 #8000000 #2 ]', ), )
    region1=a.Surface(side1Faces=side1Faces1, name='m_Surf-7')
    s1 = a.instances['ShortSpacerPart-1'].faces
    side1Faces1 = s1.getSequenceFromMask(mask=('[#112 ]', ), )
    s2 = a.instances['LongSpacerPart-1'].faces
    side1Faces2 = s2.getSequenceFromMask(mask=('[#4c ]', ), )
    s3 = a.instances['ShortSpacerPart-2'].faces
    side1Faces3 = s3.getSequenceFromMask(mask=('[#c4 ]', ), )
    s4 = a.instances['LongSpacerPart-2'].faces
    side1Faces4 = s4.getSequenceFromMask(mask=('[#980 ]', ), )
    region2=a.Surface(side1Faces=side1Faces1+side1Faces2+side1Faces3+side1Faces4,
        name='s_Surf-7')
    mdb.models['ParameterStudy' + repr(fIncrement)].SurfaceToSurfaceContactStd(name='GlassSpacer1',
        createStepName='Initial', master=region1, slave=region2, sliding=FINITE,
        thickness=OFF, interactionProperty='InteractionSpacerGlass',
        adjustMethod=TOLERANCE, initialClearance=OMIT, datumAxis=None,
        clearanceRegion=None, tied=OFF, adjustTolerance=tieTolerance)

    # # # ----------------------------------------------------------------
    # # Apply boundary conditions

    if oneWay == 1:
        #Encastre the subconstruction
        a = mdb.models['ParameterStudy' + repr(fIncrement)].rootAssembly
        f1 = a.instances['SubconstructionPart-1'].faces
        faces1 = f1.getSequenceFromMask(mask=('[#7fff ]', ), )
        e1 = a.instances['SubconstructionPart-1'].edges
        edges1 = e1.getSequenceFromMask(mask=('[#ffffffff #3f ]', ), )
        v1 = a.instances['SubconstructionPart-1'].vertices
        verts1 = v1.getSequenceFromMask(mask=('[#ffffff ]', ), )
        f2 = a.instances['SubconstructionPart-2'].faces
        faces2 = f2.getSequenceFromMask(mask=('[#7fff ]', ), )
        e2 = a.instances['SubconstructionPart-2'].edges
        edges2 = e2.getSequenceFromMask(mask=('[#ffffffff #3f ]', ), )
        v2 = a.instances['SubconstructionPart-2'].vertices
```

```
        verts2 = v2.getSequenceFromMask(mask=('[#ffffff ]', ), )
        region = a.Set(vertices=verts1+verts2, edges=edges1+edges2, faces=faces1+\
            faces2, name='Set-1')
        mdb.models['ParameterStudy' + repr(fIncrement)].EncastreBC(name='SubConstructionEncastre',
            createStepName='Initial', region=region, localCsys=None)

        #EnforcedDisplacement
        enforcedDisplacement = radiusSubConstr*(1-math.sin(math.pi/2-lengthPane/radiusSubConstr))-0.0005
        a = mdb.models['ParameterStudy' + repr(fIncrement)].rootAssembly
        e1 = a.instances['GlassPanePart1-1'].edges
        edges1 = e1.getSequenceFromMask(mask=(
            '[#0 #10014000 #0 #1 #0 #80000000 #208 ]', ), )
        region = a.Set(edges=edges1, name='Set-3')
        mdb.models['ParameterStudy' + repr(fIncrement)].DisplacementBC(name='EnforcedDisplacement',
            createStepName='ApplyLoad', region=region, u1=UNSET, u2=UNSET,
            u3=-enforcedDisplacement, ur1=UNSET, ur2=UNSET, ur3=UNSET, amplitude=UNSET, fixed=OFF,
            distributionType=UNIFORM, fieldName='', localCsys=None)

        #Pin glass pane 1 on the upper side
        a = mdb.models['ParameterStudy' + repr(fIncrement)].rootAssembly
        e1 = a.instances['GlassPanePart1-1'].edges
        edges1 = e1.getSequenceFromMask(mask=('[#240000 #0 #100000 #200 #0 #882000 ]',
            ), )
        region = a.Set(edges=edges1, name='Set-11')
        mdb.models['ParameterStudy' + repr(fIncrement)].PinnedBC(name='Pin-GlassPane1',
            createStepName='Initial', region=region, localCsys=None)

    if oneWay == 2 :
        a = mdb.models['ParameterStudy' + repr(fIncrement)].rootAssembly

        #Enforced displacement
        v1 = a.instances['GlassPanePart2-1'].vertices
        verts1 = v1.getSequenceFromMask(mask=('[#0:2 #20000000 ]', ), )
        region = a.Set(vertices=verts1, name='Set-4')
        mdb.models['ParameterStudy' + repr(fIncrement)].DisplacementBC(name='Displacement',
            createStepName='ApplyLoad', region=region, u1=UNSET, u2=UNSET, u3=displacementTwo,
            ur1=UNSET, ur2=UNSET, ur3=UNSET, amplitude=UNSET, fixed=OFF,
            distributionType=UNIFORM, fieldName='', localCsys=None)

        #Pin edges
        v1 = a.instances['GlassPanePart2-1'].vertices
        verts1 = v1.getSequenceFromMask(mask=('[#0:2 #10000 ]', ), )
        v2 = a.instances['GlassPanePart1-1'].vertices
        verts2 = v2.getSequenceFromMask(mask=('[#0:2 #4000400 ]', ), )
        region = a.Set(vertices=verts1+verts2, name='Set-7')
        mdb.models['ParameterStudy' + repr(fIncrement)].PinnedBC(name='FixEdges',
            createStepName='Initial', region=region, localCsys=None)

    # # -------------------------------------------------------------------
    # # Create the mesh

    import mesh

    meshScaler=lengthPane/3.5

    if lengthPane>3.5 :
        meshScaler=int(1)

    meshMinSize1=0.01
    meshMaxSize1=0.1*meshScaler

    meshMinSize2=0.005
    meshMaxSize2=0.05*meshScaler

    meshMinSizeSub=0.02
    meshMaxSizeSub=0.2*meshScaler
```

```
1950.
1951.     adjustMeshNumber=6
1952.
1953.     #Element types in use
1954.     elemType1 = mesh.ElemType(elemCode=C3D20, elemLibrary=STANDARD)
1955.     elemType2 = mesh.ElemType(elemCode=C3D15, elemLibrary=STANDARD)
1956.     elemType3 = mesh.ElemType(elemCode=C3D10, elemLibrary=STANDARD)
1957.     elemType4 = mesh.ElemType(elemCode=C3D20H, elemLibrary=STANDARD) #elemType1 but hybrid
1958.
1959.     elemType1Shell = mesh.ElemType(elemCode=S8R5, elemLibrary=STANDARD)
1960.     elemType2Shell = mesh.ElemType(elemCode=STRI65, elemLibrary=STANDARD)
1961.
1962.     #Mesh glass pane 1
1963.     p = mdb.models['ParameterStudy' + repr(fIncrement)].parts['GlassPanePart1']
1964.     e = p.edges
1965.     pickedEndEdges = e.getSequenceFromMask(mask=('[#ffffffff:6 #fffff ]', ), )
1966.     p.seedEdgeByBias(biasMethod=DOUBLE, endEdges=pickedEndEdges, minSize=meshMinSize1,
1967.         maxSize=meshMaxSize1, constraint=FINER)
1968.     p.generateMesh()
1969.     c = p.cells
1970.     cells = c.getSequenceFromMask(mask=('[#ffffffff #7 ]', ), )
1971.     pickedRegions =(cells, )
1972.     p.setElementType(regions=pickedRegions, elemTypes=(elemType1, elemType2,
1973.         elemType3))
1974.
1975.     #Mesh glass pane 2
1976.     p = mdb.models['ParameterStudy' + repr(fIncrement)].parts['GlassPanePart2']
1977.     e = p.edges
1978.     pickedEndEdges = e.getSequenceFromMask(mask=('[#ffffffff:6 #fffff ]', ), )
1979.     p.seedEdgeByBias(biasMethod=DOUBLE, endEdges=pickedEndEdges, minSize=meshMinSize1,
1980.         maxSize=meshMaxSize1, constraint=FINER)
1981.     p.generateMesh()
1982.     c = p.cells
1983.     cells = c.getSequenceFromMask(mask=('[#ffffffff #7 ]', ), )
1984.     pickedRegions =(cells, )
1985.     p.setElementType(regions=pickedRegions, elemTypes=(elemType1, elemType2,
1986.         elemType3))
1987.
1988.     if thicknessGlassPane3>1e-12:
1989.         #Mesh glass pane 3
1990.         p = mdb.models['ParameterStudy' + repr(fIncrement)].parts['GlassPanePart3']
1991.         e = p.edges
1992.         pickedEndEdges = e.getSequenceFromMask(mask=('[#ffffffff:6 #fffff ]', ), )
1993.         p.seedEdgeByBias(biasMethod=DOUBLE, endEdges=pickedEndEdges, minSize=meshMinSize1,
1994.             maxSize=meshMaxSize1, constraint=FINER)
1995.         p.generateMesh()
1996.         c = p.cells
1997.         cells = c.getSequenceFromMask(mask=('[#ffffffff #7 ]', ), )
1998.         pickedRegions =(cells, )
1999.         p.setElementType(regions=pickedRegions, elemTypes=(elemType1, elemType2,
2000.             elemType3))
2001.
2002.         if thicknessGlassPane4>1e-12:
2003.             #Mesh glass pane 4
2004.             p = mdb.models['ParameterStudy' + repr(fIncrement)].parts['GlassPanePart4']
2005.             e = p.edges
2006.             pickedEndEdges = e.getSequenceFromMask(mask=('[#ffffffff:6 #fffff ]', ), )
2007.             p.seedEdgeByBias(biasMethod=DOUBLE, endEdges=pickedEndEdges, minSize=meshMinSize1,
2008.                 maxSize=meshMaxSize1, constraint=FINER)
2009.             p.generateMesh()
2010.             c = p.cells
2011.             cells = c.getSequenceFromMask(mask=('[#ffffffff #7 ]', ), )
2012.             pickedRegions =(cells, )
2013.             p.setElementType(regions=pickedRegions, elemTypes=(elemType1, elemType2,
2014.                 elemType3))
2015.
```

```
    #Mesh long spacer
    p = mdb.models['ParameterStudy' + repr(fIncrement)].parts['LongSpacerPart']
    e = p.edges
    pickedEndEdges = e.getSequenceFromMask(mask=('[#ffffffff #3 ]', ), )
    p.seedEdgeByBias(biasMethod=DOUBLE, endEdges=pickedEndEdges, minSize=meshMinSize2,
        maxSize=meshMaxSize2, constraint=FINER)
    pickedEndEdges = e.getSequenceFromMask(mask=('[#4b0000 ]', ), )
    p.seedEdgeByBias(biasMethod=DOUBLE, endEdges=pickedEndEdges, ratio=1.0,
        number=adjustMeshNumber, constraint=FINER)
    pickedEndEdges = e.getSequenceFromMask(mask=('[#2000020a ]', ), )
    p.seedEdgeByBias(biasMethod=DOUBLE, endEdges=pickedEndEdges, ratio=1.0,
        number=adjustMeshNumber, constraint=FINER)
    p.generateMesh()
    f = p.faces
    faces = f.getSequenceFromMask(mask=('[#3fff ]', ), )
    pickedRegions =(faces, )
    p.setElementType(regions=pickedRegions, elemTypes=(
    elemType1Shell, elemType2Shell))

    f = p.faces
    pickedRegions = f.getSequenceFromMask(mask=('[#2010 ]', ), )
    p.deleteMesh(regions=pickedRegions)
    e = p.edges
    pickedEndEdges = e.getSequenceFromMask(mask=('[#8000a000 #2 ]', ), )
    p.seedEdgeByBias(biasMethod=DOUBLE, endEdges=pickedEndEdges, ratio=1.0,
        number=2, constraint=FINER)
    p.generateMesh()

    f = p.faces
    pickedRegions = f.getSequenceFromMask(mask=('[#9cc ]', ), )
    p.deleteMesh(regions=pickedRegions)
    e = p.edges
    pickedEndEdges = e.getSequenceFromMask(mask=('[#10b40580 ]', ), )
    p.seedEdgeByBias(biasMethod=DOUBLE, endEdges=pickedEndEdges, ratio=1.0,
        number=2, constraint=FINER)
    p.generateMesh()

    #Mesh short spacer
    p = mdb.models['ParameterStudy' + repr(fIncrement)].parts['ShortSpacerPart']
    e = p.edges
    pickedEndEdges = e.getSequenceFromMask(mask=('[#3ffffff ]', ), )
    p.seedEdgeByBias(biasMethod=DOUBLE, endEdges=pickedEndEdges, minSize=meshMinSize2,
        maxSize=meshMaxSize2, constraint=FINER)
    p.generateMesh()
    p = mdb.models['ParameterStudy' + repr(fIncrement)].parts['ShortSpacerPart']
    f = p.faces
    faces = f.getSequenceFromMask(mask=('[#3ff ]', ), )
    pickedRegions =(faces, )
    p.setElementType(regions=pickedRegions, elemTypes=(elemType1Shell, elemType2Shell))

    f = p.faces
    pickedRegions = f.getSequenceFromMask(mask=('[#38e ]', ), )
    p.deleteMesh(regions=pickedRegions)
    e = p.edges
    pickedEndEdges = e.getSequenceFromMask(mask=('[#c05aa0 ]', ), )
    p.seedEdgeByBias(biasMethod=DOUBLE, endEdges=pickedEndEdges, ratio=1.0,
        number=2, constraint=FINER)
    f = p.faces
    pickedRegions = f.getSequenceFromMask(mask=('[#50 ]', ), )
    p.deleteMesh(regions=pickedRegions)
    e = p.edges
    pickedEndEdges = e.getSequenceFromMask(mask=('[#1310550 ]', ), )
    p.seedEdgeByBias(biasMethod=DOUBLE, endEdges=pickedEndEdges, ratio=1.0,
        number=2, constraint=FINER)
    p.generateMesh()

```

```
    #Mesh secondary seal
    p = mdb.models['ParameterStudy' + repr(fIncrement)].parts['SecSealPart']
    e = p.edges
    pickedEndEdges = e.getSequenceFromMask(mask=('[#ffffffff:5 ]', ), )
    p.seedEdgeByBias(biasMethod=DOUBLE, endEdges=pickedEndEdges, minSize=meshMinSize2,
    maxSize=meshMaxSize2, constraint=FINER)
    e = p.edges
    pickedEndEdges = e.getSequenceFromMask(mask=('[#0 #1a0000 #0:2 #4000000 ]', ),
        )
    p.seedEdgeByBias(biasMethod=DOUBLE, endEdges=pickedEndEdges, ratio=1.0,
        number=adjustMeshNumber, constraint=FINER)
    e = p.edges
    pickedEndEdges = e.getSequenceFromMask(mask=('[#1a00000 #0:2 #1000 ]', ), )
    p.seedEdgeByBias(biasMethod=DOUBLE, endEdges=pickedEndEdges, ratio=1.0,
        number=adjustMeshNumber, constraint=FINER)
    e = p.edges
    pickedEndEdges = e.getSequenceFromMask(mask=('[#450 #0:2 #40000 ]', ), )
    p.seedEdgeByBias(biasMethod=DOUBLE, endEdges=pickedEndEdges, ratio=1.0,
        number=adjustMeshNumber, constraint=FINER)
    e = p.edges
    pickedEndEdges = e.getSequenceFromMask(mask=('[#0 #68 #0:2 #2000000 ]', ), )
    p.seedEdgeByBias(biasMethod=DOUBLE, endEdges=pickedEndEdges, ratio=1.0,
        number=adjustMeshNumber, constraint=FINER)
    p.generateMesh()
    c = p.cells
    cells = c.getSequenceFromMask(mask=('[#fffff ]', ), )
    pickedRegions =(cells, )
    #hybrid elements
    p.setElementType(regions=pickedRegions, elemTypes=(elemType4, elemType2,
        elemType3))

    c = p.cells
    pickedRegions = c.getSequenceFromMask(mask=('[#fffff ]', ), )
    p.deleteMesh(regions=pickedRegions)
    p = mdb.models['ParameterStudy' + repr(fIncrement)].parts['SecSealPart']
    e = p.edges
    pickedEndEdges = e.getSequenceFromMask(mask=(
        '[#52094905 #25209610 #12090148 #4408149 #4082a021 ]', ), )
    p.seedEdgeByBias(biasMethod=DOUBLE, endEdges=pickedEndEdges, ratio=1.0,
        number=3, constraint=FINER)
    e = p.edges
    pickedEndEdges = e.getSequenceFromMask(mask=(
        '[#ac56b2aa #5ac56987 #ad762eb1 #79b042b6 #b97d5fde ]', ), )
    p.seedEdgeByBias(biasMethod=DOUBLE, endEdges=pickedEndEdges, ratio=1.0,
        number=2, constraint=FINER)
    p.generateMesh()

    if oneWay == 1:
        #Mesh the subconstruction
        p = mdb.models['ParameterStudy' + repr(fIncrement)].parts['SubconstructionPart']
        e = p.edges
        pickedEndEdges = e.getSequenceFromMask(mask=('[#ffffffff #3f ]', ), )
        p.seedEdgeByBias(biasMethod=DOUBLE, endEdges=pickedEndEdges, minSize=meshMinSizeSub,
            maxSize=meshMaxSizeSub, constraint=FINER)
        f = p.faces
        faces = f.getSequenceFromMask(mask=('[#7fff ]', ), )
        pickedRegions =(faces, )
        p.setElementType(regions=pickedRegions, elemTypes=(elemType1Shell, elemType2Shell))
        p.generateMesh()

    # # ----------------------------------------------------------------
    # # Create and run the job

    import job

    mdb.models['ParameterStudy' + repr(fIncrement)].setValues(
```

```
2148.       description='This is an automatic generated model based on a python script by Franz Polzl from TU Graz, 2016/2017 \n',
2149.       absoluteZero=-275.15, universalGas=8.3144598)
2150.
2151.       # Create the job
2152.       job_name='PS' + repr(fIncrement)
2153.       mdb.Job(name=job_name, model='ParameterStudy' + repr(fIncrement), description='', type=ANALYSIS,
2154.               explicitPrecision=SINGLE, nodalOutputPrecision=SINGLE,
2155.               parallelizationMethodExplicit=DOMAIN, multiprocessingMode=DEFAULT,
2156.               numDomains=CPU_in_use, userSubroutine='', numCpus=CPU_in_use, memory=max_Memory,
2157.               memoryUnits=PERCENTAGE, scratch='', echoPrint=OFF, modelPrint=OFF,
2158.               contactPrint=OFF, historyPrint=OFF, numGPUs=1)
2159.
2160.       # Run the job
2161.       timeStart = datetime.datetime.now()
2162.       if calculation == 1:
2163.           mdb.jobs[job_name].submit(consistencyChecking=OFF)
2164.
2165.       # Do not return control till job is finished running
2166.       if calculation == 1:
2167.           mdb.jobs[job_name].waitForCompletion()
2168.
2169.           #To get Calculationtime
2170.           timeEnd = datetime.datetime.now()
2171.           print '!MA Job ' + repr(BearingType) + ' done! used time ' + str(timeEnd-timeStart)
2172.
2173.       #-----------------------------------------------------------------------------
2174.   # -----------------------------------------------------------------------------
2175. # -----------------------------------------------------------------------------
```